

©Copyright by Greg Bryan, 1996

THE NUMERICAL SIMULATION OF X-RAY CLUSTERS

BY

GREG BRYAN

B.S., University of Calgary, 1989

THESIS

Submitted in partial fulfillment of the requirements
for the degree of Doctor of Philosophy in Astronomy
in the Graduate College of the
University of Illinois at Urbana-Champaign, 1996

Urbana, Illinois

NUMERICAL SIMULATIONS OF X-RAY CLUSTERS

Greg Bryan, Ph.D.

Department of Astronomy

University of Illinois at Urbana-Champaign, 1996

Michael Norman, Advisor

We describe efforts to model the formation and evolution of X-ray clusters. After summarizing the current state of cluster observations, we describe the computational method used to model both the hot gas as well as the dark, collisionless component that observations imply. This code employs a higher-order accurate fluid-dynamics method for improved resolution and its accuracy is tested by a suite of tests.

Using this method, we have modeled the large-scale distribution of clusters for both the Cold Dark Matter (CDM) and Cold plus Hot Dark Matter (CHDM) scenarios. We find that CDM produces too many clusters when compared to observations. The CHDM model seems to match the observed distribution, both in terms of temperature and luminosity, although the luminosity of a cluster is not well determined in these simulations, due to limited resolution.

We compare the simulated clusters against analytic laws which provide scaling relations between the clusters' bulk properties and redshift. These are found to agree relatively well for the mass, velocity dispersion and temperature of a cluster. Although the luminosity does not agree as well, this is well explained by the fixed resolution of the simulations. These scaling relations are combined with a simple prescription for determining the number density as a function of mass to compute differential temperature and luminosity distributions including the effects of limited bandwidth and metallicity.

We also examine the structure of cluster halos with higher resolution simulations, showing that shocks play an important role in cluster formation. Turbulent motions in the gas provide some support against gravity and decrease the temperature below that required by hydrostatic equilibrium. The temperature structure of the halos are directly compared to recent x-ray satellite observations.

Finally, we briefly describe, and present first results from, a new Adaptive Mesh Refinement (AMR) cosmological simulation code. The algorithm has the benefits of

Eulerian hydrodynamics techniques as well as adaptive resolution that follows the solution as it evolves. Results are presented from a simulation of an X-ray cluster that achieved a nominal spatial resolution (box length/cell size) of more than 8000, in selected regions.

Acknowledgments

This work was supported in part by National Science Foundation grant ASC 93-18185 and NASA Long Term Space Astrophysics grant NAGW-3152.

This is really the work of many people and I am grateful to all of them for their help and encouragement. First I would like to thank my advisor, Michael Norman, who started me on this path many years ago and has been a constant source of inspiration and help, not to mention funding. His clear insight and intuition have helped to shape my own understanding of the subject. I thank another of Mike's Canadian students, Jim Stone, who gently guided me in the right direction when I first arrived in Illinois. Also, my appreciation to the rest of my committee: Ed Bertschinger, Susan Lamb and Laird Thompson, who have all provided good grounding.

My collaborators on much of the work described here, Jack Burns, Renyue Cen, Anatoly Klypin, Chris Loken, Jeremiah Ostriker, and Kurt Roettiger are all due a note of appreciation. Thanks to Jean Soliday and Carol Stickrod for much administrative magic, all done with a smile. I am grateful also to the kindness of friends: Jennifer Barrows, Racheal Freyman, Kelly Grant, Brian McNurlen and especially Michele Plante, whose patience seemed without end.

I would also like to thank my colleagues at NCSA and the Astronomy Department: Tom Abel, Bob 'Robert' Fiedler, Pat Moran, Ray Plante, Doug Roberts, Barry Sanders, John Shalf, Chris Song, Doug Swesty, Rolaine Young-Owl and many others, too numerous to mention. I am especially grateful to those who helped me to better understand astronomy and cosmology, Peter Anninos, B.I. Jun and Yu Zhang. Particular thanks to Henry Neeman, for sanity preserved.

Throughout this endeavor, my family has provided much support and encouragement: Dawn, Richard, Joel and Aphra, but especially my parents, Larry and Eleanor, whose love and generosity made all of this possible. Thank you.

Table of Contents

Chapter

1	Introduction	1
1.1	Structure of the Dissertation	2
2	Review of Observations	5
2.1	Statistical measures	5
2.1.1	Optical	6
2.1.2	X-ray	8
2.2	Cluster Structure	10
3	A Piecewise Parabolic Method for Cosmological Hydrodynamics	15
3.1	Introduction	15
3.2	Numerical Methodology	17
3.2.1	Structure of the cosmological equations of hydrodynamics	19
3.2.2	The piecewise parabolic method in cosmology	22
3.2.3	Adding gravity to the PPM scheme	26
3.2.4	The dual energy formulation for high Mach flows	27
3.2.5	The correction to the Riemannn solver	29
3.2.6	The Layzer-Irvine cosmic energy equation	30
3.2.7	Code structure and overview	30
3.3	Cosmological Tests	32
3.3.1	One dimensional pressureless collapse	32

3.3.2	The Jeans instability	34
3.3.3	Adiabatic expansion	34
3.3.4	The linear phase of the one dimensional Zel'dovich pancake	35
3.3.5	The non-linear phase of the one dimensional Zel'dovich pancake .	36
3.3.6	The double pancake with a strong and weak shock	42
3.3.7	Two dimensional self-convergence tests	46
3.3.8	Comparison with other codes	50
3.4	Conclusions	50
4	X-Ray Clusters from a Hydrodynamic Simulation of the CDM Universe	52
4.1	Introduction	52
4.2	Method And Initial Conditions	55
4.2.1	Initial Conditions	56
4.3	Results	56
4.4	Conclusion	71
5	The Evolution of X-ray Clusters in a Cold plus Hot Dark Matter Uni-	
verse	78
5.1	Introduction	78
5.2	Simulations	79
5.3	Results and Discussion	82
5.3.1	Luminosity and Temperature Distribution Functions	82
5.3.2	Discussion of Errors	85
5.4	Conclusions	87
6	Statistical Properties of X-ray Clusters: Analytic and Numerical Com-	
parisons	89
6.1	Introduction	89
6.2	Scaling Relations	91
6.2.1	Scaling review and normalization	92

6.2.2	Resolution effects	94
6.2.3	Comparison to simulations	95
6.3	Distribution Functions	107
6.3.1	Metallicity Effects	117
6.4	Cluster structure	118
6.5	Conclusion	122
7	The Formation and Structure of Cluster X-Ray Halos	125
7.1	Introduction	125
7.2	Simulations	126
7.3	Radial profiles	127
7.4	Cluster structure	134
7.4.1	Projected images	134
7.4.2	Slices	142
7.5	Comparison to Observations	147
7.6	Conclusion	153
8	Adaptive Mesh Refinement Simulations of X-ray Clusters: Preliminary	
Results	155
8.1	Introduction	155
8.2	Methodology	157
8.2.1	The Grid Hierarchy	157
8.2.2	Hydrodynamics	158
8.2.3	Dark matter	159
8.2.4	Gravity	160
8.2.5	Tests	160
8.3	Results	161
8.4	Conclusions	168

9 Conclusion	172
9.1 Summary	172
9.2 Future Work	174
List of References	176
Curriculum Vitae	189

Chapter 1

Introduction

Clusters of galaxies present two challenges: how were they formed? and how did their current distribution in space come about? The answers to these questions provide important clues to the kind of a universe we live in as well as its final fate. Clusters are also interesting for their own sake: they are the largest known virialized structures and are also among the brighter objects in the X-ray sky.

Because of their high intrinsic luminosity ($L_{\text{X-ray}} \sim 10^{45}$ erg/s) they can be seen to immense distances; the process of mapping the cluster distribution at $z \sim 0 - 1$ has already begun and the continued launching of more sensitive and versatile X-ray telescopes (such as ROSAT, ASCA and AXAF) promises that this progress will continue. Only quasars serve as more distant lighthouses. The distribution of clusters, like that of galaxies, gives us hints to the mechanism of structure formation. However, in order to make direct comparisons between such theories and the observed distribution of X-ray clusters, we must be able to accurately predict when a cluster will form and, once formed, what its properties will be: temperature, mass and luminosity.

These requirements imply a detailed understand of the internal dynamics of X-ray clusters. Once thought to be spherical balls of hot, virialized gas, it has become clear in recent years, that even previously prototypically relaxed clusters, such as Coma, show, on closer inspection, a myriad of substructure and dynamic behaviour (White, Briel & Henry 1993). This implies that they have recently been disturbed by their environment. The

word recent here means within a few crossing times, a number that can be a substantial fraction of the length of the universe for the largest clusters.

This exterior influence, almost surely due to infalling material (some of which can be seen in high-resolution X-ray images) highlights the difficulty and promise of modeling clusters. Clusters cannot be simulated in isolation as they appear to be formed in large measure by merging with other, smaller, clusters. Also, they are affected by the tidal influences of the neighbouring mass distribution. After this infall is cut off, clusters will, of course, revert — like stars — to a state of hydrostatic equilibrium; a situation much easier to understand and model. Observations, both optical studies of the distribution of galaxies within clusters and X-ray observations of the hot gas itself, show that this has not yet occurred for at least a sizable fraction of the objects (Jones & Forman 1992). Although making them more difficult to understand, it also ensures that they contain clues to their formation and environment.

These two problems, then, the large-scale distribution of X-ray clusters and their internal structure, are intertwined and must be studied together. To obtain answers to these questions we will follow a two-pronged approach in this thesis. On one side, large volumes of space must be simulated in order to obtain a sufficient number of clusters for statistical analysis. On the other hand, individual clusters contain structure that cannot be sufficiently resolved in simulations of such large volumes but may be modeled one at a time with high resolution grids. In fashioning such a solution, it is important to create not just a one-shot scheme, but a generalized tool that is capable of answering a wide variety of cosmological questions.

1.1 Structure of the Dissertation

In the next chapter (chapter 2) we briefly explore some observations of clusters of galaxies. These are grouped into two sections: the large-scale distribution of clusters from optical and X-ray surveys and observations that provide information about the structure of clusters themselves.

The numerical methodology that we will use throughout the paper (except for Chapter 8) is described in detail in Chapter 3. This includes both a description of the numerical algorithm as well as the cosmological tests that we use to characterize the code's performance. The majority of this chapter has been previously published (Bryan et al. 1995).

The next three chapters examine statistical properties of a fairly large number of clusters and together, they form the first prong of the approach described above. The first two address specific cosmological models, looking at the level of agreement between predicted properties and observed ones, while the third chapter takes a detailed look at the accordance (or lack thereof) between analytic relations and numerical results.

The Cold Dark Matter (CDM) model is investigated through X-ray clusters in Chapter 4. In it, we are primarily interested how the number density of clusters at the present day (as a function of luminosity, temperature and radius) constrains the viability of the model. However, we also examine a number of other features, such as the evolution of the luminosity function and the total emissivity of the gas, the relation between cluster temperature and luminosity, as well as some indications of cluster structure. The chapter, as included here, has been published elsewhere (Bryan et al. 1994a).

The next chapter is shorter and looks only at luminosity and temperature distribution functions, as well as the relation between a cluster's temperature and luminosity. This is done for the Cold plus Hot Dark Matter (CHDM) model which seems to make a better match with observations than that described in Chapter 3. We also make a very brief foray into the affects of resolution, but this is mostly left for the next chapter. This is the last section to have been previously published (Bryan et al. 1994b).

In Chapter 6, we examine a set of analytic scaling laws that relate various bulk quantities of the cluster (such as mass, temperature, velocity dispersion and luminosity) to one another and to redshift. We redevelop these relations from first principles (except for the cluster luminosity) and compare them to simulated clusters using the simulations previously discussed and a new, higher resolution simulation in order to gauge the effects of resolution and cosmology. We address the accuracy of the Press-Schechter prescription for

determining the number of collapsed halos, as well as extending it to model temperature and luminosity, including the effects of limited band-pass and metallicity.

The previous chapter includes some discussion of cluster structure and serves as a segue into the detailed description presented in Chapter 7. We select our most highly resolved clusters of the high-resolution simulation from Chapter 6 and a new, even higher-resolution CDM simulation. With these, we investigate azimuthally-averaged radial profiles of density, temperature and various velocity-related terms in order to compare the behaviour of the dark matter and gas. We also examine projected temperature maps and various slices, ending with a comparison with recent ROSAT and ASCA observational results.

Chapter 8 describes some preliminary results from the first cosmological simulation using our newly-developed Adaptive Mesh Refinement (AMR) algorithm. After briefly describing the fundamentals of this method, we examine results from a simulation of a single cluster in a box 64 Mpc on side with a nominal resolution (in very small regions) as high as 8 kpc. We continue the examination of cluster structure, focusing on the central regions.

Finally, in the last chapter we summarize the major new results presented in this thesis and discuss directions for future work.

Chapter 2

Review of Observations

Clusters of galaxies were first observed through optical telescopes as close groupings of galaxies on the sky. Although optical observations will be briefly described in this chapter, more time will be spent on results from the relatively small number of X-ray satellites launched in the much more recent past. These telescopes directly observe the hot gas in clusters, providing information that is often easier to interpret than that provided by galaxies. Clusters are also easier to identify via the free-free emission of their hot gas, which is a function of the square of their baryonic density, whereas galaxy counts are simply proportional to the density. This has caused confusion in the past, as optical clusters can be difficult to pick out against the relatively high background of field galaxies, or, worse yet, a spurious large cluster can appear when two, unconnected, smaller agglomerations are projected near each other in the sky. Also, the integration time for X-ray observations can be made, in principle, arbitrarily large, while there are a limited number of galaxies in a cluster. Finally, the hot gas component is much easier to simulate than the dense, multi-phase galaxies.

2.1 Statistical measures

Here we sketch the distribution functions and clustering properties of clusters of galaxies, breaking this into optical and X-ray observations.

2.1.1 Optical

Although there are a number of difficulties in constructing complete, unbiased optical cluster samples, by far the largest cluster catalogues come from identifying galaxy excesses in surveys. Here we don't attempt an exhaustive list, but simply present a summary of a few representative works.

Abell (1958, 1965) was the first to produce a systematically identified catalogue of clusters by identifying overdensities of galaxies within a fixed, metric radius of $1.5 h^{-1}\text{Mpc}$. He identified about 1700 of the nearest clusters to approximately $z \sim 0.2$ in the northern hemisphere. The mean space density of Abell cluster (of richness class 1 and above) is about $10^{-5} h^3 \text{Mpc}^{-3}$ (Bahcall 1988). This work was extended to the southern hemisphere (Abell, Corwin & Olowin 1989) with a sample of over 4000 rich clusters.

While this work still remains the largest volume cluster survey, there is some evidence that the catalogue is affected by selection biases (Sutherland 1988, Efstathiou et al. 1992b). Thus, there have been a number of attempts to produce more uniform samples, such as from automated plate scanners, as in the APM redshift survey (Dalton et al. 1992, Maddox et al. 1990).

One of the results of such samples is the number density of clusters as a function of richness. Unfortunately, this is highly sensitive to one's definition of cluster richness: the number of galaxies detected in a cluster is strongly dependent on the limiting magnitude of the underlying survey. While the luminosity function of a small number of clusters can be found (e.g. Schechter 1976), even this is difficult to compare to simulations which do not yet directly produce galaxies with reliable luminosities (or, indeed, produce reliable galaxies). Therefore, we turn to other statistics which are somewhat easier to compare to simulations.

The mass function of clusters tries to circumvent this problem by using the total mass within a fixed radius. While this is relatively easy to determine analytically or numerically, it is a difficult observational feat. One attempt (Bahcall & Cen 1993), used optical and X-ray mass determinations to find the mass within a fixed radius ($1.5 h^{-1}$

Mpc) of a collection of groups and clusters. The resulting distribution is well fit from 10^{13} – $10^{15} h^{-1} M_{\odot}$ by a Schechter function:

$$n(> M) = 4 \times 10^{-5} (M/M_*)^{-1} \exp(-M/M_*) h^3 \text{Mpc}^{-3}. \quad (2.1)$$

where $M_* = (1.8 \pm 0.3) \times 10^{14} h^{-1} M_{\odot}$. A power-law distribution was found by Biviano et al. (1993) for a set of 74 nearby Abell clusters for the differential mass function for the narrow range of 4×10^{14} – $2 \times 10^{15} h^{-1} M_{\odot}$:

$$n(M) dM = 3\text{--}5 \times 10^{-6} h^{1.7} (M/10^{15} M_{\odot})^{-2.3} \text{Mpc}^{-3} (10^{15} M_{\odot})^{-1}. \quad (2.2)$$

Unfortunately, the mass determination of clusters to such large radii is fraught with uncertainty, both statistical and systematic.

Closely related to this is the distribution of σ , the line-of-sight cluster velocity dispersion. If the clusters are relaxed and galaxies trace the mass distribution, this quantity is simply related to the mass distribution; however it can be compared directly to simulations without making these assumptions. Frenk et al. (1990) make detailed comparisons between the the velocity dispersion distribution function of 93 Abell clusters and simulated (CDM) clusters. They found that when clusters were identified in two dimensions using the same procedure as Abell (1958), projections effects strongly influenced the results, producing a spurious tail of high-velocity dispersion clusters resulting from chance projections between nearby clusters, as well as missing many low- σ clusters against the sky background.

Another statistic is the two-point correlation function of clusters with a number density n defined through the joint probability of two clusters being separated by a distance r in volume elements V_1 and V_2 :

$$dP = n^2 [1 + \xi(r)] dV_1 dV_2. \quad (2.3)$$

This is found observationally (Bahcall 1988) to be $\xi(r) = (r_0/r)^{1.8}$ where r_0 is the correlation length. The value of r_0 is somewhat uncertain, with Abell clusters giving $r_0 \sim 20 - 25 h^{-1} \text{Mpc}$ (Klypin & Kopylov 1983) and the smaller, more uniform surveys

(such as the APM survey) result in $r_0 = 13 - 16 h^{-1}$ Mpc. The Abell surveys also indicate that the correlation length increases with cluster richness according to $r_0 \sim 0.4d$ where d is the mean intercluster separation (Bahcall & Burgett 1986, Bahcall & Cen 1994). This may explain the discrepancy. For analytic work on this problem in the context of cosmological models see Mo, Jing & White (1996).

If the true distance to a large number of clusters with known redshifts can be found, the resulting peculiar velocities may be used to check for large-scale motions of the survey volume. If the largest scales probed are homogeneous, then one expects that the resulting motion (often referred to as a dipole due to the resulting sky distribution) should agree closely with the inertial frame defined by the cosmic background radiation (Kogut et al. 1993). A number of attempts have been made to measure this dipole, with conflicting results. Branchini, Plionis & Sciamia (1996) use a dynamical reconstruction procedure based on the gravitational linear instability to deduce a dipole within 25,000 km/s that agrees well with the one measured by COBE. Similar results have been found by a number of authors using Abell clusters (Scaramella, Vettolani, Zamorani 1991), SNIa (Riess, Press & Kirshner 1995) and X-ray clusters (Lahav et al. 1989). On the other hand, a survey using the brightest cluster galaxy to determine distances to clusters within 15,000 km/s (Lauer & Postman 1994) finds a dipole direction almost 90° away from the CBR; for a discussion of this discrepancy, see Watkins & Feldman (1995). There is also an interesting review by Dekel (1994).

Other statistical measures that have been used to characterize and compare observational samples are the integral of the two-point correlation function (known as the J_3 integral), the smoothed density probability function as well as higher moments of the density field (Borgani et al. 1994, Cappi & Maurogordato 1995).

2.1.2 X-ray

The easiest X-ray information to obtain about a cluster aside from its position in the sky, is its intrinsic X-ray luminosity (usually within a given passband). This can be obtained from its flux and a few redshifts or other distance indicators. To find the temperature

of a cluster requires collecting enough photons for a spectral fit. This means that the luminosity distribution for nearby clusters is well known, although most catalogs are flux-limited, rather than volume-limited and hence must be treated with some caution.

Two of the best collections are the *Einstein* Extended Medium Sensitivity Survey (Gioia et al. 1990) and a catalog extracted from the archives of *UHURU*, *Ariel-V* and *HEAO-1* (Edge et al. 1990). The resulting distribution is well fit over its entire range by a power law (although there is some indication of a cutoff at high luminosity). The 2 – 10 keV luminosity function of the Edge et al. sample is given by:

$$\frac{dN}{dL_{2-10}} = 3 \times 10^{-7} (L_{2-10}/10^{44} \text{ erg/s})^{-2.2} (10^{44} \text{ erg s}^{-1})^{-1} \text{ Mpc}^{-3}. \quad (2.4)$$

This sample used clusters for which temperatures could be determined, so a temperature distribution function was also computed,

$$\frac{dN}{dT} = 1 \times 10^{-4} T^{-4.9} \text{ Mpc}^{-3} \text{ keV}^{-1}. \quad (2.5)$$

Although this is the average temperature of a cluster (weighted by X-ray emission), the few clusters for which the spatial temperature distribution has been resolved shows that most of the gas is at or near this characteristic temperature.

It was also noted from early on that there exists a strong correlation between a cluster's temperature and its luminosity. This relation (Davis & Mushotzky 1993; Edge & Stewart 1991a), $L \sim T^{\sim 3.5}$, does not agree with simple scaling arguments ($L \propto M^2 \propto T^2$), the reasons for which are not well understood (Navarro, Frenk & White 1994). There are also correlations between the gas mass within 0.5 Mpc and the luminosity and temperature as well a strong correlation between luminosity and the cluster spiral fraction (Edge & Stewart 1991a; Edge & Stewart 1991b).

The ROSAT all-sky survey and pointed observations have, in conjunction with shuttle borne missions such as *Spartan 1*, *BBXRT* and *Astro D*, provided the enhanced sensitivity needed to detect the medium redshift ($z \sim 0.5$) clusters. Although the ROSAT results are incomplete, there are some indications that the largest clusters have undergone substantial changes in the recent past.

This evolution was first hinted at in the lower redshift surveys already mentioned. Additional evidence comes from surveys at intermediate and high redshifts: $z \approx 0.22$ (Henry 1992); $z \approx 0.4$ (Bower et al. 1994); $z \approx 0.7$ (Castander et al. 1993; Nichol et al. 1994). Unfortunately, the completeness of samples decreases strongly with distance and the highest redshift results depend on a handful of clusters.

Larger surveys such as that produced by ROSAT (Ebeling et al. 1996) have already produced X-ray selected luminosity function for bright clusters to a distance of $z = 0.25$ (Ebeling et al. 1995), producing a luminosity function in the softer 0.1-2.4 keV band:

$$\frac{dN}{dL_{0.1-2.4}} = 5.7 \times 10^{-7} (L_{0.1-2.4}/8.92 \times 10^{44})^{-1.78} (10^{44} \text{ erg s}^{-1})^{-1} \text{ Mpc}^{-3}. \quad (2.6)$$

The luminosity function of small clusters and groups is also an important cosmological constraint; recent ROSAT results (albeit of optically selected clusters) have found that the luminosity distribution of nearby low luminosity clusters joins smoothly onto the power law distribution of higher clusters (Burns et al. 1996; Henry et al. 1995).

2.2 Cluster Structure

Given a spherical, idealized galaxy cluster, the equation of hydrostatic equilibrium for galaxies is:

$$\frac{1}{n_{gal}} \frac{d(n_{gal} \sigma_r^2)}{dr} + 2 \frac{\sigma_r^2 - \sigma_t^2}{r} = - \frac{GM(r)}{r^2}, \quad (2.7)$$

where $n_{gal}(r)$ is the number density of galaxies, $M(r)$ is the total mass inside radius r and σ_r, σ_t are the radial and tangential velocity dispersions. If the orbits are isotropic so $\sigma_r = \sigma_t$ (or given some other definite relation between σ_r and σ_t), and if we assume that the galaxy distribution is representative of the primary mass component (usually dark matter), then we can compute the cluster mass at a given radius. Unfortunately, it is not clear how well these assumptions are met and if they are incorrect, the mass estimates can be in serious error (The & White 1986; Merritt 1987).

We can write a similar expression for the gas by assuming, again, a spherical cluster in equilibrium but now combined with the ideal gas law:

$$M(r) = -\frac{kTr}{G\mu m_p} \left(\frac{d \ln \rho_g}{d \ln r} + \frac{d \ln T}{d \ln r} \right). \quad (2.8)$$

Here, $T(r)$ is the gas temperature, $\rho_g(r)$ is the gas density and μ is the mean mass per particle. Given the gas density and temperature distributions, the total enclosed mass $M(r)$ can be found. The gas density can be obtained from the X-ray luminosity, but the temperature structure is more difficult as it requires resolved X-ray spectroscopy; nevertheless, temperature distributions are slowly becoming available (Böhringer et al. 1992; Markevitch 1996; Henriksen & Markevitch 1996).

The most common assumption for the form of the gas distribution is

$$\rho_g(r) = \rho_0 \left(1 + \frac{r^2}{r_c^2} \right)^{-3\beta_f/2}. \quad (2.9)$$

The fitting constants β_f , which corresponds to the steepness of the power-law slope, and the core radius r_c , take on typical values of $\beta_f \approx 2/3$ and $r_c \approx 0.15h^{-1}$ Mpc (Jones & Forman 1984). If we assume that the cluster is isothermal (see also Tsai, Katz & Bertschinger 1994), this form is easy to deal with because all of the associated integrals can be done in closed form. The resulting (projected) X-ray surface brightness is given by

$$S(R) = S_0 \left(1 + \frac{r^2}{r_c^2} \right)^{1/2-3\beta_f}. \quad (2.10)$$

This particular analysis is due to Cavaliere & Fusco-Femiano (1976) but is not limited to isothermal forms and can be easily extended to include polytropic equations of state (Cowie et al. 1987).

Once the total and baryonic mass distributions have been obtained in this manner, the gas fraction (ρ_{gas}/ρ_{total}) or baryon fraction ($\rho_{gas+galaxies}/\rho_{total}$) can be computed. This has been done for a number of clusters and although there is a fair amount of scatter, a baryon fraction of 20% is typical for a Hubble constant of 50 km/s/Mpc. (Jones & Forman 1992). When combined with predictions from big-bang nucleosynthesis, $\Omega_{baryon} \approx 0.05$ (Walker et al. 1990), this implies $\Omega_{total} \approx 0.3$ (for the same Hubble constant). The baryon

fraction scales as $h^{-1.5}$ while Ω_b from BBNS scales as h^{-2} , so a larger Hubble constant means a slightly lower value of Ω ($h = 1$ implies $\Omega \approx 0.2$).

Combining equations 2.7 and 2.8 by eliminating $M(r)$ and assuming isotropic galaxy orbits and strict isothermal distributions: $\sigma_r = \sigma_t = \text{constant}$ and $T = \text{constant}$, we obtain:

$$\rho_g \propto n_{gal}^{\beta_T}, \quad (2.11)$$

where $\beta_T = \mu m_p \sigma_r^2 / kT$. The quantity β_T gives an indication of the match between the temperatures of the galaxy and gas distributions. From observations, this quantity is, on average, one (Mushotzky 1984; Edge & Stewart 1991b). If, as is often done, the galaxy distribution is assumed to follow a King profile:

$$n_{gal} = n_0 \left(1 + \frac{r^2}{r_c^2} \right)^{-3/2}, \quad (2.12)$$

then the relation $\beta_f = \beta_T$ should hold. The fact that it does not is known as the ‘ β discrepancy’ (see also Bahcall & Lubin 1995; Evrard 1990).

An independent way to find the cluster mass is through observations of gravitational lensing of background sources by the cluster. A number of techniques have been developed, the simplest of which uses the rare but impressive gravitational arcs (Grossman & Narayan 1989; Mellier, Fort & Kneib 1993). Although these provide a straightforward approach to mass determination, few clusters contain clear, giant arcs. More information is available from the small but observable distortion of background galaxies; however, the analysis for such data is complicated (Kaiser et al. 1994). Nevertheless, some clusters have been observed with such techniques. Results are still mixed, with some clusters showing a significantly higher lensing mass than X-ray or optical determinations (Wu 1994; Miralda-Escudé & Babul; Fahlman et al. 1994), while others are in good agreement (Squires et al. 1996)

The mostly easily observable line in X-ray spectra of the hot gas is the iron K-line (actually a blend) which has been used as a probe for metallicity in many clusters. Typical values range from 0.2 to 1.0 of solar abundance, with some tendency for hotter, larger clusters to have more metals (Mushotzky 1992). A small number of clusters — Virgo,

Coma and Perseus — have been observed with imaging spectrometers and although the results are slightly contradictory, seem to show a radial gradient, with the highest metallicity gas near the core (Kowalski et al. 1994; Edge 1990). However, more recent results from the ASCA satellite do not confirm this finding (Henriksen & Markevitch 1996).

Cluster magnetic fields have been observed through Faraday rotation measures of radio sources that are either behind or embedded in the cluster itself. Such observations imply typical fields of $B \sim 1\mu\text{G}$; however, the rotation measure detects the average parallel component of the magnetic field along the line of sight and hence there remains the possibility of strong fields tangled on smaller scales. Another way to determine B in clusters with diffuse radio emission comes from observation of high-energy X-rays produced through the scattering of microwave background photons off of high-energy cosmic ray electrons. These electrons produce diffuse radio emission which is proportional both to the energy density in the electrons and in the magnetic field, assuming equipartition. So far, no reliable detections of non-thermal 100+ keV X-rays have been made (Raphaelli et al. 1994), which implies an upper limit on the number of cosmic-ray electrons. This upper limit translates into a lower limit on the magnetic field. To date, these limits are quite weak ($B > 0.1\mu\text{G}$), but have the advantage that they measure the total magnetic energy and not just the average field.

If the plasma is thick enough, the inverse-Compton scattering of cosmic microwave background (CMB) photons off of hot electrons (with temperature T_e) can scatter an appreciable number of photons to higher energy. Since this Sunyaev-Zel'dovich effect (Sunyaev & Zel'dovich 1972) causes an energy shift in the Wien part of the spectrum, it appears as a temperature decrement in microwave observations. This is often parameterized through the y parameter:

$$y = \int_0^\infty \frac{kT_e}{m_e c^2} \sigma_T n_e dl, \quad (2.13)$$

where σ_T is the Thompson cross-section, n_e is the electron density and the integral is along the line of sight. Two things are evident: the SZ effect provides information about

the electron pressure in a cluster and the change in the y -parameter is independent of distance. This is both a help and a handicap, as it allows us to make distant observations, but it makes interpretations vulnerable to confusion and projection effects. Measurements of the y -parameter provide a potentially powerful tool for probing the cluster gas, but so far such observations have mostly been used as a method to determine the Hubble constant (Myers et al. 1994; Herbig et al. 1995).

Although they will not be important to this investigation, we briefly mention the existence of cooling flows in the central 100-200 kpc of some clusters. These are regions of extreme X-ray surface brightness with cooling times less than a Hubble time. They are observed in 70-80% of clusters (Edge, Stewart & Fabian 1992). Models describing the behaviour of the cooling gas (Fabian, Arnaud & Nulsen 1985; Waxman & Miralda-Escudé 1995) imply large mass deposition rates (some over $500 M_{\odot}/\text{yr}$), although there is very little direct evidence of this in other wavebands (Fabian 1994).

Another aspect of clusters that will be mentioned only tangentially in this thesis is the recent realization that many, if not most, clusters show some signs of substructure. This was first noticed in X-ray images (Forman et al. 1981; Davis & Mushotzky 1993) but is also apparent in optical studies (Geller & Beers 1982; Bird 1994). Since these fluctuations should damp after a time, their relative strength is an indication of the value of Ω (which in turn controls when the infall stops). A number of studies have attempted to use these results to constrain Ω with mixed results (Richstone, Loeb & Turner; Mohr et al. 1995).

Chapter 3

A Piecewise Parabolic Method for Cosmological Hydrodynamics

3.1 Introduction

The standard view of the universe tells us that there are two kinds of matter: a baryonic component which makes up about 5% of the mass required to stop the universe from expanding forever, and a collisionless dark matter that appears to dominate the gravitational evolution of the universe and many of its components. Because the dark matter controls the dynamical evolution of the largest structures ($r \geq 5$ Mpc), and because the physics of the gaseous component is intrinsically much more complex, much effort has been focused on this component (Efstathiou et al. 1985; Davis et al. 1985). Unfortunately, we cannot directly observe dark matter and thus have, until recently, depended on the assumption that ‘light follows mass’ (i.e. that the baryonic component will generally follow the distribution of dark matter). This is known to be incorrect on scales up to cluster sizes (see, e.g. Cen & Ostriker 1992; Cen & Ostriker 1993b; Katz, Hernquist & Weinberg 1992) indicating a need to include the more difficult baryonic physics.

The physics of collisionless systems has led naturally to the development of particle based methods (Hockney & Eastwood 1980), while much success has been achieved in gas dynamics through the use of Eulerian techniques. Therefore, we combine a momentum

conserving particle-mesh (PM) scheme for the collisionless component with the Godunov-based piecewise parabolic method (PPM) (Colella & Woodward 1984, CW84 henceforth) for the gas. We have taken pains to use a state-of-the-art gas dynamics algorithm because of the demands of hydrodynamic cosmology. Temperatures can range over eight orders of magnitude, densities over six orders (neglecting the structure within galaxies) and pressures over 14 orders of magnitude. Even worse, many length scales are operating simultaneously: the ratio of the separation between clusters to the size of a cluster is about 100, requiring a minimum of 10^6 resolution elements in three dimensions. PPM is one of the most effective of the shock capturing methods that have been developed recently (Woodward & Colella 1984); it is formally third order accurate in space, easy to parallelize and quite robust in modelling cosmological flows. Even so, the unusual rigors of the cosmological simulation regime require certain modifications to the basic scheme. We also describe the changes necessary to make the PPM scheme function under limits of low resolution. This is extremely important due to the spectrum of length scales that are active in cosmological simulations. Short wavelength fluctuations are modulated by longer ones so both need to be treated as accurately as possible. Therefore we must insure that cosmologically interesting phenomena can be modelled with as small a number of zones as possible. To document and test the algorithms we have also developed a suite of cosmological test problems, the results of which are detailed.

Other approaches to numerical cosmology have been taken. Almost all use particle formulations of one sort or another for the dark matter, but they divide into two classes for the hydrodynamics: Lagrangean particle methods such as smooth particle hydrodynamics (SPH) (Hernquist & Katz 1989; Evrard 1988) and the Eulerian, hybrid methods (Cen & Ostriker 1992; Ryu et al. 1993).

There are still many physical processes that we have not included: the ionization state of the gas (due both to radiation and collisions), as well as radiative processes and radiative transfer effects. We will describe our efforts to implement the first two in a future paper, however the self-consistent inclusion of radiative transfer in such codes must await improved algorithms and better computers. Finally, we remark that magnetic fields

and heat conduction may play a role in cluster formation (and surely must be important in galaxy formation); however, their effects have not been examined here.

In section 2, we describe the numerical methods used, with only a cursory description of PM and PPM, as they have both been described in adequate detail elsewhere. The cosmological test suite is presented in section 3 and our conclusions are drawn in section 4.

3.2 Numerical Methodology

The first ingredient, which we will not discuss in detail, is to implement a particle-in-cell algorithm to trace the evolution of the dark matter. Such systems have been in use for many years and are well understood and well tested; for a fine description of their application to cosmology, see Efstathiou et al. (1985) and Davis et al. (1985). To be explicit, we implement a particle-mesh, cloud-in-cell (Hockney & Eastwood 1980) method with a grid size equal to the hydrodynamic mesh to facilitate the gravitational interaction. The computation of the gravitational potential is done by Fourier transform. Since this aspect is well described elsewhere, we start with a description of the hydrodynamic algorithm.

The usual Eulerian equations of gas dynamics with gravity are given by

$$\left(\frac{\partial \rho'}{\partial t}\right)_r + \vec{v}' \cdot \nabla_r \rho' = -\rho' \nabla_r \cdot \vec{v}', \quad (3.1)$$

$$\left(\frac{\partial \vec{v}'}{\partial t}\right)_r + (\vec{v}' \cdot \nabla_r) \vec{v}' = -\frac{1}{\rho'} \nabla_r p' - \nabla_r \phi', \quad (3.2)$$

$$\left(\frac{\partial E'}{\partial t}\right)_r + \vec{v}' \cdot \nabla_r E' = -\frac{1}{\rho'} \nabla_r \cdot (p' \vec{v}') - \vec{v}' \cdot \nabla_r \phi'. \quad (3.3)$$

Here E , e , ρ , \vec{v} and p are the baryonic total specific fluid energy, the baryonic specific thermal energy, the baryonic density, velocity and pressure, respectively. We use primes to indicate variables defined in the absolute frame of reference (most of the rest of this paper will use a comoving frame). The first equation represents conservation of mass, the second, conservation of momentum, and the third, conservation of total fluid (kinetic

plus thermal) energy. They are respectively, the first, second and third moments of the Boltzman equation. The total fluid specific energy (E') is given by:

$$E' = e' + \frac{1}{2} \vec{v}' \cdot \vec{v}'. \quad (3.4)$$

We actively solve the equation of total energy because of the need to enforce local energy conservation in any shock capturing scheme. Terms representing radiative cooling and/or heating will enter on the right-hand side of the energy equation (3.3).

The equations are closed with the equation of state and Poisson's equation (we work in the Newtonian limit):

$$e' = p' / [(\gamma - 1)\rho'], \quad (3.5)$$

$$\nabla_r^2 \phi' = 4\pi G(\rho'_{total} + 3p'_{total}/c^2) - \Lambda. \quad (3.6)$$

For simplicity, the equation of state is shown here for an ideal gas with a ratio of specific heats γ . Equation (3.6) includes contributions to the gravitational potential ϕ' from all non-relativistic populations (ρ'_{total}) as well as any radiation or massless neutrino background (p'_{total}) or cosmological constant (Λ).

We now transform to a coordinate system that is comoving with the expanding universe (c.f. Peebles 1980). Specifically, we define:

$$\vec{x} = \vec{r}/a, \quad (3.7)$$

$$\vec{v} = a d\vec{x}/dt = \vec{v}' - \dot{a}\vec{x}, \quad (3.8)$$

$$\rho = a^3 \rho', \quad (3.9)$$

$$p = a^3 p', \quad (3.10)$$

$$E = E' - \dot{a}\vec{x} \cdot \vec{v} - \frac{1}{2}\dot{a}^2 \vec{x}^2, \quad (3.11)$$

$$\phi = \phi' + \frac{1}{2}a\ddot{a}\vec{x}^2. \quad (3.12)$$

These definitions result in the following comoving equivalents to eqs. (3.1)-(3.6).

$$\frac{\partial \rho}{\partial t} + \frac{1}{a} \vec{v} \cdot \nabla \rho = -\frac{1}{a} \rho \nabla \cdot \vec{v}, \quad (3.13)$$

$$\frac{\partial \vec{v}}{\partial t} + \frac{1}{a}(\vec{v} \cdot \nabla)\vec{v} = -\frac{\dot{a}}{a}\vec{v} - \frac{1}{a\rho}\nabla p - \frac{1}{a}\nabla\phi, \quad (3.14)$$

$$\frac{\partial E}{\partial t} + \frac{1}{a}\vec{v} \cdot \nabla E = -\frac{\dot{a}}{a}\left(3\frac{p}{\rho} + \vec{v}^2\right) - \frac{1}{a\rho}\nabla \cdot (p\vec{v}) - \frac{1}{a}\vec{v} \cdot \nabla\phi. \quad (3.15)$$

$$E = e + \frac{1}{2}\vec{v}^2, \quad (3.16)$$

$$e = p/[(\gamma - 1)\rho], \quad (3.17)$$

$$\nabla^2\phi = \frac{4\pi G}{a}(\rho_{total} - \rho_0). \quad (3.18)$$

The expansion parameter $a \equiv 1/(1+z)$ follows the expansion of a smooth, homogeneous background, where z , the redshift, is a function only of t . All derivatives are determined with respect to the comoving position \vec{x} , which is defined simply to remove the universal expansion from the coordinate system.

The evolution of $a(t)$ is governed by the formula for the expansion of an isotropic, homogeneous universe:

$$\frac{\ddot{a}}{a} = -\frac{4\pi G}{3a^3}(\rho_0 + 3p_0/c^2) + \Lambda/3. \quad (3.19)$$

Here, ρ_0 is the mean (baryonic and dark) comoving mass density and p_0 is the comoving background pressure contribution (usually negligible). This system of equations is limited to the non-relativistic regime and assumes that curvature effects are not important — both assumptions are reasonable as long as the size of the simulated region is small compared to the radius of curvature and the Hubble length c/H (c is the speed of light and H is the Hubble constant).

The particles are governed by Newton's equations in comoving coordinates:

$$\frac{d\vec{x}_{dm}}{dt} = \frac{1}{a}\vec{v}_{dm}, \quad (3.20)$$

$$\frac{d\vec{v}_{dm}}{dt} = -\frac{\dot{a}}{a}\vec{v}_{dm} - \frac{1}{a}\nabla\phi, \quad (3.21)$$

The subscript 'dm' refers to dark matter particles.

An outline for the solution of these equations as well as the associated machinery that any simulation code must supply is given in Figure 3.1. We will return to this figure in section 2.7, after describing, in some detail, the action of each step.

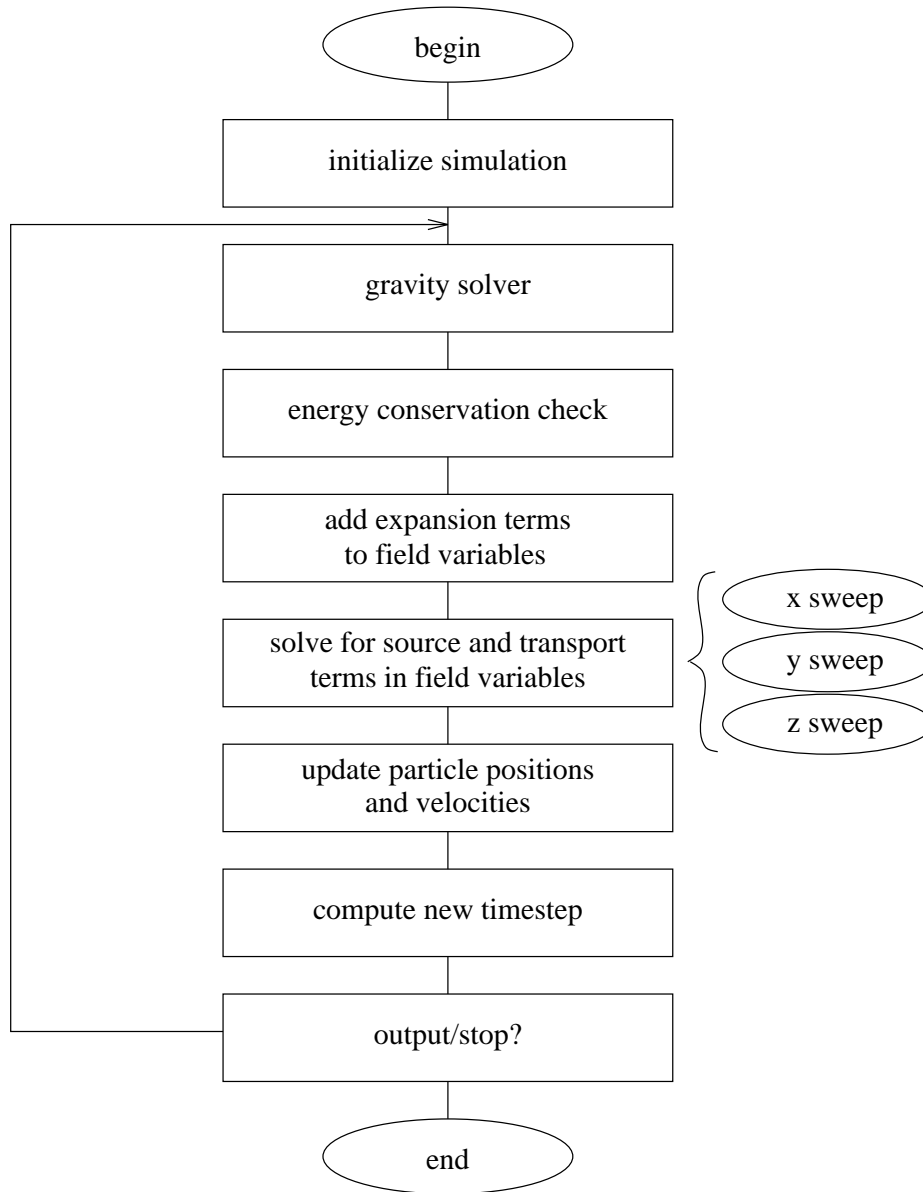


Figure 3.1. Overview of KRONOS operations.

3.2.1 Structure of the cosmological equations of hydrodynamics

We can examine the structure of eqs. (3.13)-(3.15) to obtain a better understanding of the effect of each term. The derivatives are first order in time and provide us with the dependent variables that will be evaluated each time step: ρ , \vec{v} , and E .

The second term on the left hand side of each relation is due to our choice of Eulerian coordinates and corresponds to advection, the flow of conserved quantities (ρ , $\rho\vec{v}$, and ρE) across the mesh. These will be termed the transport terms.

The first term on the right hand side of eqs. (3.14) and (3.15) comes from our choice of comoving coordinates (a similar term also appears in eq. (3.21), the velocity relation for the dark matter particles). It does not appear in the mass conservation equation (3.13) because of the comoving density definition. We note that these expansion terms could be eliminated entirely by the proper choice of variables (including time), although we have not done so here, as they do not constitute a major source of error.

The remainder of the terms (due to pressure and gravity) are denoted as source terms. They drive instabilities and discontinuities in the flow. We make these distinctions because each of the three groups of terms have different numerical behaviour and are therefore treated differently. The source and transport steps will be solved in a self-consistent fashion by the PPM scheme while the expansion terms, which are spatially localized, are split off and solved in a separate step (as would be radiative cooling and heating, if present). This operator splitting has the effect of introducing a constraint on the timestep by requiring that the coefficient \dot{a}/a be small. Specifically, we insist that the expansion factor increase slowly,

$$\frac{\Delta a}{a} \leq C_a, \quad (3.22)$$

where Δa is the change in the expansion factor a per time step and C_a is a safety factor, which must be less than one for stability. To insure comparable accuracy with the rest of the scheme, we use $C_a = 0.01$. In practice, the timestep constraint implied by this restriction is only important near the beginning of a simulation when the gas and

dark matter are cold and fluctuations are small. At later times, as we shall see, other constraints place tighter limits on the timestep.

The remainder of the terms (transport and source) in the fluid equations involve derivatives. Because we are interested in phenomena with no special geometry, we will restrict discussion to Cartesian coordinates. Once again we use the concept of operator splitting, but now apply it spatially. Here also, we split off the transport terms, writing the one dimensional Lagrangean versions of eqs. (3.13)–(3.15) as:

$$\frac{\partial}{\partial t} \frac{1}{\rho} = \frac{1}{a\rho} \frac{\partial v}{\partial x}. \quad (3.23)$$

$$\frac{\partial v}{\partial t} = -\frac{1}{a\rho} \frac{\partial p}{\partial x} - \frac{1}{a} \frac{\partial \phi}{\partial x}, \quad (3.24)$$

$$\frac{\partial E}{\partial t} = -\frac{1}{a\rho} \frac{\partial (pv)}{\partial x} - \frac{v}{a} \frac{\partial \phi}{\partial x}, \quad (3.25)$$

Now, x and v refer to the one dimensional comoving position and peculiar velocity of the baryonic gas. These equations are now in a form that can be solved by the PPM scheme.

3.2.2 The piecewise parabolic method in cosmology

We now restrict ourselves to the solution of eqs. (3.23)–(3.25), plus transport, in one dimension. This is accomplished by using a Lagrange plus remap scheme. There are two phases: first, solve the equations in Lagrangean form, and then remap the resulting distribution to Eulerian cells. This is described in detail in Colella & Woodward (1984), but we will briefly outline the procedure in order to place the required changes in context. A schematic overview of the process is shown in Figure 3.2. Additions required for a successful cosmological adaptation of the scheme are also shown and will be described in sections 2.3–2.5.

The Lagrangean difference equations are:

$$\rho_j^{n+1} = \frac{a^n \rho_j^n \Delta x_j^n}{a^n \Delta x_j^n + \Delta t (\bar{v}_{j+1/2} - \bar{v}_{j-1/2})} \quad (3.26)$$

$$v_j^{n+1} = v_j^n + \frac{\Delta t}{\Delta m_j} (\bar{p}_{j-1/2} - \bar{p}_{j+1/2}) + \Delta t (g_j^{n+1/2}), \quad (3.27)$$

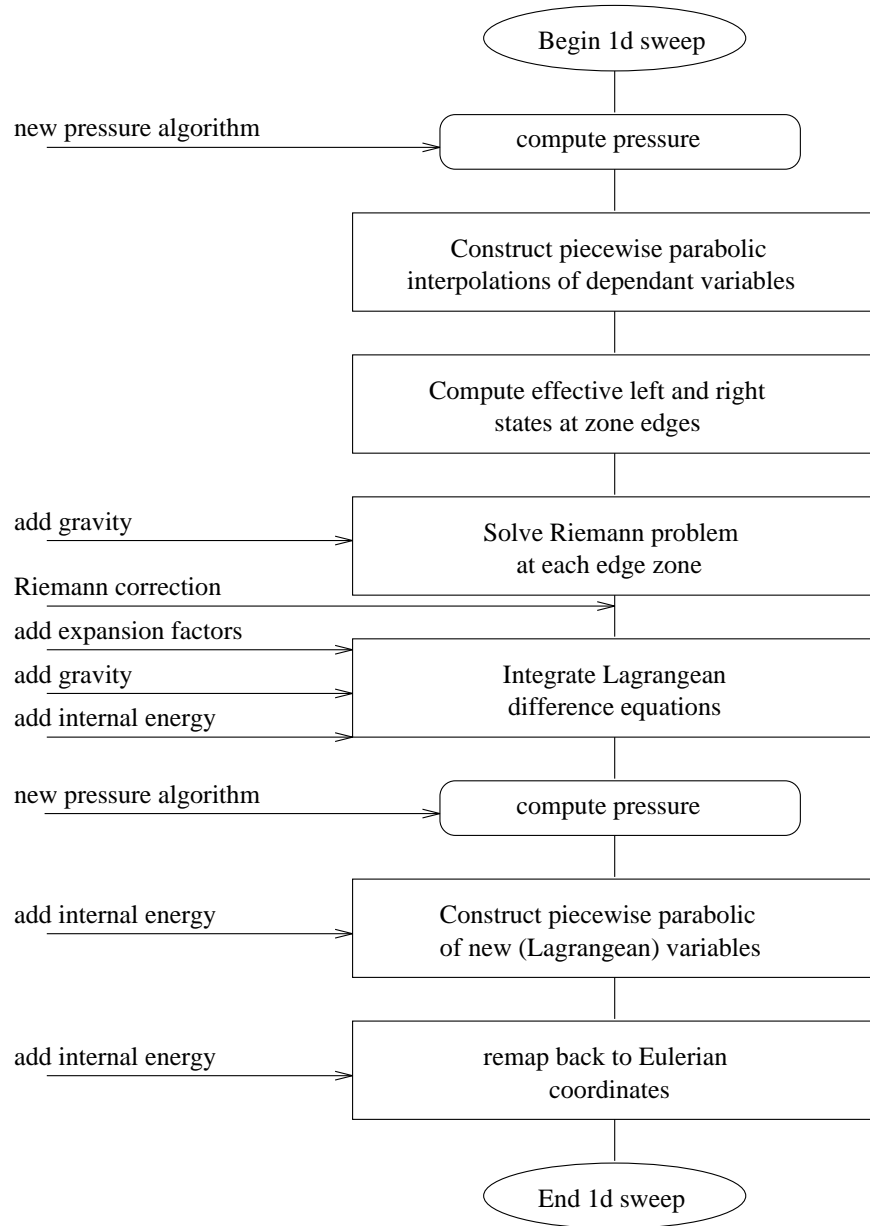


Figure 3.2. Steps in a one-dimensional sweep to solve the fluid equations. Additions to the basic PPM scheme are labeled with arrows.

$$E^{n+1} = E^n + \frac{\Delta t}{\Delta m_j} \left(\bar{v}_{j-1/2} \bar{p}_{j-1/2} - \bar{v}_{j+1/2} \bar{p}_{j+1/2} \right) + \frac{\Delta t}{2} \left(v_j^n + v_j^{n+1} \right) g_j^{n+1/2}. \quad (3.28)$$

We have used subscripts to indicate zone-centered (j) and face-centered ($j + 1/2$) quantities, while superscripts refer to position in time. The Lagrangean nature insures that the mass of an element $\Delta m_j = a^n \rho_j^n \Delta x_j^n$ does not change during the timestep. Although they have been discretized in space, the accuracy of the update depends on how well we can compute the fluxes into and out of the cell during Δt . This in turn depends on our ability to compute the time-averaged (over Δt) values of p and v at the cell interfaces, denoted here by $\bar{p}_{j\pm 1/2}$ and $\bar{v}_{j\pm 1/2}$. We now describe the steps required to compute these quantities. Note that these difference equations (and the remap step that follows) are conservative.

We first construct monotonic piecewise parabolic (third order) interpolations in one dimension for each of ρ , v and p . The pressure is determined from eq. (3.17), the equation of state. We have dropped the subscript b in this and the following two sections because we will be referring solely to baryonic quantities.

The interpolation formula for some quantity q (one of ρ , v and p) is given by:

$$\begin{aligned} q(m) &= q_{L,j} + x(\Delta q_j + q_{6,j}(1 - x)), \\ x &\equiv \frac{m - m_{j-1/2}}{\Delta m_j}, \quad m_{j-1/2} \leq m \leq m_{j+1/2}. \end{aligned} \quad (3.29)$$

This is eq. (1.4) of CW84. The mass coordinate m is the natural variable for interpolating in the Lagrangean step. The zones edges in the mass coordinates are $m_{j-1/2}$ and $m_{j+1/2}$ for the left and right edges, respectively. The quantities $q_{L,j}$, Δq_j , and $q_{6,j}$ can be viewed simply as interpolation constants; however, they also have more intuitive meanings. For example, $q_{L,j}$ is the value of q at the left edge of zone j , while Δq_j and $q_{6,j}$ are analogous to the slope and first order correction to the slope of q (see CW84 for a complete discussion):

$$\Delta q_j \equiv q_{R,j} - q_{L,j} \quad q_{6,j} \equiv 6 [q_j - 1/2 (q_{L,j} + q_{R,j})]. \quad (3.30)$$

We have reduced the problem to finding $q_{L,j}$ and $q_{R,j}$. While this is simple in principle, it is complicated somewhat by the requirement that these values be of sufficient accuracy and that the resulting distribution be monotonic. That is, no new maxima or minima

are introduced. The resulting formulae are straightforward but complicated and are not reproduced here (but see eqs. 1.7 to 1.10 of CW84).

Once we have the interpolation constants we compute the characteristic domain for each zone edge. This is simply the farthest a sound wave could travel in order to reach the interface by the end of a timestep. The characteristic domain encompasses all of the information that can reach the zone edge during the current timestep.

Here is the crux of the method: an average is taken over each of these domains to create, in effect, two constant states separated by a discontinuity. The advantage is that the solution to such a problem (called a Riemann problem) is well-known, self-similar and relatively easy to determine (although much work has gone into approximations that are quick to compute). Its application insures that the Rankine-Hugoniot conditions are satisfied across a shock, thus avoiding the necessity of employing explicit artificial viscosity. It is implemented so that in the limit of smooth flow and no discontinuities, we solve the characteristic equations that produce time-centered quantities for p and v .

To determine the effective left and right states, we average over the domain of dependence on the appropriate side of the cell interface. This is given by:

$$\begin{aligned} q_{j+1/2}^+ &= f_{j+1/2,L}(\Delta t C_j^n), \\ q_{j+1/2}^- &= f_{j+1/2,R}(\Delta t C_{j+1}^n), \end{aligned} \tag{3.31}$$

where q^+ (q^-) refers to the left (right) characteristic. Notice that we have approximated the characteristic sound speed as a constant within a cell. Here we use the Lagrangean sound speed $C^2 = \gamma p \rho$ rather than the Eulerian speed $c^2 = \gamma p / \rho$ because the interpolation is over mass. The functions f are just integrals over the parabolic interpolation formula:

$$\begin{aligned} f_{j+1/2,L}(y) &= \frac{1}{y} \int_{m_{j+1/2}-y}^{m_{j+1/2}} a(m) dm, \\ f_{j+1/2,R}(y) &= \frac{1}{y} \int_{m_{j+1/2}}^{m_{j+1/2}+y} a(m) dm. \end{aligned} \tag{3.32}$$

With these effective states, an approximation to the Riemann problem is found with an iterative approach (see Woodward 1986), producing estimates for $\bar{p}_{j\pm 1/2}$ and $\bar{v}_{j\pm 1/2}$ that are third order accurate in space and second order accurate in time.

After solving the difference eqs. (3.26)–(3.28) for ρ^{n+1} , v^{n+1} , and E^{n+1} , we must remap these Lagrangean distributions to the original cells. The procedure is straightforward: construct piecewise parabolic interpolations (but now using E instead of p and including the transverse velocities v_y and v_z), and integrate over the distance each cell interface has moved. This is determined from $\bar{v}_{j+1/2}$.

3.2.3 Adding gravity to the PPM scheme

We need the time-centered gravitational acceleration $g^{n+1/2}$ for eq. (3.28), computed here by finite differencing the potential $\phi^{n+1/2}$. If FFT's are used, a direct determination of the acceleration is possible (Hockney & Eastwood 1980), but would require four transforms instead of two. This time-centered quantity should come from the advanced density distribution ($\rho^{n+1/2}$); however, that would render the scheme implicit. Therefore, we use a linear extrapolation from the previous two timesteps:

$$\phi^{n+1/2} = \phi^n \left(1 + \frac{\Delta t^n}{2\Delta t^{n-1}} \right) - \phi^{n-1} \frac{\Delta t^n}{2\Delta t^{n-1}}. \quad (3.33)$$

Since the potential varies slowly, this is sufficiently accurate as long as the timestep does not increase suddenly (a condition which we enforce, see below).

The acceleration required in eq. (3.27) is actually the acceleration felt by the entire zone and not just at the zone center. Therefore, we find the mass weighted average acceleration over the zone by expanding the density and acceleration distributions and retaining all terms up to second order in Δx :

$$g_j^{n+1/2} = \frac{1}{2a^{n+1/2}\delta x_j} \left[\phi_{j+1}^{n+1/2} - \phi_{j-1}^{n+1/2} + \frac{1}{12} \left(\phi_{j+1}^{n+1/2} - 2\phi_j^{n+1/2} + \phi_{j-1}^{n+1/2} \right) \frac{\delta d_j}{d_j} \right]. \quad (3.34)$$

The success of the interpolation schemes in this method depends on the preservation of monotonicity. This must be done for the density slope δd_j , but not for the potential because it is only slowly varying,

$$\begin{aligned} \delta d_j &= \min(|d_{j+1} - d_{j-1}|, 2|d_j^n - d_{j-1}^n|, 2|d_j^n - d_{j+1}^n|) \operatorname{sign}(d_{j+1} - d_{j-1}) \\ &\quad \text{if } (d_{j+1} - d_j)(d_j - d_{j-1}) < 0, \\ &= 0 \quad \text{otherwise.} \end{aligned} \quad (3.35)$$

This guarantees that the slope will not cause any interpolated value to exceed the density in the left or right zone, or, if the density at j is a local maxima or minima, it sets the slope to zero.

The other change required to adapt PPM for a body force is described in CW84 and involves modifying the Riemann solver to account for gravity with the inclusion of a linear corrective term (not to be confused with the *post hoc* Riemann correction described in Section 2.5). This is relatively straightforward, although we note that a factor of one-half is missing from their eq. (2.9): the factor Δt should read $\Delta t/2$.

3.2.4 The dual energy formulation for high Mach flows

The system described so far works well for gravitating systems with reasonable Mach numbers (< 100) as long as the structures are well resolved. This section and the next detail changes that are required to correctly account for situations in which one or both of these requirements are not met.

Large, hypersonic bulk flows appear to be very common in cosmological simulations and they present a problem because of the high ratio of kinetic energy E_k to gas internal energy e , which can reach as high as 10^8 . Inverted, we see that the internal energy consists of an extremely small portion of the total energy. The pressure then, proportional to $E - E_k$, is the small difference between two large numbers: a disastrous numerical situation. This is not as large a problem as it may at first appear because it only occurs when the pressure is negligibly small. Therefore, even if we suffer large errors in the pressure distribution in these regions, the dynamics and total energy budget of the flow will remain unaffected. Nevertheless, if the temperature distribution is required for other reasons (e.g. radiative processes), a remedy is required.

To overcome this, we also solve the internal energy equation:

$$\frac{\partial e}{\partial t} + \frac{1}{a} \vec{v} \cdot \nabla e = -3 \frac{\dot{a}}{a} \frac{p}{\rho} - \frac{p}{a\rho} \nabla \cdot \vec{v} \quad (3.36)$$

in comoving co-ordinates. The structure is similar to the total energy equation; the second term on the left hand side represents transport, while the first term on the right

is due to expansion of the coordinate system. These are treated as before. It is differenced (again, in Lagrangean form without the expansion term) as,

$$e_j^{n+1} = e_j^n + \frac{\Delta t}{\Delta m_j} p_j^{n+1/2} (\bar{v}_{j-1/2} - \bar{v}_{j+1/2}). \quad (3.37)$$

The time-centering of the pressure in this equation is essential to avoid the accumulation of entropy errors, but we would still like to retain the explicit nature of the algorithm. Therefore, we adopt $p_j^{n+1/2} = (\bar{p}_{j-1/2} + \bar{p}_{j+1/2})/2$.

It is necessary, however, to conserve the total energy so that the conversion of kinetic to thermal energy is performed properly. We must therefore, combine the two formulations without allowing the separately advected internal energy e to play a role in the gas dynamics. This is done by carrying both terms through the simulation and using the total energy E for hydrodynamic routines and the internal energy e when the temperature profile is required. One way to view this procedure is to treat e as enhanced precision (extra digits) for E that automatically ‘floats’ to where it is needed. We only require that they be kept synchronized when the two levels of precision overlap.

When the pressure is required solely for dynamic purposes, the selection criterion operates on a cell by cell basis using,

$$p = \begin{cases} \rho(\gamma - 1)(E - \bar{v}^2/2), & (E - \bar{v}^2/2)/E > \eta_1; \\ \rho(\gamma - 1)e, & (E - \bar{v}^2/2)/E < \eta_1. \end{cases} \quad (3.38)$$

It should be stressed that as long as the parameter η_1 is small enough the dual energy method *will have no dynamical effect*. We use $\eta_1 = 10^{-3}$ which is consistent with the truncation error of the scheme. We are now free to select the method by which the internal energy field variable e is updated so that it will not become contaminated with errors advected by the total energy formulation but still give the correct distribution in shocked regions. Since we are concerned with the advection of errors, the selection criterion must look at each cell’s local neighbourhood. In one dimension, this is done with,

$$e = \begin{cases} (E - \bar{v}^2/2), & \rho(E - \bar{v}^2/2)/\max(\rho_{j-1}E_{j-1}, \rho_jE_j, \rho_{j+1}E_{j+1}) > \eta_2, \\ e, & \rho(E - \bar{v}^2/2)/\max(\rho_{j-1}E_{j-1}, \rho_jE_j, \rho_{j+1}E_{j+1}) < \eta_2. \end{cases} \quad (3.39)$$

Thus, η_2 determines when the synchronization (of e with E) occurs. Too high a value may mask relatively weak shocks, while spurious heating (via contamination) may occur if it is set too low. After some experimentation, we have chosen $\eta_2 = 0.08$, a somewhat conservative value.

We note that others have independently developed a similar but distinct scheme for dealing with this problem, which is endemic to methods adopting the total energy equation. In reference Ryu et al. (1993) the two variables adopted are total energy and entropy (rather than total energy and thermal energy), with an analogous scheme for choosing which variable to employ.

3.2.5 The correction to the Riemannn solver

Body forces, such as gravity, are included in the Riemannn solver as a linear term (CW84). This is sufficient as long as the structures being computed are resolved and we can clearly distinguish between gravity-induced pressure gradients and shock waves. Unfortunately, this is not always possible in gravitational clustering. The problem manifests itself in the early stages of an object's collapse, when it is contained within two zones (the resolution element for most shock capturing codes). Here, the scheme underestimates the time averaged pressure ($\bar{p}_{j+1/2}$) between the zones. This is a consequence both of the fact that the body force is only included to first order in the Riemann solver and the monotonicity constraints which tend to clip local peaks in the density and pressure distributions. We therefore apply a correction of the form,

$$\bar{p}_{j+1/2} = \max \left[\bar{p}_{j+1/2}, (v_j - v_{j+1}) \max(d_j, d_{j+1}) \max(0, v_j - v_{j+1}) \right]. \quad (3.40)$$

This largely *ad hoc* estimate converts the energy of motion between the two zones into thermal energy if they are colliding. This thermal energy is then used as a new estimate for the time-averaged pressure between zones only if it is larger than the estimate from solving the Riemann problem. To prevent its application outside of underresolved, collapsing regions, we also demand that a strong overdensity be present:

$$d_j/d_{j-1} > 2 \quad \text{and} \quad d_{j+1}/d_{j+2} > 2. \quad (3.41)$$

The factor of two in this constraint comes from applying the method to underresolved distributions with known solutions, such as the spherical collapse (Bertschinger 1985) and the Zel’dovich pancake (Zel’dovich 1970; Yuan 1991) as well as self-convergence tests.

This correction must also be applied to $p_j^{n+1/2}$, the pressure used in the internal energy update. Here we are dealing with zone centers, so the correction becomes

$$p_j^{n+1/2} = \max \left[p_j^{n+1/2}, d_j^n \left(\bar{v}_{j-1/2} - \bar{v}_{j+1/2} \right) \max \left(0, \bar{v}_{j-1/2} - \bar{v}_{j+1/2} \right) \right], \quad (3.42)$$

again with the requirement of a (zone-centered) overdensity of factor two.

To maintain consistency with the dual energy formulation, we reset $p_j^{n+1/2}$ to $(\gamma - 1)e_j\rho_j$ if this cell used the total energy (3.39) to obtain its pressure.

3.2.6 The Layzer-Irvine cosmic energy equation

An important test of any numerical method is energy conservation. Following Peebles (1980), we write the comoving equation of total (gravitational plus fluid) energy conservation (c.f. Layzer 1964; Irvine 1965) as,

$$\frac{d}{dt}(K + U + W) + \frac{\dot{a}}{a}(2K + 3P + W) = 0. \quad (3.43)$$

The symbols K , U , and W refer to the average comoving kinetic, internal and potential energies, respectively and we have defined P to be the average comoving pressure.

The expression can be integrated over time and discretized to read:

$$a^n(K^n + W^n + U^n) + \sum_{m=1}^n [K^{m-1/2} + (3\gamma - 4)U^{m-1/2}] \Delta a^{m-1/2} = a^0(K^0 + W^0 + U^0). \quad (3.44)$$

In the limit of no expansion ($a = 1$ and $\dot{a} = 0$), we recover the usual conservation of total energy. We integrate this equation along with the dynamical equations to monitor energy conservation.

3.2.7 Code structure and overview

We now return to the organizational structure of the code (Figure 3.1). The first step must be to create or load the initial conditions. We use the Zel’dovich approximation

to set up the particle distribution (Efstathiou et al. 1985). For a set of particles initially placed at grid centers, this produces displacement vectors and velocities for each of the particles. The velocities found for the particles via the Zel'dovich approximation are used to determine the baryon density at the grid center through the linear relation:

$$\delta = -\frac{\nabla \cdot \vec{v}}{aHf}, \quad (3.45)$$

where $\delta = \rho/\bar{\rho} - 1$ and f is the logarithmic derivative of the growing mode of the linear growth function, with respect to the expansion factor of the universe, a :

$$f = \frac{d \log \delta}{d \log a} \quad (3.46)$$

$$\approx \Omega^{0.6} + \frac{\Omega_\Lambda}{70} \left(1 + \frac{\Omega}{2}\right). \quad (3.47)$$

Here, Ω is the ratio of the mean density (baryon plus dark matter) to the density required to close the universe, Λ is the cosmological constant and $\Omega_\Lambda = \Lambda/3H_0^2$.

Next we enter the main loop, calculating the potential using fast Fourier transform techniques Hockney & Eastwood 1980, and then checking energy conservation for adiabatic simulations (Section 2.6). The expansion terms are updated and then the PPM scheme is used to solve for the hydrodynamic variables. Finally, the particle positions and velocities are updated with a time centered second order method.

The timestep is chosen from the minimum of the expansion timestep (3.22), the Courant condition and the requirement that a particle move no more than half a cell's length in a single time step.

The Courant condition is given by:

$$\Delta t \leq \min \{ [C_0 a(t) \Delta x] / [C_s + \max(|v_x|, |v_y|, |v_z|)] \}, \quad (3.48)$$

where C_s is the local sound speed, v_x, v_y, v_z are the local fluid velocities and C_0 is the Courant number, typically $C_0 \approx 0.5$. The minimum is over all cells. We also demand that the timestep increase by no more than 25% from its previous value and add the requirement that the universe expand by no more than 2% in linear dimension within one time step.

The code uses dimensionless units. Specifically, length is in units of the box width, density is in units of the mean comoving density

$$\rho_{mean} = \rho_0(1+z)^3 = \frac{3\Omega_0 H_0^2}{8\pi G}(1+z)^3,$$

and time is normalized by $1/\sqrt{4\pi G\rho_0(1+z_i)^3}$, where H_0 is the Hubble constant at the current epoch and z_i is the redshift at which the simulation began.

3.3 Cosmological Tests

The PPM method has been subjected to a number of pure hydrodynamic tests many of which have been described in detail elsewhere (Woodward & Colella 1984). It performs very well on tests involving strong shocks, common in astrophysical flows. Similarly particle-mesh codes have been benchmarked (Hockney & Eastwood 1980; Efstathiou et al. 1985). We will therefore concentrate on tests that model physical situations which are expected to arise in cosmological simulations.

3.3.1 One dimensional pressureless collapse

As a first test of the gravity solver and advection routines we model the two sided one-dimensional collapse of a homogeneous plane parallel cloud in Cartesian coordinates. This is similar to the gravitational collapse of a sphere in spherical coordinates (Hunter 1962) and an analytic solution describes the collapse of every mass layer,

$$(x/x_0) = 1 - 2\pi G\rho_0 t^2, \quad (\rho/\rho_0) = (1 - 2\pi G\rho_0 t^2)^{-1}, \quad (3.49)$$

Here, the time for any mass layer to reach the origin (the free fall time) is $t_{ff} = \sqrt{1/(2\pi G\rho_0)}$. The initial density at $t = 0$ is ρ_0 and the fluid starts at rest. To make the run, we use units such that $\rho_0 = 1$ and $G = 1$, making $t_{ff} = 0.399$. Isolated boundary conditions are used (Eastwood & Brownrigg 1979). In Figure 3.3, we show the density distribution at $t = 0.37$, considerably advanced in the evolution. For a numerical

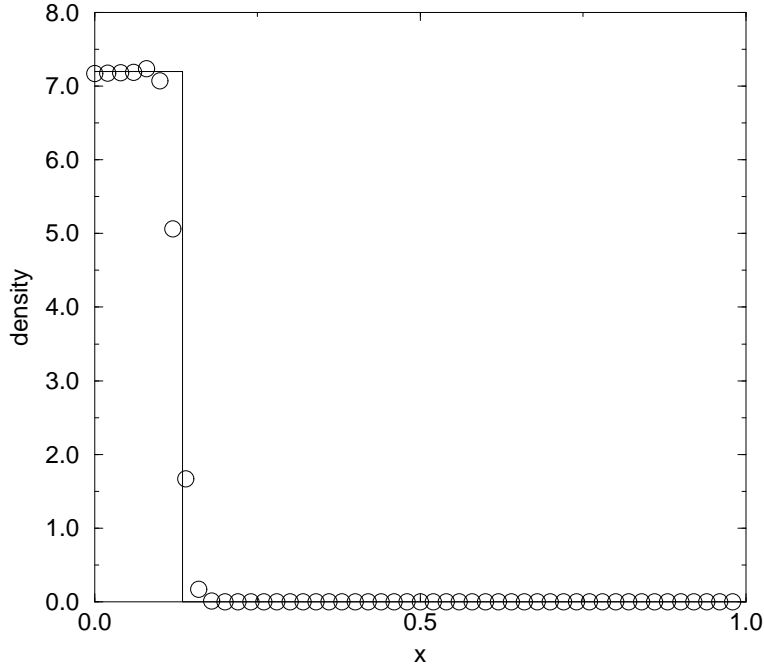


Figure 3.3. The density distribution of the planar one dimensional pressureless collapse at 0.927 free fall times. The analytic solution is denoted by a solid line.

example of this problem in spherical coordinates, see Stone & Norman (1992). Note that the universal expansion terms are not used in either this problem or the next (i.e. $a = 1$).

3.3.2 The Jeans instability

As a natural extension of the previous problem, we add pressure forces. This introduces a length scale but also produces a non-linear system of equations with no general analytic solution. However, by linearizing the equations around the homogeneous solution (pressure p_0 and density ρ_0) we obtain a solution with two cases: a travelling wave or a growing perturbation. The condition that differentiates these two situations is the familiar Jeans criterion, which we write as

$$p_c = \frac{G\rho_0^2\lambda^2}{\gamma\pi}, \quad (3.50)$$

where λ is the wavelength of the perturbation and p_c is the critical pressure. If the ambient pressure is above it, the wave oscillates and if it is below, the wave grows.

In order to determine the code’s ability to discriminate between these two cases, we impose a perturbation wavelength of 64 zones and vary the pressure in small increments around the critical pressure. We find that the value given in eq. (3.50) is reproduced to within $\Delta p/p_c = 0.01$.

3.3.3 Adiabatic expansion

In order to test the time-integration accuracy of the expansion terms, we turn universal expansion on and adopt a completely homogeneous universe with initial temperature $T_i = 100$ K and $v_i = 100$ km/s at an initial redshift of $z_i = 20$. The expansion terms in eqs. (3.13)–(3.15) operate like drag terms, so that in the absence of a source, the velocity decreases as $v = v_i a^{-1}$ and the temperature as $T = T_i a^{-2}$. Using $C_a = 0.01$, the computed temperature at $z = 0$ was $T_f = 0.2122$ K, 6.4 % below the analytic result of 0.2268 K. The final computed velocity was $v_f = 4.749$ km/s, compared to 4.762 km/s, a 0.27 % discrepancy.

3.3.4 The linear phase of the one dimensional Zel’dovich pancake

This test (described in sections 3.4 and 3.5) is particularly pertinent to cosmological studies not only because it encompasses all of the physics (hydrodynamics, expansion and self-gravity), but also because it represents an idealized, isolated caustic formation. One can think of the problem as a single-mode analysis of the full three dimensional simulation. The initial conditions are relatively simple; we simply place a sinusoidal perturbation in a one-dimensional box and follow its evolution. Neglecting the pressure term in the momentum equation, a solution to the equations for a flat cosmology is given by (Zel’dovich 1970; Yuan 1991):

$$\rho(x_l) = \rho_0 \left[1 - \frac{1+z_c}{1+z} \cos(kx_l) \right]^{-1},$$

$$v(x_l) = -H_0 \frac{1+z_c}{(1+z)^{1/2}} \frac{\sin(kx_l)}{k}. \quad (3.51)$$

Here, z_c is a free parameter and is the redshift at which the Zel'dovich results ‘pancake’, or form caustics. H_0 is the current value of the Hubble constant, often parameterized as $H_0 = 100h$ km/s/Mpc, and $k = 2\pi/\lambda$ where λ is the perturbation wavelength. We note that this solution is exact in one dimension up until the point of caustic formation. However, these expressions are in terms of Lagrangean positions x_l , so we need to convert the Eulerian coordinates of the code (x_e) into Lagrangean coordinates:

$$x_l - \frac{1+z_c}{1+z} \frac{\sin(kx_l)}{k} = x_e. \quad (3.52)$$

As a check of the linear evolution, we run a model from an initial redshift $z_i = 100$ to $z_f = 20$ with the following parameters: 256 zones, $T_{init} = 10^2 K$, $\lambda = 64h^{-1}$ Mpc, $h = 0.5$ and $z_c = 1$. Defining the L_1 error norm as

$$(\Delta\rho) = \frac{1}{N} \sum_{i=1}^N \left| \frac{\rho(x_l) - \rho_{numerical}}{\rho_0} \right|, \quad (3.53)$$

for density and adopting a similar definitions for v (but using the average analytic velocity to normalize the error), we make the run with N , the number of grid points spanning the perturbation, ranging from 8 to 64. The errors should decrease as Δx^{-r} where r is the convergence rate. In fig. 3.4, we plot both the error and the convergence rate, as found by computing the slope of the logarithmic derivative of the error with respect to N . We see that the velocity converges as $r \sim 2$ and the density as $r \sim 1.5$.

3.3.5 The non-linear phase of the one dimensional Zel’dovich pancake

The non-linear phase of evolution for the caustic is of more practical interest in cosmology, as well as being more difficult than the linear evolution. Figure 3.5 shows the solution at $z = 0$ (using the same initial conditions as in section 3.4) at a resolution of 256 zones, demonstrating the strong shocks and large gradients involved. The shock is well

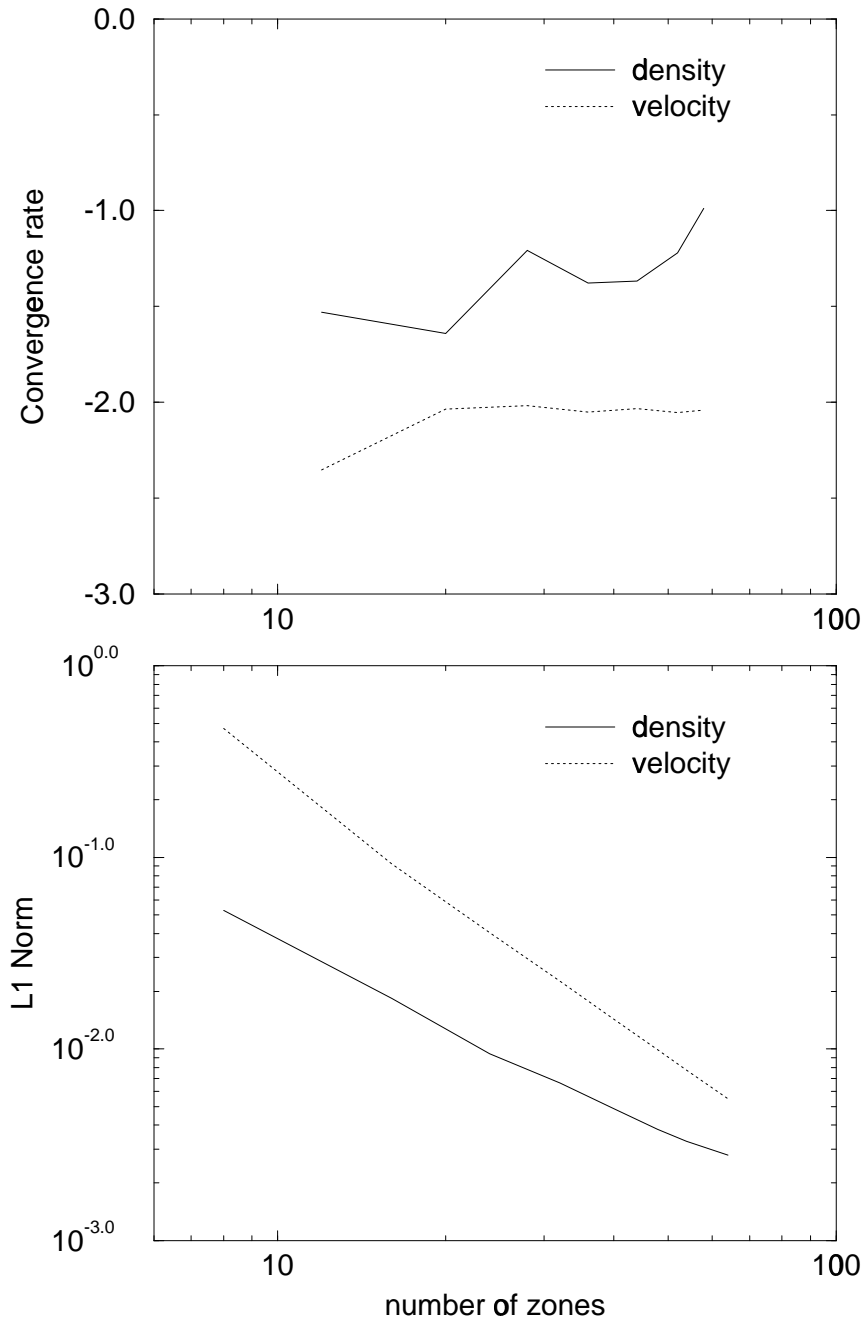


Figure 3.4. Convergence rates and L1 error norms for the density and velocity fields in the one dimension Zel'dovich pancake.

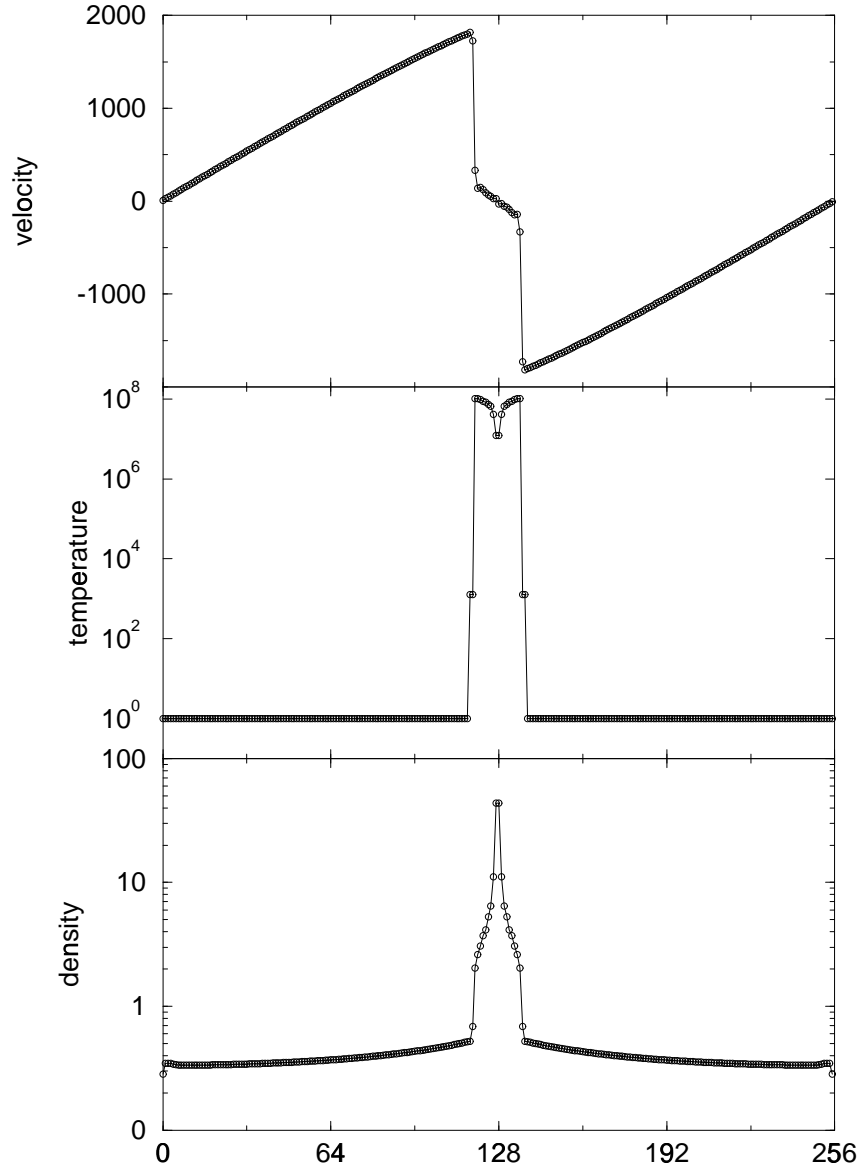


Figure 3.5. The velocity (top), temperature (middle) and density (bottom) for a one dimensional Zel'dovich pancake at a redshift of $z = 0$. Velocity is in km/s, temperature in K, while the density is in units of the current background density required for a flat universe.

delineated and the temperature profile of the very cold gas is still accurate (until it drops below 1 K which we have instituted as an artificial minimum).

We have also performed this test at a number of different resolutions in order to gauge the method's ability to resolve the evolution with a small number of zones. This characteristic is crucial because of the range of wavelengths active in hierarchical cosmological models. The results (at $z = 0$) using 8, 16 and 32 zones are shown in Figure 3.6. Solid lines represent the solution computed at a much higher resolution (1024 zones) and then degraded to the appropriate scale. We do not show examples with more than 32 zones because they exhibit almost no difference from the converged solution (once it is binned to the lower resolution).

Clearly, even with eight zones the main features are right: a sharp central density peak causes a shock to form and move outward from the central plane. The density distribution in each case is very close to its correct shape, although the zones next to the peak are slightly elevated (this is due to the monotonicity of the scheme and not to an explicit diffusion). The pressure and temperature in the central peak are somewhat below the high resolution results, especially for the eight zone test. This is unavoidable as the artificially widened peak (a minimum of two zones for the symmetric case considered here) puts a limit on how much potential energy can be converted to kinetic and thermal energy (see figure 3.8). There is some low temperature jitter (caused by the dual energy formulation), but the most important characteristics are the sharp shocks and low diffusion, even at poor resolution.

In order to gauge the self-convergence rate in the non-linear regime, we must redefine the error norm because the strong shock causes changes in some quantities by a factor of 10^8 . We adopt, for a quantity q (one of T , v or ρ),

$$(\Delta q) = \frac{1}{N} \sum_{i=1}^N \frac{|q_i - q_{1024,i}|}{\max(|q_i|, |q_{1024,i}|)}, \quad (3.54)$$

where $q_{1024,i}$ is computed by linear interpolating between points of a high resolution solution computed with 1024 cells. The effect of using the maximum of the two quantities in the denominator is to force each term in the error to be between zero and one. Figure 3.7

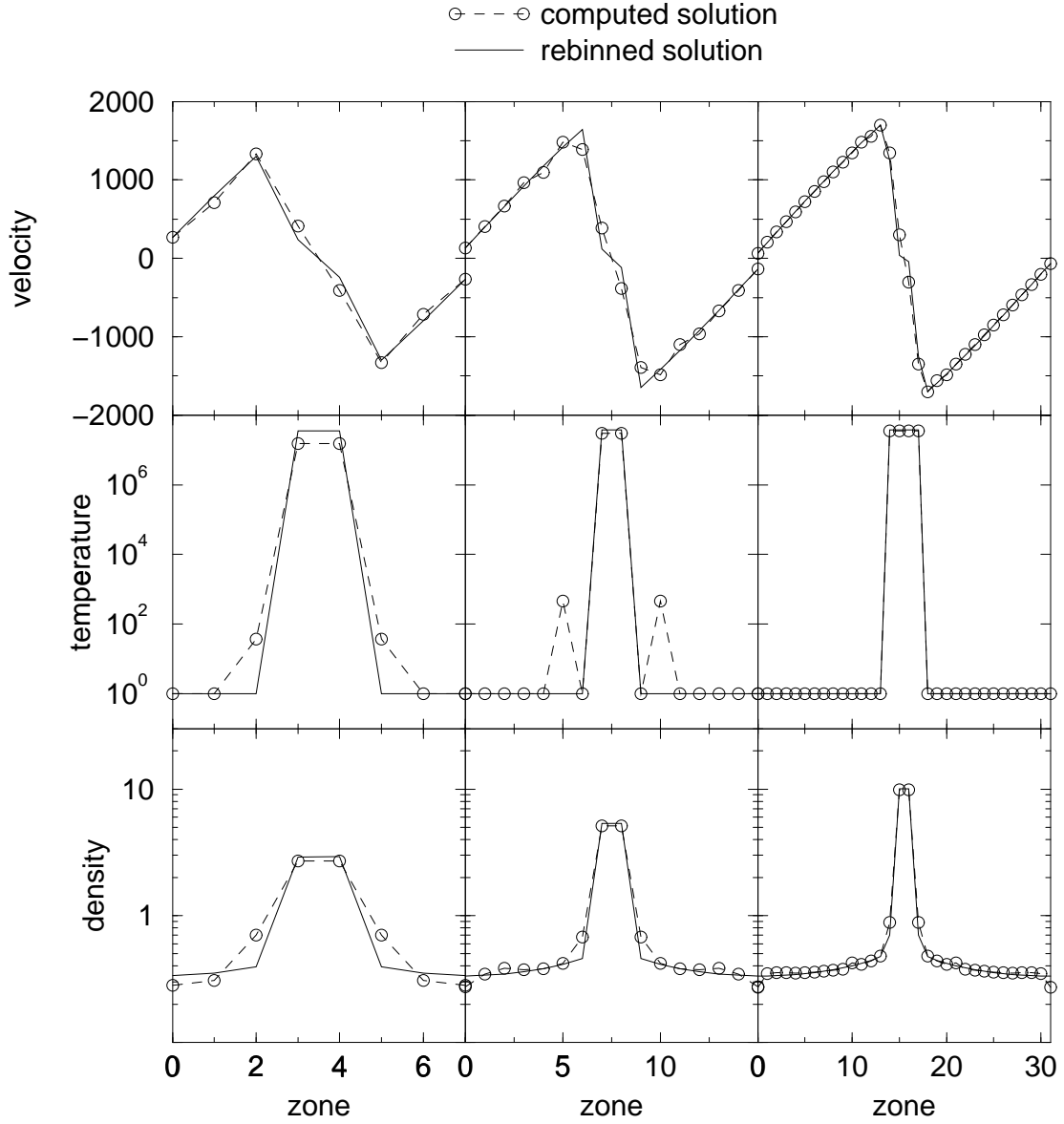


Figure 3.6. The velocity (top), temperature (middle) and density (bottom) for a one dimensional Zel'dovich pancake at a redshift of $z = 0$. Open circles with dotted lines depict the solution computed with 8, 16 or 32 zones (left, center or right panels), while the solid lines represent the solution computed with 1024 zones and degraded to the appropriate number of zones. Units are as in the previous figure.

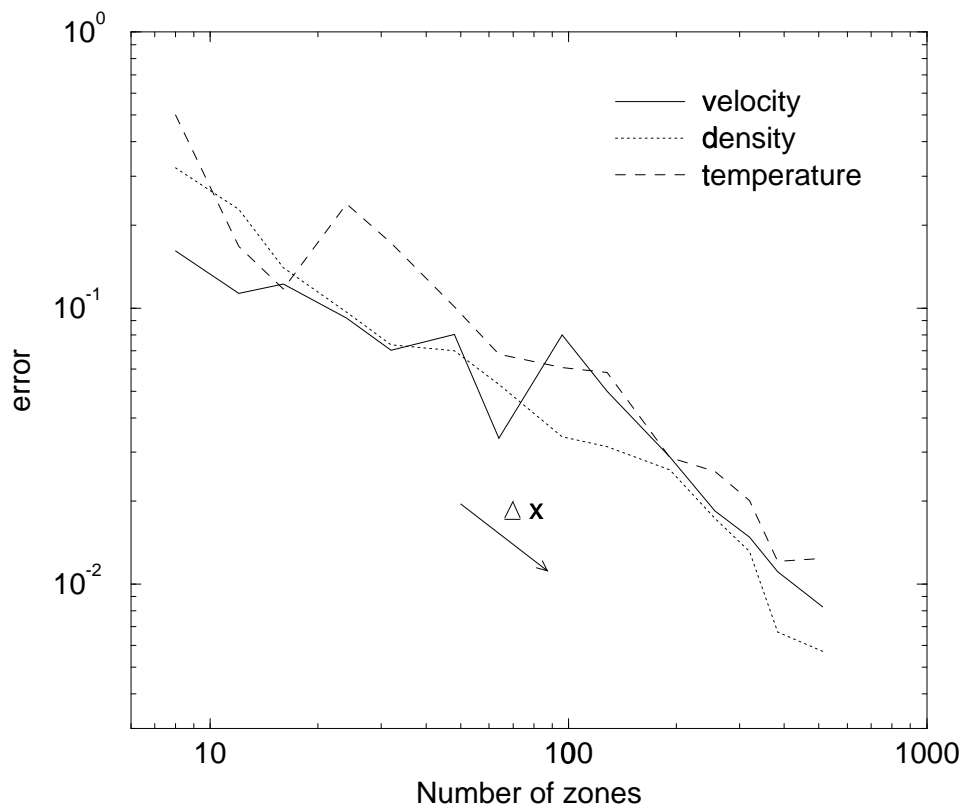


Figure 3.7. The self-convergence error (see text for a definition) of the non-linear phase ($z = 0$) of the Zel'dovich pancake. The arrow shows a convergence rate of 1.

shows the error for a number of different resolutions. Although the sharp shock causes some noise, the convergence rate appears to be $r \sim 1$. The presence of a discontinuity prevents a convergence rate better than one.

In figure 3.8, we show the dependence of the various energy terms on resolution, as well as the fractional energy gain or loss (defined as the ratio of the difference between the right and left hand sides of eq. (3.44) to $a^n W^n$). The drop in thermal energy seen below 32 zones is due to the inability of the small mesh to represent such a narrow central peak. This makes the magnitude of the potential energy too small. The thermal energy mirrors this, but the kinetic energy remains constant and does not decline as it should. Once again, this is due to a lack of resolution. Immediately after the peak is formed, it is two

zones wide (due to the symmetry of the initial conditions), while the true distribution is much narrower. Insufficient thermal energy has been produced to support this artificially thick structure and it should collapse further but is prevented by the coarseness of the grid. One can think of this as a fictitious ‘grid’ force that is not represented in the energy equation and so shows up as a violation of energy conservation. It applies to highly under-sampled structures and represents only a small amount of energy compared to larger and better resolved wavelengths. We also point out that the problem is not specifically related to the scheme chosen and should be present in any grid based method that produces such narrow density distributions.

3.3.6 The double pancake with a strong and weak shock

In order to subject the dual energy formulation to a stringent test we have superimposed a smaller perturbation with one fourth of the wavelength onto the pancake described above. Using the same formulation as in the previous problem, we adopt $z_{c2} = 0.45$ and $\lambda_2 = 16h^{-1}Mpc$. Note that z_c no longer refers to the redshift of peak formation (since the two perturbations interact) but is related to the amplitude of the imposed sinusoid. In figure 3.9, we show a high resolution computation at $z = 0$, by which time the two central peaks have nearly combined. The side peaks are present but at a much smaller amplitude because they are in the low density region created by the main collapse. The ratio of kinetic to thermal energy in the two smaller peaks is about 10^3 , illustrating an occasion when the dual energy formalism is required.

Figure 3.10 shows the results computed with 64 grid points and contrasted with the 1024 zone solution degraded to 64 zones. The strong central shocks on either side of high density plateau are well realized and near their correct locations. The smaller peaks have been stretched by the velocity field of the stronger, inner fluctuations making the profiles wider than in the high resolution run. The shocks are also much weaker, having been modulated by ϵ , the internal energy formulation. Notice that while this produces wider, less clearly defined shocks, they are still reasonably accurate. The main features of the flow are present even though the thermal energy in the smaller shocks is one tenth of

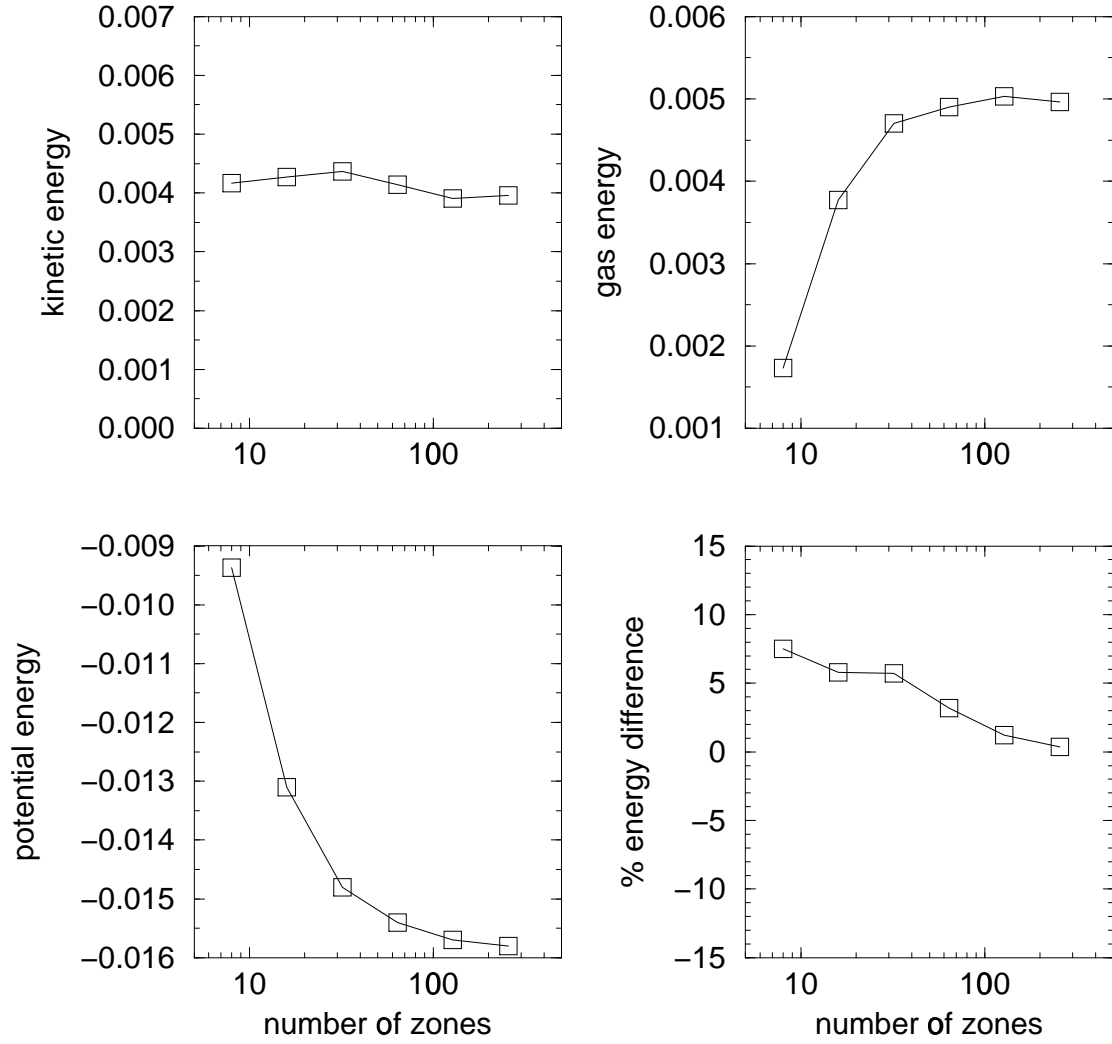


Figure 3.8. The kinetic energy (top right), thermal energy (top left), gravitational potential energy (bottom left) and fractional energy gain or loss (bottom right) for the one dimensional Zel'dovich pancake at various resolutions. All energies are in dimensionless units.

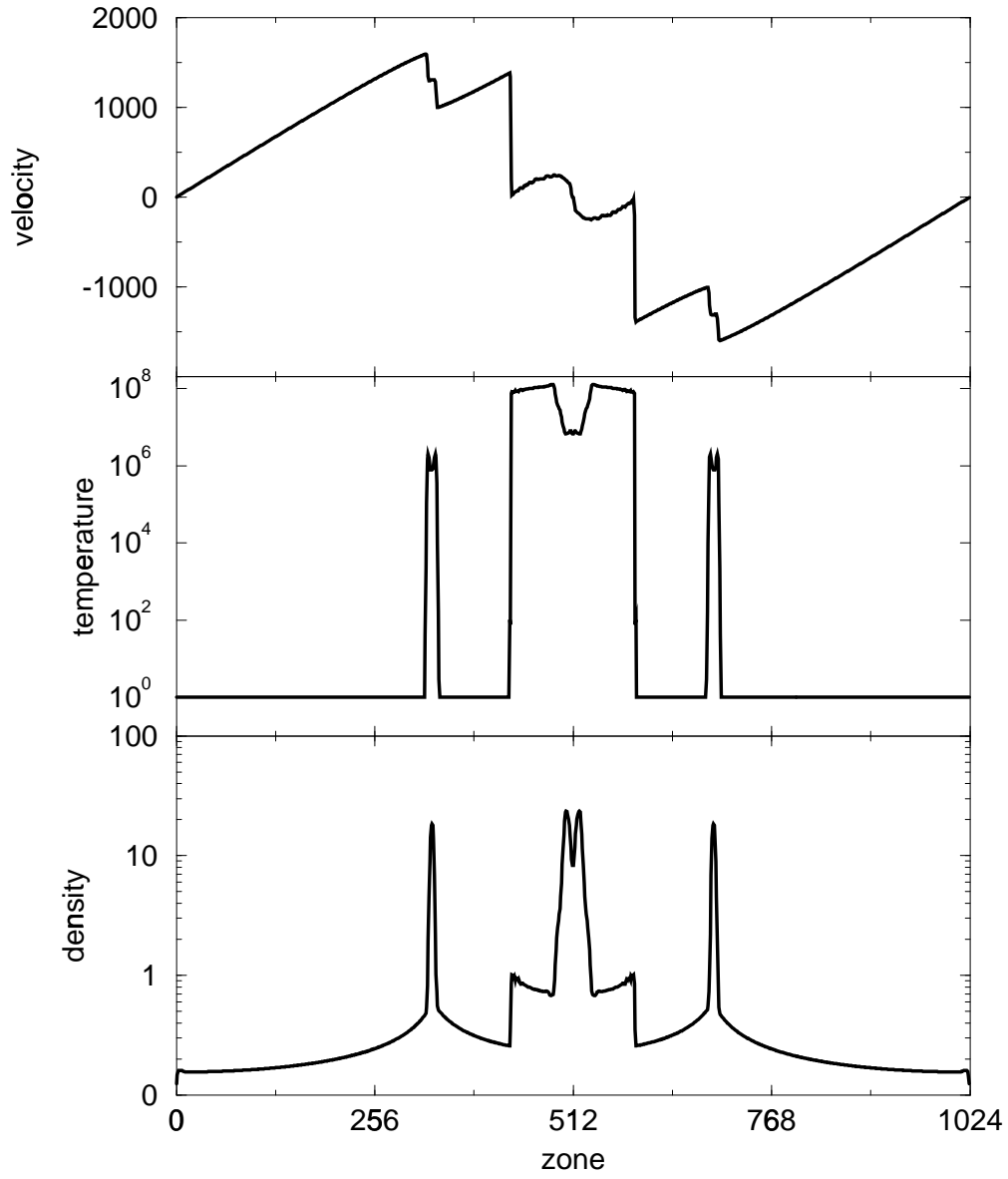


Figure 3.9. The velocity (top), temperature (middle) and density (bottom) for a double one dimensional Zel'dovich pancake at a redshift of $z = 0$. Units are as in the previous figures.

one percent of their energy of bulk motion and each wavelength is resolved by less than sixteen zones. These last two conditions make this a difficult test for any cosmological code.

3.3.7 Two dimensional self-convergence tests

As a final test, we compute a two-dimensional cold dark matter universe in order to test the self-convergence in a more realistic, multi-dimensional test (the parameters are identical to those in the next section, except, of course, for being two dimensional). Performing these tests in only two dimensions increases the dynamical range that can be obtained with only a modest expenditure of computational resources. We run the simulations at a variety of resolutions in order to investigate the self-convergence properties of the code. In order to do this, however, we must insure that the physical problem we are solving is the same at each resolution. Since the initial conditions contain a spectrum of length scales, we must introduce an artificial cutoff in the power spectrum of initial perturbations. This is done such that the shortest wavelength used for the initial conditions is the the Nyquist wavelength of the smallest box to be examined, here 64 zones on a side.

The results at the end of the simulation ($z = 0$) for 64^2 , 128^2 and 256^2 grid points are shown in figure 11. Since the shortest perturbations are just two zones in the 64^2 box we do not expect such short wavelengths to be accurately evolved. Nonetheless, the correspondence between recognizable features in the three simulations is gratifying. It is clear from a visual inspection that the structures created are quite robust, despite the fact that they are often intrinsically much thinner than the grid can handle. Larger simulations have been computed, up to 1024^2 , and no new features are observed, although the caustics continue to be thinner at higher resolution.

In order to be more quantitative, we have degraded the 1024^2 zone solution by averaging the density (and density weighted temperature) of all the high resolution cells that lie within a lower resolution zone. This gives a one-to-one correspondence between solutions computed with different resolutions. Scatter plots are presented for the 64^2 solution in figure 3.12 and 256^2 in figure 3.13. Our earlier statements are confirmed.

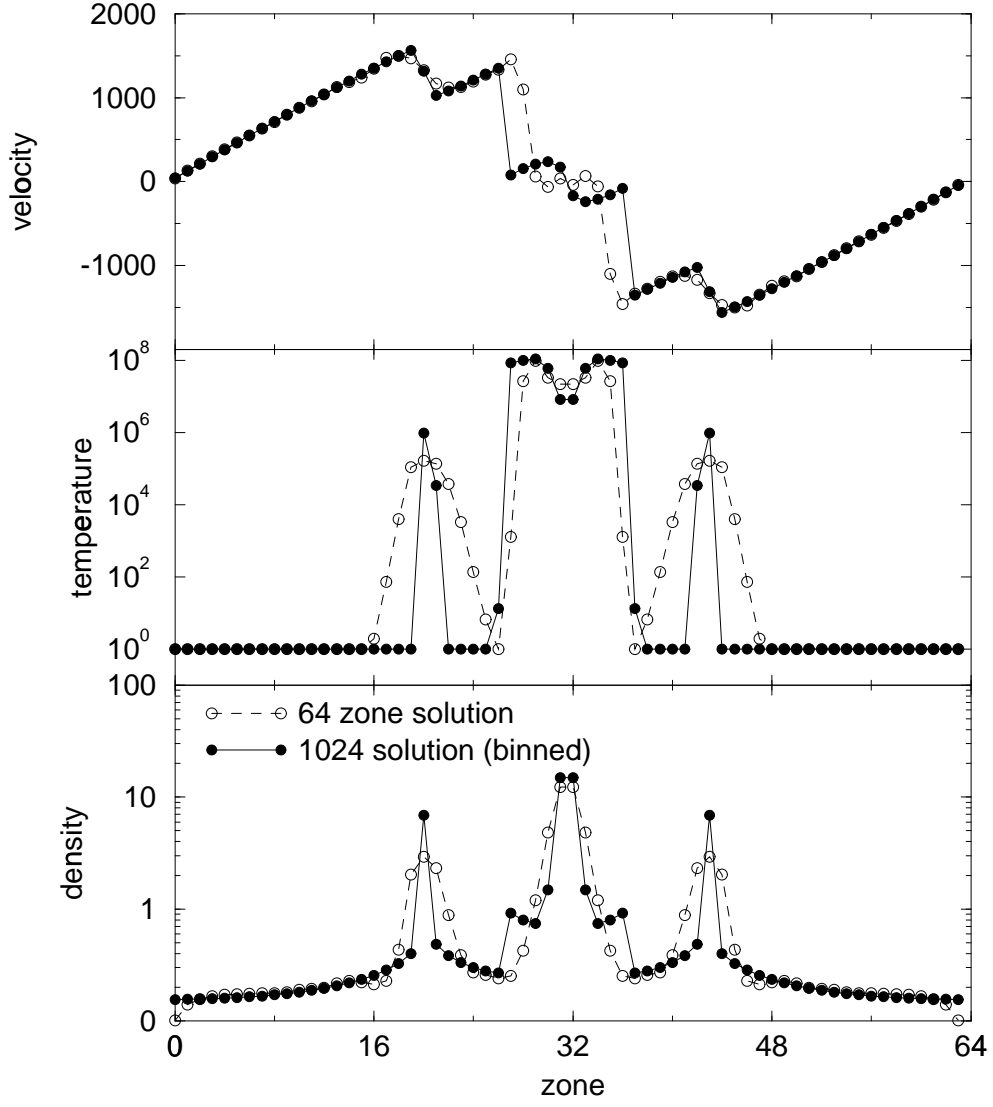


Figure 3.10. The velocity (top), temperature (middle) and density (bottom) for a double one dimensional Zel'dovich pancake at a redshift of $z = 0$. Open circles with dotted lines depict the solution computed with 64 zones, while the solid lines with filled circles represent the solution computed with 1024 cells and degraded to 64 zones. Units are as in the previous figure.

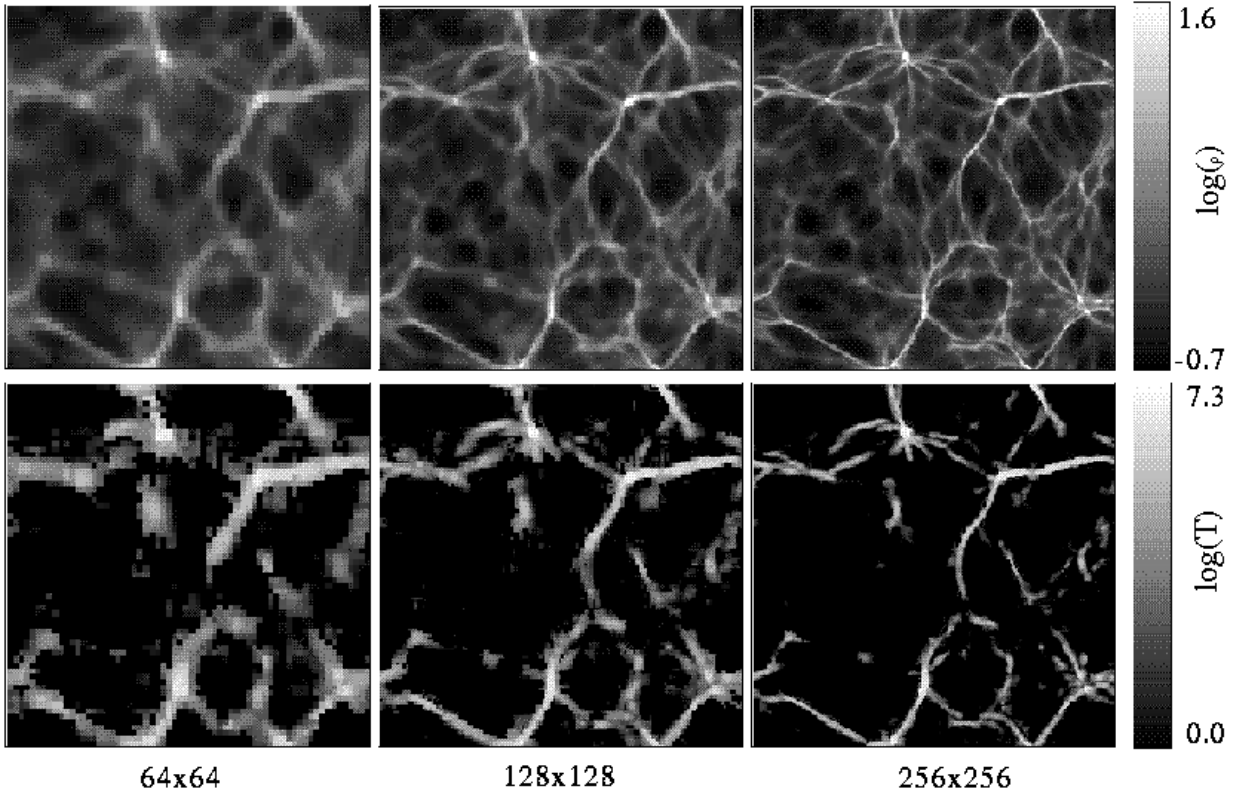


Figure 3.11. Greyscale plots of the logarithm of density (top three panels) and temperature (bottom three panels) for a two dimensional CDM simulation computed with the same initial conditions at three different resolutions: 64×64 (left panels), 128×128 (central panels) and 256×256 zones (right panels). Temperature is in degrees Kelvin, density in units of the present density required to close the universe.

Although the scatter is fairly large in the first figure, there is correspondence over four orders of magnitude in temperature and two orders in density. The second plot displays even better agreement between the lower and high resolution runs.

3.3.8 Comparison with other codes

We have also, with others, carried out a comparison of this method with other modern cosmological codes, both Eulerian and Lagrangean. In order to examine a realistic model with the effects of dark matter, we computed the evolution of a flat, pure baryon universe using initial conditions from the cold dark matter (CDM) scenario. Although this is not a viable model, it does present a clearly defined test problem that does not depend on the

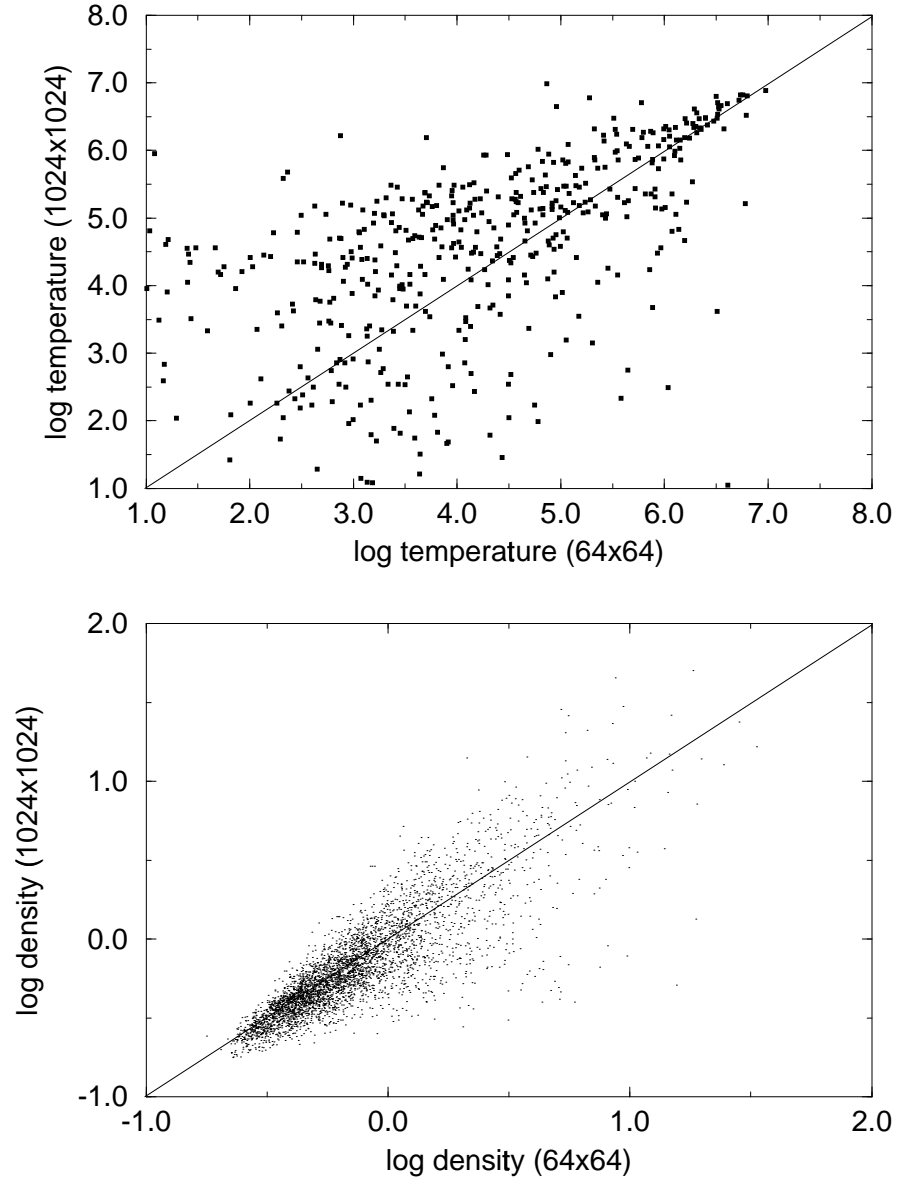


Figure 3.12. Scatter plots of temperature (top) and density (bottom) for a two dimensional CDM simulation computed with 64×64 zones compared on a cell-by-cell basis against a simulation computed with 1024×1024 cells and degraded to 64×64 . Temperature is in degrees Kelvin, density in units of the present density required to close the universe.

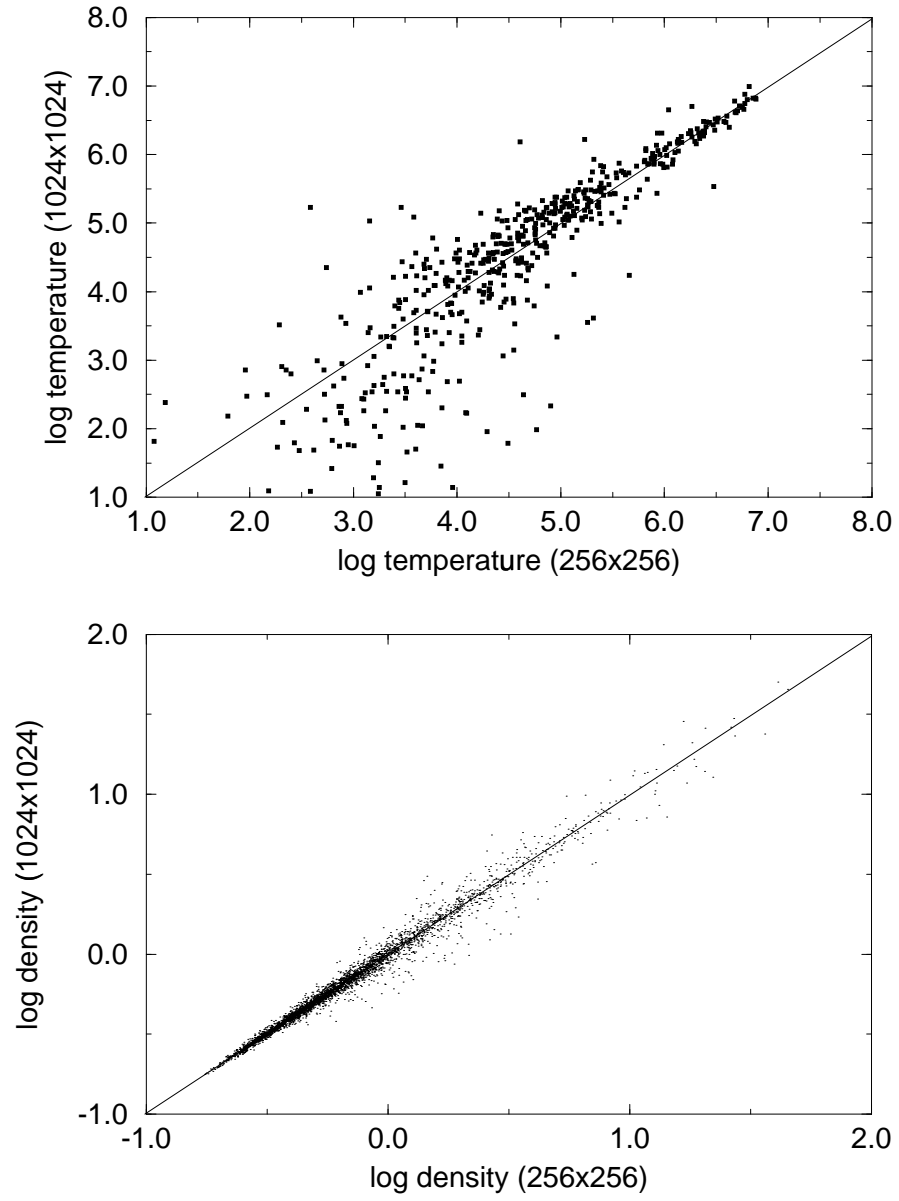


Figure 3.13. Similar plots as in the previous figure, except for a simulation computed with 256×256 zones.

N-body solver. The model can be parameterized in terms of Ω , the ratio of the average density to that required to close the universe and σ_8 , the amplitude of mass fluctuations in a sphere of radius $8h^{-1}$ Mpc at $z = 0$. We choose the canonical values $\Omega = 1$, $\sigma_8 = 1$, $h = 0.5$ and used a physical box of length $64 h^{-1}$ Mpc. Four runs were performed, using grids of 32^3 , 64^3 , 128^3 and 256^3 with the same initial conditions smoothed to the Nyquist wavelength of the 64^3 cube. The simulations were run from $z_{init} = 20$ to $z = 0$.

The simulations are analyzed in detail elsewhere (Kang et al. 1994b) and we will not repeat the analysis here, except to comment that the results only serve to strengthen our conclusion that this scheme is robust and accurate.

3.4 Conclusions

We have described the changes necessary for applying the third order accurate, shock capturing hydrodynamics scheme PPM to cosmological systems. The range of scales makes this a very difficult problem and has forced the adoption of an unusual method for dealing with the presence of weak shocks in supersonic flows. Although this method is not particularly elegant it does seem to produce the correct results. The correction to the Riemannnn solver is also somewhat *ad hoc* and work is underway to incorporate self gravity in a more self-consistent fashion.

We have also presented the results of a series of tests selected for their relevance to cosmological studies. The guiding philosophy in presenting this test suite is not only to show that the correct results are produced with sufficient resolution, but also to demonstrate that the solutions under conditions of low resolution approach those that are as good as the resolution allows. Since simulations are often run that depend on the accurate evolution of small wavelengths, this last point is important. We conclude that a higher order, shock capturing scheme such as PPM is essential for cosmological work and also that the modifications described here produce a robust, high resolution code.

The code has been written in FORTRAN 77 and runs at 1.3×10^4 zone-cycles per second on one processor of a Convex 3880 (1.7×10^4 zone-cycles per second without the

N-body solver and Poisson solver). It has also been converted to CM FORTRAN, a data parallel language similar to FORTRAN 90 that is used on the massively parallel Connection Machine 5. It runs at 1×10^6 zone-cycles per second on 512 nodes (2×10^6 zone-cycles per second without the N-body solver and 4×10^6 without the Poisson solver).

Chapter 4

X-Ray Clusters from a Hydrodynamic Simulation of the CDM Universe

4.1 Introduction

The X-ray emission from hot gas in clusters of galaxies has been studied for over a generation (c.f. Gursky et al. 1971), with new satellite observations by ROSAT (Trumper 1990) and other space instruments rapidly increasing our knowledge. It has recently been realized that these systems provide the opportunity for critical tests of cosmological theories proposing to explain the growth of structure in the universe (c.f. references in Frenk et al. 1990 and in Ostriker 1993). The great clusters of galaxies, which have size of the order $1h^{-1}$ Mpc and separations of order $50h^{-1}$ Mpc, provide a measure of the nonlinearity of the density fluctuations on intermediate scales close to the usual normalization scale: $\sigma_8^2 \equiv \langle (\delta M/M)^2 \rangle_8$, where the subscript “8” designates the $8h^{-1}$ Mpc scale, which is the radius of the top-hat filter used to calibrate the standard fluctuation measure.

In most optical studies of clusters one directly measures $\int n_g ds$ along the line of sight through the cluster or measures some moment of this such as $\int v_{||}^2 n_g ds / \int n_g ds$, where n_g is the galaxy volume density and $v_{||}$ the galaxy velocity dispersion. Since n_g is of order 10^3 times $\langle n_g \rangle$, and the cluster pathlength Δl is of order 10^{-3} Mpc times the Hubble length, c/H_0 , the surface overdensities, $(\int n_g ds - \int \langle n_g \rangle ds) / \int \langle n_g \rangle ds$, are only of order unity, leading to intense discussion (c.f. Dekel et al. 1989; Frenk et al. 1990) concerning foreground and background contamination of samples, chance projection effects, etc. But the X-ray bremsstrahlung intensity towards a resolved cluster is proportional to $\int \rho^2 T^{-1/2} ds$, with the result that the contrast between the cluster and background in the X-ray band is enormous (of order $10^2 - 10^3$) in contrast to optical band measurements.

Theoretical predictions of cluster properties will of course be uncertain to the extent that we do not know three things: $\Omega_b \equiv \rho_{baryon} / \rho_{crit}$; how large a fraction of the baryons has been transformed to galaxies; and finally how representative are the clusters, i.e., what is the ratio

$$b_x \equiv (\rho_{b,cl} / \rho_{tot,cl}) / (\Omega_b / \Omega_{tot}). \quad (4.1)$$

On each of these issues our understanding has now reached the point where the uncertainties are minor. With regard to Ω_b , light element nucleosynthesis gives $\Omega_b = 0.06 \pm 0.01$ [we adopt a value slightly larger than that given by Walker et al. (1991), 0.05 ± 0.01] within the standard paradigm. In addition, since whatever this ratio is, it is not time dependent, we can make comparisons of the X-ray cluster luminosity functions (or other properties) at $z = 0$ with those at higher redshift independent of a precise knowledge of Ω_b . Second, recent observations have indicated that the baryons in the clusters are predominantly in the hot gaseous phase (White 1992), so corrections for the condensed (galactic) fraction are small. Finally, numerical hydrodynamical investigations such as the current paper addresses this issue directly, indicating that the clusters are slightly anti-biased with respect to the global averages, i.e., the number $b_x \approx 1/1.5$, or less.

In addition, the physical state of the gas in the great clusters is rather simple to model. In a cluster with central density $n_H = 1 \times 10^{-3} \text{cm}^{-3}$ and central temperature

$kT_x = 5\text{keV}$ the cooling time is 2.0×10^{10} yrs, longer than the Hubble time. Thus, an adiabatic treatment is legitimate as long as the only entropy input is from shock fronts where atomic collisions transform the kinetic energy of converging gas flows into thermal energy.

The primary difficulty in accurately predicting the state of gas in the great clusters is numerical. The ratio of cluster separation to cluster core size is greater than 10^2 . Thus, in order to obtain both a reasonable statistical sample of clusters and also to resolve individual clusters, a ratio of box size to resolution element ($L/\Delta l$) $> 10^2$ is needed. This of course translates to $N > 10^6$ cells and dark matter particles in an Eulerian+PM code and requires that the true code resolution be of order the cell size or else a corresponding increase in machine capacity is required. From initial exploratory work by Chiang, Ryu, & Vishniac (1989) and Ryu, Vishniac, & Chiang (1990) with 32^3 particles and cells to recent work (Cen, Gnedin & Ostriker 1993; Cen & Ostriker 1993a) with 200^3 particles and cells there has been a steady improvement of the numerical treatment.

But these papers all used a diffusive (Richtmyer & Morton 1967) treatment of shocks with an “artificial viscosity” which spreads shocks over 4-5 cells. Recently 3-D shock capturing codes have been developed which contain shocks within two zones. Ryu et al. (1993) implemented the Total Variation Diminishing (TVD) scheme for cosmological applications and another paper (Kang et al. 1994a = KCOR) used this code to study the standard CDM scenario.

Needless to say, serious questions remain concerning the accuracy and reliability of the numerical codes. We have performed a detailed comparison of several different codes, including Eulerian as well as Smoothed Particle Hydrodynamic (SPH) methods (Kang et al. 1994b). The SPH (Lagrangian) approach taken by Evrard, Summers, & Davis (1994) and Katz, Hernquist & Weinberg (1993) has considerably higher spatial resolution than do equivalent Eulerian methods, but this is obtained at a cost that makes investigation of large cosmological volumes possible only with relatively poor mass resolution. Here we use an alternative Eulerian code based on the Piecewise Parabolic Method (PPM), which

has resolution higher than that of the TVD code. The accuracy of energy conservation is, however, slightly lower in this PPM code.

The two codes have been developed independently and a comparison of the results obtained by the two methods utilizing identical initial conditions should help indicate which results are robust and which are still significantly uncertain due to numerical effects. In section 4.2 we outline the method and initial conditions, in section 4.3 the results and in section 4.4 we assemble our conclusions with primary emphasis on the comparison between the PPM and TVD results.

4.2 Method And Initial Conditions

A hybrid code was used to perform these calculations; a standard N-body particle code (more specifically, a particle-mesh technique) was combined with our implementation of the grid-based piecewise parabolic method (PPM) to solve the hydrodynamic equations. The PPM algorithm is described by Colella and Woodward (1984) and provides higher order accuracy along with the ability to capture shocks in a small number of zones while avoiding post shock oscillations. The net result is an increase in resolution for the same number of zones, crucial for cosmology, where many length scales are important.

However, a number of modifications were required to make the method suitable for cosmological simulations. These modifications, along with the details of testing, described in chapter 3 (Bryan et al. 1995), are briefly summarized here. Gravitational forces both from the gas and the dark matter were included, as was the Hubble expansion. The code solves both the total energy and thermal energy equations in order to obtain the correct pressure distribution, both in cold flows, where kinetic energy terms dominate, and in strong shocks, where most of the energy is thermalized. Finally, a new pressure interpolation was adopted for thin, collapsing structures in order to better model strongly peaked features.

The PPM technique has been subjected to many hydrodynamic tests, some of which are described in Woodward and Colella (1984). We have also applied this specific code

to a suite of cosmological test problems, including a one dimensional Zeldovich pancake collapse and resolution studies involving the standard CDM model.

4.2.1 Initial Conditions

We adopt the standard CDM power spectrum with the transfer function given by Bardeen et al. (1984). The following parameters are used: $n = 1$, $h = 0.5$, $\Omega = 1$, $\Omega_b = 0.06$ and $\sigma_8 = 1.05$, the same as utilized by KCOR. Note that the amplitude normalization of the power spectrum is determined by COBE observations (c.f. Efstathiou, Bond & White 1992), parameterized by σ_8 to translate into conventional notation. Our box size is $85h^{-1}$ Mpc with 270^3 cells and 135^3 dark matter particles (again the same as KCOR) so our nominal resolution is $0.31h^{-1}$ Mpc. The choice of Ω_b is consistent with light element nucleosynthesis (Walker et al. 1991). The same initial conditions were used as in KCOR.

4.3 Results

The X-ray clusters in the simulation are identified as follows. We first calculate the total X-ray luminosity due to thermal Bremsstrahlung (assuming primeval composition and neglecting lines) for each cell given the cell density and temperature assuming cosmic abundances with both hydrogen and helium fully ionized. The detailed formulae were presented in KCOR. Note that in the following discussion all units of length are given in co-moving not metric coordinates.

The cells with the total X-ray luminosity higher than 10^{38} erg s $^{-1}$ are selected as X-ray bright cells. Then we find the local maxima (by comparing L_{ff} of each X-ray bright cell with that of 26 neighbouring cells) and identify them as the centers of the X-ray clusters. Having defined the centers of the X-ray clusters, we go back to the whole simulation box to define our X-ray clusters. We analyze the simulation in two different ways (which correspond to spheres of radius $0.5h^{-1}$ Mpc and $1.0h^{-1}$ Mpc) as follows. First, each cluster core consists of 27 cells (26 cells surrounding the central cell plus the central cell). These 27 cells are weighted so that total volume of the cluster equals the volume of

a sphere of radius $0.5h^{-1}\text{Mpc}$ as appropriate for observationally defined X-ray clusters. That is, we define a weight $w = R_v$ for the central cell and the 6 cells that share the faces with the central cell, $w = (3/4)R_v$ for 12 cells that share the edges with the central cell, and $w = (1/2)R_v$ for 8 cells that shares only the corners with the central cell, where $R_v = (4\pi 0.5^3/3)/(20\Delta x^3) = 0.839$. This weighting scheme compensates for the adoption of slightly too large a volume by lowering the weight per cell. For concentrated clusters we may be underestimating the luminosity by as much as 16% a correction small compared to other errors. Second, the total X-ray cluster volume consists of 125 cells (124 cells surrounding the central cell plus the central cell) and each cell is weighted equally which gives a volume equivalent to a sphere of radius $0.98h^{-1}\text{ Mpc}$.

Our $(85h^{-1}\text{ Mpc})^3$ box at $z = 0$ contained (1,0) clusters with (total, core) luminosity brighter than 10^{45} erg/s , (10,4) brighter than 10^{44} erg/s , (43,29) brighter than 10^{43} erg/s , (189,127) brighter than 10^{42} erg/s and (433,360) brighter than 10^{41} erg/s . We attribute the small number of clusters brighter than 10^{45} erg/s as simply due to the size of our box. An additional factor of at least two in scale (and 8 in computer resources) would be required to significantly improve on the quoted results. An immediate comparison to the KCOR results is possible if one notes that for $L_x > 10^{44}\text{ erg/s}$ that paper found (8,1) clusters with (total, core) luminosity higher than the specified limit compared to (10,4) in this work. This paper finds higher luminosities, especially core luminosities, due to slightly higher resolution.

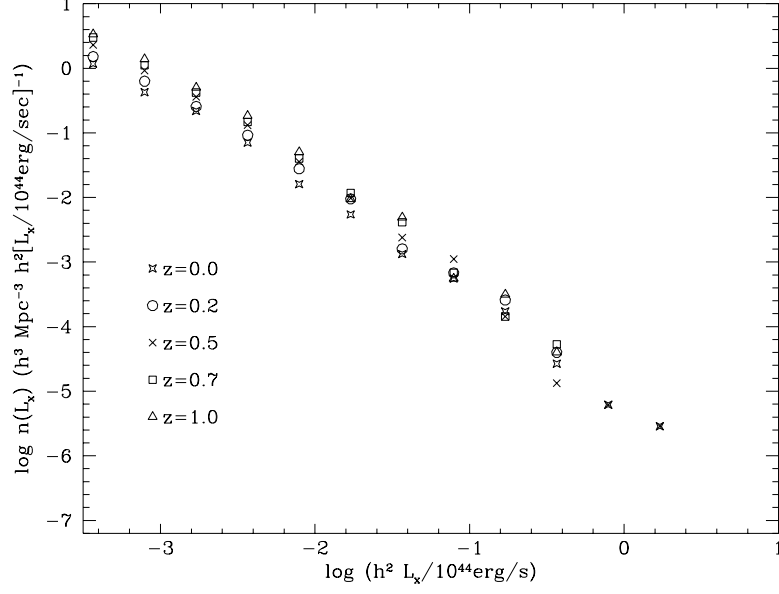
It is convenient to fit the luminosity function to the three parameter Schechter function:

$$n(L)dL = n_0(L/L_*)^{-\alpha}e^{-L/L_*}d(L/L_*) \quad (4.2)$$

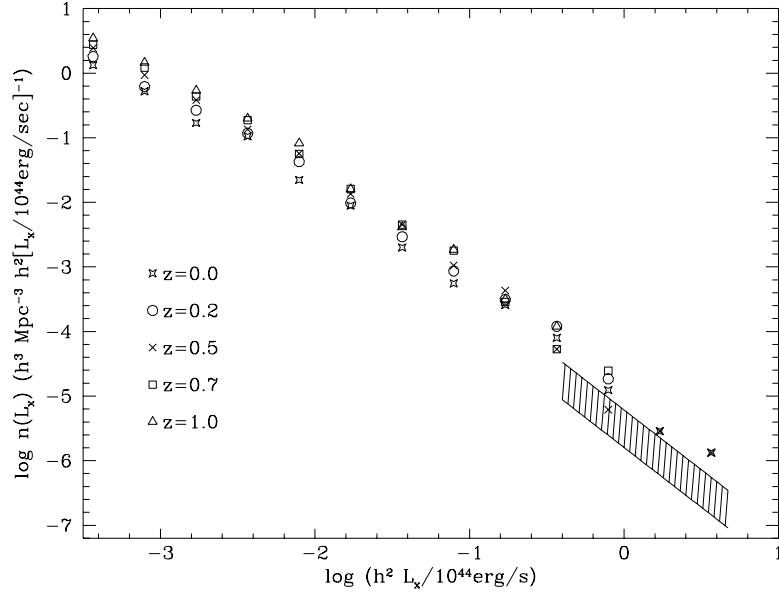
Luminosity functions for cluster cores were computed in four frequency bands: total Bremsstrahlung luminosity, $0.3 - 3.5\text{ keV}$, $0.5 - 4.5\text{ keV}$ and $2 - 10\text{ keV}$ and are displayed in Figures 4.1a, 4.2a, 4.3a, and 4.4a, respectively. The results for entire clusters (emission from a $1h^{-1}\text{ Mpc}$ sphere) are presented for the same frequency bands in Figures 4.1b, 4.2b, 4.3b, and 4.4b. The figures show the range of cluster properties which are most accessible to observation: $10^{40}\text{ erg/s} \leq L_x \leq 10^{44}\text{ erg/s}$ and $0 \leq z \leq 1$. Also shown in Figure 4.1b

and 4.4b are the observations from Henry & Arnaud (1991) and from Henry (1992), respectively. We see that the computed number densities of bright clusters ($h^2 L \sim 10^{43}$ erg/s) are above the observed ones by a factor of 5 to 10. We have computed approximate Schechter function fits to the results, with the numerical parameters (n_0, L^*, α) as a function of redshift collected in Tables 4.1–4.4, and the simulated data extended to $z = 5$. Also in these tables we integrate over the cluster luminosity function, using the Schechter fit $j_{cl} \equiv n_0 L^* \Gamma(2 - \alpha)$, showing the result in the second to last column and give also, in the last column, the total emissivity from the box as j_{gas} , which includes the emission from lower density regions further from cluster cores than $0.5h^{-1}$ Mpc and also from clusters whose central emissivity is less than our cutoff value. We estimate that α is well constrained (± 0.03) and the product $n_0 L^*$ is also fairly well constrained, but individual values (n_0, L^*) are poorly determined because L^* is dependent on the quite uncertain highest luminosity clusters. To estimate the purely statistical uncertainty we reanalyzed the $z = 0$ data from the lower panel of Table 4.1 (total, integrated X-ray cluster properties) looking separately at two halves of the box. The fractional differences ($\Delta Q/Q$) for $Q \equiv (\alpha, L_x^*, kT_x, n_0, j_{cl}, j_{gas})$ were found to be (0.032, 0.83, 0.20, 0.54, 0.38, 0.33) respectively. The fact that even the integral j varies significantly between the two halves of the box reminds us again of the “cosmic variance”. Our sample volume is not large enough to give us a robust estimate for the cosmic mean value of j .

We see that the cluster cores, as we have defined them, contain between 1/2 and 1/3 of the total X-ray emission in the regions studied, comparable to the results of KCOR. The total cluster luminosity in the box is typically 5/6 of the X-ray emission from the box, a slightly higher fraction than found by KCOR although the bright clusters ($L \geq 10^{43}$ erg/s) occupy a volume which is less than 10^{-3} of the total, i.e., the emissivity is very concentrated at bright peaks. For the total luminosity the Schechter α parameter is approximately 1.4 (as compared to 1.5 in KCOR) with little evolution and α for the few keV bands is typically slightly flatter at 1.2 (compared to 1.4 in KCOR). For $\alpha < 2$, as we have noted, most of the luminosity arises from bright clusters. These differences between the two methods are of marginal statistical significance.

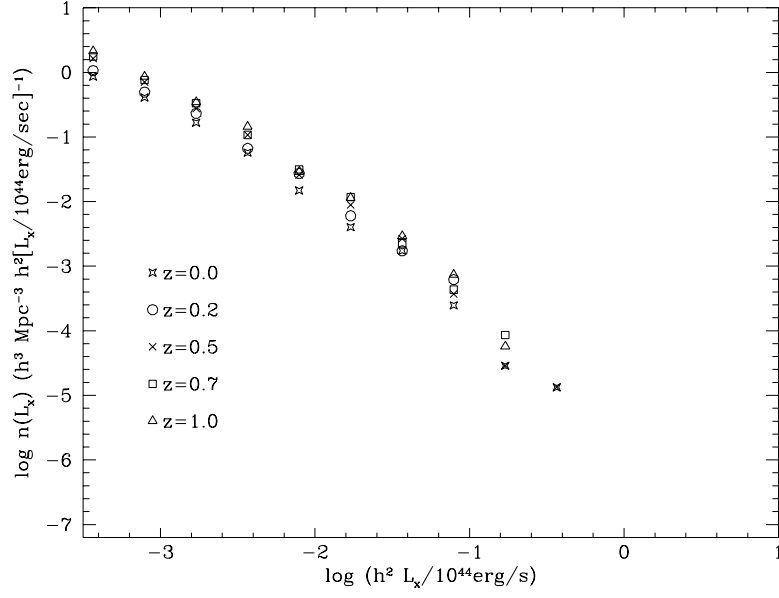


(a)

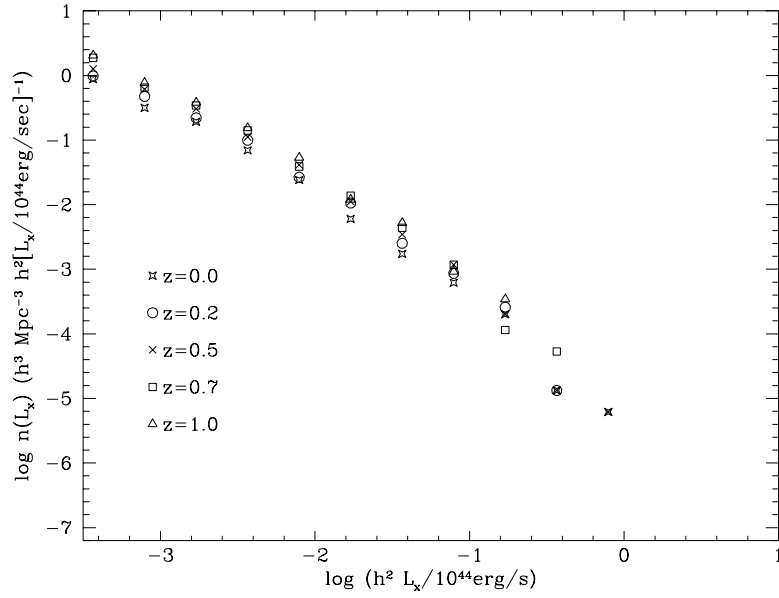


(b)

Figure 4.1. (a) X-ray cluster bremsstrahlung luminosity (from central $< 0.5h^{-1}\text{Mpc}$ regions) function integrated over the whole frequency range at five different redshifts $z = (0, 0.2, 0.5, 0.7, 1.0)$. (b) X-ray cluster bremsstrahlung luminosity (from $< 1.0h^{-1}\text{Mpc}$ region) function integrated over the whole frequency range at the same five different redshifts. The cross-hatched area shows the observations (Henry & Arnaud 1991, $\{3.1^{+4.5}_{-1.8} \times 10^{-6} h^3 \text{Mpc}^{-3} h^2 [L_{44}(\text{bol})]^{-1}\} \times [h^2 L_{44}(\text{bol})]^{-1.85 \pm 0.4}$).

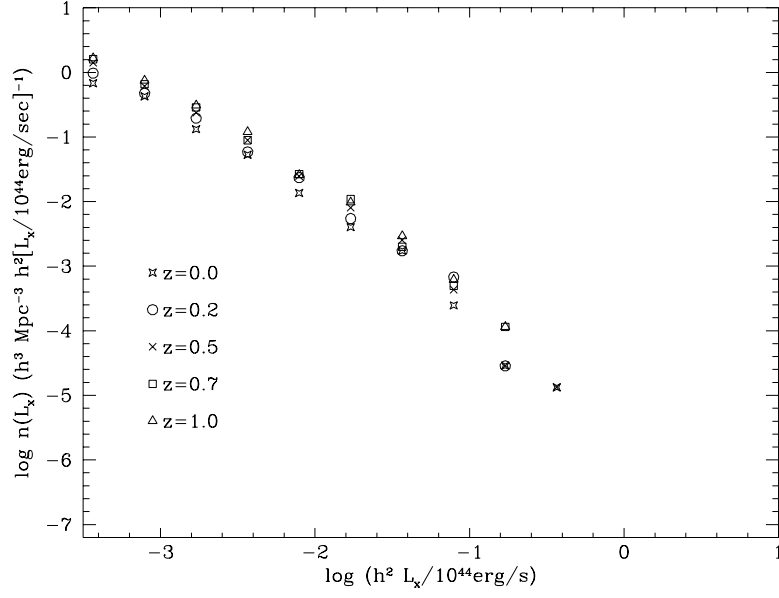


(a)

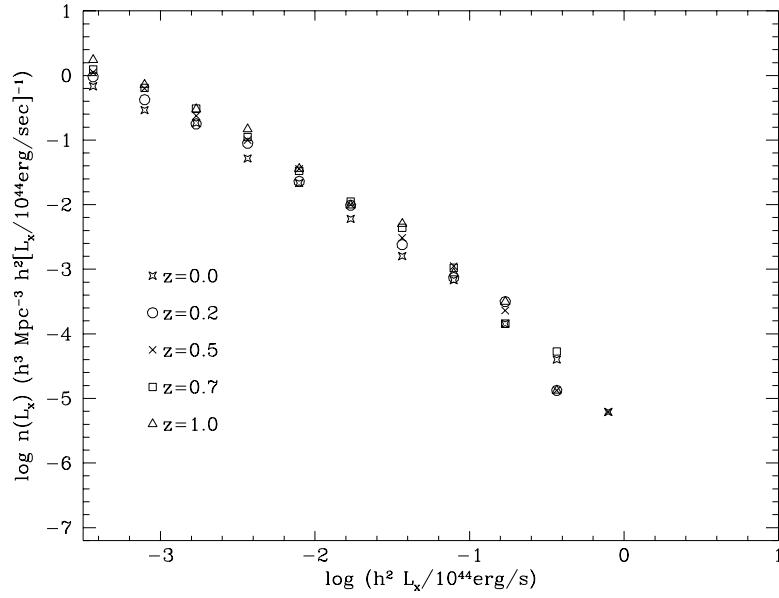


(b)

Figure 4.2. Same as Figure 4.1 but for the luminosities integrated over the 0.3-3.5 keV energy range.

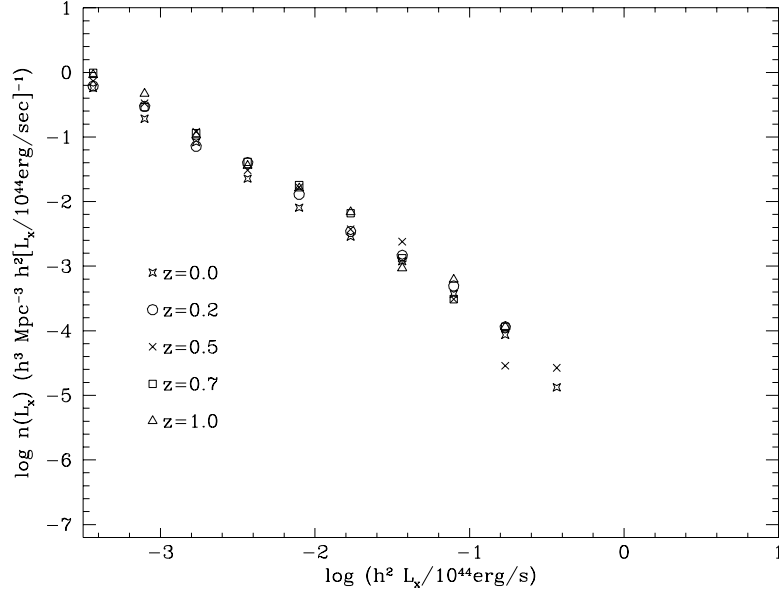


(a)

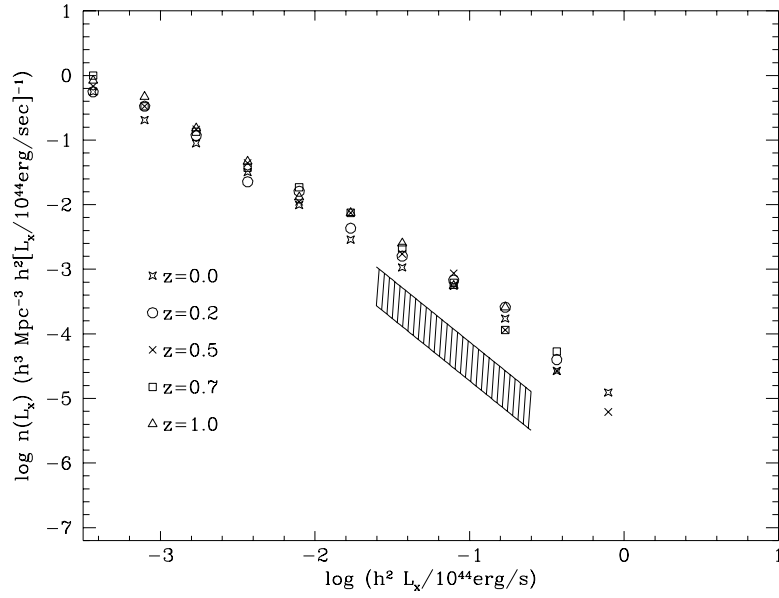


(b)

Figure 4.3. Same as Figure 4.1 but for the luminosities integrated over the 0.5-4.5 keV energy range.



(a)



(b)

Figure 4.4. Same as Figure 4.1 but for the luminosities integrated over the 2-10 keV energy range.

The number density of bright clusters peaks at intermediate redshift and the typical luminosity is (for small redshift) relatively constant, so there is a peak emissivity at approximately $z = 0.5 - 1.0$ for the several keV bands. Thus, crudely speaking, in this model one expects weak “positive” evolution until nearly $z = 1$ and then negative evolution thereafter.

We believe that the peak in emission seen in both simulations at moderate redshift is real. The reasons for this are discussed in KCOR. The approximate Press-Schechter formalism, which does not allow for a variety of effects, can not easily mimic the full non-equilibrium hydrodynamic treatment.

While the integrated X-ray emissivity evolves fairly slowly over the period surveyed in Table 4.1, L_* and n_0 tend to evolve more rapidly and in opposite directions, with more and more lower and lower luminosity clusters at higher redshifts. To highlight the negative evolution of the bright end of the luminosity function we computed the fifth and sixth columns of Tables 4.2–4.4 (sixth and seventh columns of Table 4.1), the comoving density of clusters having luminosity greater than 10^{43} erg/s and 10^{44} erg/s. For reasons stated earlier (based on our limited box size) we use the Schechter fit rather than direct counts to compute these columns. Comparing columns 4 and 6 (5 and 7 of Table 4.1) we see that, although the total number density n_0 of clusters increases with redshift (until $z = 3$), the number density of the highest luminosity ($L_x > 10^{44}$ erg/s) clusters decreases for $z > 0.5$ (the same place as the peak was found in KCOR). This is presumably one of the effects leading to the observational appearance of “negative evolution”. Statistical fluctuations in our results are still quite significant due to the limited box size, especially for $n(L_x > 10^{44}$ erg/s).

Redshift effects strongly exaggerate this tendency to observe negative evolution, since higher redshift clusters tended to have lower temperatures (c.f. column 4 of Table 4.1 and Figure 4.5) and both effects will reduce the energy observed by satellites measuring the X-ray flux in high energy bands. Note that the negative evolution in the density of clusters with $L > 10^{44}$ erg/s is more and more steep in the tables as one looks at higher energy bands, although statistical fluctuations are large.

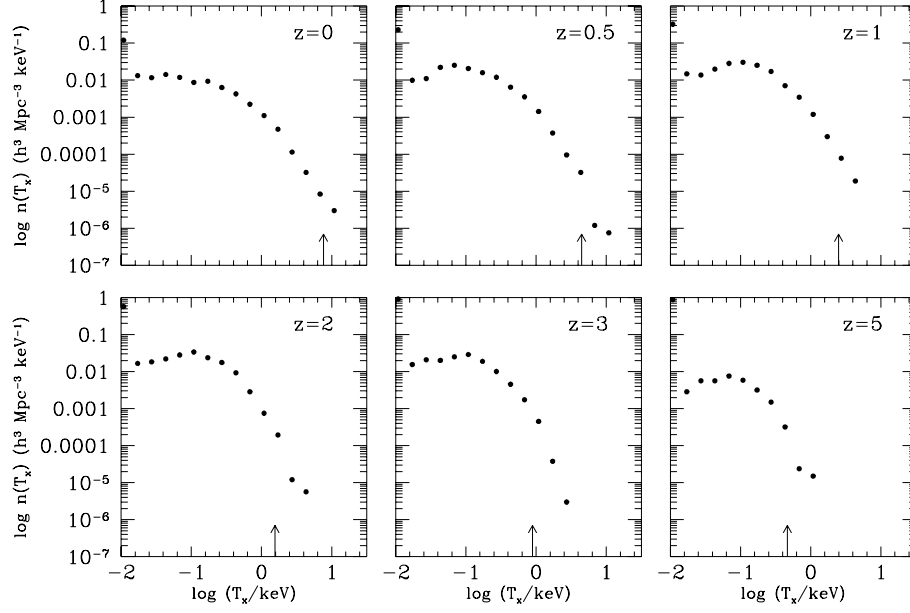
The emission-weighted temperature, T_x of each cluster is calculated and the distributions are shown in Figure 4.5. The arrow in each panel indicates the average cluster temperature (weighted by luminosity) at the given epoch. Also shown in Figure 4.5b (hatched area) is the observed temperature function from Henry & Arnaud (1991) as the cross-shaded area. Note that the computed temperature function is higher than the observed one and shows a much flatter slope than its observational counterpart at the high temperature end. This is consistent with other, independent tests such as the cluster mass function (Bahcall & Cen 1992). We see that at all epochs the coolest clusters dominate the statistics (the turnover at low T_x is presumably caused by our definition of the minimum cell luminosity necessary to constitute an X-ray bright cell), but the mean is determined by the high mass, high luminosity, high temperature end of the distribution. The increase of the mean with increasing time is for the usual reason, $T_x \propto (H\lambda)^2$, with the wavelength of nonlinear waves increasing with time faster than H decreases. The mean temperatures, indicated by arrows, are included in column 3 of Table 4.1. The results are very close to those found in KCOR with $(\bar{T}_{PPM}/\bar{T}_{TVD}) = 0.99$ for entire clusters after averaging over the five most recent tabulated cosmological epochs. Looking ahead to Figure ??a we see the strong correlation found between T_x and total luminosity (clusters are shown at $z = 0$).

Now let us turn again to the total cluster luminosity (vs core luminosity) as shown in the lower panels of the tables and in Figures 4.1b–??b, the quantity normally measured by satellite observations. The ratio of $(j_{cl,tot}/j_{cl,core})$ is near 2.0 ± 0.1 for the redshift range $0 < z < 1$, slightly, and perhaps not significantly, less than the ratio 2.2 ± 0.1 found by KCOR.

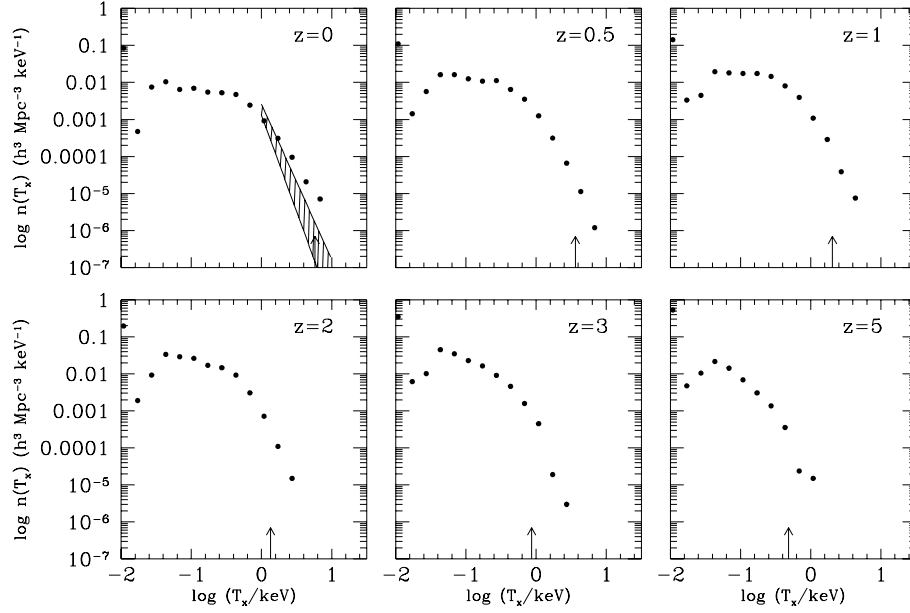
We can also roughly estimate the effective radii of the clusters by assuming that the emission has a profile

$$j = \frac{j_0}{[1 + (r/r_x)^2]^2} \quad (4.3)$$

and determining, from the ratio of the luminosity (integrated over frequency) of the central cell to the total cluster luminosity, the value of r_x which would produce this ratio. We show in Figure 4.6 the radii determined in this fashion. The peaks seen in the



(a)



(b)

Figure 4.5. The X-ray cluster temperature (T_x , emission-weighted temperature) function at six different redshifts $z = (0, 0.5, 1, 2, 3, 5)$. Arrows indicate the luminosity-weighted average temperature \bar{T}_x at each epoch. In the first ($z = 0$) panel in (b) the cross-shaded area is the observed temperature function from Henry & Arnaud (1991) $[(1.8^{+0.8}_{-0.5} \times 10^{-3} h^3 \text{ Mpc}^{-3} \text{ keV}^{-1})(kT)^{-4.7 \pm 0.5}]$.

panels of this figure are, of course, artificially induced by our cell size of $0.31h^{-1}$ Mpc, but the distribution to larger radii should be reasonably accurate. Arrows indicate the luminosity-weighted average values. Since brighter clusters tend to be resolved, these numbers should be reliable. We see a weak trend of increasing size with increasing time which is in the theoretically anticipated direction. Longer wavelengths became nonlinear later producing larger clusters, and smaller clusters merge to produce larger clusters with increasing time.

Now in Figures 4.7 and 4.8, we show the scatter plots of (T_X, r_x) vs L_{tot} (integrated over frequency). We see that there is a clear correlation between L and T_x . But we do not see any strong correlation between L and r_x . The best fit lines (dashed) indicate that a slope of (0.42, 0.34) for core and total cluster temperature. KCOR found for these slopes (0.39, 0.37) respectively. The observed correlation between \bar{T}_x and total cluster luminosity is

$$\log_{10} \bar{T}_x (\text{keV}) = \log_{10}(4.2^{+1.0}_{-0.8}) + (0.265 \pm 0.035) \log_{10}(h^2 L_{44}) \quad (4.4)$$

according to Henry & Arnaud (1991).

Finally, we address temperature variations within clusters. Given our limited resolution there is little that can be accurately determined on this issue from our simulations, but we are able to compare the central cell (Volume = $3.1 \times 10^{-2} h^{-1}$ Mpc³) with the surrounding cells ($3^3 - 1^3$) (volume of size $5.9 \times 10^{-1} h^{-3}$ Mpc³) and the cells surrounding these cells ($5^3 - 3^3$, vol = $3.0 h^{-3}$ Mpc³). We define the ratio of the inner cell to the next cube as T_c/T_{shell} (volume-weighted average) and show the scatter diagram in Figure 4.9. No trend is seen with luminosity and the median value, indicated by the dashed line is 1.5. The cluster gas deviates significantly from isothermality with a 5% – 10% temperature decline typically found by a radius of $0.4 - 0.5 h^{-1}$ Mpc but a sharp fall off indicated by $1 h^{-1}$ Mpc. In Figure 4.10 we compare the (luminosity-weighted) temperatures found in the three regions noted above, normalized to the temperature in the central cell. The large dispersion is indicated by the error bar.

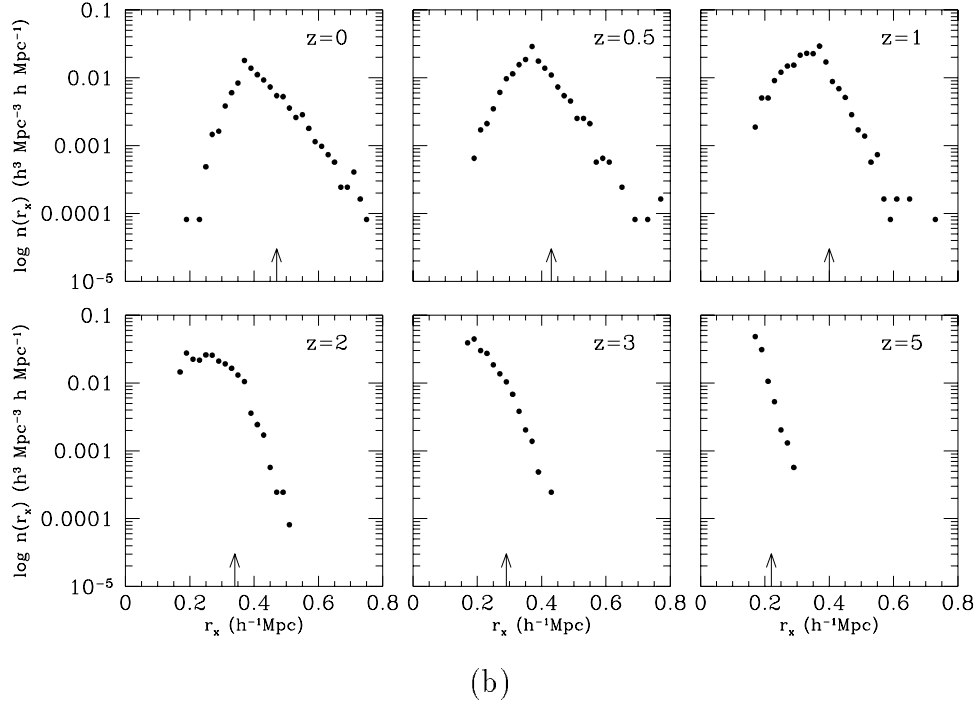
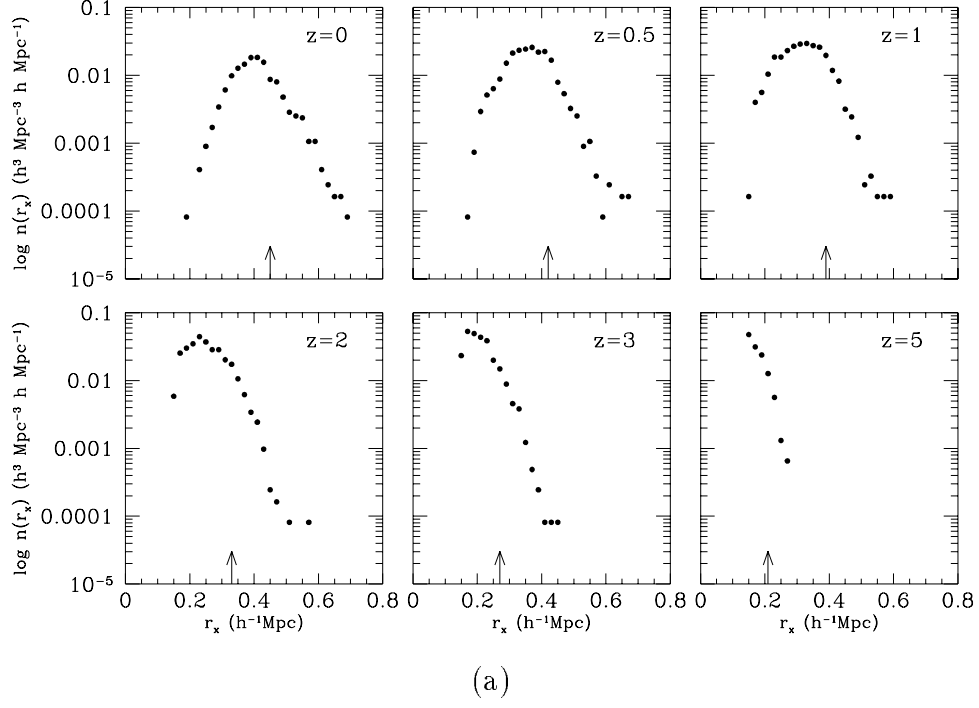


Figure 4.6. The X-ray cluster effective radius (r_x) distribution (c.f. equation 4.3). Arrows indicate the luminosity-weighted effective radius at each epoch.

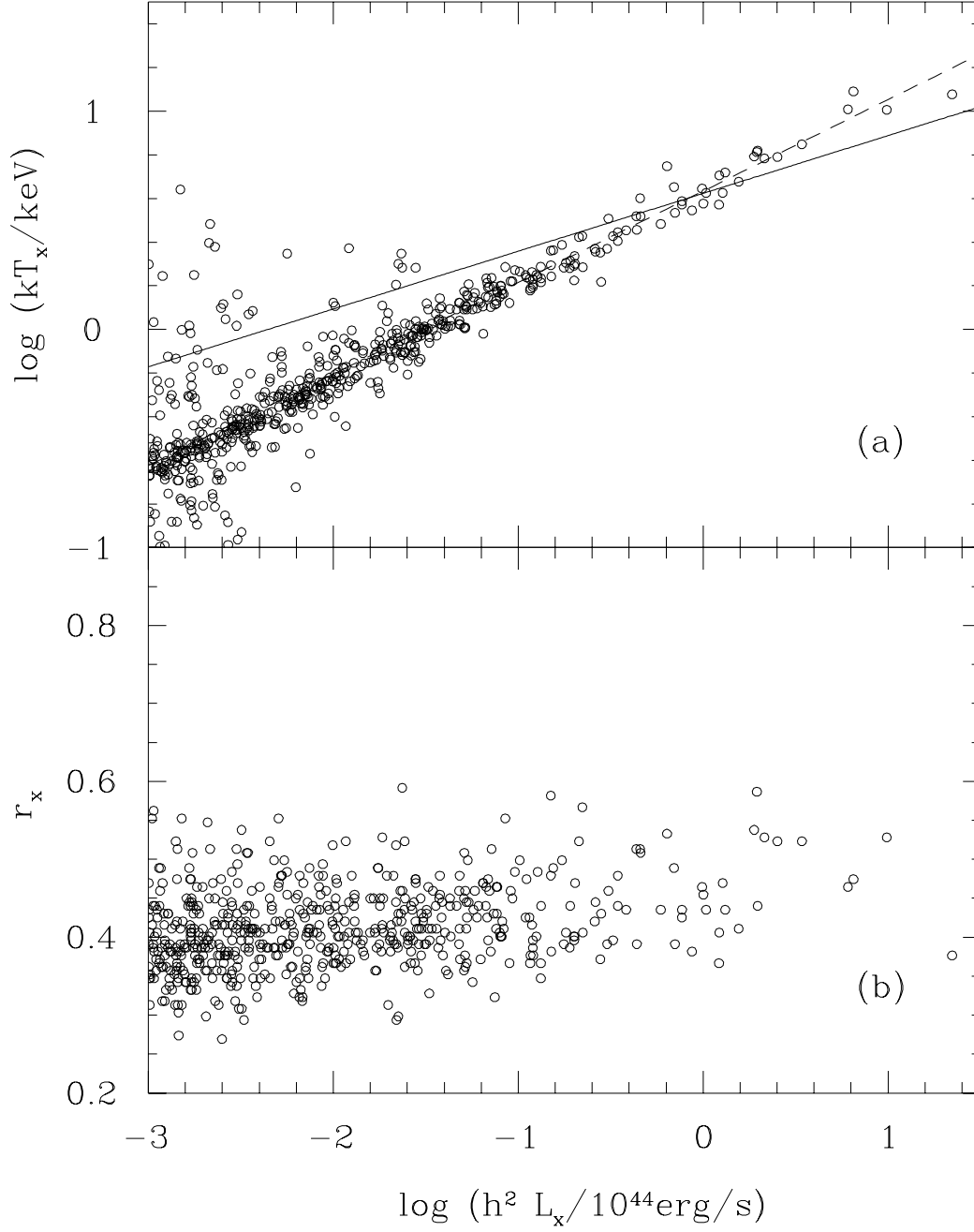


Figure 4.7. Top panels: Scatter plot of T_x vs L_{tot} at $z = 0$ for entire clusters. The dashed line is the best fit to the simulation results. The solid lines indicates the observations of Henry & Arnaud (1991). Bottom panels: Scatter plot of r_x vs L_{tot} at $z = 0$.

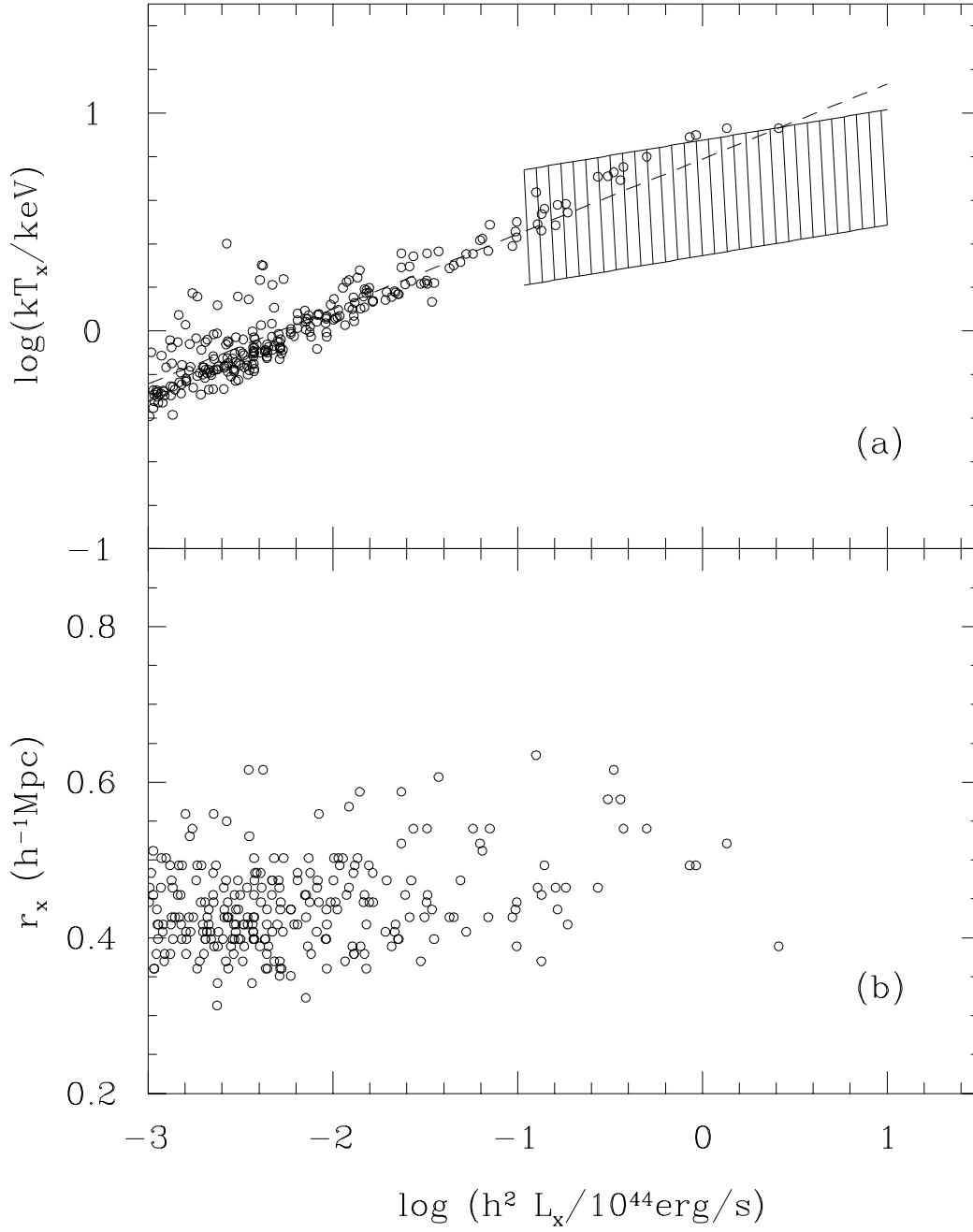


Figure 4.8. Same as the previous figure, but for cluster cores only. The hatched area indicates the observations of Henry & Arnaud (1991).

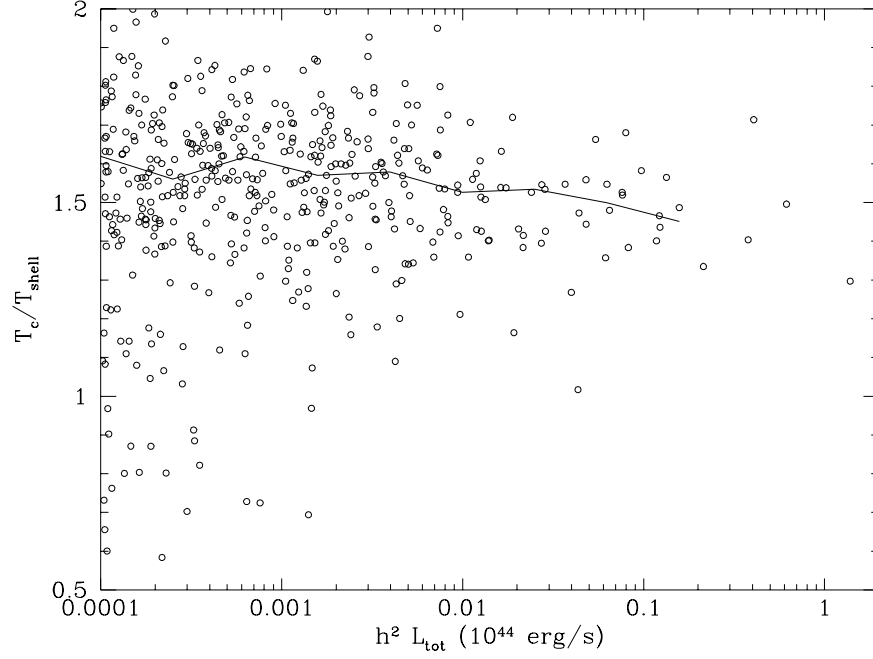


Figure 4.9. The ratio of the central cell temperature to the temperature of its surrounding shell (\sim one cell thick) as a function of L_{tot} .

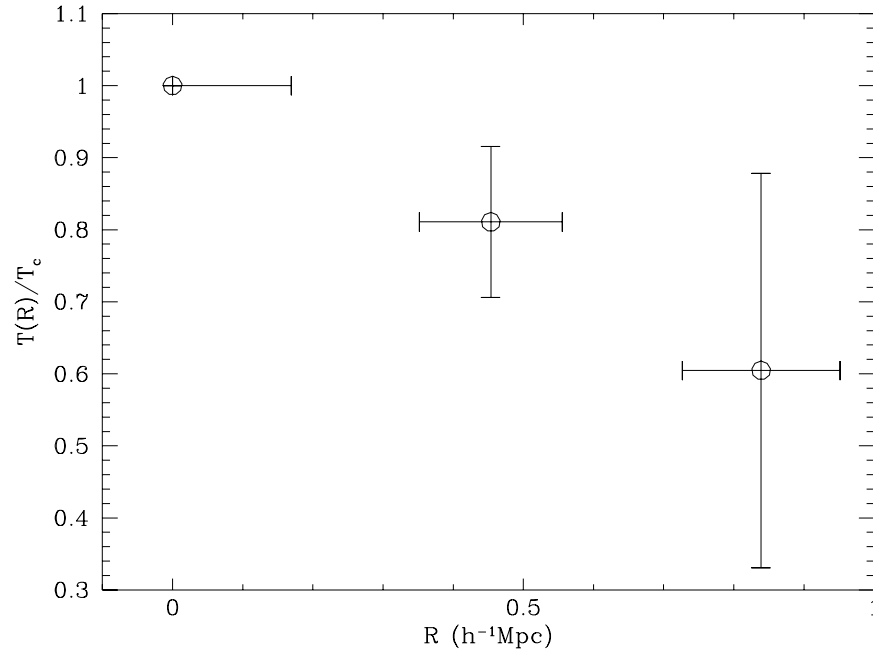


Figure 4.10. Comparison of the (luminosity-weighted) temperatures found in the three regions (central cell, the shell surrounding the central and the next outer shell) and normalized to the temperature in the central cell. Note the errorbars are 1σ .

4.4 Conclusion

In Figures 4.1–4.4, we showed the evolution of the cluster luminosity function expected in the CDM scenario. In the easily observed range of parameters ($0 \leq z \leq 1$, 10^{40} erg/s $\leq L_x \leq 10^{44}$ erg/s) little evolution is seen (for comoving observers) in any of the computed bands aside from a decline in the number of brightest sources (somewhat uncertain due to our limited box size) and a modest increase (by about a factor of two) in the luminosity function for fainter objects. The likely explanation for this has been mentioned: it is largely coincidental and due to the balancing of two effects: new breaking waves increase the luminosity density but mergers decrease it. It just happens that for this spectrum at this epoch the net rate of change is small. In other scenarios we expect the results to be different, but only detailed calculations can prove this.

However, Figures 4.5 and 4.6 did show substantial rates of change in other quantities, the temperatures and clusters radii. These important trends are summarized in Figures 4.11 and 4.12 where we see a factor of 2-3 decline in both these quantities by redshift 1 and a 37% decline in the (luminosity-weighted) mean temperature even in the small redshift range $z = 0 \rightarrow 0.5$. This trend should be detectable even with a relatively “soft” X-ray instrument such as ROSAT. It provides a test of $\Omega = 1$ models since in open, $\Omega < 1$ models the structure is expected to freeze out at early epochs ($z \sim 1/\Omega$) with cluster temperatures not changing substantially after that time. In Figures 4.11 and 4.12 we also show, as solid lines, the best fit power law dependences $R_x \propto (1+z)^{-2}$ and $T_x \propto (1+z)^{-1}$ anticipated by Kaiser (1986). We see that the temperature trend is as expected but the variation in radius is less steep than anticipated by the simple theoretical modelling, although of course our accuracy for R_x is affected by our limited resolution.

The primary conclusion of KCOR was that this model for growth of structure (standard CDM as normalized to COBE) produces too much structure at intermediate scales. Specifically there are too many bright X-ray clusters produced (c.f. Figure 4.4b) and too much integrated background X-ray intensity. Those results are strengthened by the

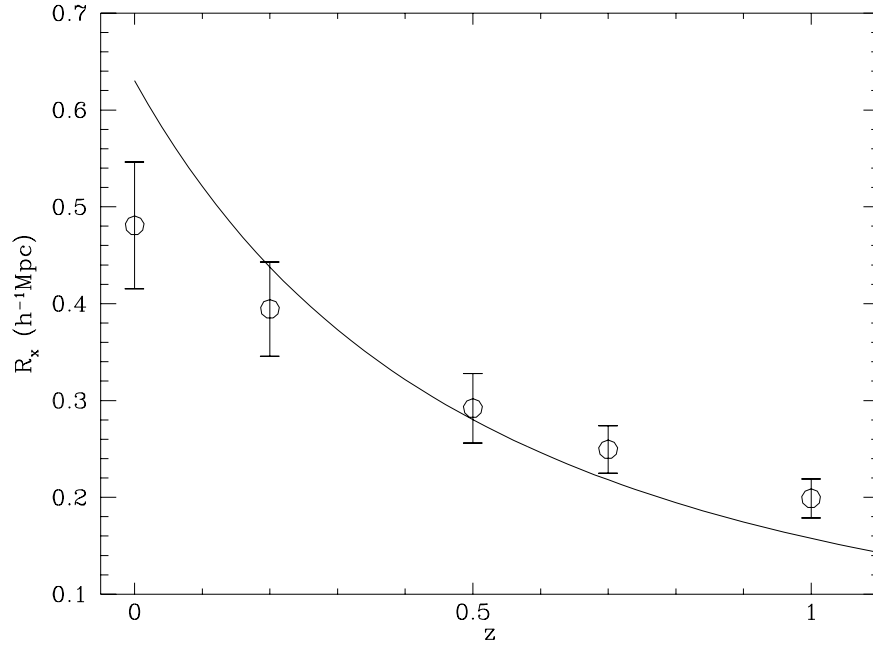


Figure 4.11. Average cluster core radii in physical units as a function of redshift for clusters with luminosity in the 0.5 – 4.5 keV band greater than 10^{43} erg/s.

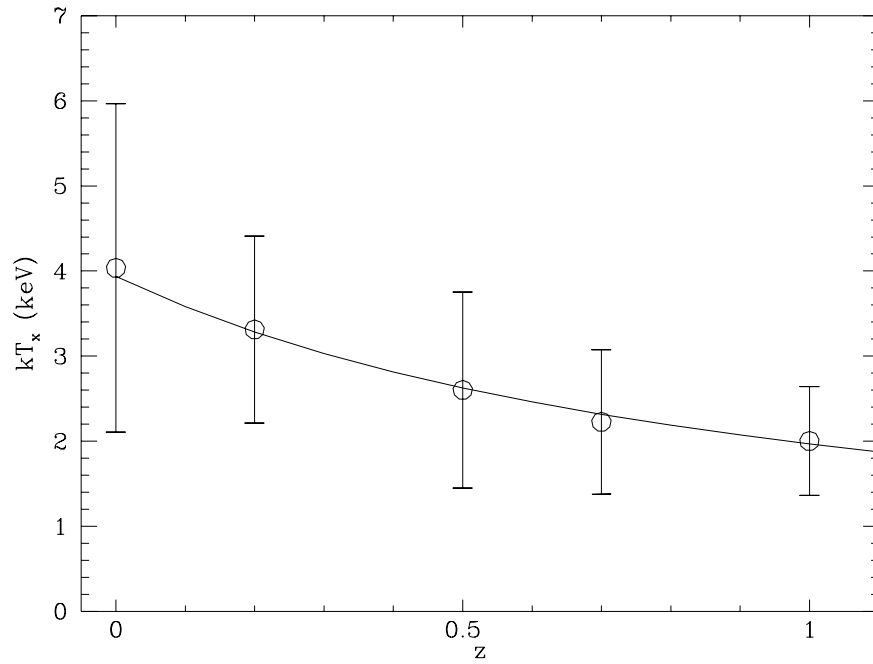


Figure 4.12. Average cluster temperature as a function of redshift for clusters with luminosity in the 0.5 – 4.5 keV band greater than 10^{43} erg/s.

current paper which confirms all the trends seen in the earlier paper but finds still more high luminosity clusters, further increasing the discrepancy with observations.

At fixed luminosity the predicted number density is an order of magnitude too high and at a fixed number density the luminosity is perhaps a factor of three too large. Thus, to fit observations we would need to reduce the density Ω_b by more than 40% which would put it more than one sigma below the Walker et al. (1991) value. But, even if we were to fit the observed luminosity function by this contrivance, the model would still fail due to the fact that the predicted temperatures are too high (c.f. Figures 4.5b and ??b). Improvement of our numerical techniques to obtain higher spatial resolution would lead to a further increase in these discrepancies. Frenk et al. (1990) combined hydrodynamical modelling of individual clusters with large scale dark matter $P^3 M$ simulations. They found that CDM with an amplitude of $\sigma_8 = 0.4 - 0.5$ would produce a satisfactory fit to observations but that unbiased models (such as that adopted here to match the COBE normalization) would produce too many high luminosity, high temperature clusters. The direct methods adopted in KCOR and the present paper confirm and strengthen these earlier results.

The methods used here, if combined with adaptive mesh refinement, should enable one to compare details of cluster structure with developing X-ray observations. Comparing results from simulations based on other cosmological scenarios for the growth of structure should help us decide which, if any, of our current models is correct.

Table 4.1. Parameters of Schechter fits for the X-ray cluster luminosity function integrated over the entire frequency range.

z	α	L_x^*	$k\bar{T}$ (keV)	n_0	$n(L > 10^{43})$	$n(L > 10^{44})$	j_{cl}	j_{gas}
X-ray Cluster Core Luminosity ($< 0.5h^{-1}$ Mpc)								
0	1.44	5.82	7.63	3.88	17.1	3.32	0.36	0.87
0.2	1.35	1.16	4.09	18.6	25.0	2.02	0.30	0.76
0.5	1.51	4.80	4.44	4.61	21.8	3.48	0.40	0.95
0.7	1.39	0.94	3.09	26.0	31.7	1.86	0.36	0.85
1	1.38	0.84	2.49	32.1	35.2	1.81	0.39	0.84
2	1.44	0.59	1.02	33.3	28.9	0.75	0.31	0.63
3	1.32	0.17	0.89	81.7	16.4	8.0×10^{-3}	0.18	0.36
5	1.57	0.20	0.47	5.62	1.46	1.3×10^{-3}	0.02	0.04
X-ray Cluster Total Luminosity ($< 1h^{-1}$ Mpc)								
0	1.40	11.2	5.80	4.50	25.2	6.32	0.74	0.87
0.2	1.31	2.39	3.51	19.8	39.2	6.19	0.62	0.76
0.5	1.45	9.20	3.62	5.48	32.3	7.07	0.81	0.95
0.7	1.34	1.86	2.53	27.8	50.1	6.33	0.71	0.85
1	1.29	1.01	2.04	52.0	58.5	4.47	0.67	0.84
2	1.31	0.56	1.35	64.2	47.1	1.40	0.47	0.63
3	1.18	0.18	0.86	138.6	30.0	0.026	0.29	0.36
5	1.50	0.20	0.48	8.07	2.07	1.7×10^{-3}	0.03	0.04

Note. — Here L_x^* and L are in units of 10^{44} erg/s; n_0 , $n(L > 10^{43})$ and $n(L > 10^{44})$ are in units of $10^{-6}h^3 \text{ Mpc}^{-3}$; j_{cl} and j_{gas} are in units of $10^{40} \text{ erg/s/h}^{-3} \text{ Mpc}^3$, and j_{cl} may be larger than j_{gas} due to the inaccuracy of the Schechter fit.

Table 4.2. Parameters of Schechter fits for the X-ray cluster luminosity function in the 0.3-3.5 keV Band

z	α	L_x^*	n_0	$n(L > 10^{43})$	$n(L > 10^{44})$	j_{cl}	j_{gas}
X-ray Cluster Core Luminosity ($< 0.5h^{-1}$ Mpc)							
0	1.33	0.63	13.0	10.7	0.38	0.11	0.33
0.2	1.20	0.27	45.3	15.7	8.0×10^{-2}	0.14	0.37
0.5	1.32	0.48	26.2	17.6	0.36	0.17	0.45
0.7	1.24	0.27	57.4	20.2	9.5×10^{-2}	0.19	0.45
1	1.22	0.23	76.6	22.4	5.8×10^{-2}	0.21	0.46
2	1.29	0.22	62.5	17.6	3.3×10^{-2}	0.18	0.35
3	1.31	0.089	78.3	5.20	1.5×10^{-5}	0.091	0.19
5	1.65	0.19	2.92	0.71	3.3×10^{-4}	0.014	0.014
X-ray Cluster Total Luminosity ($< 1h^{-1}$ Mpc)							
0	1.27	1.26	15.8	20.0	2.02	0.25	0.33
0.2	1.14	0.44	55.3	29.2	0.70	0.27	0.37
0.5	1.26	0.98	29.1	30.9	2.39	0.35	0.45
0.7	1.21	0.62	51.3	37.4	1.60	0.37	0.45
1	1.17	0.42	80.9	42.0	0.85	0.38	0.46
2	1.26	0.41	56.7	30.5	0.50	0.29	0.35
3	1.20	0.17	70.1	14.1	8.6×10^{-3}	0.14	0.19
5	1.44	1.43	1.24	2.22	0.19	0.028	0.014

Table 4.3. Parameters of Schechter fits for the X-ray cluster luminosity function in the 0.5-4.5 keV Band

z	α	L_x^*	n_0	$n(L > 10^{43})$	$n(L > 10^{44})$	j_{cl}	j_{gas}
X-ray Cluster Core Luminosity ($< 0.5h^{-1}$ Mpc)							
0	1.30	0.62	13.5	10.7	0.39	0.11	0.34
0.2	1.15	0.21	52.7	13.7	2.7×10^{-2}	0.12	0.37
0.5	1.29	0.48	26.3	16.6	0.37	0.16	0.44
0.7	1.24	0.34	46.4	20.7	0.21	0.19	0.43
1	1.22	0.32	56.9	23.7	0.21	0.22	0.44
2	1.31	0.29	40.9	16.0	8.5×10^{-2}	0.16	0.30
3	1.31	0.10	60.1	5.03	5.2×10^{-5}	0.079	0.15
5	1.65	0.09	1.60	0.09	1.7×10^{-7}	0.004	0.009
X-ray Cluster Total Luminosity ($< 1h^{-1}$ Mpc)							
0	1.23	1.36	17.2	21.5	2.50	0.28	0.34
0.2	1.14	0.47	48.7	27.2	0.75	0.25	0.37
0.5	1.24	0.99	28.3	29.5	2.39	0.34	0.44
0.7	1.19	0.66	47.7	35.7	1.76	0.36	0.43
1	1.16	0.42	71.8	37.1	0.76	0.34	0.44
2	1.28	0.45	42.2	25.0	0.49	0.24	0.30
3	1.21	0.18	50.0	10.8	8.9×10^{-3}	0.11	0.15
5	1.43	5.95	0.47	2.05	0.41	0.044	0.009

Table 4.4. Parameters of Schechter fits for the X-ray cluster luminosity function in the 2-10 keV Band

z	α	L_x^*	n_0	$n(L > 10^{43})$	$n(L > 10^{44})$	j_{cl}	j_{gas}
X-ray Cluster Core Luminosity ($< 0.5h^{-1}$ Mpc)							
0	1.21	0.74	13.1	10.8	0.62	0.11	0.35
0.2	1.20	0.62	18.9	13.6	0.59	0.14	0.31
0.5	1.31	0.90	11.0	11.7	0.75	0.13	0.35
0.7	1.25	0.51	21.2	13.7	0.38	0.13	0.30
1	1.24	0.59	20.6	14.8	0.55	0.15	0.27
2	1.38	0.53	9.35	6.95	0.16	0.07	0.14
3	1.30	0.07	20.0	0.78	1.6×10^{-7}	0.018	0.038
5	1.33	0.40	0.51	0.28	3.8×10^{-3}	2.8×10^{-3}	1.4×10^{-3}
X-ray Cluster Total Luminosity ($< 1h^{-1}$ Mpc)							
0	1.22	2.46	9.49	16.1	3.00	0.28	0.35
0.2	1.18	1.18	18.8	20.2	2.21	0.25	0.31
0.5	1.24	1.36	15.4	19.6	2.23	0.25	0.35
0.7	1.23	1.12	19.1	21.3	2.02	0.26	0.30
1	1.21	0.91	24.4	23.2	1.78	0.26	0.27
2	1.31	0.69	12.5	10.9	0.47	0.11	0.14
3	1.26	0.15	16.0	2.68	7.0×10^{-4}	0.030	0.038
5	1.62	0.20	0.18	0.05	3.0×10^{-5}	8.2×10^{-4}	1.4×10^{-3}

Chapter 5

The Evolution of X-ray Clusters in a Cold plus Hot Dark Matter Universe

5.1 Introduction

X-ray observations of clusters of galaxies provide an important cosmological probe which can, for example, be used to estimate the amplitude and shape of the fluctuation spectrum (Henry & Arnaud 1991), the mean density of the universe (Richstone et al. 1992) and the fraction of mass in baryons (White 1992 and White et al. 1993). X-ray clusters have a reduced likelihood of confusion with the background and of chance projection effects from smaller clusters, an occurrence which can plague optical studies (Frenk et al. 1990; Dekel et al. 1989). It is also easier to self-consistently model the X-ray emitting gas which is thought to dominate over the mass in galaxies (White 1992) than to follow the evolution of the much smaller and denser galaxies.

The CHDM scenario has scored a number of successes in explaining observations: the galaxy correlation function, galaxy pairwise velocities, bulk velocities (Klypin et al. 1993 = KHPR), the number and virial properties of groups (Nolthenius et al. 1994), the cluster-cluster correlation function (Holtzman & Primack 1993; Klypin & Rhee 1994). Perhaps its severest challenge comes from the large number of damped Lyman- α systems observed at moderate to high redshifts (Lanzetta 1993, Lanzetta et al. 1995). Mo &

Miralda-Escudé (1994) and Kauffmann & Charlot (1994) have claimed that the model predicts too few high redshift damped Lyman- α systems ($z \approx 3$). The situation depends on the identification of the observational data at these redshifts: large galaxies (Briggs et al. 1989) or dwarfs (Hunstead, Pettini, & Fletcher 1990). Klypin et al. (1994) propose a variant of the CHDM model ($\Omega_{cold}/\Omega_{hot}/\Omega_{baryon} = 0.725/0.2/0.075$), which has similar properties on large scales and predicts more high redshift objects as compared with the standard CHDM (but see also Ma & Bertschinger 1994).

In this paper we test the standard CHDM model at cluster lengths for both the dark matter and baryonic components. Predictions of cluster parameters for the model have been made by a number of groups using a variety of methods. The correlation function was estimated by both analytical (Holtzman & Primack 1993) and numerical methods (Jing & Fang 1994; Jing et al. 1993; Klypin & Rhee 1994; Cen & Ostriker 1994). Predictions for X-ray emission were made by Bartlett & Silk (1993) using the Press-Schechter approximation and by Klypin & Rhee (1994) using N-body simulations and assuming the cluster gas temperature was proportional to the square of the cold component's velocity dispersion.

To our knowledge, this paper presents the first self-consistent hydrodynamic plus N-body treatment of X-ray clusters for the CHDM model. We stress the importance of such simulations. Clusters in the model (and probably in the real universe) form at relatively low redshifts, therefore one should expect that the results of recent violent creation, mergers, and accretion will be of importance.

5.2 Simulations

The numerical method used to simulate the gas has been described in detail elsewhere (Bryan et al. 1995), as has the general scheme for generating initial conditions (KHPR), so we restrict ourselves to a brief overview. The cold and hot components were followed with a standard particle-mesh (PM) simulation using a 256^3 grid with 128^3 cold particles and 2×128^3 hot particles in order to better sample the neutrino phase space. The gas

was represented with a 256^3 grid and evolved with the higher-order accurate piecewise-parabolic method. This is an Eulerian scheme that features third order advection with multi-dimensional shock capturing and has been modified and extensively tested for cosmological applications. We did not include any radiative effects as this will have little effect on the hot cluster gas which has a cooling timescale on order of the Hubble time.

The initial power spectrum and growth rate came from analytic fits given in KHPR (“note added in proof”), with the hot particles being set up in pairs. Each particle in a pair had the same initial position and perturbation-driven velocity but were given equal but opposite thermal velocities drawn from relativistic Fermi-Dirac statistics. We used a box size of $85 h^{-1}$ Mpc, with $\Omega_{hot} = 0.3$, $\Omega_{cold} = 0.6$ and $\Omega_{baryon} = 0.1$. We write the Hubble constant $H = 100h \text{ km s}^{-1} \text{ Mpc}^{-1}$ and use $h = 0.5$ throughout. A normalization which produces a $15.5 \mu\text{K}$ rms quadrupole of the microwave background anisotropy was chosen. This corresponds to a bias parameter of $b = 1.65$, very close to that given by COBE. We began the simulation at a redshift $z = 15$.

Clusters are identified through their X-ray signature: the thermal Bremsstrahlung emission is computed for each cell in the energy band of interest. We assume primordial abundances (76% H and 24% He by mass) with both hydrogen and helium fully ionized (Spitzer 1978). We neglect lines; however, tests with a full ionization equilibrium code (Raymond & Smith 1977) indicate that we are underestimating the luminosity by about 20–40%. The free-free Gaunt factor is approximated with numerical fits given by Kellogg, Baldwin & Koch (1975).

Cells are tagged as potential cluster centers provided they have a luminosity greater than $10^{38} \text{ erg s}^{-1}$ and are local maxima compared to all 26 neighbouring cells. We then attempt to estimate the cluster center by finding the center-of-mass within a $0.5h^{-1}$ Mpc sphere. This is done by dividing the sphere into a new grid of zones in spherical coordinates, equally spaced in both the azimuthal direction and the cosine of the polar angle, but logarithmically spaced in radius. The density in each cell is found by a linear interpolation from the nearest original grid points. After the center-of-mass is found, the procedure is repeated at the new position until convergence occurs. Once the list

is constructed, clusters whose centers are separated by less than a comoving distance of $2 h^{-1}$ Mpc are merged. Cluster characteristics such as mass and luminosity are then computed by a similar technique, integrating over a sphere with a comoving radius of $1 h^{-1}$ Mpc.

We have also tested a number of other schemes for identifying cluster centers and computing their properties, including the procedure described in Kang et al. (1994). We find that there is little sensitivity to methodology although the Kang et al. technique for computing the luminosity-weighted temperature appears to slightly overestimate cluster temperatures as compared to other schemes. We also note that the results are largely unchanged if we increase the cutoff radii, indicating that we are capturing the majority of the emission.

In order to improve our ability to compare with observations, we have computed a large PM CHDM realization with 768^3 zones and 256^3 particles in a box $255 h^{-1}$ Mpc on a side, giving us the same resolution as in the hydrodynamic simulation. Although we do not have thermodynamic information, we can fix the relation between the one-dimensional dark matter velocity dispersion and temperature from the smaller gas dynamical simulation. We adopt the relation $T(\text{keV}) = (v/v_*)^2$ where v is the cold particle one-dimensional velocity dispersion in km/s, computed in spheres of $1.5 h^{-1}$ Mpc and $v_* = 410$ km/s. The value of v_* seems to be slightly scale dependent, therefore we fix this normalization with the largest clusters in our $85 h^{-1}$ Mpc box. Because there are a limited number of such clusters, the uncertainty in the quoted v_* is relatively large. Similarly, one can obtain a 2-10 keV luminosity-velocity relation. We use the following fit to the data:

$$L = 5 \times 10^{44} \left(\frac{v}{1000 \text{ km/s}} \right)^7 \text{ erg/s.} \quad (5.1)$$

This is compatible with the adopted T - v relation combined with the observed luminosity temperature relation, $L \propto T^{3.5}$, and provides a good fit to the brighter ($L_{2-10} > 10^{42}$ erg/s) simulated clusters.

5.3 Results and Discussion

5.3.1 Luminosity and Temperature Distribution Functions

In Figure 5.1, we show the 2-10 keV luminosity-weighted temperature distribution function for gas in clusters at $z = 0$ and compare it to data from the volume-limited sample of Edge et al. (1990). The fit is quite good. There are almost no high temperature clusters ($T \sim 10$ keV), however these clusters correspond to rare events in the initial density field and we believe that their absence is simply due to the limited volume of our simulated box (which is much smaller than the observational survey). Also shown are the results from the larger PM simulation with the normalization described above. Within uncertainties, they agree well with observations over a wide range of length scales. The cluster temperature, which we find to be nearly constant over the entire cluster, is our most reliable result, as the numerical scheme conserves energy and is adept at correctly modeling strong shocks.

The 2-10 keV luminosity function at the present epoch is plotted in Figure 5.2a, along with data from Edge et al. (1990). Again, our box is too small to contain the large, rare clusters; however, in the region of overlap, the fit is reasonably good.

In order to investigate the evolution of the clusters, we compute the luminosity function in the 0.3-3.5 keV range (observer's frame) at $z = 0.2$ (Figure 5.2b) and compare it to the *Einstein* Extended Medium Sensitivity Survey (Henry et al. 1992 and Henry 1992). The authors present evidence for the evolution of the luminosity function in three redshift shells; unfortunately, the strongest changes occur for the brightest clusters, which are outside of our luminosity range.

In Figure 5.2c we plot the luminosity function in the ROSAT bandpass (0.5–2.5 keV) at a redshift of $z = 0.5$. Also plotted is the $z = 0.41$ luminosity function from Bower et al. (1994). We also note that pointed observations of likely cluster candidates (Nichol et al. 1994 and Castander et al. 1993) have produced a lower limit for the number density of X-ray clusters of $1.2 \times 10^{-7} \text{ Mpc}^{-3}$ for clusters with a luminosity around 10^{44} erg/s . Our luminosity function for the same epoch is consistent with this number which represents a

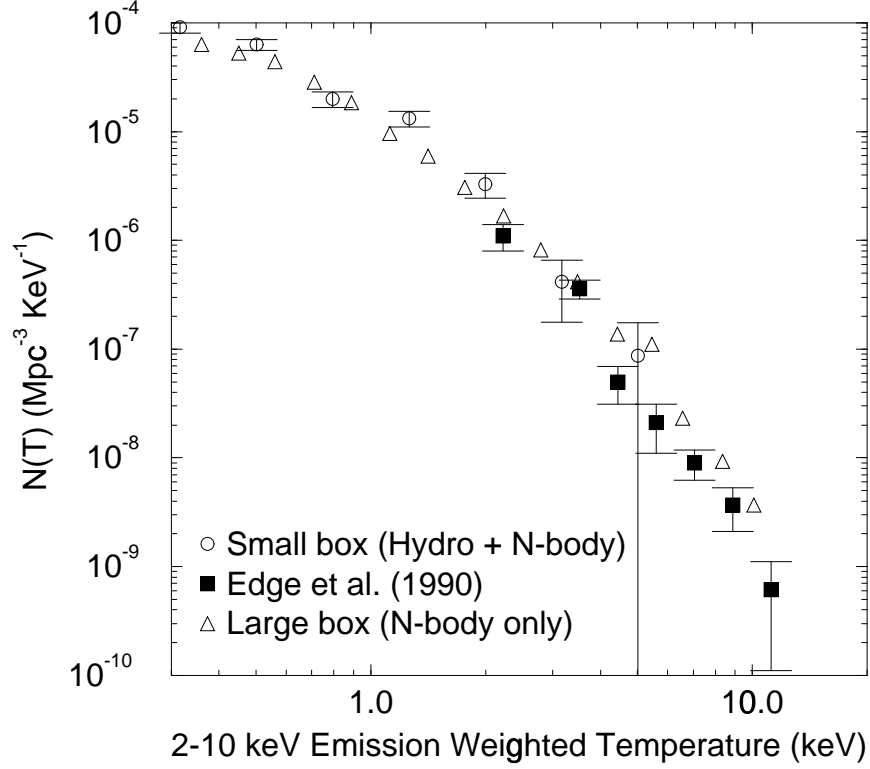


Figure 5.1. The 2–10 keV luminosity-weighted temperature distribution function at $z = 0$ with $\Omega_{\text{baryon}} = 0.1$ and $h = 0.5$. The open circles are from the $85 h^{-1}$ Mpc box computed with our full hydrodynamics plus N-body code. The triangles are from a particle-mesh simulation with a $255 h^{-1}$ Mpc box normalized to the results from the smaller box (see text). The open squares are points from the volume-limited sample of the Edge et al. (1990) data.

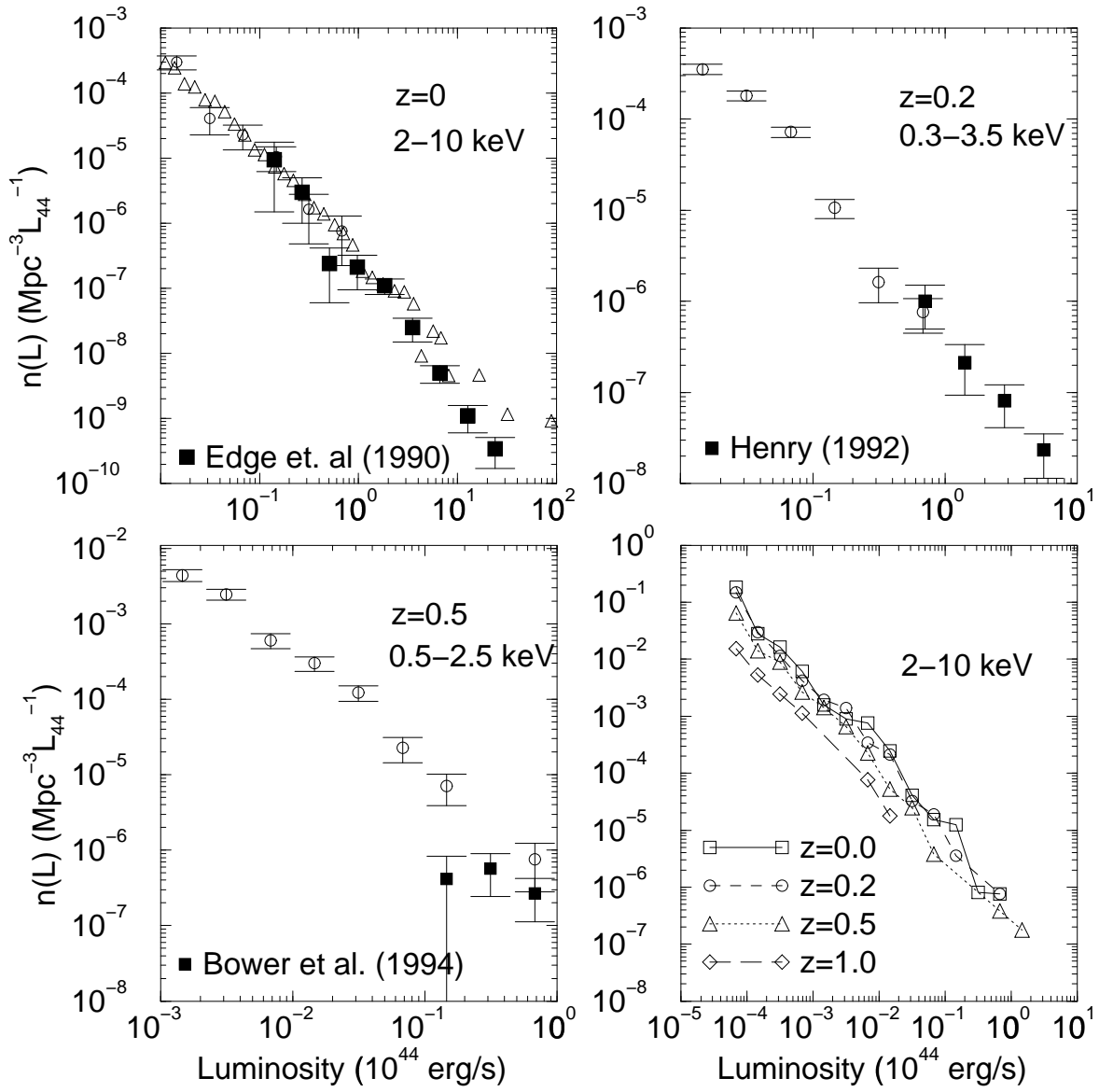


Figure 5.2. Luminosity functions at a variety of redshifts with $\Omega_{\text{baryon}} = 0.1$ and $h = 0.5$. In (a-c) open symbols are as in Figure 5.1, while filled squares are observational data. We show luminosity functions in the (cluster rest frame's) energy range (a), 2–10 keV ($z = 0$), (b) 0.3–3.5 keV ($z = 0.2$), (c) 0.5–2.5 keV ($z = 0.5$). In (d) we show the predicted evolution of the 2–10 keV luminosity function with redshift.

substantial evolutionary effect. This is reinforced by Figure 5.2d which shows the strong negative evolution with increasing redshift predicted in CHDM. This provides a strong check on the model: COBE normalized CDM, for example, predicts weak evolution in the opposite sense (Bryan et al. 1994a; Kang et al. 1994). The cluster luminosity is not as well constrained as the temperature and it is possible that we have substantially underestimated the cluster luminosity (see below).

The relation between a cluster's temperature and its luminosity should be less sensitive to the power spectrum and normalization. We show this relation in Figure 5.3 along with observational points from David, et al. (1993). The slopes match quite closely; however, due to the uncertainties in our cluster luminosities, it is not clear how well the simulated slope is determined. In order for the curves to align, it must be assumed that we are underestimating the luminosities by a factor of two, but this is well within our systematic uncertainties for computed cluster luminosities.

5.3.2 Discussion of Errors

With a cell size of $330 h^{-1}$ kpc, we obviously cannot fully resolve a cluster. In order to gauge the extent of the error committed, we have performed some tests using smaller physical boxes with higher resolution and find that cluster temperatures are very well constrained, but central cluster densities increase as the resolution increases. Since free-free emission is proportional to the square of the density, this means that formally, we can only calculate a lower bound to a cluster's true luminosity. We are also performing a more complete resolution study (Anninos & Norman 1994) which seems to imply that without other physical processes (such as star formation), we do not produce resolvable cores (at least to a resolution level of $50 - 100 h^{-1}$ kpc).

Real clusters, however, do have identifiable cores, therefore we must ask how our results compare to clusters as seen by X-ray telescopes. These seem to follow a profile of the form (Jones & Forman 1984)

$$\rho = \rho_0 [1 + (r^2/R_c^2)]^{-3\beta/2}, \quad (5.2)$$

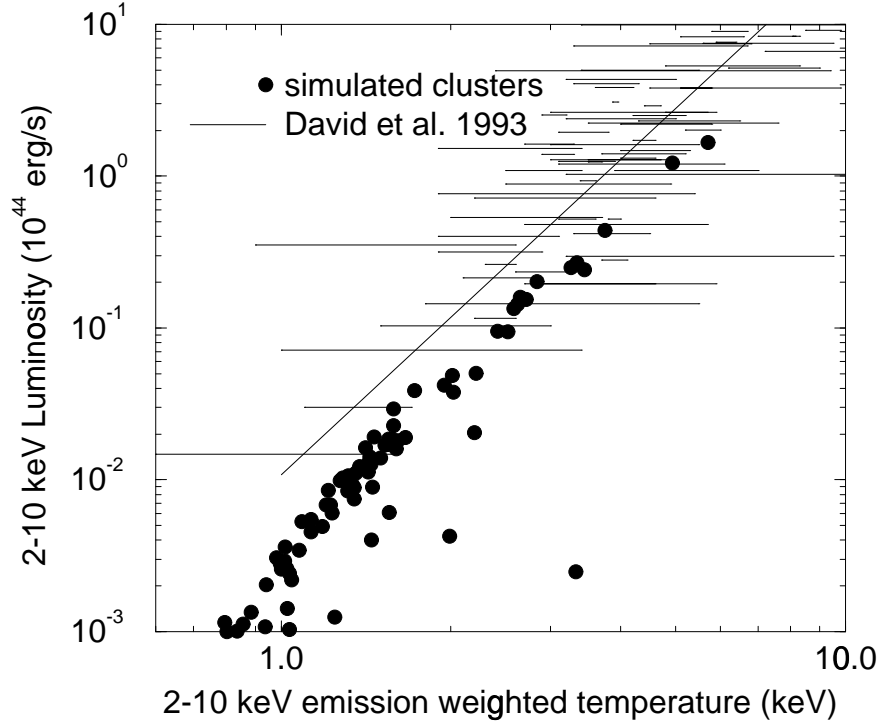


Figure 5.3. The luminosity-temperature relation at $z = 0$. The filled circles are simulated clusters while the temperature of clusters from the David et al. (1993) sample are plotted to show the uncertainty in the observed L-T relation. The solid line is the best fit power law to the observed distribution.

with $\beta \sim 0.8$ and $R_c \sim 150 h^{-1}$ kpc. This assumes that the clusters are roughly isothermal, a conclusion in reasonable agreement with the simulation. In order to compare this typical observational cluster, we fit the same profile to our simulated clusters, obtaining values of $\beta \sim 1.4$ and $R_c \sim 0.7 h^{-1}$ Mpc. These parameters are quite different from most observed clusters, but how much does this affect the resulting luminosity? To compare, we must specify the remaining free parameter: ρ_0 . This is done by demanding that both clusters (simulated and observed) have the same mass within a $1 h^{-1}$ Mpc radius. Despite the extremely disparate core sizes, the real cluster's luminosity is only about three times higher.

Besides resolution, the absence of a number of physical effects could change the calculated luminosity. These include: line emission from metals, although the omission of this effect is probably limited to an increase of the luminosity by 20–40%; radiative cooling, which would enhance the flux in denser, cooler regions; and galaxy formation, which would decrease the available baryons and hence the luminosity of the cluster.

5.4 Conclusions

By performing hydrodynamic plus N-body simulations of the CHDM model, we have removed a layer of assumptions between theory and observations. The simulation directly provides the thermodynamic state of the hot gas in clusters, allowing us to test the model against easily understood observations. We find that the CHDM model is consistent with X-ray observations of cluster-sized perturbations in the available redshift range under a few well-motivated assumptions.

These results, however, are quite sensitive to our choice of Ω_{baryon} since the luminosity depends on the square of the baryon density. For our choice of $h = 0.5$, light element nucleosynthesis predicts $\Omega_{baryon} = 0.05$ (Walker et al. 1990). If this figure were adopted it would imply a global decrease in the computed luminosity by about a factor of four. These large factors may in fact be compatible with the model due to the possibility that we are substantially underestimating cluster luminosities (because of limited resolution). We are

not, on the other hand, overestimating luminosities, therefore a higher $\Omega_{baryon}(> 0.1)$, as might be indicated by cluster virial estimates (White 1992) is incompatible with the model as it would push the predicted luminosity function above observations.

As a caution, we observe that it is not yet possible to have the large dynamic range required to both accurately compute the internal physics of an individual cluster and to simulate a sufficient region to include the brightest clusters, although the results presented here show that we have made significant progress towards this goal. Simulations with higher resolution and larger boxes are in progress (Bryan & Norman 1996).

Finally, we note that it would be helpful to have an observational luminosity (and temperature) function that extended to lower luminosities, to circumvent the difficulties of simulating large volumes of space. Thus we stress the need for X-ray observations of poor clusters and groups.

Chapter 6

Statistical Properties of X-ray Clusters: Analytic and Numerical Comparisons

6.1 Introduction

The statistics of X-ray clusters can serve as an excellent probe of cosmology. The luminosity function of clusters is defined in a straightforward manner both observationally (Henry 1992; Ebeling et al. 1995; Burns et al. 1996) and numerically (Cen & Ostriker 1992; Bryan et al. 1994b) although as we shall see this is a computationally difficult task. The temperature function is similarly obtainable (Henry & Arnaud 1991; Davis & Mushotzky 1993) although here it is the observational data which is more challenging to obtain.

One uncertainty in performing this comparison is the possibility of systematic errors in the theoretically derived cluster temperatures and luminosities. This has been investigated in a number of ways, primarily by testing the individual methods developed against analytic results (which are necessarily very simplified problems). So, the Lagrangian Smoothed Particle Hydrodynamics (SPH) method combined with a P³M code

for computing the gravitational interaction was examined by Evrard (1988) and Couchman, Thomas & Pearce (1995); while SPH with a gravitational tree code was tested in a number of papers (Hernquist & Katz 1989; Katz, Weinberg & Hernquist 1996; Navarro & White 1993). A novel modification of SPH was described by Shapiro et al. (1996), along with a number of comparisons against known results. For Eulerian codes, method papers with some tests include: Cen (1992) for a first-order grid based code; Ryu et al. (1993) for a total variation diminishing method; Anninos, Norman & Clarke (1994) for a two-level nested grid scheme, and Bryan et al. (1995) for a code based on the piecewise parabolic method.

However, a number of recent papers have taken up the question of accuracy and consistency as their primary focus. For Eulerian codes (with fixed comoving spatial resolution), this issue has been addressed by Anninos & Norman (1996) (hereafter AN96) who performed simulations with a two level hierarchical method and simulated the formation of a moderately rich cluster with five different resolutions ranging from 1600 to 100 kpc per cell. They found that although the temperature, mass and velocity dispersion of a cluster were reasonably well determined with the lower-resolution simulations, the total luminosity had not converged even for the highest resolution run. The bolometric luminosity (for this single cluster) behaved as

$$L_{tot} \propto \frac{1}{\Delta r^\alpha} \quad (6.1)$$

where Δr is the spatial resolution of the simulation and $\alpha = 1.17$.

Another way to check the results of simulations is to compare them against the predictions of approximate analytic models. Although agreement does not guarantee correctness (as both methods are only approximations to the full solution), concordance would increase our confidence in both methods. Also, simple analytic arguments may only identify a scaling property between quantities without specifying a normalization, which can however, be fixed by numerical simulation (or by further assumptions). This describes the scaling laws that come from considering clusters as spherical clouds of gas in hydrostatic equilibrium. Navarro, Frenk & White (1994) (hereafter NFW) recently

compared the results of six clusters simulated with SPH in a Cold Dark Matter (CDM) cosmogony against these scaling relations (at $z = 0$). They find good agreement over a wide range of luminosity, mass and temperature, but claim that clusters from Eulerian simulations (such as in Kang et al. 1994a and Bryan et al. 1994a) do not.

Another analytic method is that initially described by Press & Schechter (1974), which predicts the mass distribution of collapsed objects. There have been a number of comparisons between its predictions and the results of N-body simulations (Efstathiou et al. 1988; Bond et al. 1991; Lacey & Cole 1996). Using the scaling results, this theory can be extended to produce the temperature (Eke, Cole & Frenk 1996) and luminosity distribution functions.

In this chapter, we make a detailed comparison between simulation results and the adiabatic scaling laws as well as the Press-Schechter formalism with extensions. This allows us to gauge the accuracy and consistency of our results, leading to firmer conclusions regarding the viability of the cosmology modelled. The paper is laid out as follows. In section 6.2, we review the scaling relations, including a modification to take into account the finite resolution of Eulerian codes. We then compare these to the results of CDM and Cold plus Hot Dark Matter (CHDM) simulations at a variety of redshifts. In section 6.3, we examine the mass, temperature and luminosity distribution functions, including the effects of finite band-pass and line emission. These are compared against the Press-Schechter plus scaling theory (extended to include the additional complications in the luminosity function). In section 6.4 we examine the profiles of temperature and velocity dispersion and assess the accuracy of the isothermal models assumed in extending the Press-Schechter work. Finally, in section 6.5, we discuss our results and comment on the viability of the models simulated.

6.2 Scaling Relations

Here we develop the scaling relations through the assumption of a pressure supported isothermal sphere for both the gas temperature T and one-dimensional collisionless veloc-

ity dispersion σ of the dark matter particles. The assumption of a specific density profile (here the isothermal sphere) is not strictly required to obtain the scaling behaviour, but is needed to determine the constant of proportionality between the given quantities.

These relations were used by Kaiser (1986) to describe the evolution of ‘characteristic’ quantities, largely driven by the non-linear mass (M_{nl}), defined via equation (6.17) below, as well as to derive relations between distribution functions at different epochs. We do not explicitly test these because they are uniquely specified by the non-linear mass (which we do examine) and the scaling relations discussed below; further, it is difficult to observationally or computationally define something like the ‘characteristic’ temperature.

6.2.1 Scaling review and normalization

In the isothermal distribution function, the density is related to the velocity dispersion (Binney & Tremaine 1987):

$$\rho(r) = \frac{\sigma^2}{2\pi Gr}. \quad (6.2)$$

If we define the virial radius as the radius of a spherical volume within which the mean density is Δ_c times the critical density at that redshift ($M_{vir} = 4\pi r_{vir}^3 \rho_{crit} \Delta_c / 3$), then there is a relation between the virial mass and the velocity dispersion:

$$\begin{aligned} M_{vir} &= \sigma^3 \left(\frac{16}{\Delta_c G^2 H^2(z)} \right)^{1/2} \\ &= \frac{1.4 \times 10^6 M_\odot}{(1+z)^{3/2}} \left(\frac{1}{f_\sigma} \frac{\sigma}{\text{km/s}} \right)^3. \end{aligned} \quad (6.3)$$

The critical density is given by $\rho_{crit} = 3H(z)^2/8\pi G$ where $H(z)$ is the redshift-dependent Hubble constant. It can be written as $H(z) = H_0 E(z)$ with the function $E^2(z) = \Omega_0(1+z)^3 + \Omega_R(1+z)^2 + \Omega_\Lambda$ dependent on the three contributions:

$$\Omega_0 = \frac{8\pi G \rho_0}{3H_0^2} \quad \Omega_R = \frac{1}{(H_0 R)^2} \quad \Omega_\Lambda = \frac{\Lambda}{3H_0^2}. \quad (6.4)$$

Here, ρ_0 is the non-relativistic matter density, R is the radius of curvature and Λ is the cosmological constant.

The second line of equation (6.3) assumes a flat universe with $\Omega_0 = 1$, $H_0 = 50$ km/s/Mpc and $\Delta_c = 178$. This last value comes from the solution to the collapse of a spherical top-hot perturbation (Peebles 1980; Lacey & Cole 1993). We have also introduced a factor f_σ which will be used to match the normalization from the simulations.

If the distribution of the baryonic gas is also isothermal we can define a ratio of the ‘temperature’ of the collisionless material ($T_\sigma = \mu m_p \sigma^2 / k$) to the gas temperature:

$$\beta = \frac{\mu m_p \sigma^2}{kT}. \quad (6.5)$$

We take $\mu = 0.59$. Given equations (6.3) and (6.5), the relation between temperature and mass is:

$$\begin{aligned} kT &= \frac{GM_{vir}^{2/3} \mu m_p}{2\beta} \left(\frac{H^2(z) \Delta_c}{2G} \right)^{1/3} \\ &= \frac{5.02 \text{ keV}}{f_T} \left(\frac{M_{vir}}{10^{15} M_\odot} \right)^{2/3} (1+z). \end{aligned} \quad (6.6)$$

Here, the second line assumes $\beta = 1$. Since these relations will be examined separately, we insert a normalization factor f_T (although f_T and β function in the same way in equation (6.6), they do not necessarily have the same value).

We can easily find the scaling behaviour of a cluster’s X-ray luminosity by assuming bolometric Bremsstrahlung emission and ignoring the temperature dependence of the Gaunt factor (see, for example, Spitzer 1978),

$$L_{bol} \propto M \rho T^{1/2} \propto M^{4/3} (1+z)^{7/2} \quad (6.7)$$

where we have used the redshift dependence of the critical density $\rho \propto (1+z)^3$ and equation (6.6). We could compute the luminosity by using the isothermal sphere approximation, however this is either infinite, if there is no rollover in density as $r \rightarrow 0$, or we must arbitrarily select a core radius. Instead, we will assume the normalization found by NFW:

$$L_{bol} = 1.1 \times 10^{45} \left(\frac{M_{vir}}{10^{15} M_\odot} \right)^{4/3} \left(\frac{\Omega_b}{0.1} \right)^2 (1+z)^{7/2} \text{ erg/s} \quad (6.8)$$

This has been adjusted slightly to match our definition of M_{vir} and to account for the effects of changing the baryonic mass density (Ω_b).

Other scaling laws can easily be derived from these; we write down two others for completeness:

$$L_{bol} = 1.1 \times 10^{45} \left(\frac{kT/\beta}{5.0 \text{ keV}} \right)^2 \left(\frac{\Omega_b}{0.1} \right)^2 (1+z)^{3/2} \text{ erg/s} \quad (6.9)$$

$$L_{bol} = 1.1 \times 10^{45} \left(\frac{\sigma}{895 \text{ km/s}} \right)^4 \left(\frac{\Omega_b}{0.1} \right)^2 (1+z)^{3/2} \text{ erg/s} \quad (6.10)$$

6.2.2 Resolution effects

While we do not expect the first three bulk properties (mass, temperature and velocity dispersion) to be strongly dependent on the numerical resolution, the x-ray emissivity is very sensitive to the density profile of the cluster since it originates primarily from the central region of the cluster. In order to examine the expected luminosity behaviour with resolution, we take the density profile fit from high-resolution N-body simulations found in Navarro, Frenk & White (1996):

$$\frac{\rho(r)}{\rho_{crit}} = \frac{\delta_0}{(r/r_s)(1 + r/r_s)^2} \quad (6.11)$$

For these clusters, a reasonable parameter choice is $r_s = r_{vir}/5$, although our results will not be sensitive to small changes in this value. This is a fit to the collisionless component and not the baryonic gas as would be more appropriate, however the difference only becomes important at $r/r_{vir} \leq 0.04$ (c.f. Navarro, Frenk & White 1994; and chapter 8) which will not substantially affect our results.

In order to approximate the effect of finite numerical resolution we filter the density distribution:

$$\rho_{sm}(\vec{r}, r_{sm}) = \frac{\int \rho(\vec{r}') W_G \left(\frac{|\vec{r}' - \vec{r}|}{r_{sm}} \right) d^3 \vec{r}'}{\int W_G \left(\frac{|\vec{r}' - \vec{r}|}{r_{sm}} \right) d^3 \vec{r}'} \quad (6.12)$$

The smoothing kernel is a gaussian ($W_G(x) = e^{-x^2/2}$) and r_{sm} is the smoothing radius. Using symmetry, this integral can be partially computed analytically:

$$\rho_{sm}(r, r_{sm}) = \frac{1}{(2\pi)^{1/2} r r_{sm}} \int_0^\infty \rho(r') r' \left(e^{-\frac{(r'-r)^2}{2r_{sm}^2}} - e^{-\frac{(r'+r)^2}{2r_{sm}^2}} \right) dr' \quad (6.13)$$

In Figure 6.1a, we show the effects of various smoothing radii to the adopted density profile. The mass is conserved by the smoothing process, in the sense that the total

mass within some fixed fraction $r/r_{sm} \gg 1$ is constant as r_{sm} changes (the total mass of equation (6.11) does not converge as $r \rightarrow \infty$). This results in mass being transferred from small to large radii, causing the profile to steepen outside the smoothing radius, another feature observed by AN96. Assuming the temperature profile does not change, the bolometric free-free luminosity can be computed as a function of r_{sm} and the result is shown in Figure 6.1b. Also shown is the scaling result found by AN96 and given by equation (6.1), which they found to be approximately valid in the range $0.1 > r_{sm}/r_{vir} > 1$. The agreement is good enough that we will adopt their value ($\alpha = 1.17$), although it should be kept in mind that this power-law behaviour is only approximately correct.

If all density profiles can be scaled by the virial radius and critical density to agree with equation (6.11) regardless of mass (at least in a statistical sense), then the luminosity will scale in general as $L_{bol} \propto (r_{vir}/r_{sm})^\alpha$. Recent work (Navarro, Frenk & White 1996; Cole & Lacey 1996) indicates that, in fact, this is not true and lower mass objects form earlier and have steeper profiles. Nevertheless it appears to be a good approximation over the range of masses examined here and we will adopt it.

Using the relation between the virial radius and virial mass, $r_{vir} \propto M_{vir}^{1/3}/(1+z)$, we can include the effects of numerical resolution in equation (6.8):

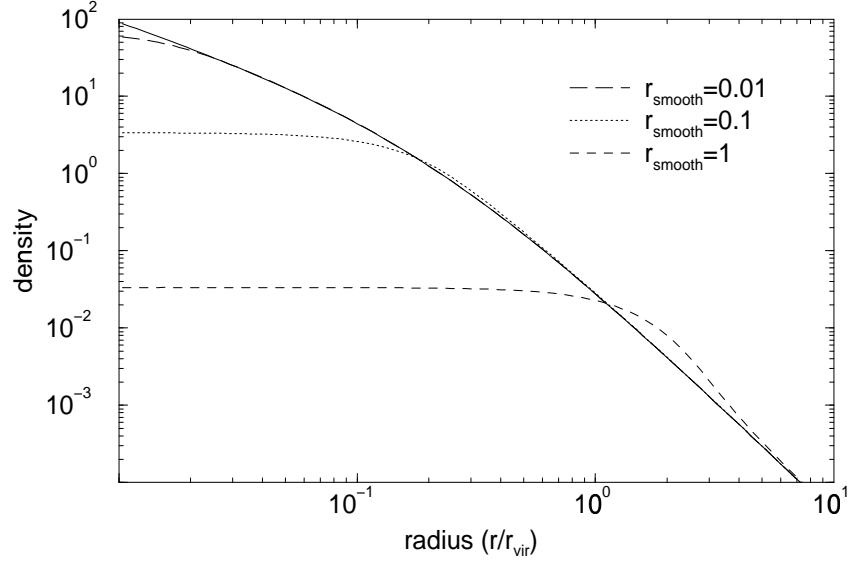
$$L'_{bol} = 1.1 \times 10^{45} \left(\frac{M_{vir}}{10^{15} M_\odot} \right)^{\frac{4+\alpha}{3}} \left(\frac{\Omega_b}{0.1} \right)^2 \left(\frac{100 \text{ kpc}}{\Delta x} \right)^\alpha (1+z)^{7/2} \text{ erg/s.} \quad (6.14)$$

Here we have written the resolution in terms of the comoving cell size Δx and normalized by assuming that $\Delta x = 100 \text{ kpc}$ will correctly reproduce the observed core radius of a $10^{15} M_\odot$ cluster (c.f. AN96). The resulting L'_{bol} - T and L'_{bol} - σ relations are

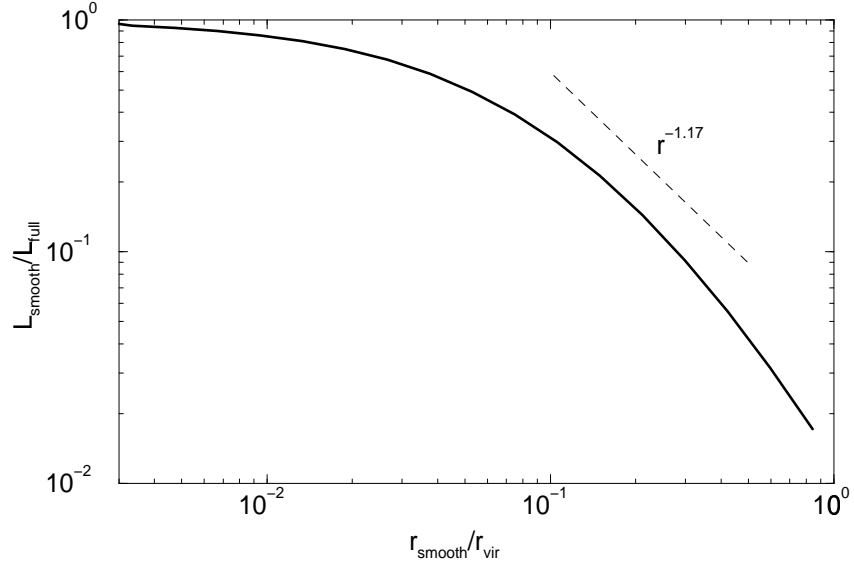
$$\begin{aligned} L'_{bol} &= 1.1 \times 10^{45} \left(\frac{kT\beta}{5.0 \text{ keV}} \right)^{\frac{4+\alpha}{2}} \left(\frac{\Omega_b}{0.1} \right)^2 \left(\frac{100 \text{ kpc}}{\Delta x} \right)^\alpha (1+z)^{\frac{3-\alpha}{2}} \text{ erg/s} \\ L'_{bol} &= 1.1 \times 10^{45} \left(\frac{\sigma}{895 \text{ km/s}} \right)^{4+\alpha} \left(\frac{\Omega_b}{0.1} \right)^2 \left(\frac{100 \text{ kpc}}{\Delta x} \right)^\alpha (1+z)^{\frac{3-\alpha}{2}} \text{ erg/s} \end{aligned} \quad (6.15)$$

6.2.3 Comparison to simulations

We have analyzed three simulations with parameters shown in Table 6.1, presenting results from the CHDM512 and CDM270 models. We also list a third model (CHDM256),



(a)



(b)

Figure 6.1. (a) The density profile in equation (6.11) smoothed by a gaussian filter with three different values of the smoothing radius. (b) The relative bolometric bremsstrahlung luminosity of the smoothed density profile as a function of smoothing radius. The dashed line shows the result found by direct numerical simulation (AN96).

Table 6.1. Simulation parameters

designation	Ω_{cold}	Ω_{hot}	Ω_{baryon}	h	m_ν (eV)	σ_8	N_{cell}	N_{part}	L_{box} (Mpc)
CDM270	0.94	0.0	0.06	0.5	0	1.05	270^3	135^3	170
CHDM512	0.725	0.2	0.075	0.5	2×2.3	0.7	512^3	3×256^3	100
CHDM256	0.6	0.3	0.1	0.5	7.0	0.67	256^3	3×128^3	170

for which the results have been analyzed and are in sufficiently good agreement with the other two runs that we do not comment on it further. Gravity is computed via a particle-mesh method so the resolution is a few times the cell width. None of the simulations include radiative cooling as (a) this will disrupt the scaling relations and (b) it may be a reasonable approximation for rich clusters, in which the hot gas has a cooling time larger than a Hubble time. All the models are approximately in agreement with COBE fluctuations on large scales. We use $h = 0.5$ throughout. For more details on these simulations, see chapters 4 and 5 (Bryan et al. 1994a; Bryan et al. 1994b); chapter 3 (Bryan et al. 1995) describes the computational method.

To identify clusters we adopt a technique very similar to the spherical overdensity algorithm described in Lacey & Cole (1996), using a mean overdensity of 178 to specify the virial radius and mass (the difference being that we use the density on the mesh to identify an initial list of possible halo positions, although the particles are used to find the virial radius and iterate on the center of mass). Note also that we will use the word ‘cluster’ to denote any collapsed object despite the fact that some of the smaller systems are closer to groups of galaxies. First, we will briefly examine the CDM270 model and then study the better resolved CHDM512 model in more detail, comparing to previous work.

In Figure 6.2, the mass-weighted velocity dispersion and virial mass of clusters identified in the CDM270 model are plotted along with the scaling relation from equation (6.3) for three different redshifts: $z = 0, 0.5$ and 1. We use $f_\sigma = 1.2$, as an unshifted normalization would produce significantly low masses. Concentrating on the higher velocity

dispersion clusters ($\sigma > 650$ km/s), we see that both the slope and redshift behaviour are well reproduced by the simulated clusters. For smaller clusters, the velocity dispersion drops below the value expected for a given mass. This is almost surely due to our gravitational softening: at $3 \times 10^{14} M_{\odot}$, the virial radius is about 2.5 cell widths.

The mass-temperature relation for clusters is shown in Figure 6.3, again for the CDM270 simulation and with the scaling relation from equation (6.6) with $f_T = 1.3$. The temperature actually appears to be a computationally more secure indicator of the virial mass than the velocity dispersion, a result which is somewhat surprising given the unresolved nature of the low-temperature clusters.

The relation between temperature and velocity dispersion is plotted in Figure 6.4, along with equation (6.5) for three values of β (0.8, 1, 1.2). For reasonably resolved clusters, the mean value is close to one, although there is substantial scatter.

Figure 6.5 shows the CDM270 mass-luminosity relation. Also, the appropriate scaling laws are shown with both the original version, equation (6.8), and the resolution-adjusted version, equation (6.14). The reasonably resolved simulated clusters agree well with the second relation. We also note that although the slope differs between the two versions, the relative evolution in redshift is very similar. This point will be important when examining the redshift evolution of the luminosity function in section 6.3.

The final comparison for this cosmology is the luminosity-temperature relation (Figure 6.6). This is the only relation presented for which direct measurements have been obtained in both quantities. The observations indicate a slope of $L \sim T^{2.7-3.5}$ (Edge & Stewart 1991a,b; Davis & Mushotzky 1993), steeper than predicted by equation (6.9). Bryan et al. (1994b) found a slope in agreement with observations for the 2–10 keV luminosity-temperature (as opposed to the bolometric result presented here). As we see here, this was partly (about 1/3) due to resolution effects but mostly resulted from the finite band-pass which strongly curtails the luminosity for clusters under a few keV (see section 6.3.1). Thus, the basic discrepancy between the observed and predicted bolometric $L - T$ relation remains unresolved.

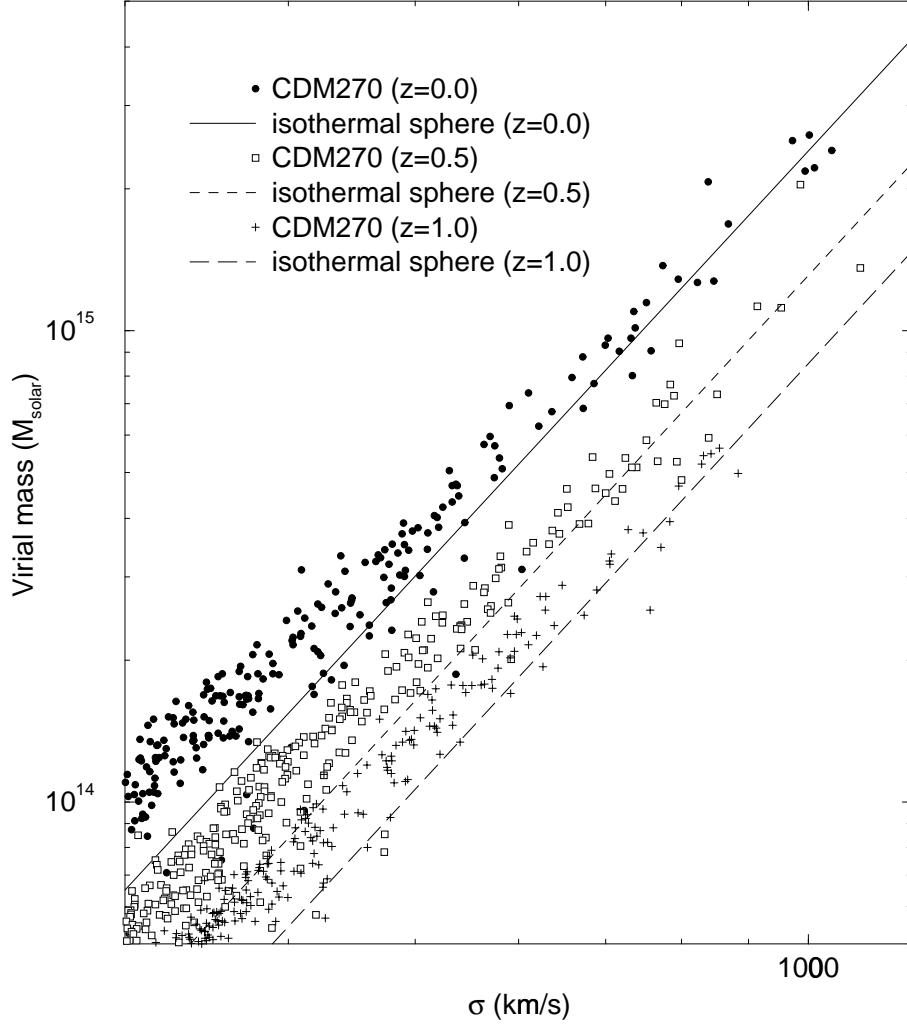


Figure 6.2. The virial mass and one-dimensional velocity dispersion of clusters identified in the CDM270 simulation for three different redshifts ($z = 0, 0.5$ and 1) along with the scaling relation from equation (6.3) for $f_{\sigma} = 1.2$.

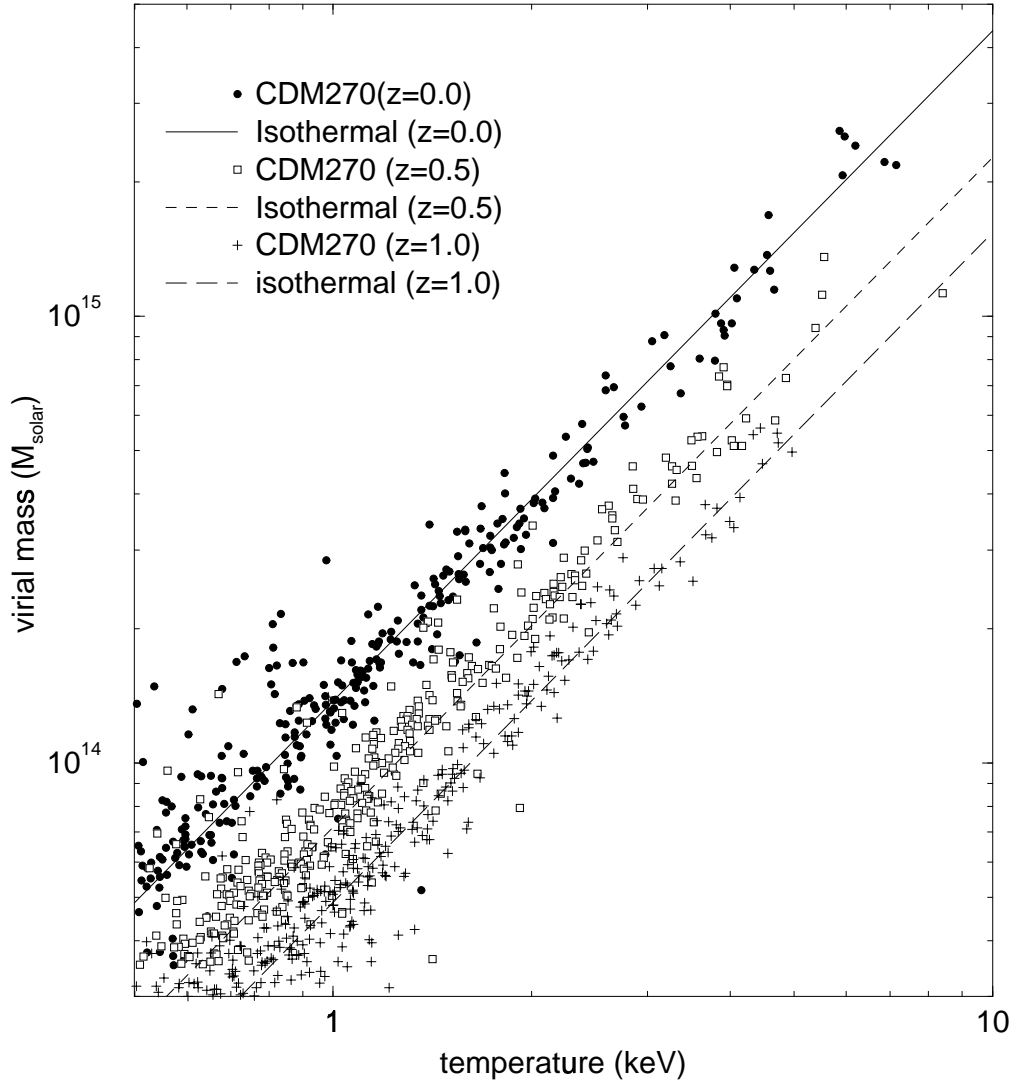


Figure 6.3. The virial mass and emissivity-weighted temperature of clusters identified in the CDM270 simulation for three different redshifts ($z = 0, 0.5$ and 1) along with the scaling relation from equation (6.6) for $f_T = 1.3$.

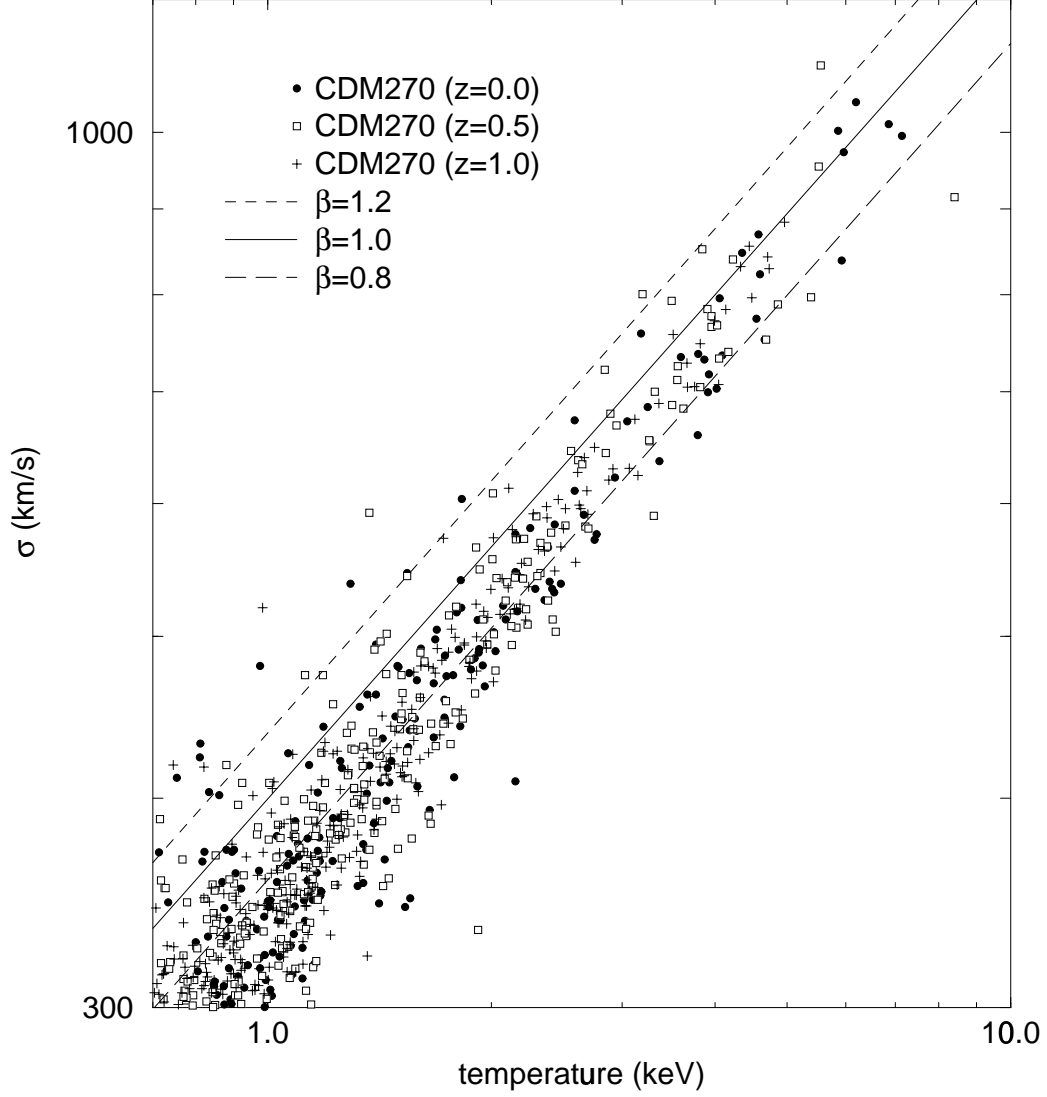


Figure 6.4. The velocity-dispersion and emissivity-weighted temperature of clusters identified in the CDM270 simulation for three different redshifts ($z = 0, 0.5$ and 1) along with the scaling relation from equation (6.5).

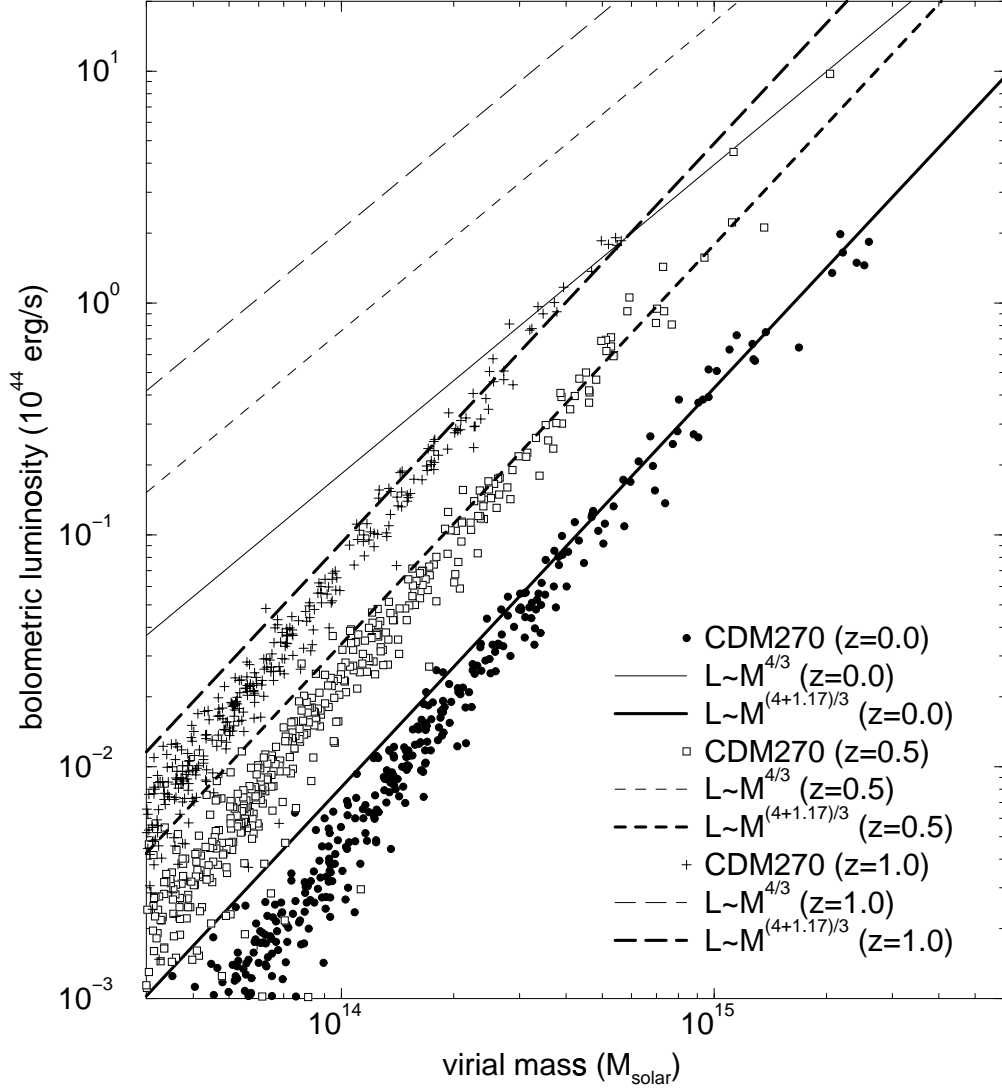


Figure 6.5. The mass and bolometric luminosity of clusters identified in the CDM270 simulation for three different redshifts ($z = 0, 0.5$ and 1) along with the scaling relations from equations (6.8) and (6.14).

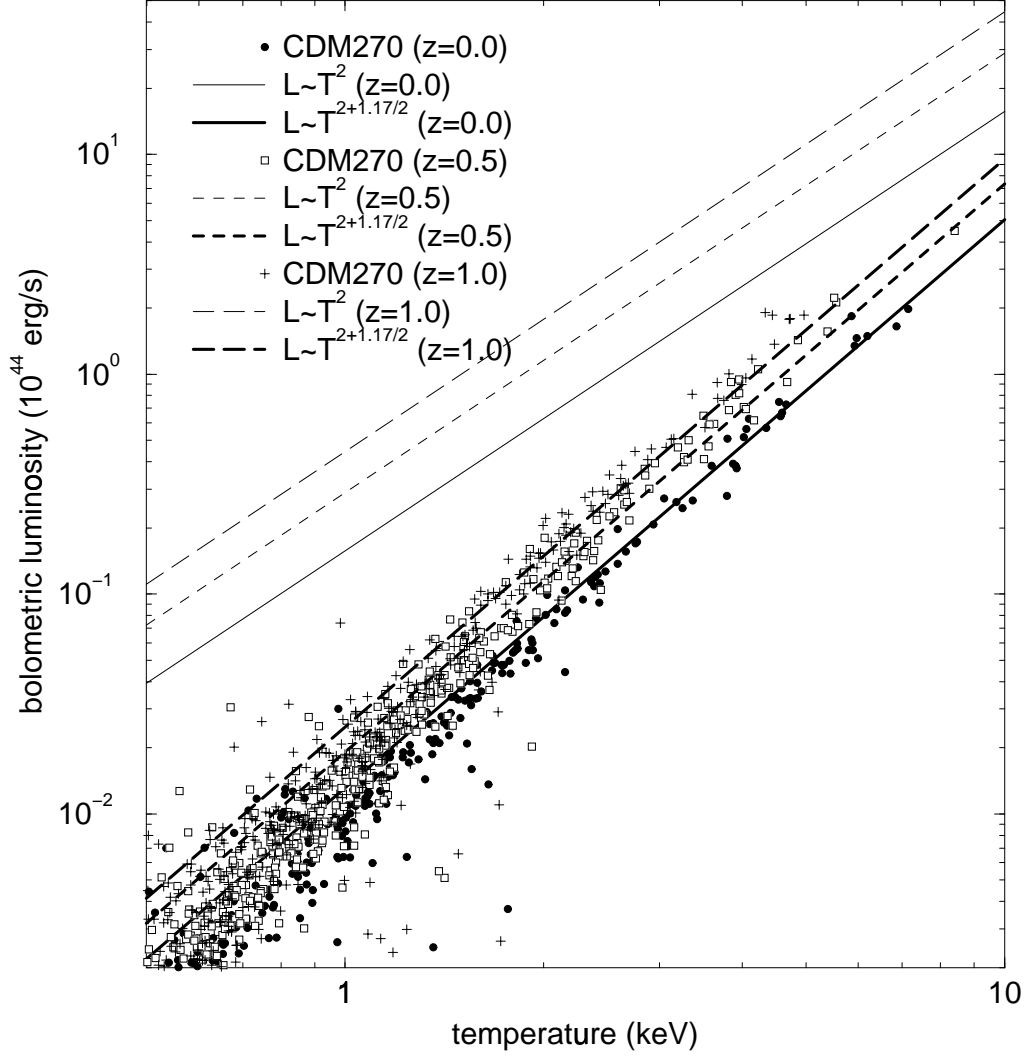


Figure 6.6. The temperature and bolometric luminosity of clusters identified in the CDM270 simulation for three different redshifts ($z = 0, 0.5$ and 1) along with the scaling relations from equations (6.9) and (6.15).

In Figures 6.7 to 6.11, we show the same relations for the CHDM512 model. The cell width has decreased by over a factor of three as compared to the CDM270 model so a cluster with the same virial radius is much better resolved in this calculation. On the other hand, the normalization on cluster scales is much lower (which is simply a consequence of the COBE normalization combined with CHDM's steeper slope). This means that the number density of clusters of a given mass is reduced.

The relation between mass and velocity dispersion again shows good agreement between the simulated clusters and the scaling relations, although this time we use a normalization of $f_\sigma = 1.1$ (instead of 1.2). This is not too surprising given Figure 6.2 which does not show convincingly that the high mass clusters have converged to the analytic slope. This indicates that the velocity dispersion requires very high resolution to be obtained exactly. Indeed, it is not clear that the higher resolution simulation has produced a final result and so we must view this as an upper limit. We also note that NFW show a similar plot for a smaller number of $z = 0$ clusters that is compatible with $f_\sigma \approx 1.06$. The scale free simulations of Cole & Lacey (1996) appear to agree with $f_\sigma \approx 1$ and also do not deviate from the scaling relation for small masses due to the improved spatial resolution of P³M. The same method was used by Crone & Geller (1995) but with a range of cosmologies including open models. They also find $f_\sigma \approx 1.06$ for their $\Omega = 1$, $n = -1$ simulation. Jing & Fang (1994) argue for $f_\sigma = 1.1$ – 1.2 , but this is based on N-body and Press-Schechter comparisons, rather than directly from the $M - \sigma$ relation. Finally, Walter & Klypin (1996) studied this relation, but used a fixed cluster radius rather than one based on the mean overdensity, making a direct comparison difficult.

In contrast to the velocity-dispersion, fitting equation (6.6) to the CHDM512 mass-temperature relation results in the same normalization as found for the CDM270 run ($f_T = 1.3$). Combined with the fact that the simulated results and the scaling relation agree even for small cluster masses, this bolsters both our suggestion that the temperature is an excellent virial mass indicator (for simulated clusters), as well as this particular value of the normalization constant. Although they do not measure a value, this number is also in concordance with the $z = 0$ results of NFW (their figure 11). The size of deviations

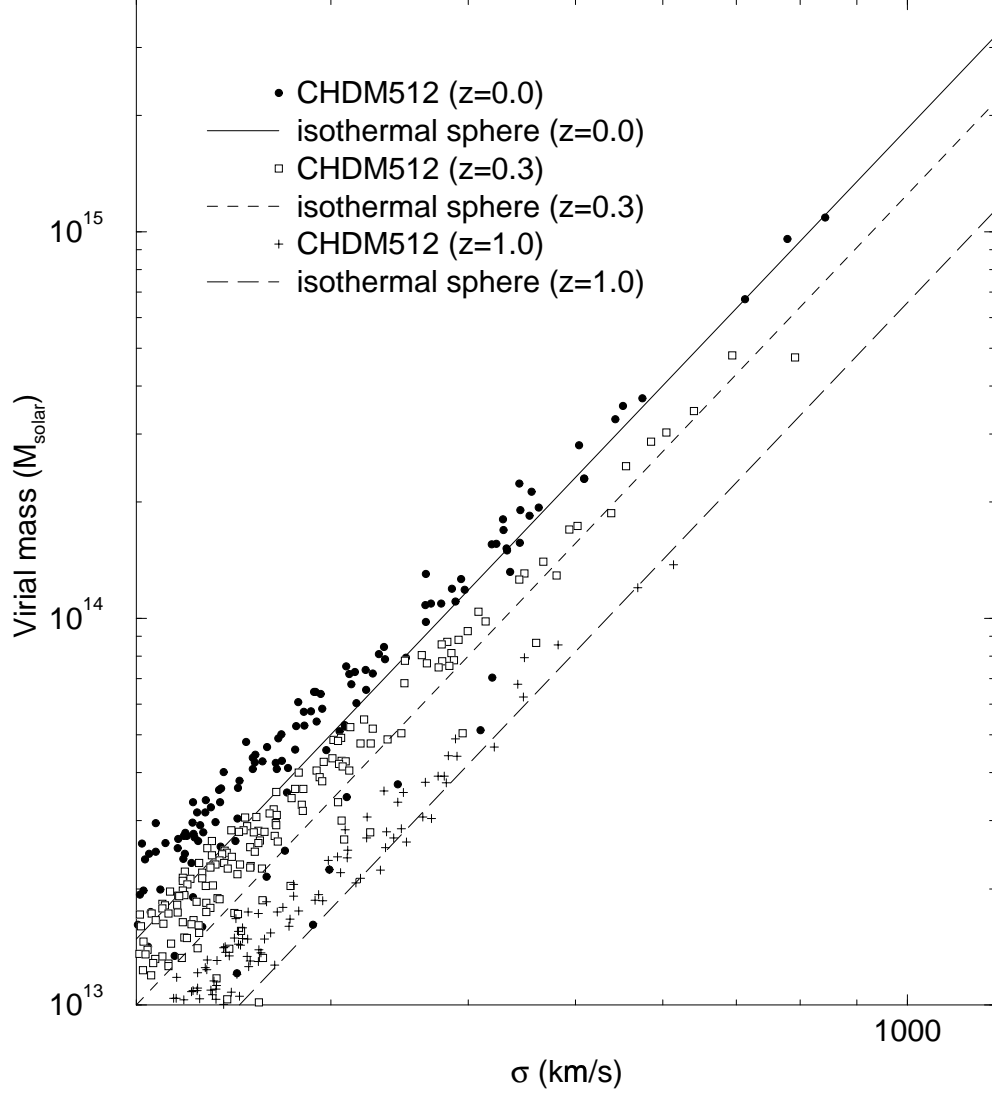


Figure 6.7. The virial mass and one-dimensional velocity dispersion of clusters identified in the CHDM512 simulation for three different redshifts ($z = 0, 0.3$ and 1) along with the scaling relation from equation 6.3 for $f_{\sigma} = 1.1$.

from a purely hydrostatic equilibrium are reflected in the scatter of points around this value.

As in the CDM270 model, the clusters of the CHDM512 simulation show a trend with cluster resolution in the velocity dispersion–temperature plane (Figure 6.9), moving from low to high values of β . The most well-resolved clusters, in fact, have values above one, as the previous two plots would suggest ($\beta = f_T/f_\sigma^2 \sim 1.07$). This value is somewhat lower than the mean of $\beta = 1.16$ for six clusters obtained by NFW. There are a number of possible reasons for $\beta \neq 1$. One is incomplete thermalization in the hot gas component which would result in a lower mean temperature. Since the two values are computed and observed in different ways (mass-weighted for the velocity dispersion but luminosity-weighted for the temperature) different profiles in the gas and dark matter can result in differing values for σ and T . Observationally, the quantity β has been the subject of some investigation, with values being generally compatible with one (Girardi et al. 1996; Lubin & Bahcall 1993), although this is for the galaxy velocity dispersion rather than the collisionless component.

The two relations which include luminosity (Figures 6.10 and 6.11) show substantially increased luminosity for fixed virial mass as compared to the CDM270 simulation, as expected. There is good agreement between simulated clusters and the modified scaling relations from equations (6.14) and (6.15) despite changes in the cell width, baryon fraction and cosmological model.

6.3 Distribution Functions

The scaling relations discussed in the previous section can be combined with a prediction of the mass distribution function of virialized objects to make predictions of more easily observed distribution functions. Although there are a number of prescriptions for obtaining the number of collapsed objects given a power spectrum of linear initial perturbations (e.g. Lacey & Cole 1993; Kitayama & Suto 1996; Bond & Myers 1996), we adopt Press-Schechter because it is relatively simple and widely used.

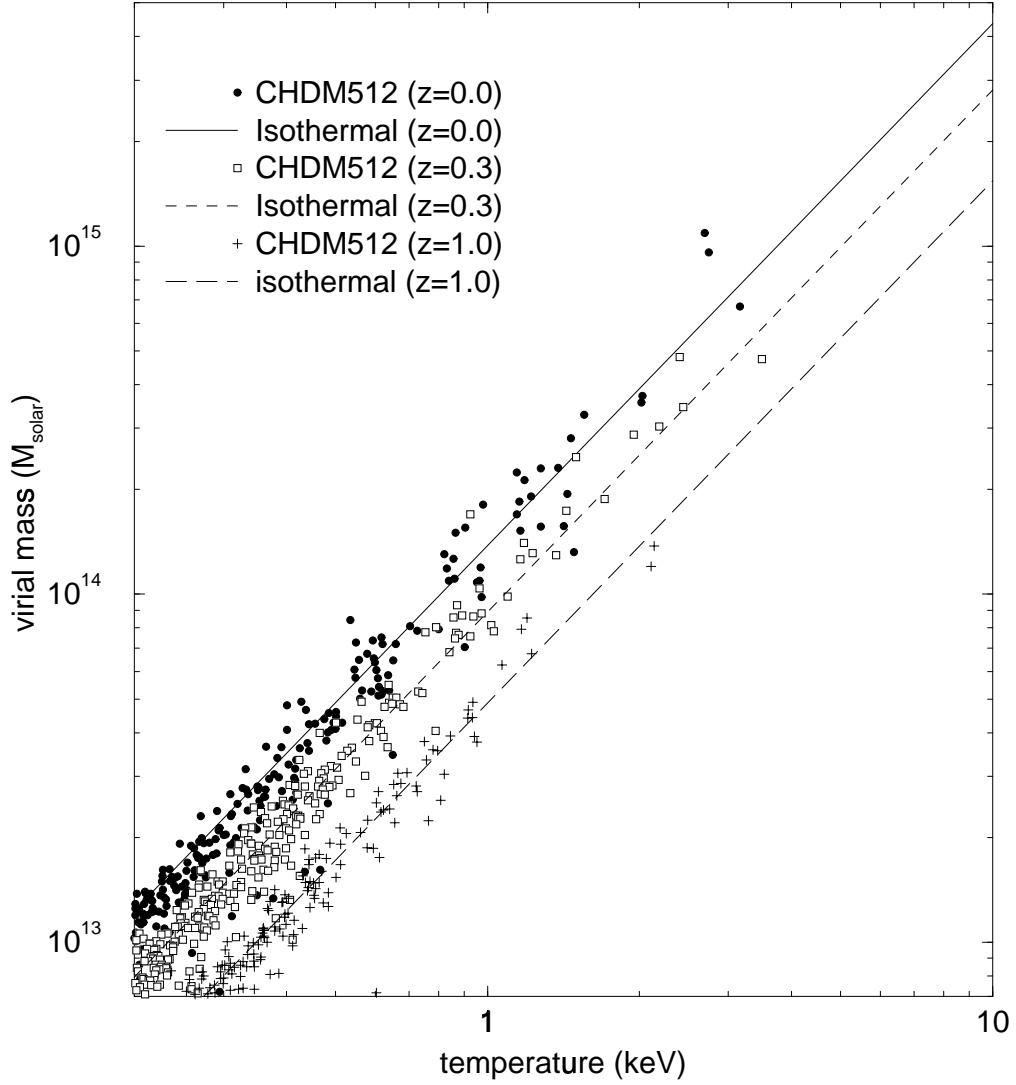


Figure 6.8. The virial mass and emissivity-weighted temperature of clusters identified in the CHDM512 simulation for three different redshifts ($z = 0, 0.3$ and 1) along with the scaling relation from equation (6.6) for $f_T = 1.3$.

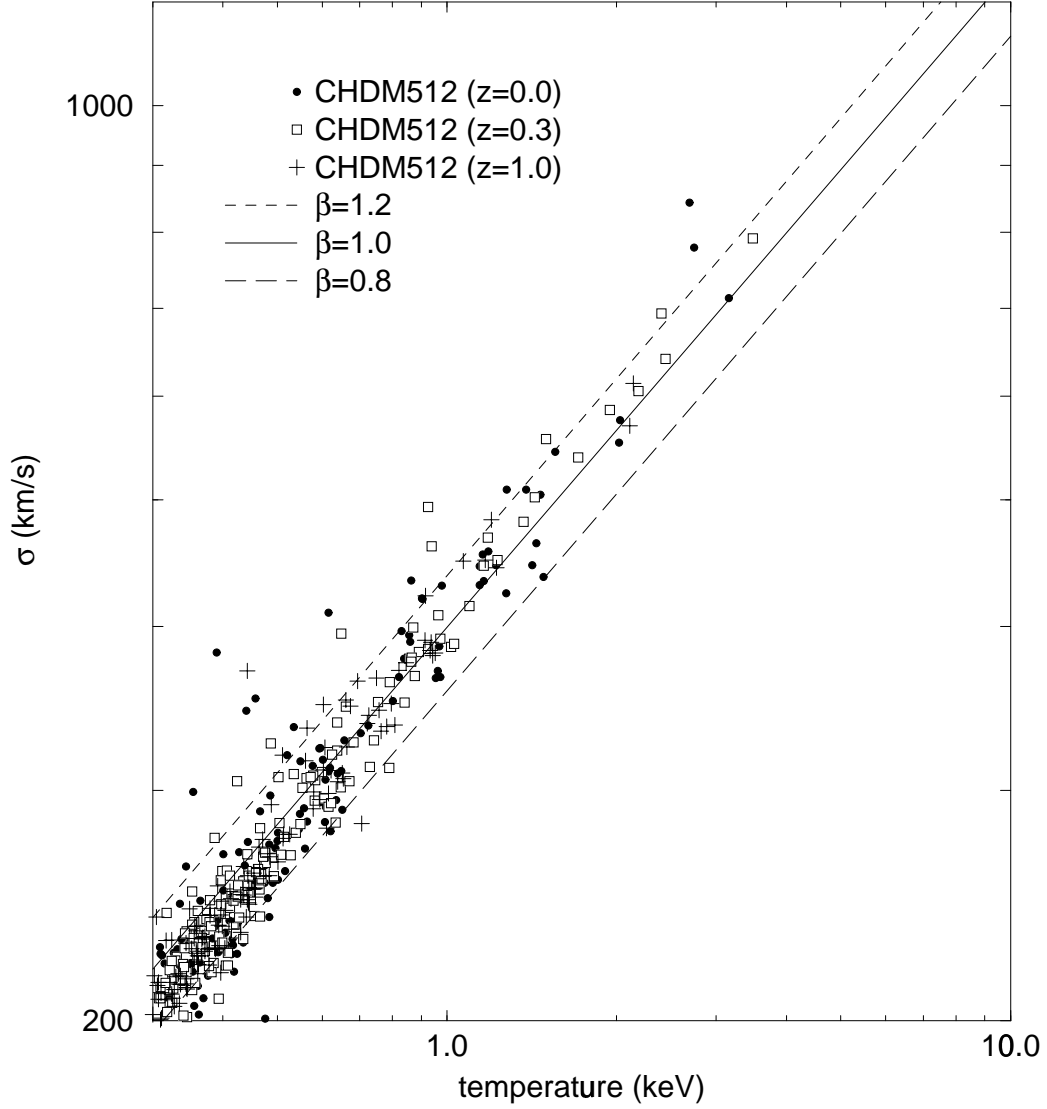


Figure 6.9. The velocity-dispersion and emissivity-weighted temperature of clusters identified in the CHDM512 simulation for three different redshifts ($z = 0, 0.3$ and 1) along with the scaling relation from equation (6.5).

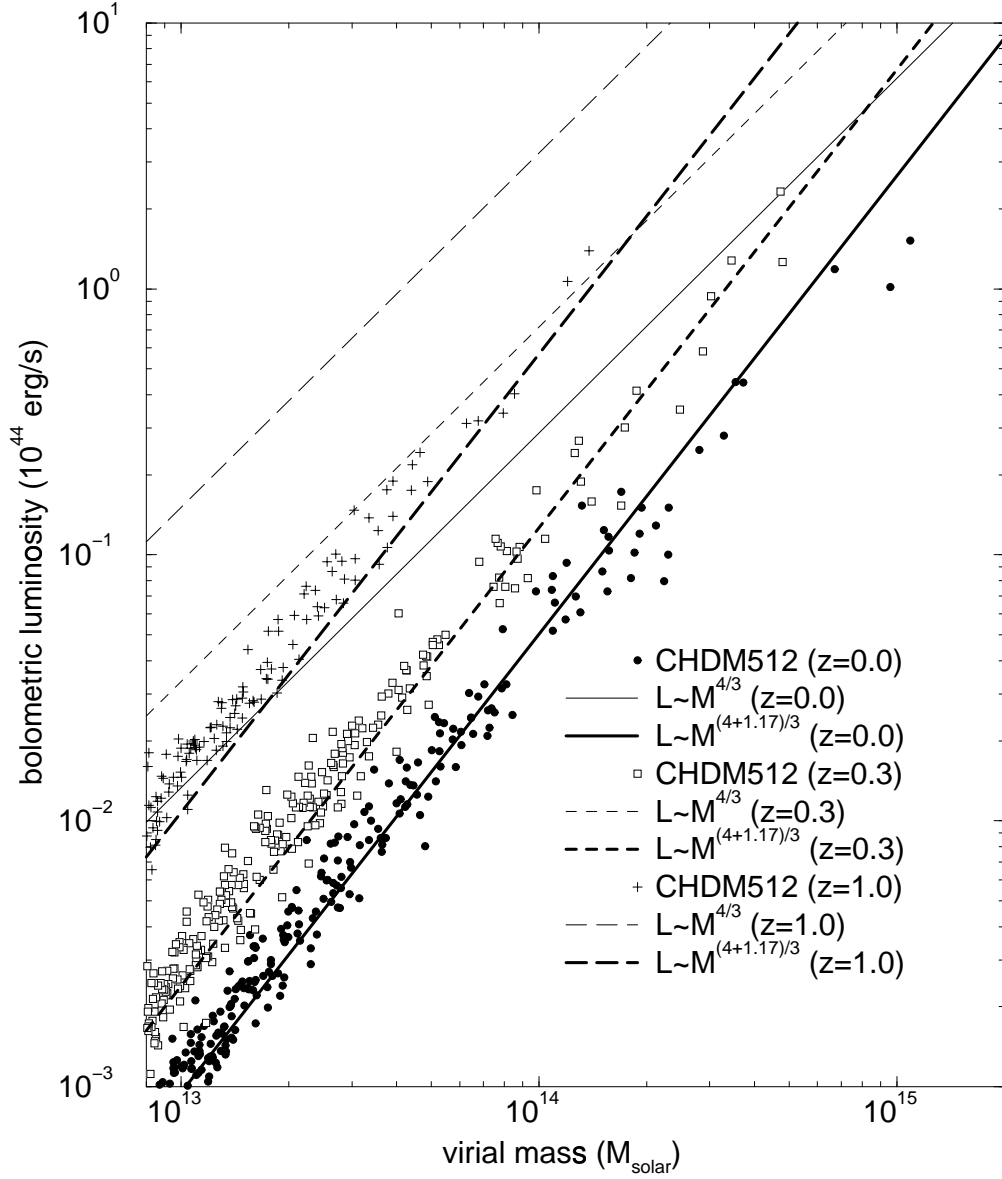


Figure 6.10. The mass and bolometric luminosity of clusters identified in the CHDM512 simulation for three different redshifts ($z = 0, 0.3$ and 1) along with the scaling relations from equations (6.8) and (6.14).

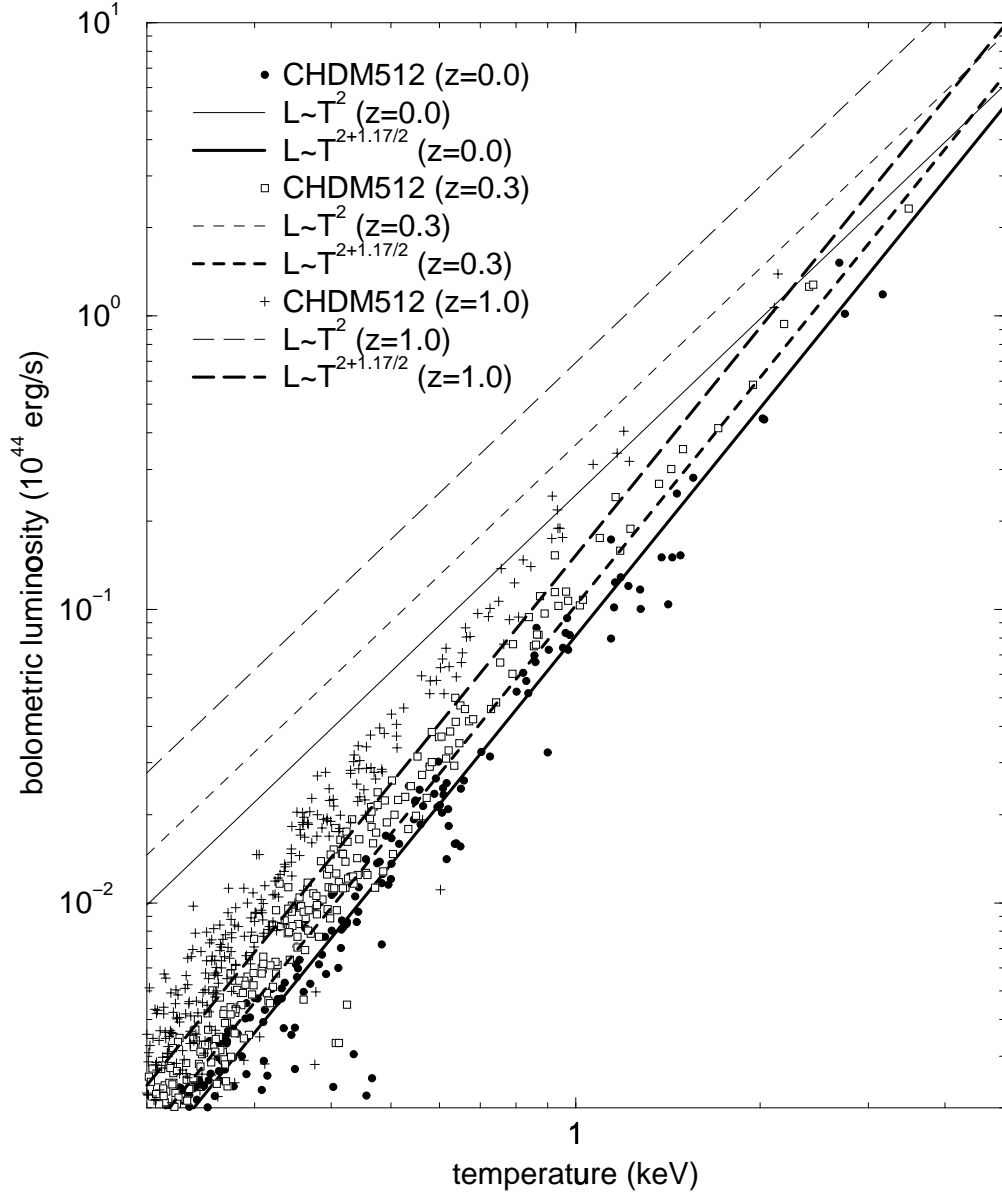


Figure 6.11. The temperature and bolometric luminosity of clusters identified in the CHDM512 simulation for three different redshifts ($z = 0, 0.3$ and 1) along with the scaling relations from equations (6.9) and (6.15).

The comoving number of virialized objects of mass M in mass interval dM is given by (Press & Schechter 1974),

$$\frac{dn}{dM} = \left(\frac{2}{\pi}\right)^{1/2} \frac{\bar{\rho}}{M} \frac{\nu_c}{\sigma(M)} \frac{d\bar{\sigma}}{dM} e^{-\nu_c^2/2}. \quad (6.16)$$

where $\bar{\rho}$ is the mean density and $\nu_c = \delta_c/\sigma(M)$. The linear rms density fluctuations of the power spectrum is given by

$$\sigma^2(M) = \int W_T^2(kR) P(k) d^3k \quad (6.17)$$

on the scale $M = 4\pi R^3 \bar{\rho}/3$ with a top-hat smoothing filter $W_T(x) = 3(\sin(x)/x - \cos(x))/x^2$ (note the difference between the velocity dispersion σ and the rms density fluctuation $\sigma(M)$). The numerical value of δ_c has been the topic of some debate; we adopt $\delta_c = 1.68$ based on the prediction of the spherical top-hot collapse model.

The linear CDM power spectrum is taken from Bardeen et al. (1986) while we use a fit from Ma (1996) to the CHDM (mass-weighted) power-spectrum:

$$P(k, a, \Omega_\nu) = P_c(k, a, \Omega_\nu = 0) \left(\frac{1 + d_1 x^{d_4/2} + d_2 x^{d_4}}{1 + d_3 x_0^{d_4}} \right)^{\Omega_\nu^{1.05}} \quad x = \frac{k}{\Gamma_\nu} \quad (6.18)$$

where $P_c(k, a, \Omega_\nu = 0)$ is the power spectrum for the CDM model, $\Gamma_\nu = a^{1/2} \Omega_\nu h^2$ and x_0 is x at $z = 0$. The numerical fitting parameters are $d_1 = 0.004321$, $d_2 = 2.217 \times 10^{-6}$, $d_3 = 11.63$ and $d_4 = 3.317$. This is for a single neutrino species, while our model assumes two neutrinos of half the mass, increasing the free-streaming length.

In Figure 6.12 we show the result of comparing halos from the simulation (identified with the spherical overdensity scheme described earlier) with the predictions from equation (6.16) for the CDM270 and CHDM512 models at a few different redshifts. The indicated uncertainty is solely from Poisson fluctuations. Although the analytic result is offset from the numerical results for CDM270 by a small factor (for all redshifts analyzed), the slope and redshift behaviour is in remarkably good agreement for reasonably well resolved clusters ($M \geq 10^{14} M_\odot$). The agreement is even better with the CHDM512 simulation. This relatively close agreement is in accordance with comparisons performed by other authors (e.g. Eke, Cole & Frenk 1996; Klypin et al. 1994). For a rather complete discussion of the mass function of halos for the CDM model see Gelb & Bertschinger

(1994). Both cosmological models produce fewer high-mass clusters with increasing redshift, although the evolution is clearly much stronger in the model with neutrinos (in fact, the difference would be even larger if the CDM model had a normalization closer to that adopted for CHDM). This behaviour contrasts markedly with open CDM models (Eke, Cole & Frenk 1996) which can actually have more clusters at higher redshift for the mass range considered here.

The high-end cutoff of the mass function is controlled by the non-linear mass (M_{nl}), defined as the mass within a spherical volume for which the mean overdensity from equation (6.17) is equal to 1.68. Figure 6.13 shows the evolution of this quantity, using both the linear power spectrum and the fully non-linear (N-body) spectrum (for a more complete discussion in terms of the CDM model, see Jain & Bertschinger 1994). The linear results for CDM are closer to the non-linear than for the CHDM model because of the shallower spectral profile (smaller logarithmic slope). In other words, the CHDM slope is close enough to $P(k) \sim k^{-3}$ that the extremely rapid evolution of M_{nl} requires more accuracy to obtain a good estimate of the non-linear mass. Also plotted are curves (with arbitrary normalization) showing how the non-linear mass would evolve for scale-free spectra with spectral index n ($M_{nl} \propto (1+z)^{-6/(n+3)}$), where $n \sim -1.5$ (-2.0) is roughly appropriate for the CDM (CHDM) spectrum on cluster scales.

Although useful, the mass distribution is difficult to obtain from observations because of uncertainties in obtaining the total mass. Somewhat easier is the temperature distribution of clusters. In Figure 6.14, we plot this function for both simulated clusters from the CDM270 and CHDM512 models as well as analytic predictions using Press-Schechter and the mass-temperature relation: equations (6.16) and (6.6). From the results of section 6.2, we adopt the mass-temperature normalization $f_T = 1.3$, producing good agreement between the simulation and analytic results. Although the CDM270 Press-Schechter curves are universally high, this is due to the mass distribution (Figure 6.12). Again, there is a strong difference between the evolutionary properties: the CDM270 model produces a roughly constant comoving number density of 4 keV clusters, while the number drops by a factor of ten in the cold plus hot dark matter cosmology. When

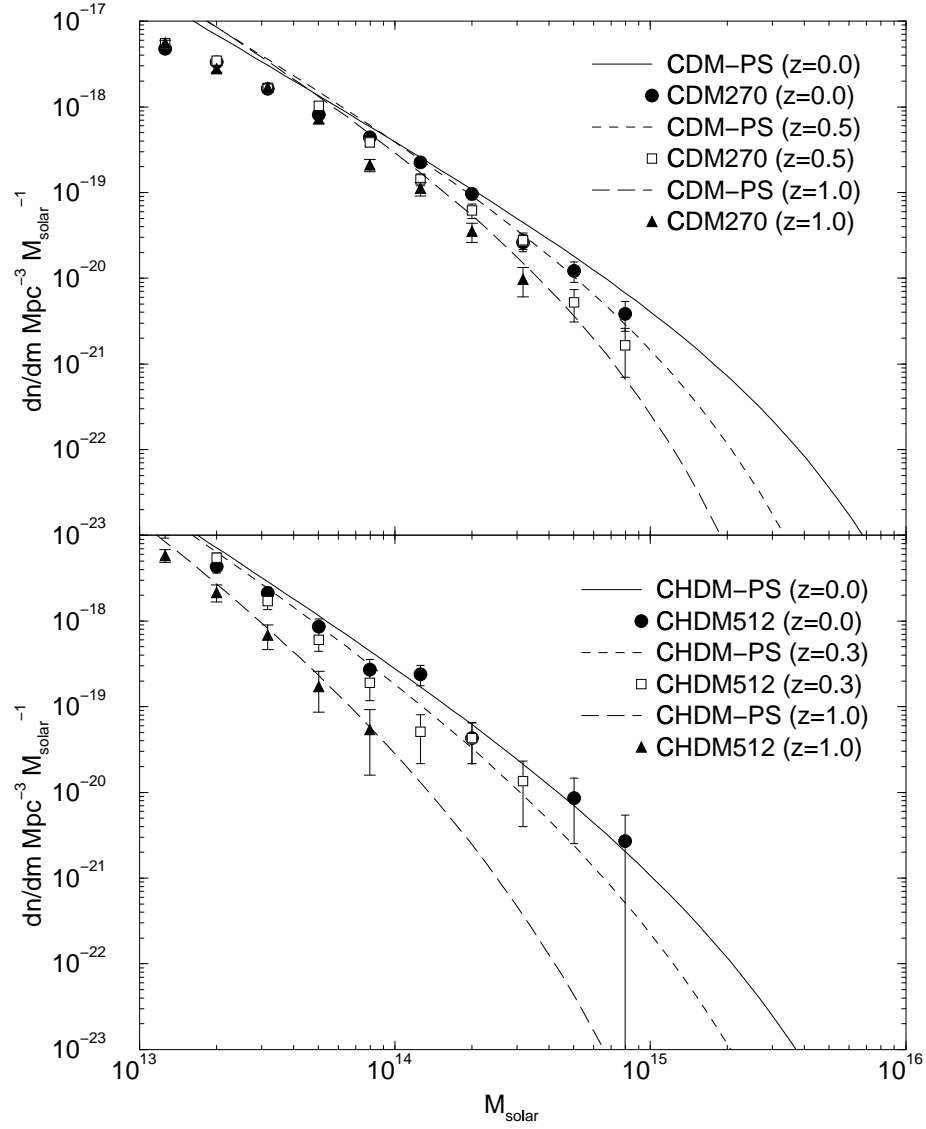


Figure 6.12. The differential mass distribution function for the CDM270 (top) and CHDM512 (bottom) models with Press-Schechter predictions ($\delta_c = 1.68$) at three redshifts: $z = 0, 0.5, 1$ for CDM, $z = 0, 0.3, 1$ for CHDM.

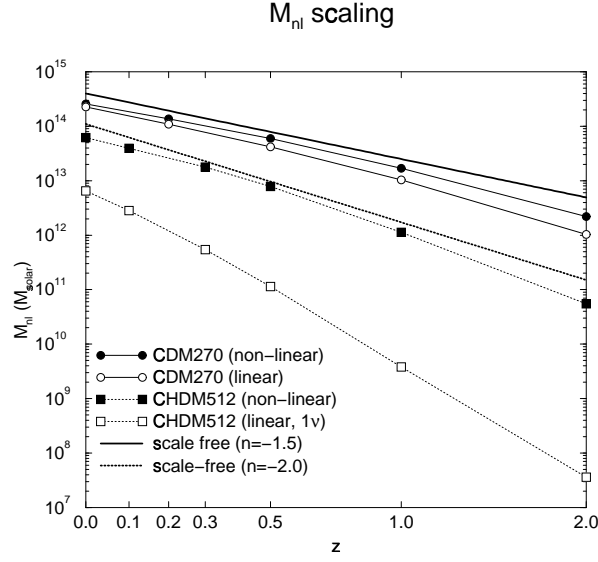


Figure 6.13. The evolution of the non-linear mass (see text for definition) for the CDM270 and CHDM512 models, computed both through the linear and non-linear (N-body) power spectra. Also, results from two scale-free spectra appropriate for the two models are also shown.

medium to high redshift cluster temperature samples become available, this will provide a strong constraint. Observational measurements are also shown and will be discussed below.

Since luminosities are more easily obtained observationally, we use equation (6.8) to determine the bolometric luminosity distribution assuming no metals (this constraint will be relaxed in the next section). These are shown as thin lines in Figure 6.15. While the simulated clusters do not match these results, including the effects of finite resolution with equation (6.8) does (at least for the reasonably well resolved clusters) produce agreement, although, of course, there is not much differentiation between different redshifts. The ‘fully’ resolved Press-Schechter predictions show that there is strong positive evolution in the CDM model, while it is much weaker for CHDM and becomes negative at a bolometric luminosity of a few times 10^{44} erg/s.

Perhaps more importantly, the difference between the thin and bold lines indicate the kind of error engendered by our limited spatial resolution. Roughly speaking, there are two effects. The first is the obvious reduction in the luminosity of all clusters, shifting

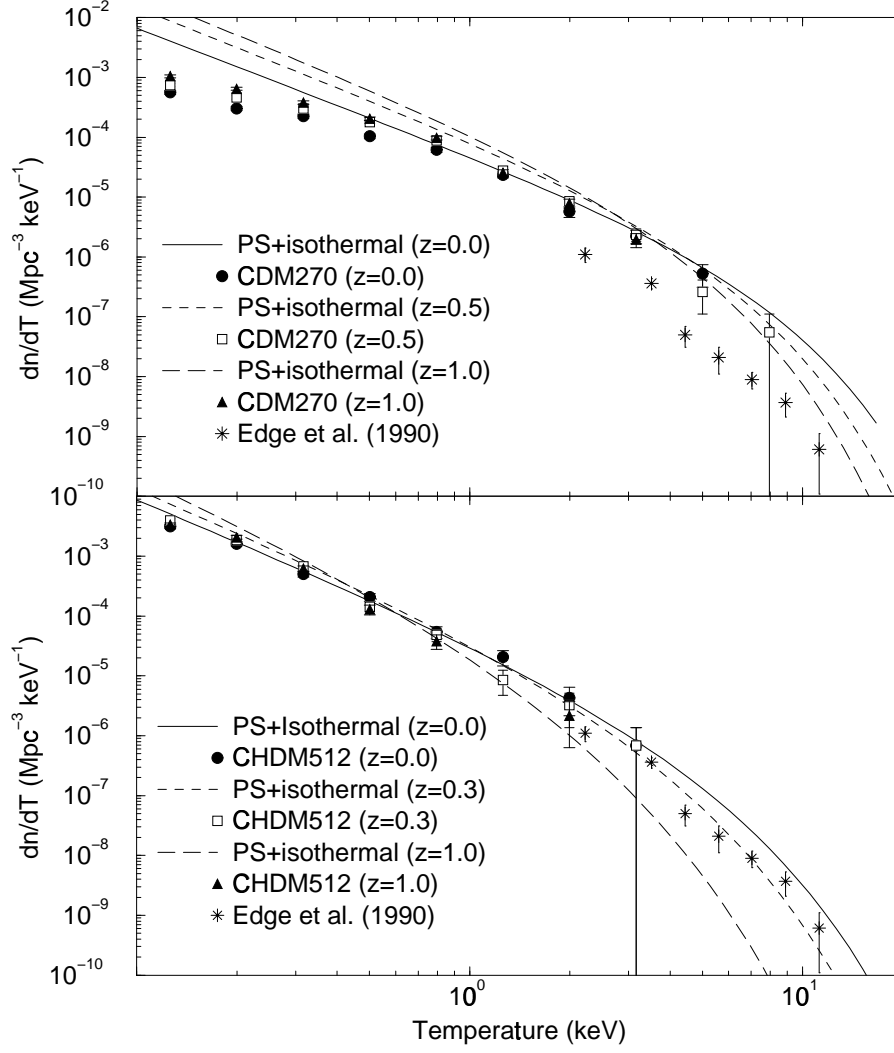


Figure 6.14. The differential temperature distribution function for the CDM270 (top) and CHDM512 (bottom) models with Press-Schechter predictions ($\delta_c = 1.68$) at three redshifts ($z = 0, 0.5, 1$ for CDM, $z = 0, 0.3, 1$ for CHDM), assuming equation (6.6) with $f_T = 1.3$. Observations at $z = 0$ are plotted as stars (Edge et al. 1990).

the curves to the left. The other is to add an additional component of negative redshift evolution, exaggerating the negative evolution at high luminosities and decreasing the positive evolution at the low end. Nevertheless, this second effect is relatively small, about the size of Poisson fluctuations due to the limited number of clusters. A further systematic uncertainty due to the lack of waves longer than the computational box is not discussed (although it appears to be small given our agreement with the Press-Schechter results which do not suffer from this shortcoming).

6.3.1 Metallicity Effects

In this section we address more realistic x-ray emissivity effects: limited band-passes and line emission from multiply ionized heavy elements in the plasma (metallicity). As we will show, for moderate and high temperature clusters, the ratio of line to continuum emission is actually quite small (a few percent), making the accurate determination of a cluster's metallicity difficult. Nevertheless, the high resolution spectroscopy performed by the ASCA satellite (as well as work done with ROSAT and other missions) seems to indicate that a value of $Z/Z_{\odot} = 0.3$ in solar units is reasonable for many clusters (Kowalski et al. 1993; Markevitch et al. 1994).

We use a Raymond-Smith model (1977, 1992 version) to compute emissivities which are shown in the top panel of Figure 6.16 for a variety of metallicities and band-passes as a function of temperature assuming a number density of electrons of 10^{-3} cm^{-3} . The effect of line emission from metals is small for $T > 2 \text{ keV}$. This means that previous results (Bryan et al. 1994a,b) computed with the assumption of zero-metallicity will not be substantially affected in the region where observational results are most plentiful. Nevertheless, this will prove important for small clusters and groups of galaxies so we extend our previous analytic results to include this effect (although, of course, our simulations do not include many other effects that may prove important for small clusters such as stellar feedback and radiative cooling).

To do this, we fit simple expressions to the full result by ignoring the gaunt factor and approximating the effect of metallicity as a power law with a cutoff. The resulting

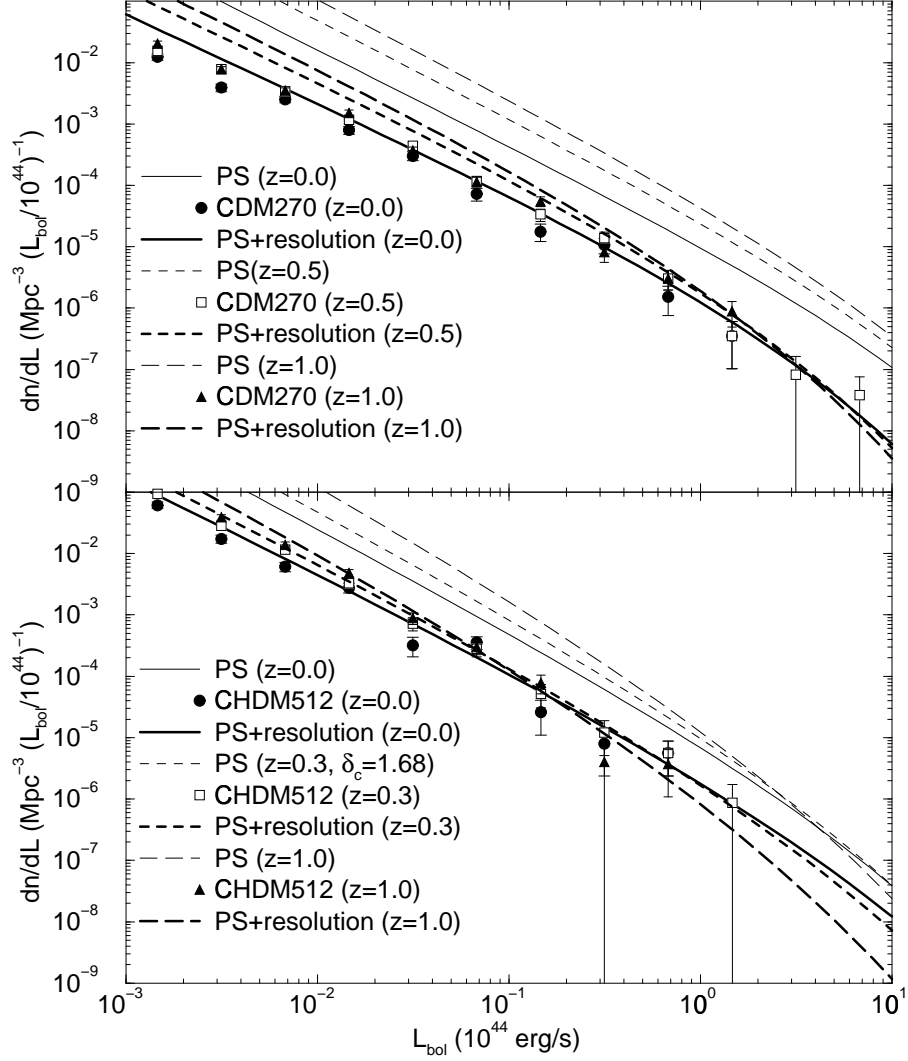


Figure 6.15. The differential bolometric luminosity distribution function for the CDM270 (top) and CHDM512 (bottom) models at three redshifts ($z = 0, 0.5, 1$ for CDM, $z = 0, 0.3, 1$ for CHDM). The Press-Schechter results for two mass-luminosity relations are also shown: thin lines use equation (6.8) while bold lines include the effects of limited resolution: equation (6.14).

formula is given in relation to the bolometric luminosity ($L_{metal} = \epsilon(Z, T, \nu_1, \nu_2)L_{bol}$, where ν_1 and ν_2 specify the band-pass) by:

$$\epsilon(Z, T, \nu_1, \nu_2) = \left[\exp\left(\frac{-h\nu_1}{kT}\right) - \exp\left(\frac{-h\nu_2}{kT}\right) \right] \begin{cases} (kT/2 \text{ keV})^{-\gamma(\frac{Z}{0.3Z_{\odot}})^{1/2}} & kT < 2 \text{ keV} \\ 1 & kT > 2 \text{ keV} \end{cases} \quad (6.19)$$

The effect of metallicity depends on the bandpass used and cannot be simply modelled, so we parameterize it through γ and tabulate values appropriate for a few common choices: $\gamma = 0.6$ for 0.1–2.4 keV; 0.9 for 0.5–2.4 keV; 0.0 for 2–10 keV; and 0.7 for bolometric luminosities. This fit is accurate to only about a factor of two, but will be sufficient for our purposes; a few examples are shown in the bottom panel of Figure 6.16.

With this extension we can now compare the analytic predictions, using the bolometric luminosities from equation (6.8), to the simulated values. The numerical cluster luminosities are computed on a cell-by-cell basis so they include the spatial variation of temperatures (see section 6.4) which the analytic models are missing. This is done in Figure 6.17 for the CDM270 and CHDM512 models, again showing the effects of full and limited resolution along with a metallicity of 0.3 solar. This demonstrates that the effects of metallicity are negligible above about 10^{44} erg/s and relatively slight above 10^{43} erg/s.

6.4 Cluster structure

In deriving some of the analytic results we assumed a spherically symmetric isothermal profile for both the gas and dark matter. In this section we examine the simulated clusters in order to determine the accuracy of these assumptions. A more complete analysis is presented in the next chapter.

In Figure 6.18 we show profiles of temperature and the one-dimensional velocity dispersion for the five most massive clusters in our two canonical models. These are normalized by their appropriate virial values (with $f_T = f_{\sigma} = \beta = 1$). To compute the profile, we redetermine the cluster centers by adopting the center of the cell with the highest gas density within $r_{vir}/2$ of the original center found through the iterated

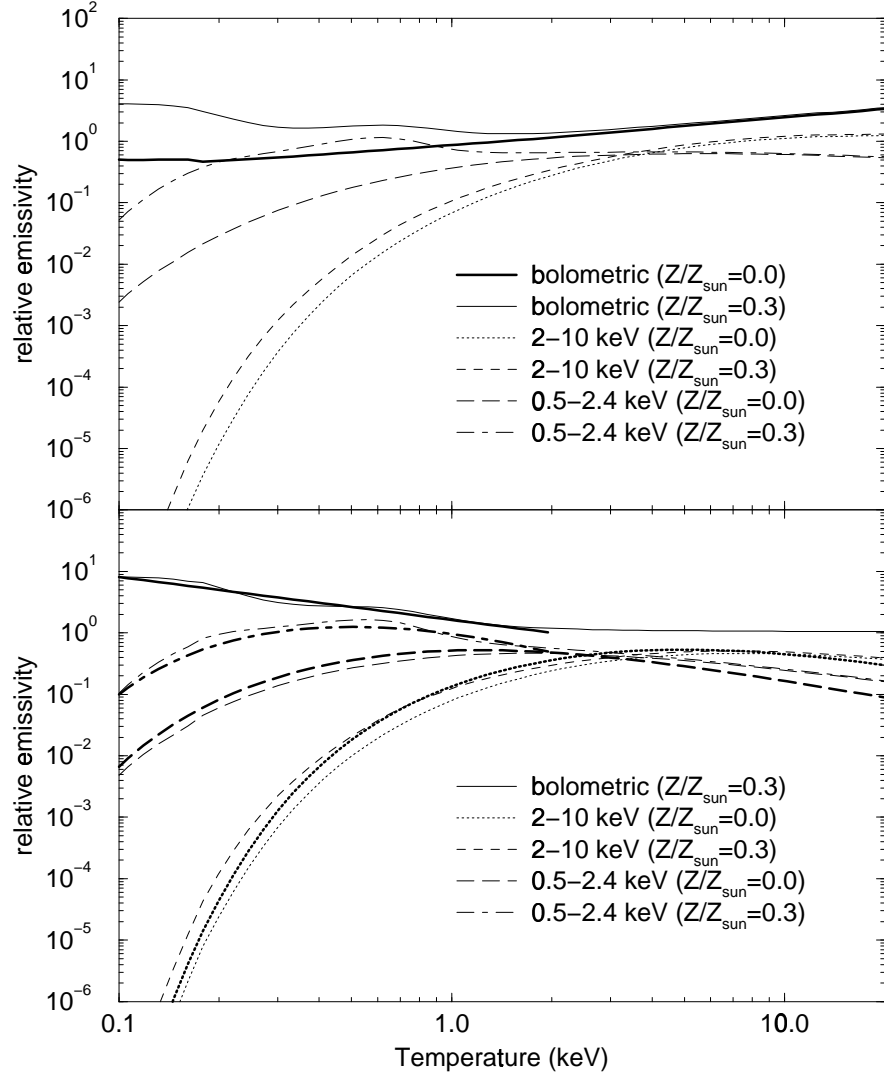


Figure 6.16. The x-ray emissivity as a function of temperature for two different metallicities and three different band-passes from a Raymond-Smith code assuming an electron density of 10^{-3} cm^{-3} (top panel). The relative x-ray emissivity (normalized to the bolometric emissivity at that temperature for a metal-free plasma) as thin lines (bottom panel). Also shown in thick lines are the approximate fits from equation (6.19).

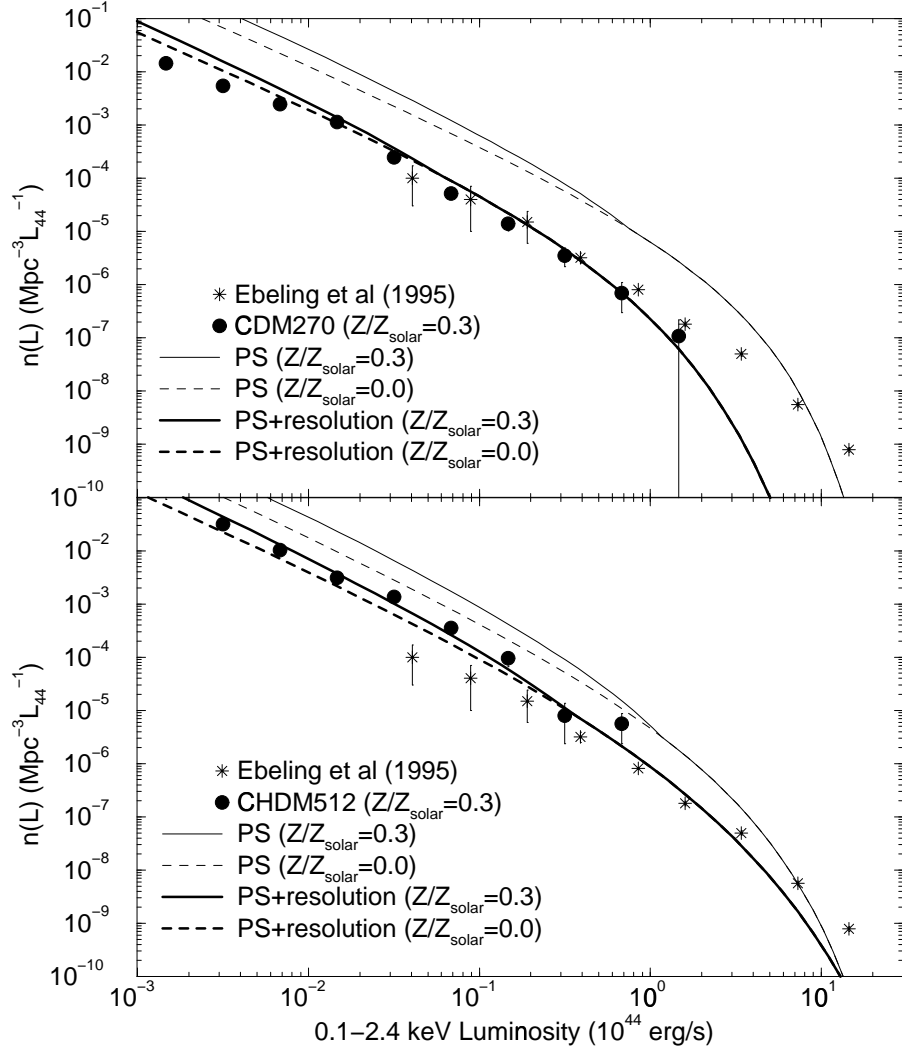


Figure 6.17. The differential 0.1-2.4 keV luminosity distribution function with and without metallicity for the CDM270 (top) and CHDM512 (bottom) models at the same redshifts as in Figure 6.12. The Press-Schechter results for two mass-luminosity relations are also shown: thin lines use equation (6.8) while bold lines include the effects of limited resolution: equation (6.14). Observations at $z = 0$ are plotted as stars (Ebeling et al. 1995).

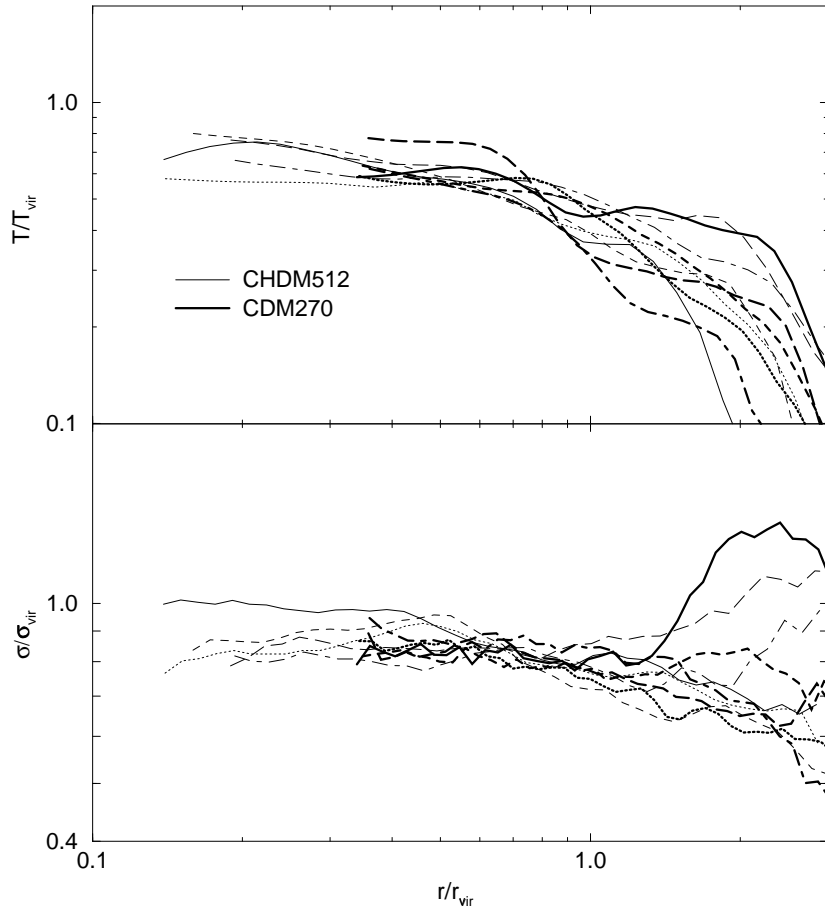


Figure 6.18. Temperature (top panel) and dark matter one-dimensional velocity dispersion (bottom panel) profiles for the CDM270 and the CHDM512 models at $z = 0$, normalized by their respective virial values.

spherical overdensity method. This procedure does a good job of finding the core of the largest mass clump. The innermost point plotted is two cell widths from the cluster center. This is very approximately our resolution limit.

The spherically-averaged temperature profiles are compatible between models and show a very slowly falling profile to about $0.7r_{vir}$, a somewhat steeper slope ($r^{-0.5}$) to about two times the virial radius and then a very sharp fall off beyond that. The one-dimensional velocity dispersion profile is much flatter, as expected from its closer agreement to the isothermal sphere solution. The hot component (we plot only the

cold particles in Figure 6.18) follows almost exactly the same profile at large r , but is systematically higher at low radii.

The velocity profiles are close to flat, although they appear to show a slight dip at and just before the virial radius. They are also slightly below their respective σ_{vir} values (implying $f_\sigma > 1$). However, this tendency may be declining as we resolve further towards the center (the other possibility is effects from the hot component). The temperature profile shows much greater variation and is less compatible with an isothermal model, even after spherical averaging. The temperature and σ profiles are in agreement with the factors $f_T = 1.3$ and $f_\sigma = 1.1$ – 1.2 derived earlier.

6.5 Conclusion

In this chapter, we have shown that X-ray clusters produced in Eulerian simulations agree well with the scaling relations involving mass, temperature and the collisionless velocity dispersion. The luminosity behaviour is more affected by resolution but can be simply and accurately modelled, although we cannot show that the adopted normalization — equation (6.8) — is correct. We also demonstrate that the isothermal profile assumed in computing the normalization of the scaling relation between M_{vir} and σ is a reasonable approximation for the dark matter (although there may be some evidence for $f_\sigma \neq 1$, it is not strong). However, the hydrostatic, isothermal assumption is not as good for the gas, which the simulations find to have systematically lower temperatures than T_{vir} (i.e. $f_T \sim 1.3$). This result seems stable to changes in resolution (for $r_{vir}/\Delta x = 1$ – 15). The addition of another length scale in the CHDM model (the neutrino free-streaming length), does not affect this results in any substantial way.

We stress here the difference between f_T , f_σ and β . The first two adjust the scaling relation normalizations of the simulations as compared to the hydrostatic isothermal sphere assumption, while β is the ratio of the mass-weighted average collisionless ‘temperature’ to luminosity-weighted gas temperature, equation (6.5). In fact, since we have

assumed $\beta \equiv 1$ for the hydrostatic isothermal sphere, these three quantities are related through $\beta = f_T/f_\sigma^2$.

Based on these findings and the Press-Schechter prescription for computing the differential number density of virialized halos, we compute the temperature distributions functions which are in good agreement with those derived from the numerical simulations (over their range of validity) and allow us to extend the range of the simulations. These show that the predicted number density of mid and high-temperature clusters is too large for the COBE normalized CDM, but approximately correct for the CHDM512 model (Figure 6.14). [Although our adopted linear power-spectrum assumes a single neutrino and adding a second would change the number-density of high- T clusters.] This result differs somewhat from Ma (1996) due to the smaller value of σ_8 which is in turn due to the addition of a second neutrino. Otherwise, for the same Q_{rms-PS} we would have to increase σ_8 by 10% (Stompor, Gorski & Banday 1995).

Analytic luminosity functions computed with the effects of finite resolution (Figure 6.15) agree well with the simulations and allow us to gauge the effects of resolution as a function of luminosity and redshift. An extension which accounts for metallicity and limited bandpasses, equation (6.19), can be used to compare directly against observational data (Figure 6.17). Although the resolution limited CHDM512 X-ray luminosity function comes close to agreeing with the observations, the corrected luminosity function produces substantially too many low-luminosity clusters. Reducing the baryon fraction will result in too few high-luminosity clusters (indeed, the highest-luminosity point is already slightly low). However, the observational luminosity-temperature relation does not agree with the scaling relations, which implies that we need to include additional physics. Feedback from galaxy formation may increase the core radius of small clusters and decrease their luminosity (c.f. NFW and Metzler & Evrard 1994). Finally, we note two other observational disadvantages to this model. The Hubble constant ($h = 0.5$) is lower than most, but not all, recent determinations (Mould et al. 1995; Ruiz-Lapuente 1996); increasing h substantially requires introducing a tilted spectrum. The second is the low cluster baryon fraction as compared to observations (White et al. 1993; White

1995). We find, in agreement with others, that neither the addition of a hot component (Kofman et al. 1995), nor observational bias (Evrard, Metzler & Navarro 1996) is sufficient to reconcile this discrepancy. The ability of this model to match the number of damped Lyman- α clouds at high redshift is unresolved (Ma & Bertschinger 1994; Klypin et al. 1994).

Chapter 7

The Formation and Structure of Cluster X-Ray Halos

7.1 Introduction

There has been much recent progress towards understanding the formation and evolution of dark matter halos in hierarchical structure formation models. This includes high-resolution N-body simulations of the Cold Dark Matter model (Navarro, Frenk & White 1996) and scale-free power spectra (Cole & Lacey 1996) as well as analytic or semi-analytic expressions which give estimates of the distribution of halos (Press & Schechter 1974; Bardeen et al. 1986; Bond & Myers 1996), their correlations (Mo, Jing & White 1996), and their formation rates (Lacey & Cole 1993; Kitayama & Suto 1996). There has also been work examining elements of the formation of the baryonic component of cluster halos (Evrard 1990; Thomas & Couchman 1992; Schindler & Müller 1993; Navarro, Frenk & White 1994; Anninos & Norman 1996 and others).

In this chapter, we examine the formation of a small number of X-ray clusters at fairly high resolution, with an emphasis on the temperature structure of the cluster and the presence and effect of shocks on the intracluster medium. This chapter is laid out as follows. In section 7.2, we describe the numerical simulations which provide our sample of clusters. In section 7.3 we present the azimuthally-averaged radial profiles of various

quantities. The next section (7.4) is a detailed examination of the three-dimensional structure of a cluster, while section 7.5 addresses the observational signatures of our simulated clusters.

7.2 Simulations

The cluster sample is drawn from two simulations performed with the same Eulerian hydrodynamics code, described in chapter 3 (Bryan et al. 1995). We will focus primarily on the three largest clusters from a flat, cold dark matter (CDM) simulation with $\Omega_{cdm} = 0.94$, $\Omega_{baryon} = 0.06$ in a box $25 h^{-1}$ Mpc on a side, with 512^3 cells and 256^3 particles. This simulation is not normalized to COBE (which would produce too many high-temperature clusters, see chapter 3, Bryan et al. 1994a), but adopts $\sigma_8 = 0.63$, where σ_8 is the present *rms* density fluctuations in a sphere of radius $8h^{-1}$ Mpc. The Hubble constant is given in terms of $100h$ km/s/Mpc and we adopt $h = 0.5$ throughout. The initial conditions are exactly the same as described in Anninos & Norman (1996), however they are evolved with a different hydrodynamics algorithm. We have performed a comparison between these results, and although we will not describe it here, the two codes produce similar results. As a caution, it should be noted that three clusters of the mass we find at $z = 0$ in a box of this size must be regarded as unusual; these objects may be more typical of clusters found in a supercluster rather than isolated clusters. This simulation will be referred to as CDM512.

The second set of clusters are much more poorly resolved and come from a cold plus hot dark matter (CHDM) model. The parameters are $\Omega_{cold} = 0.725$, $\Omega_{hot} = 0.2$, $\Omega_{baryon} = 0.075$ with two neutrinos of 2.3 keV each. The computational volume was $(50 h^{-1} \text{ Mpc})^3$ and used 512^3 cells with 256^3 cold and 2×256^3 hot particles. This simulation will be referred to as CHDM512, in keeping with the notation of the previous chapter.

In order to generalize and compare the discussion of these clusters, we will normalize the various physical quantities in terms of their ‘virial’ values, defined in the previous chapter. To convert to physical units (and to give an idea of the cluster properties),

Table 7.1. Cluster parameters

cluster	r_{vir} (Mpc)	M_{vir} ($10^{15} M_{\odot}$)	T_{vir} (keV)	σ_{vir} (km/s)
CDM1	2.58	0.890	4.63	861
CDM2	2.32	0.647	3.74	774
CDM3	2.40	0.716	4.00	801
CHDM1	2.81	1.15	5.49	938
CHDM2	2.79	1.13	5.41	933
CHDM3	2.45	0.76	4.17	817
CHDM4	2.06	0.45	2.95	686
CHDM5	2.02	0.43	2.83	676

Table 7.1 lists our adopted values of virial radius, mass, temperature and one-dimensional velocity dispersion. Clusters were found with the iterated spherical overdensity scheme described by Cole & Lacey (1996) with an overdensity of 178.

In the interests of simplicity, we do not include radiative cooling; this may be a reasonable assumption in the hot halos of large clusters as the cooling time is longer than the Hubble time. Nor do we include the effects of galactic/stellar feedback, magnetic fields or heat conduction. The gravitational softening length is very approximately 2 cells (about 200 kpc in CDM512, 400 kpc in CHDM512).

7.3 Radial profiles

In Figure 7.1 we show profiles of baryonic and dark matter density at $z = 0$ for the clusters listed in Table 7.1, normalized by their appropriate virial values. The cluster center is found by adopting the center of the cell with the highest gas density within $r_{vir}/2$ of the original center found through the iterated spherical overdensity method. This procedure does a good job of finding the center of the largest mass clump. The innermost point plotted is two cell widths from the cluster center. The CHDM512 density profiles have been adjusted by the ratio of the cold dark matter and baryonic densities in the two models to facilitate comparison.

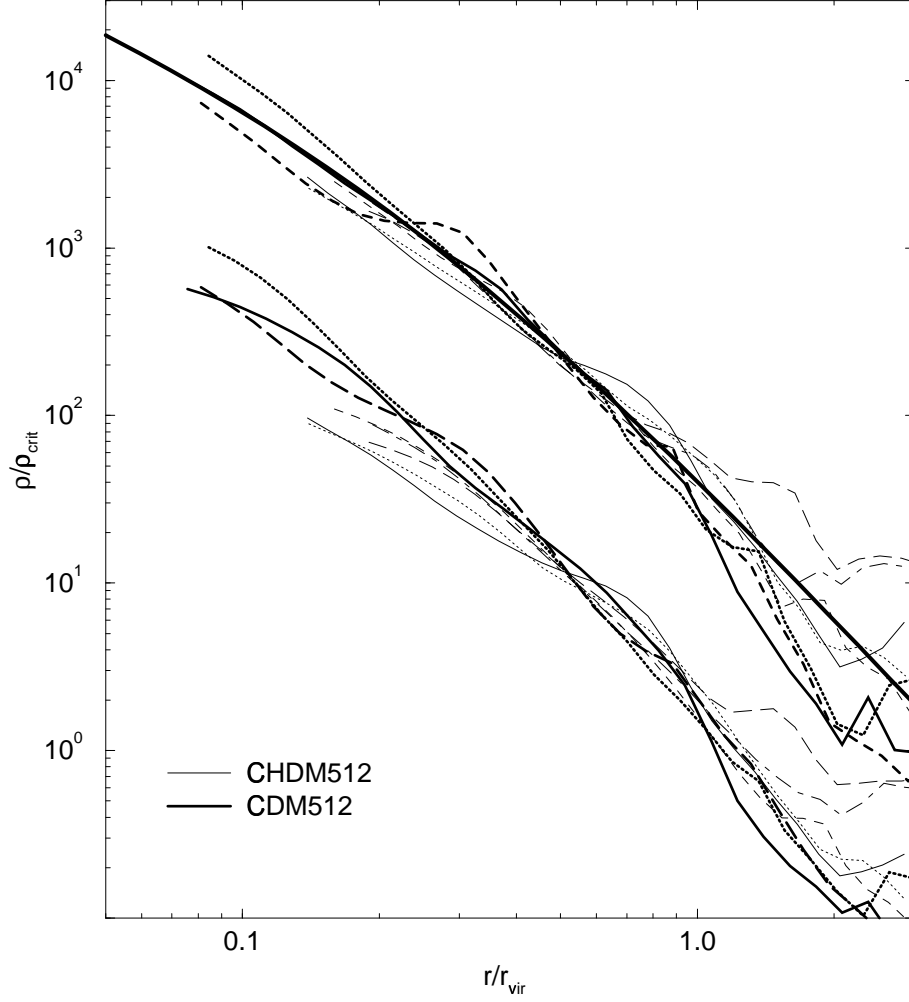


Figure 7.1. The cold dark matter (top set of curves) and baryon density azimuthally-averaged profiles for the three CHM512 clusters (bold lines) and the five CDM512 clusters (thin lines). Density is in units of the critical density, while radii are normalized by the cluster virial radius (see Table 7.1). The smooth, thick curve is a fit from equation 7.1 (see text for details).

We also plot the dark matter profile from Navarro et al. (1996),

$$\frac{\rho(r)}{\rho_{crit}} = \frac{\delta_0}{(r/r_s)(1 + r/r_s)^2}, \quad (7.1)$$

where $r_s = r_{vir}/c$ (c is a free parameter). The coefficient δ_0 is set by the requirement that the mean density within the virial radius be 178 times the critical density (this is how we define the virial density and mass). In the figure, this has been scaled by the appropriate cold fraction. We adopt $c = 5$ based on results from Cole & Lacey (1996) who show that for a spectral index of $n = -2$, a value of 4-5 is appropriate regardless of cluster mass. The fits are largely in agreement with our clusters, although we note two discrepancies. The CDM clusters show signs of a steeper profile beyond the virial radius, however this may be due to their relatively close proximity to each other. The CHDM clusters are also a little low at $r_{vir} \sim 0.2$; this is most likely due to the hot component.

As has been noted by others, the hot particles (neutrinos) avoid the central part of clusters because of their higher velocity dispersion. In Figure 7.2, we plot the ratio of the hot component to the total density as a function of radius. At large radii, the profiles assume their asymptotic value of 0.2, but are significantly suppressed below $r \sim 0.5r_{vir}$, in agreement with Kofman et al. (1995).

The azimuthally-averaged temperature profiles shown in Figure 7.3 are compatible between the CDM and CHDM models and show a very slowly falling profile from the resolution limit to about $0.7r_{vir}$, a somewhat steeper slope ($r^{-0.5}$) to about two times the virial radius and then a very sharp fall off beyond that. This is compatible with the single cluster of Anninos & Norman (1996). The first two stages of this profile are also in reasonable agreement with NFW's six clusters, but they do not show the sharp decline beyond the virial radius exhibited here. A similar statement can be made of the cluster presented by Katz & White (1993). The cluster simulated by Evrard (1990) shows a falling temperature profile in the center — not seen here — but is otherwise much the same. We also plot the temperature profile resulting from the self-similar infall solution derived by Bertschinger (1985). The radial position of the dimensionless profile is fixed

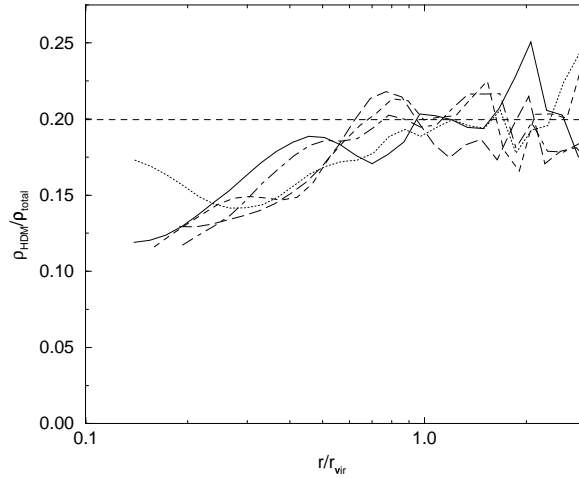


Figure 7.2. The ratio of hot to total density as a function of virial radius for the five largest clusters in the CHDM simulation.

by the turnaround velocity which is approximately $4r_{\text{vir}}$; the vertical normalization is arbitrary.

The one-dimensional velocity dispersion profile is flatter than the temperature, although σ^2 and T have similar slopes. The hot component in the CHDM clusters (we plot only the cold particles in Figure 7.3) follows almost exactly the same profile at large r , but is systematically higher at low radii.

In Figure 7.4, we plot the total velocity dispersion, radial component of the velocity dispersion and the radial velocity for both the dark matter and gas components of the three CDM clusters. They are normalized by the virial values from Table 7.1 and all velocities are relative to the center-of-mass velocity of the matter within r_{vir} . The dispersion in the radial direction is around the net radial velocity of that shell: $\sigma_r^2 = \langle (v_r - \langle v_r \rangle)^2 \rangle$.

Focusing first on the dark matter, the velocity dispersion profiles are roughly compatible with their virial values within the virial radius, but fall off quickly beyond that point. There is some preference for radial orbits around and slightly beyond r_{vir} , but at low radii, the velocities are isotropic. The radial velocity profile (bottom panel) shows evidence for infall in the $1-4r_{\text{vir}}$ range. These results are in agreement with higher-resolution N-body

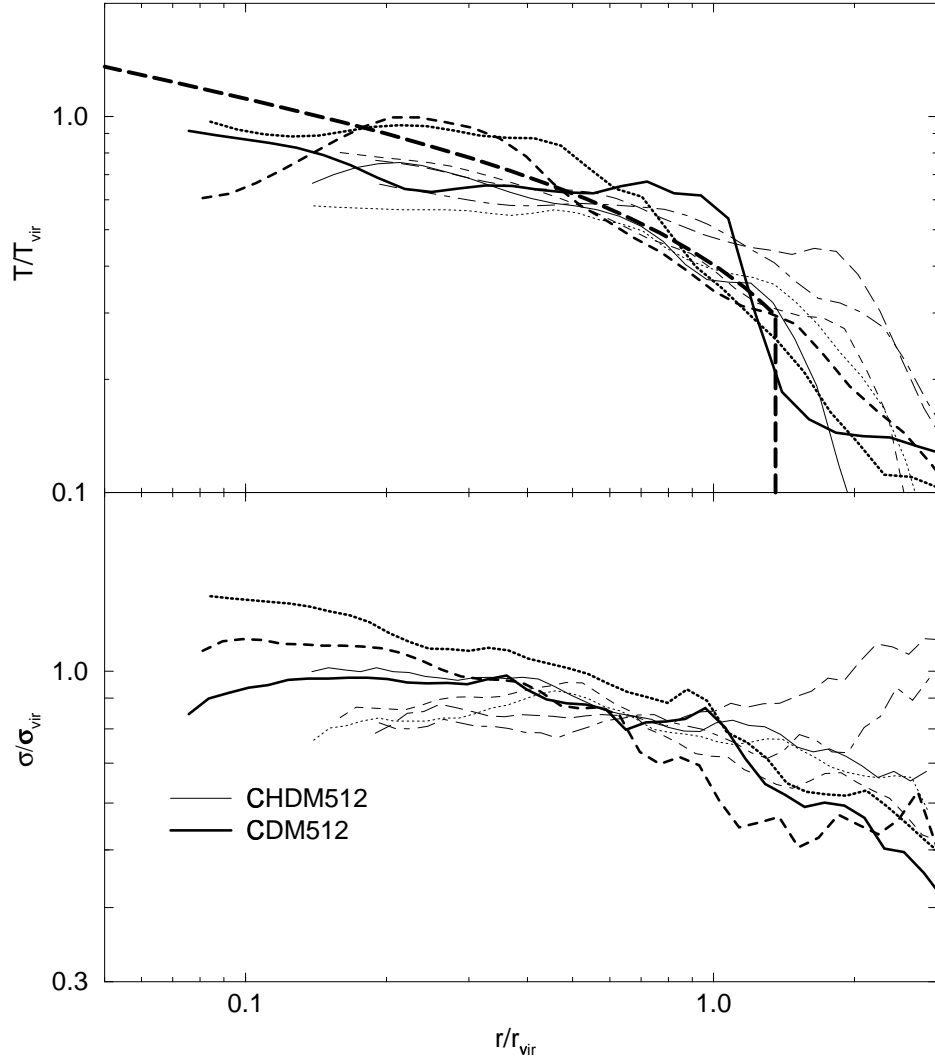


Figure 7.3. Temperature and dark matter one-dimensional velocity dispersion profiles for the same clusters as in Figure 7.1. All quantities are shown as fractions of their respective virial values. The thick, long-dashed line in the top panel is the self-similar infall solution from Bertschinger (1985).

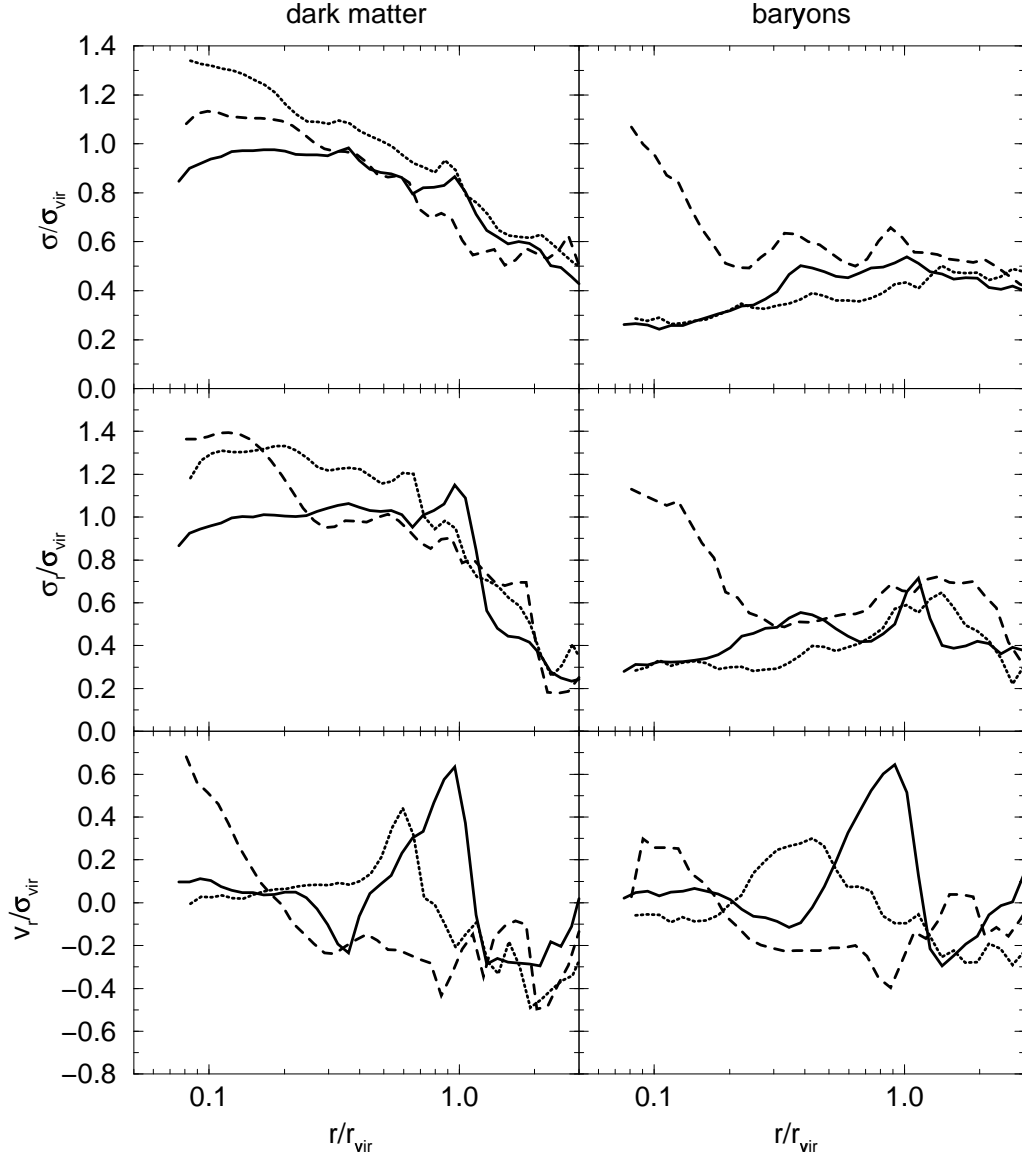


Figure 7.4. The velocity dispersion (top panels), radial velocity dispersion (middle panels) and radial velocity in shells for the dark matter (left side) and gas (right side) of the three largest clusters in the CDM512 simulation (solid/dotted/dashed lines correspond to clusters designed as CDM1/CDM2/CDM3). Profiles are normalized by their virial values (see text).

results from Cole & Lacey (1996) as well as Crone, Evrard & Richstone (1994) and others. The third cluster in this sample (dashed line) is undergoing a major merger and shows signs of enhanced bulk motions in the inner 400 kpc, although the velocity-dispersion profiles are not strongly disturbed.

The gas velocity dispersions range between 0.3 and 0.6 σ_{vir} , considerably below their dark matter counterparts, but are not insignificant. In fact, these motions contribute some additional support beyond that provided by the mean baryonic pressure gradient. We may approximate this by applying Jean’s equation to the coherent clumps of gas with velocity dispersion σ and density ρ_c . Ignoring differences between the radial and tangential velocity dispersion this becomes:

$$\frac{1}{\rho_c} \frac{d(\rho_c \sigma^2)}{dr} + \frac{1}{\rho} \frac{dP}{dr} = -\frac{GM(r)}{r^2}. \quad (7.2)$$

Since $P = \rho kT / \mu m_h$, where μm_h is mean mass per particle, we see that the temperature and σ^2 combine to support the cluster gas against gravitational collapse. We can directly compare T/T_{vir} against σ^2/σ_{vir}^2 , so the temperature provides about 75% of the support. This provides an explanation for the observation made in chapter 6 that the observed cluster temperature was about $1/f_T \sim 0.75$ below its virial value, which is also seen in Figure 7.3.

Thus we see that the gas has not completely virialized and sizable bulk motions exist. Since the mean entropy profile increases with increasing radius, the halo is globally stable, so this turbulence must be driven by external masses falling into the cluster and damped by viscous heating. The turbulence amplitude appears to be roughly compatible with this explanation since the driving timescale — approximately the Hubble time — is slightly larger than the damping timescale which is essentially the crossing time. Moreover, σ^2 seems to drop (and T approaches T_{vir}) as $r \rightarrow 0$ and the crossing time decreases.

Baryonic radial orbits appear to be slightly preferred over tangential orbits between 0.1 and 1 r_{vir} . Beyond the virial radius, the gas and dark matter profiles (for all quantities) are very similar. The large increase in σ_r and σ of the third cluster’s baryonic component near $r \sim 0.1 r_{vir}$ is a signature of the same ongoing merger noted previously.

Since the temperature is a product of the conversion of the bulk velocity of infalling material into thermal energy, the suggestion has been made that within clusters there may be a spatial correlation between the dark matter velocity dispersion and the gas temperature. We explore this possibility by examining mean quantities within evenly small, spaced spherical samples placed inside the virial radius of cluster CDM1. Two sets of samples were taken with radii of 300 and 600 kpc. The top panel of Figure 7.5 shows that there is no correlation between the mean temperature and *rms* dark matter velocity dispersion, a result which is not surprising given the chaotic nature of the velocity flow within the cluster. We also plot the relation $\beta = \mu m_h \sigma^2 / kT = 1$.

As the bottom panel illustrates, a better relation exists between the mean dark matter density within the sphere and the temperature, although there is a great deal of scatter. Also shown (as a solid line) is the relation formed by plotting the radial temperature profile against the radial velocity-dispersion profile (from Figures 7.1 and 7.3). The difference is due to disparate sampling shapes: the shells of the radial profile average over many coherent states which tends to reduce the fluctuations in temperature, while the spheres sample a more compact region, but average over a significant density profile. The dashed line in this figure shows a locus of constant entropy.

7.4 Cluster structure

7.4.1 Projected images

We now make a closer look at the formation process and resulting structure of clusters. In Figures 7.6 to 7.7, we show projections of the dark matter density, baryonic density and luminosity-weighted temperature of the three CDM512 clusters as a function of redshift (temperature and luminosity maps for CHDM clusters 1-4 are also shown in Figure 7.16). The surface density images clearly show the hierarchical formation process for these clusters, with two to five significant sub-clusters at $z = 1$ coalescing by the

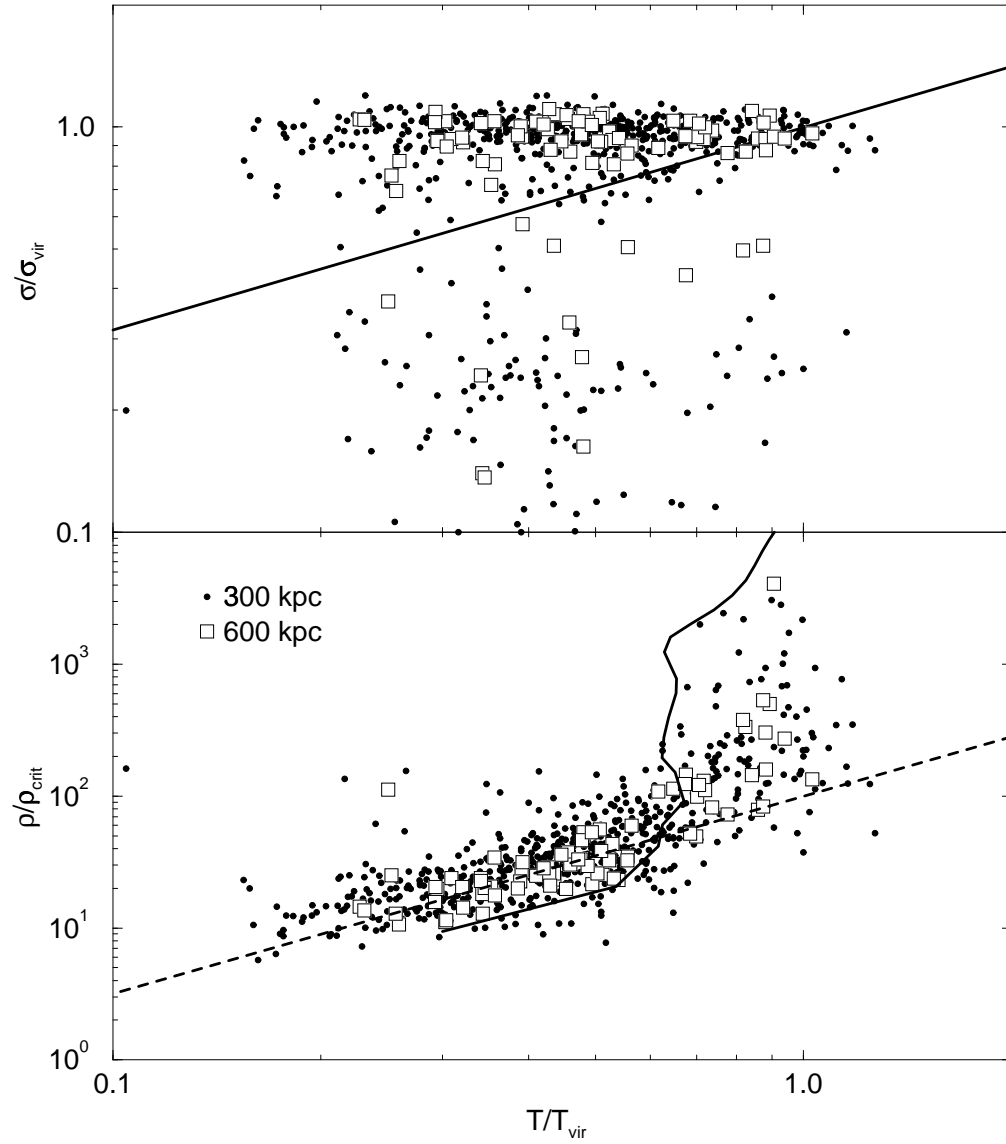


Figure 7.5. Gas temperature – dark matter velocity dispersion scatter plot (top panel) for cluster CDM1 with sample radii of 300 and 600 kpc. The bottom panel shows the relation between the mean dark matter density and temperature of the same samples. See text for the meaning of the various lines. Temperature and velocity dispersion are normalized by their virial values while the density is in units of the critical density.

present day. However, they also show the large number of even smaller clumps that rain into the cluster throughout its life.

The dark matter ellipticities vary greatly between objects and are not always good signatures of a recent merger. For example cluster CDM2 is mostly in place by $z = 0.5$ but forms primarily along a filament, causing a 2:1 elongation along the filament axis that exists to $z = 0$. The gas halo is much more nearly spherical due to its isotropic pressure tensor.

The cluster temperature distributions show an even richer set of morphologies. Each cluster at $z = 0$ is surrounded by a region of hot gas with temperatures between 0.5 and 1 of the virial value. These moderately non-spherical regions are approximately 2-4 Mpc in radius (very roughly r_{vir}) and are terminated by a clearly identified shock, which we denote as the primary cluster shock. These shocks, originating in large merger events, move outwards from the center at speeds of 300-500 km/s ($0.3-0.6 \sigma_{vir}$) and, like tree rings, provide historical evidence. For example, the two somewhat concentric halos of hotter gas visible in CDM2 arise from a pair of mergers at $z \sim 0.2$ and $z \sim 0.1$. Some of the stronger of these features can be seen in the radial velocity profiles of Figure 7.4. For example, the strong circular shock of cluster CDM1 is easily visible (solid line) as an outward moving shell at the virial radius in both the dark matter and gas. The radial temperature profile (Figure 7.3) and perhaps the density profile as well, shows a jump at this radius.

This feature is somewhat reminiscent of the one-dimensional self-similar secondary infall solution obtained by Bertschinger (1985) in which a shock in the gas and a discontinuity in the dark matter move outwards together. Here, though, the material in the shell is actually moving away from the cluster center (in the self-similar solution, gas, after being shock heated, moves slowly inward). This, however, is a transient effect and after material is processed through the shock, it turns around again and begins (on average) to fall back towards the cluster. In Figure 7.9, we show the density-weighted projection of the velocity field for this cluster (CDM1). The outflowing material in the outgoing shock dominates the flow field in the inner regions of the cluster. Beyond this,

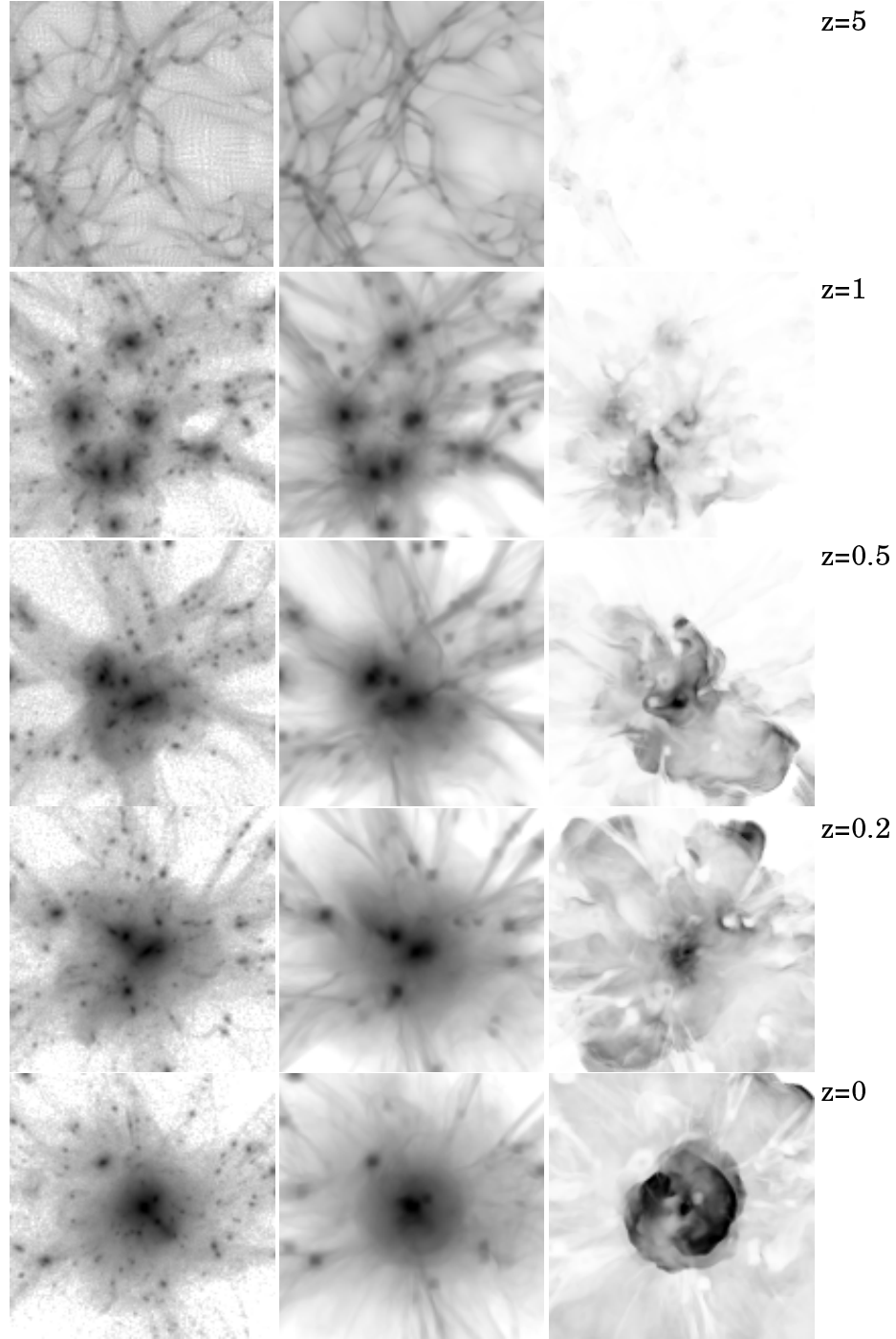


Figure 7.6. The projected dark matter (left panels), baryonic gas density (middle panels) and luminosity-weighted temperature (right panels) of cluster CDM1 as a function of redshift. The densities are normalized by the critical density and are shown as a logarithmic spread of 3.7 decades in surface density (constant in redshift). Temperature is normalized by the $z = 0$ virial value. The images are 12.8 Mpc on a side (including the projected dimension) and are centered on the $z = 0$ cluster position.

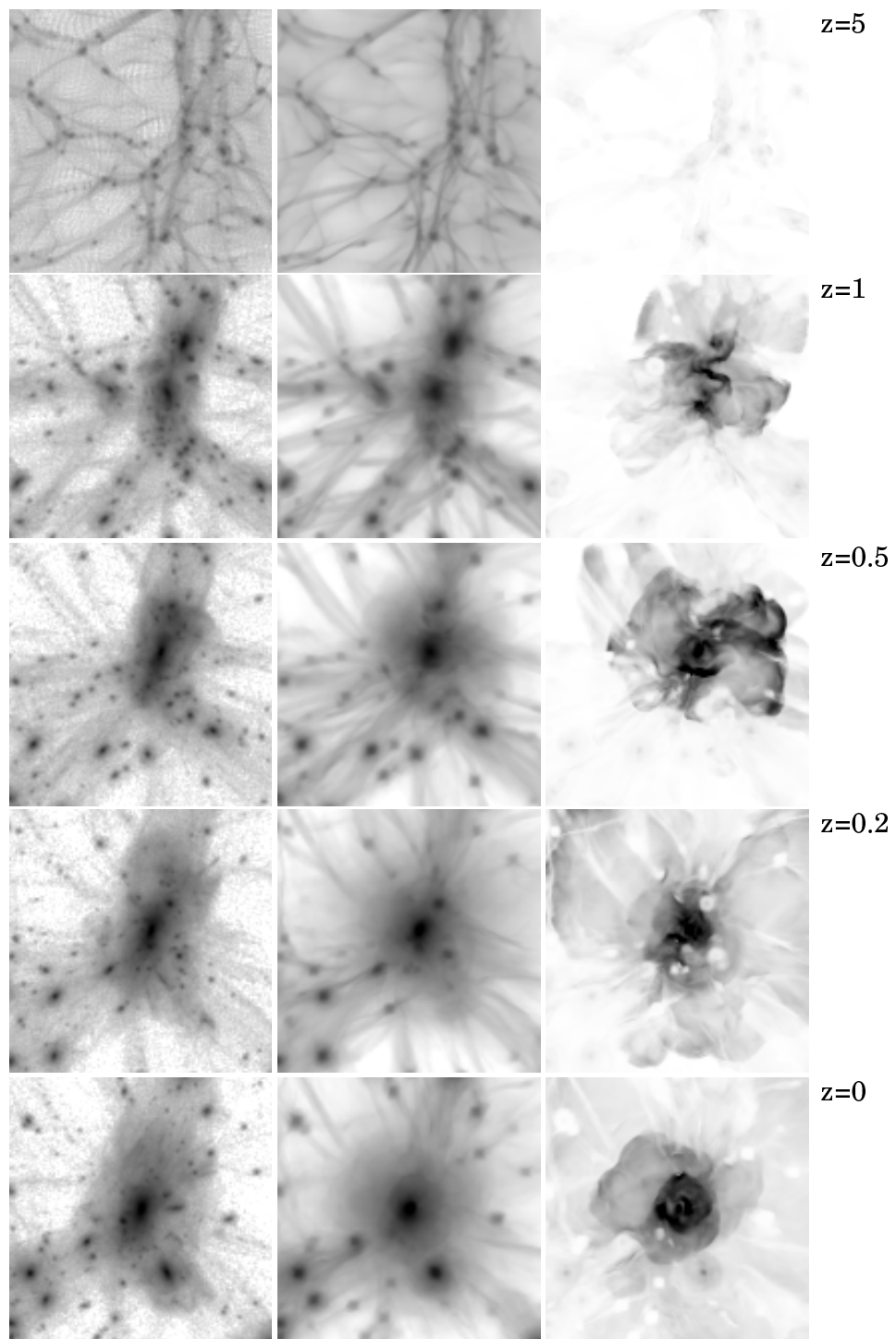


Figure 7.7. As in the previous figure, but for cluster CDM2.

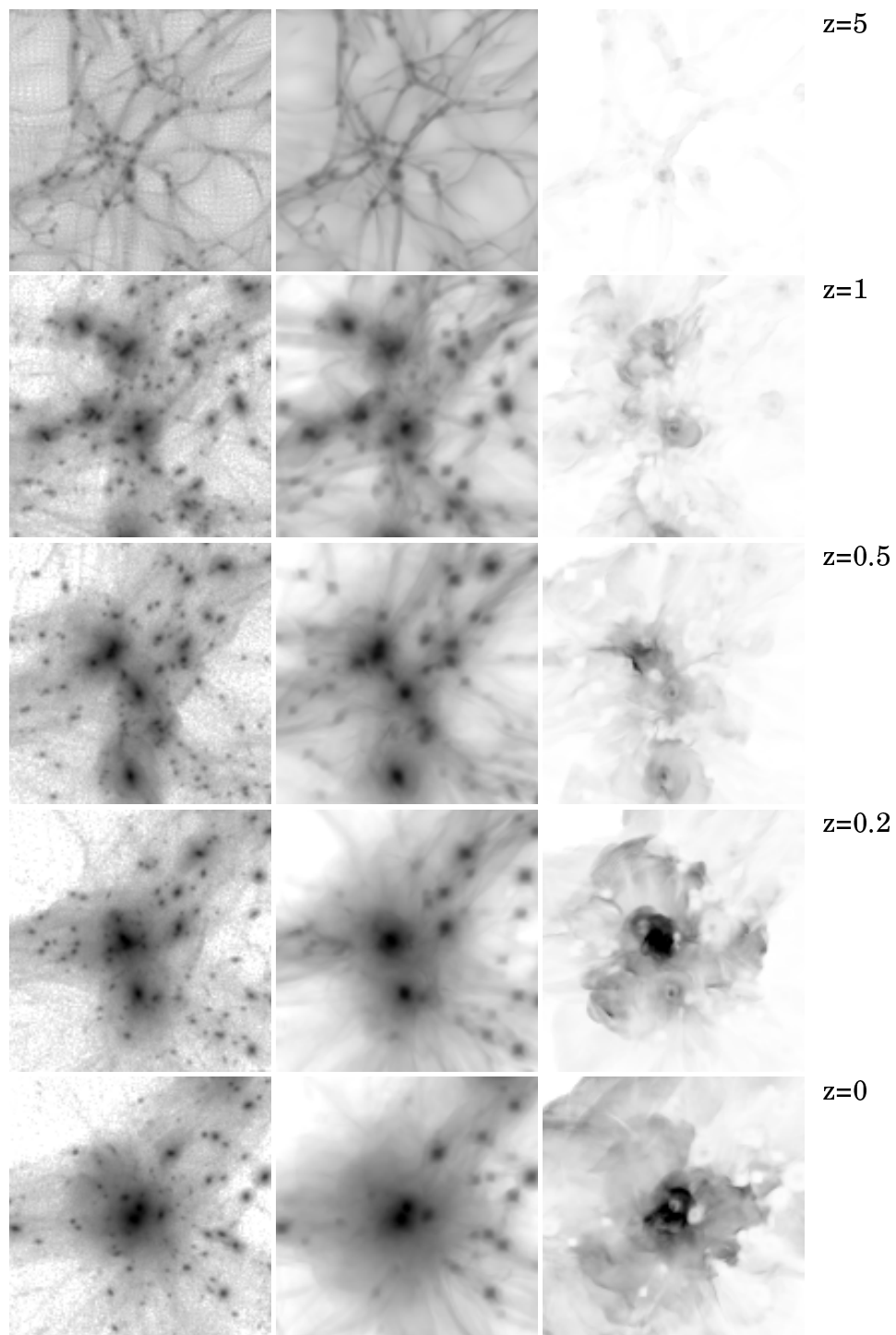


Figure 7.8. As in the previous figure, but for cluster CDM3.

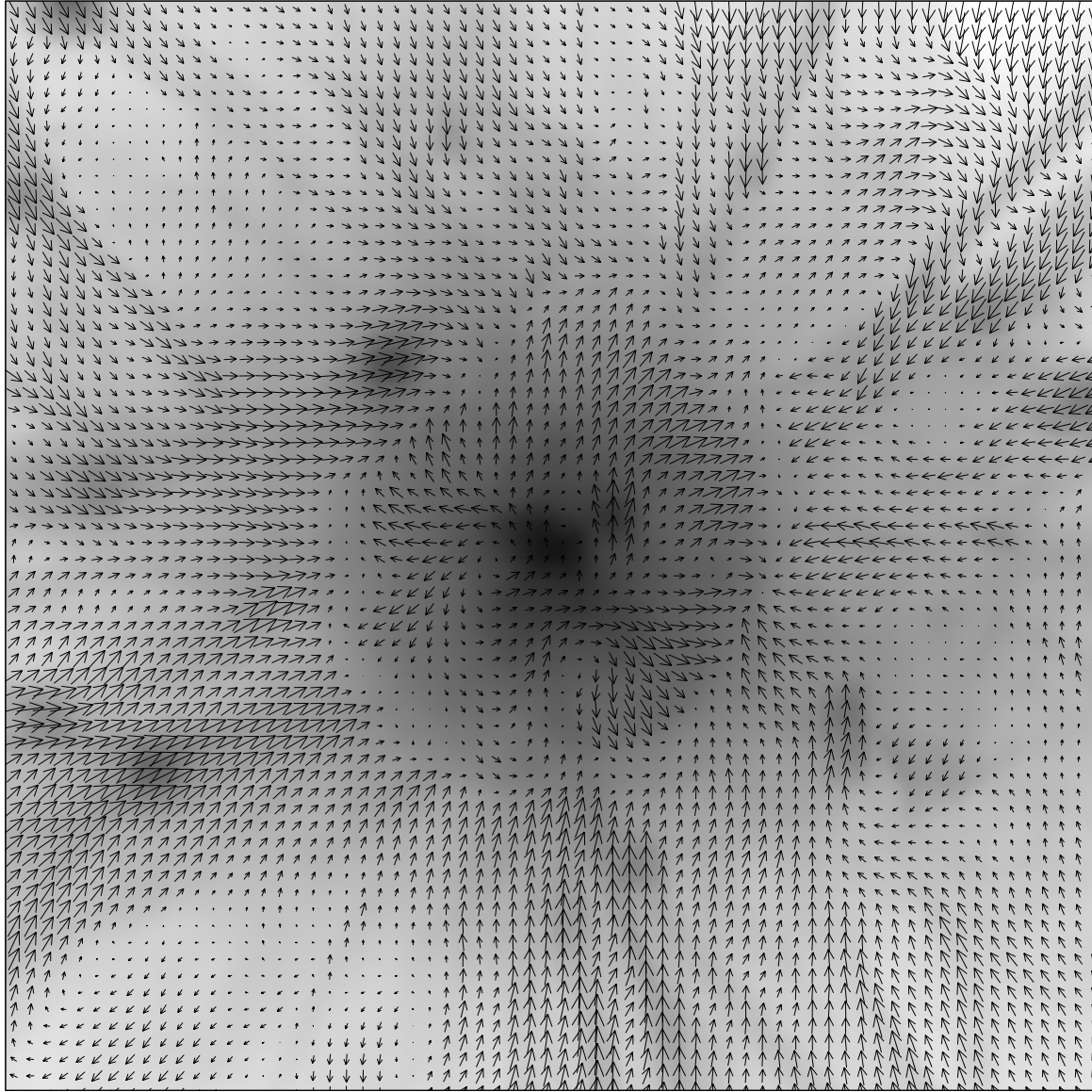
clumps of gas are falling in, as are long, slender filaments clearly visible in the velocity field. From this image, the flow appear to be quite orderly, at odds with our earlier findings of a turbulent baryon component. However, the projection averages the velocity field along a line-of-sight through the cluster, and so any random, small scale features would be suppressed. For the same reason, the velocities tend to also be fairly low, the largest shown is 793 km/s compared to a sound speed of 1040 km/s for gas with a temperature of 4 keV.

As they move down the steep density inclines, the shocks can occasionally increase in temperature and the very hottest gas in the cluster is often found far from the center, at the shock termination in low density regions (although, of course, on average the temperature falls with radius).

Although the hottest cluster gas is confined to the virial radius and within, there is an even larger envelope of cooler, but still very hot material (0.4-2 keV; $0.1-0.5 T_{vir}$), extending up to 10 Mpc ($4r_{vir}$) from the cluster center. This hot gas has been produced by the passage of many secondary shocks originating in the formation of the components that merged to become the main cluster. They encompass a large volume due to their early formation time coupled with their still large velocities ($v_{shock} \propto M^{1/3}$). Also, each subcomponent of the main cluster produces a secondary shock, so they tend to trace out the entire region from which the cluster formed (the Lagrangian volume).

With this understanding of the shock structure, we can reinterpret the temperature profiles in Figure 7.3. The central plateau out to a radius of about $0.7r_{vir}$ represents the volume heated by the primary shock, from $0.7-1.0r_{vir}$ is a transition (since the shock is aspherical) to the region heated by the secondary shocks which lasts until about 2-4 virial radii, beyond which lies much colder gas. Of course, this is only schematic as the clusters are in different stages of shock development.

At higher redshifts, this temperature structure is repeated on a smaller (and less well resolved) scale as each subcluster is surrounded by its own set of primary and secondary shocks. However, occasionally, rarer features can be observed, such as the straight shock between two colliding clusters at $z = 1$ in cluster CDM1.



$\rightarrow = 793$

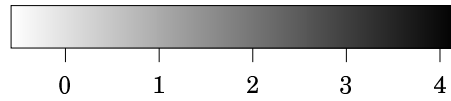


Figure 7.9. The density-weighted projected velocity map of cluster CDM1 superimposed on the logarithm of the baryon surface density (in units of the critical density). The maximum velocity shown in 793 km/s.

The filamentary nature of the $z = 5$ images is somewhat exaggerated by the lower than necessary spectral cutoff in the input power spectrum ($k_{cutoff} = k_{nyquist}/4$, where $k_{nyquist}$ is the wavenumber of the smallest wavelength that can be represented on the grid). It also shows that the effective dark matter resolution in this code is better than that of the gas: the collisionless clumps are smaller and tighter. Nevertheless, the good correspondence between the numbers and positions of collapsed objects in the two components at this early time shows that, without exterior influences, ‘light’ follows mass. However, by $z = 0$, some dark matter clumps do not appear to have corresponding gas halos, especially near the cluster cores.

These objects are extreme cases, but, most, if not all, nearby subclusters show some influence. In Figure 7.10, we plot the virial masses and luminosity-weighted temperatures of the objects clearly associated with one of the large filaments that span the computational volume (in fact this includes all objects with $kT > 0.8$ keV since the filaments are so large and the box relatively small). Also shown are clusters from the CHDM512 simulation (which has a larger physical volume and is much less dominated by a small number of large objects), as well as the scaling relation found in chapter 6. The six or seven largest CDM512 clusters follow the previous results well, however, the smaller objects show a significantly higher temperature than their virial masses would imply. We argue that is due to the pressure confinement, and possibly shock heating, from the surrounding hot gas. Although they have been heated, they are not raised to the virial temperature of the main cluster, as the luminosity-weighted temperature images show pockets of cool gas at sub-cluster locations.

To emphasize that the dark matter is relatively unaffected, Figure 7.11 shows the σ - M relation for the same objects. This exhibits much better agreement and although the velocity dispersion is still somewhat higher than the CHDM512 clusters with the same mass, this is likely to be caused by the better resolution of the CDM512 simulation (chapter 6 shows that the velocity dispersion increases slightly with resolving power).

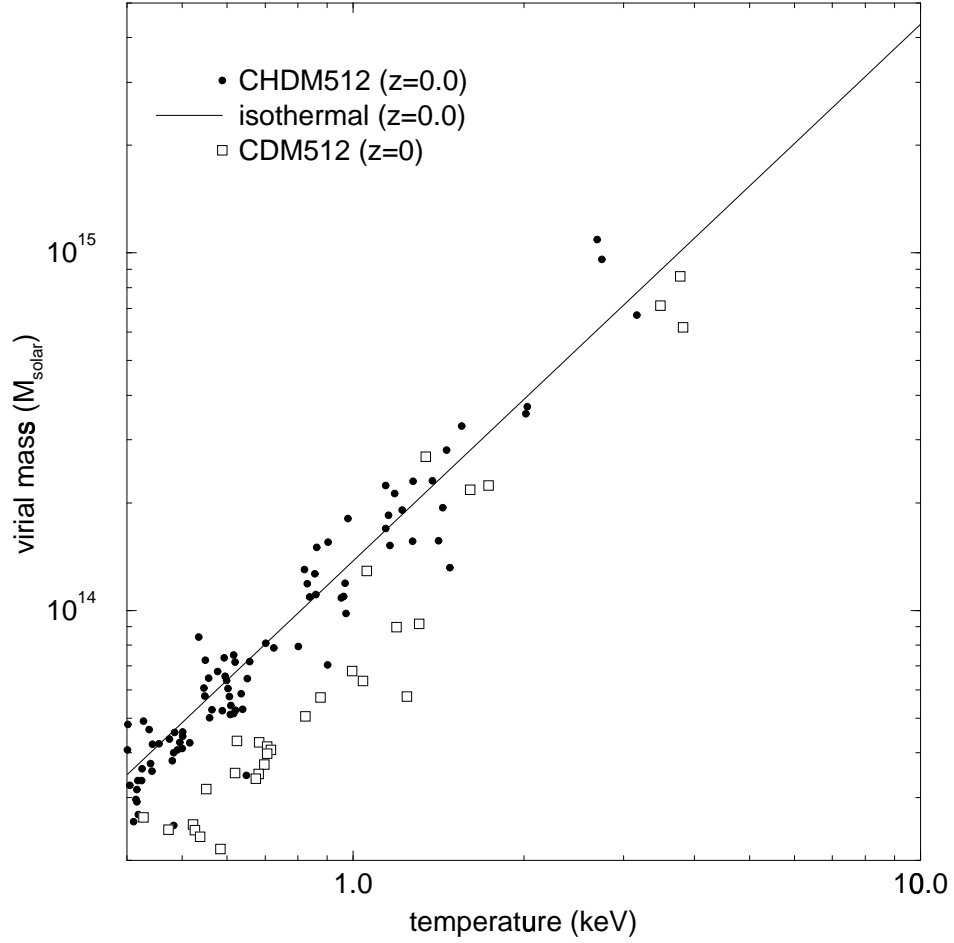


Figure 7.10. The virial mass and emissivity-weighted temperature of clusters associated with large filaments in the CDM512 simulation. Also shown are all clusters from the CHDM512 run and the scaling relation from chapter 6.

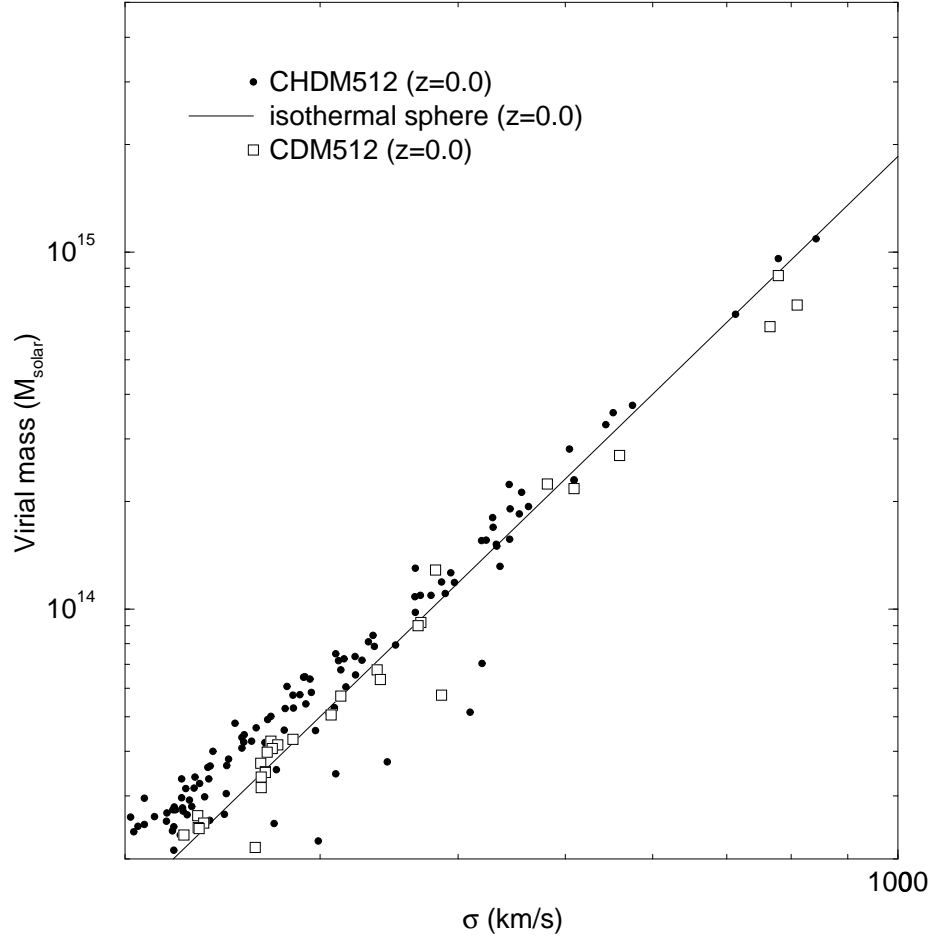


Figure 7.11. The virial mass and dark matter velocity-dispersion of clusters associated with large filaments in the CDM512 simulation. Also shown are all clusters from the CHDM512 run and the scaling relation from chapter 6.

7.4.2 Slices

While the projected cluster images presented in Figures 7.6 to 7.7 provide information about the whole cluster, they do not give a good indication of the local state of the gas. In order to show this in more detail, Figure 7.12 shows slices one cell thick (100 kpc) of several quantities extracted from the center of cluster CDM1.

The different visual impression between the dark matter and gas (which are shown in a large logarithmic stretch) is due largely to the different computation techniques used for each. The gas is represented by a fixed grid of cells, ensuring that the sampling is spatially fixed, while the collisionless particles have constant sampling in mass, leading to poor sampling in low density regions (and high sampling in high density regions). This is apparent to a lesser extent in the projected images as well.

The correspondence between dark matter and baryonic clumps is good in the outer regions (notably the two clumps in the lower left), but becomes worse in the higher pressure inner region. The strong shock discussed earlier for this cluster is visible in all the slices (except the dark matter density), but is particularly evident in the temperature and pressure. The temperature slice shows that while the the shock is roughly spherical, there is a wealth of small scale structure. This is mostly due to variations in the entropy of the gas, rather than being true sound waves, as the pressure and entropy images demonstrate. These arise from the different thermodynamic histories of the gas elements involved. The pressure slice also makes it clear that there are a large number of smaller shocks in the outer regions of the cluster.

A parcel of gas with lower (or higher) entropy than its surroundings may be in pressure equilibrium, but is unstable to small perturbations in its position. This means that a fully relaxed cluster would show a smoothly increasing entropy profile from the center to the exterior. The entropy slice shows evidence for this on a global scale but it is also clear that the cluster is not in complete equilibrium.

The lower entropy clumps and filaments (which are often physically associated) usually do not appear as features in the pressure slice, but drive flows of gas towards the

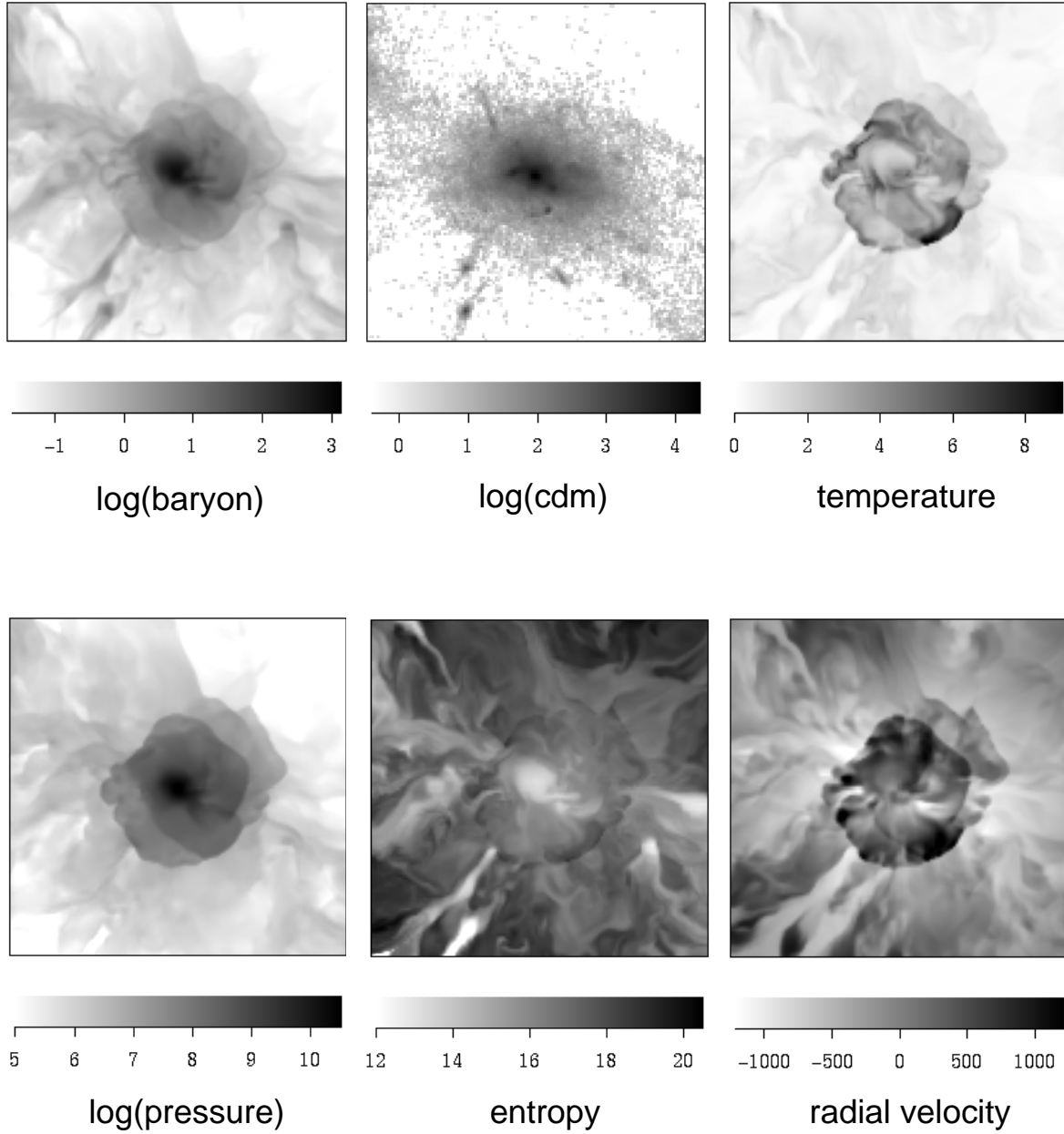


Figure 7.12. Slices (100 kpc thick) from the center of cluster CDM1. Shown are baryon and dark matter densities (in units of the critical density), temperature (in keV), pressure and entropy and the radial velocity (in km/s). The images are 12.8 Mpc on a side (including the projected dimension) and are centered on the $z = 0$ cluster position.

cluster center. These are visible in the slice showing the radial velocity of each cell (negative is infall) against the backdrop of the expanding shock. This is even more clearly evident in Figure 7.13, which shows the two-dimensional velocity field (subsamped by a factor of two in each dimension) for cluster CDM3. Here it becomes apparent that much of the mass infall consists of the low-entropy filaments, while between filaments, gas can actually move outwards. Also, the turbulent flows indicated by the one-dimensional velocity profiles from section 7.3 are visible and the field is more active than indicated by the projected velocity map. In this cluster, the very outer shock is visible in the lower and upper left corners. The undisturbed gas flow is quite uniform and impacts the shock with a range of angles. When the velocity is normal to the shock front, the gas is almost completely virialized, however, oblique impacts cause substantial vorticity in the post-shock gas. This is another source of turbulent motions in the cluster gas.

7.5 Comparison to Observations

In this section, we compare the simulated clusters to observational data, focusing primarily on the new temperature maps made available by the ASCA and ROSAT satellites (Markevitch et al. 1996; Markevitch 1996; Henriksen & Markevitch 1996; Markevitch & Vikhlinin 1996; Markevitch, Sarazin & Henriksen 1996; Markevitch, Sarazin & Irwin 1996). In Figure 7.14, we simulate the format of those observations (without including noise or instrumental limitations) by computing mean, luminosity-weighted temperatures within fixed regions near the center of the cluster. The effect of the binning procedure can be seen by comparing these images to the central region of the much higher resolution Figures 7.6–7.8. The four largest CHDM clusters are also displayed in this manner in Figure 7.15. In order to compare the fully resolved temperature (and luminosity) maps, these are shown in Figure 7.16, and include a larger volume to better set the context.

Most of the clusters discussed in the references listed above do not have cooling flows which places them amongst the minority of clusters observed. None of our simulated clusters have cooling flows either, however this is due to the lack of radiative cooling (nor

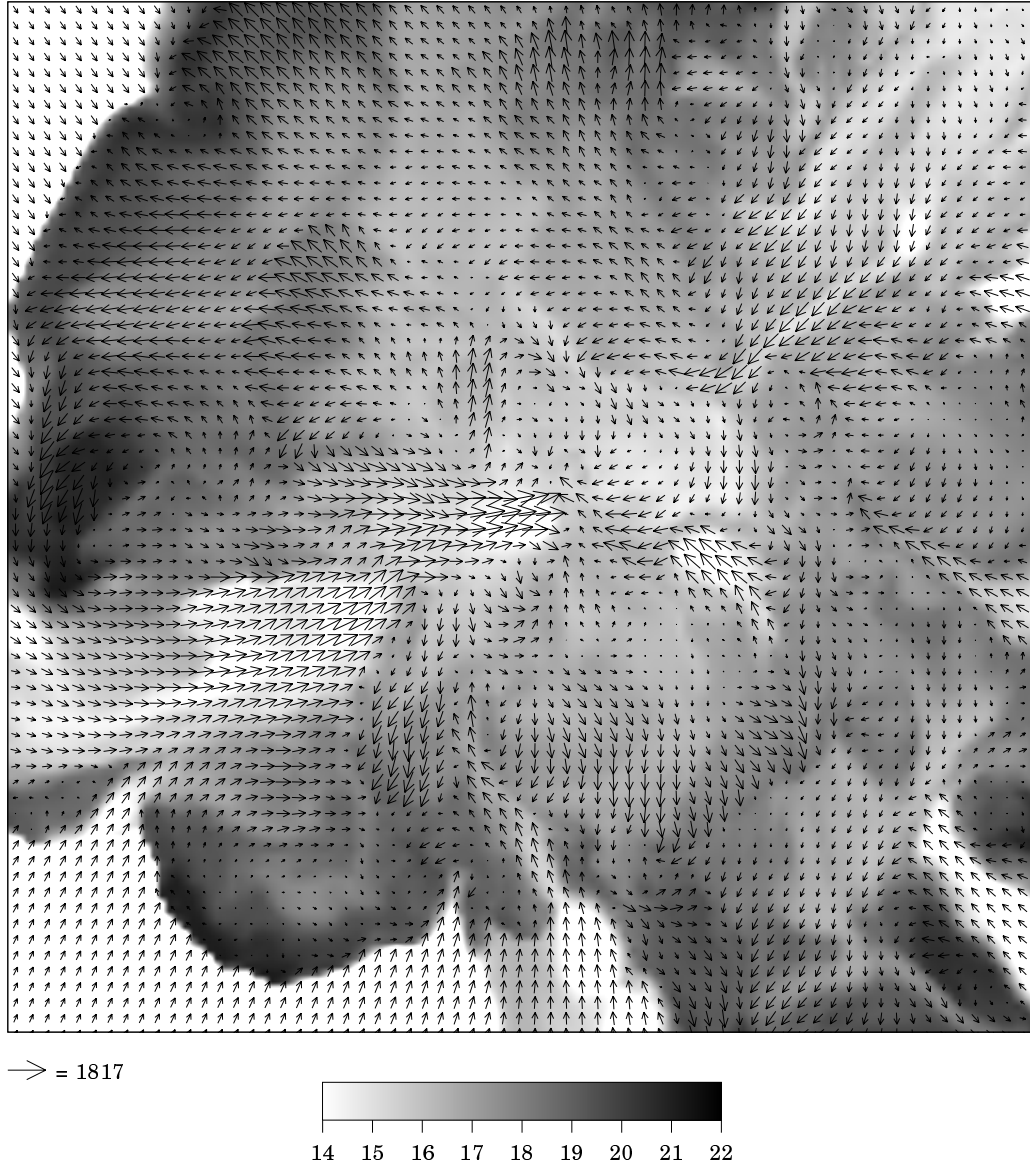


Figure 7.13. The velocity field of a slice one cell (100 kpc) thick from cluster CDM3 shown overtop the entropy field. The maximum velocity shown in 1817 km/s.

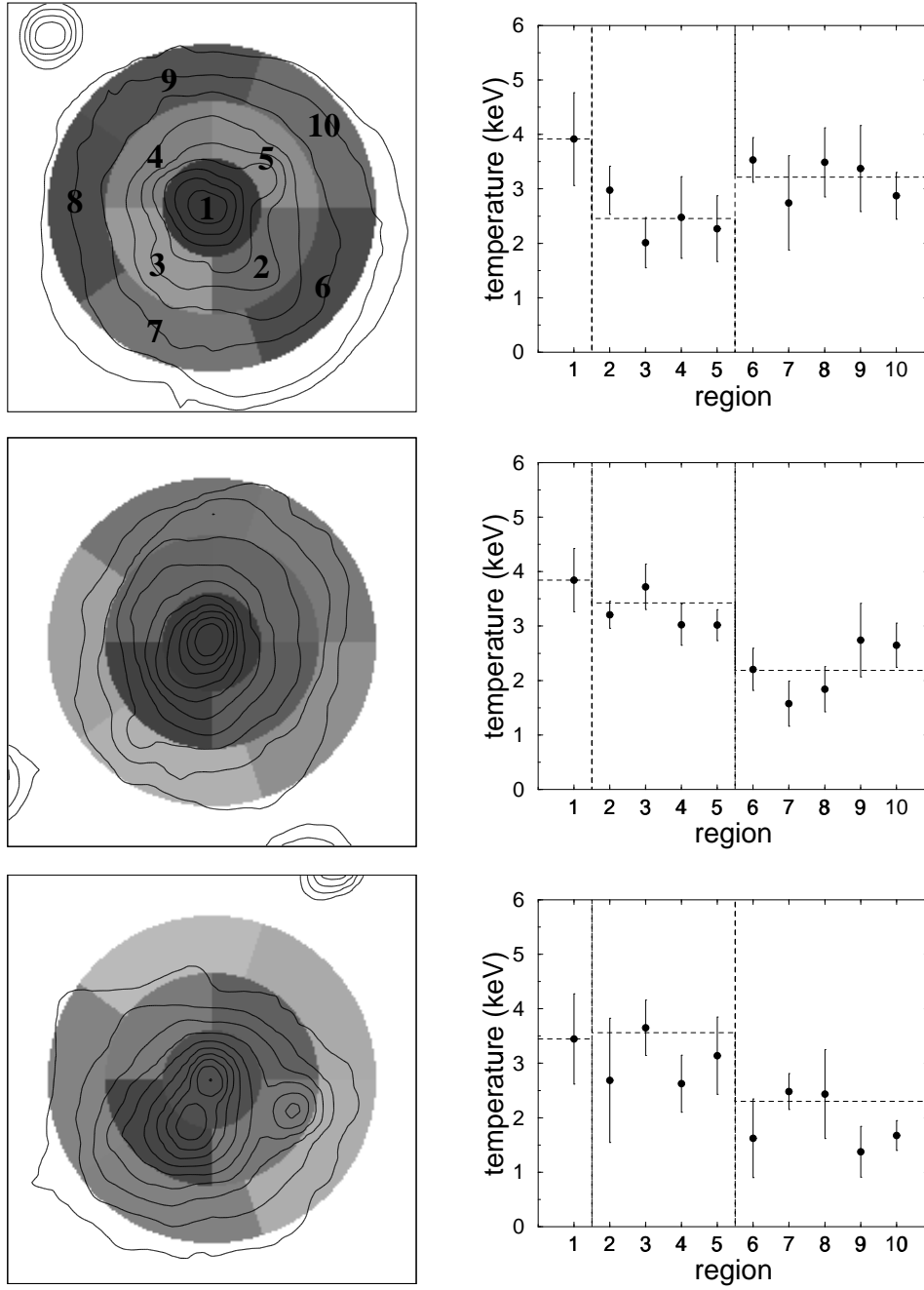


Figure 7.14. Simulated temperature maps of clusters CDM1, 2 and 3 (from top to bottom) with contours of bolometric free-free surface brightness overlaid. The images are 5 Mpc on a side. To the right, we plot the temperature of each labeled region along with the one-sigma variation within that region. Dashed lines show the mean temperature within each annulus.

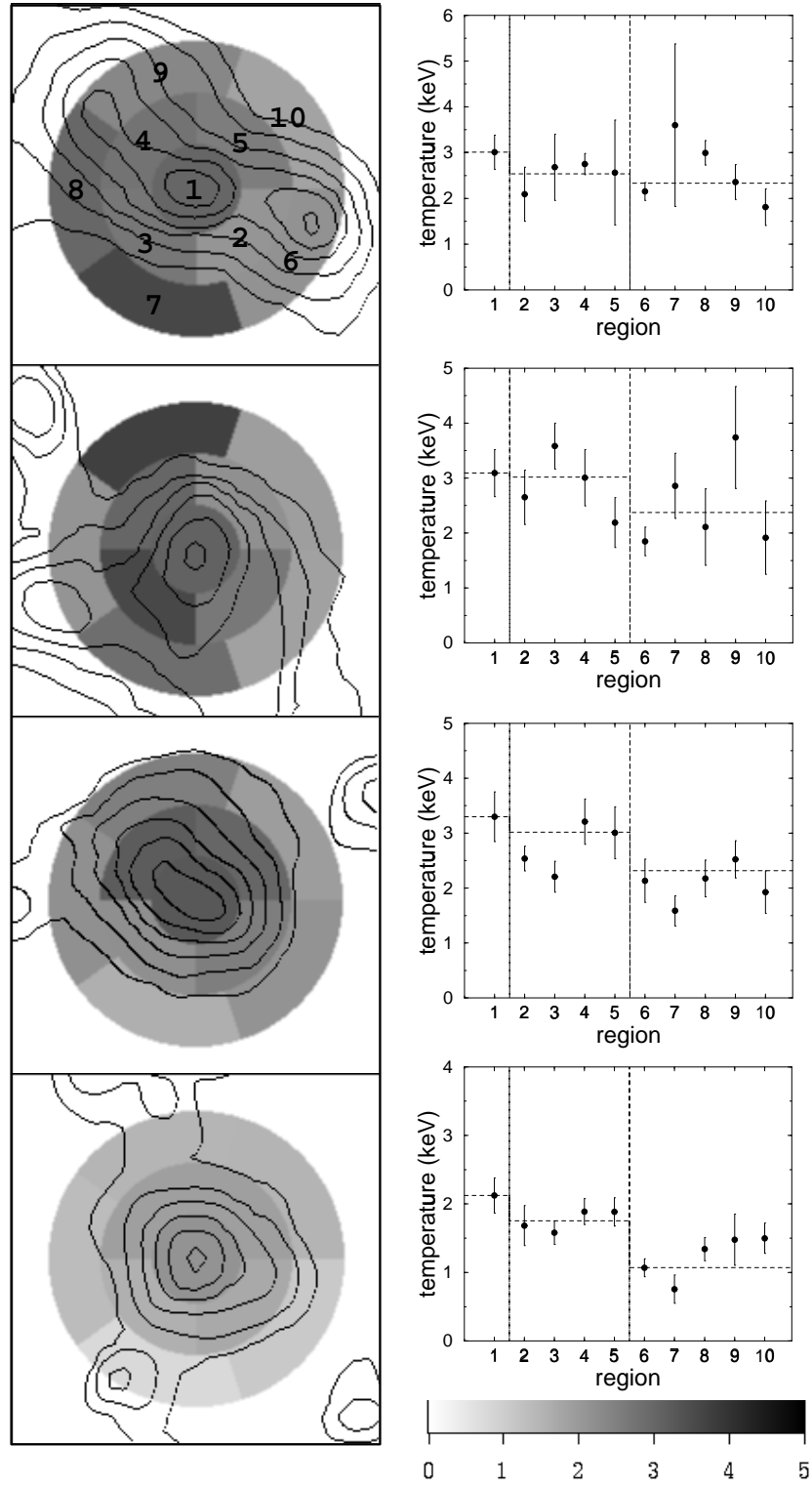


Figure 7.15. As in Figure 7.14, but for clusters CHDM1-4.

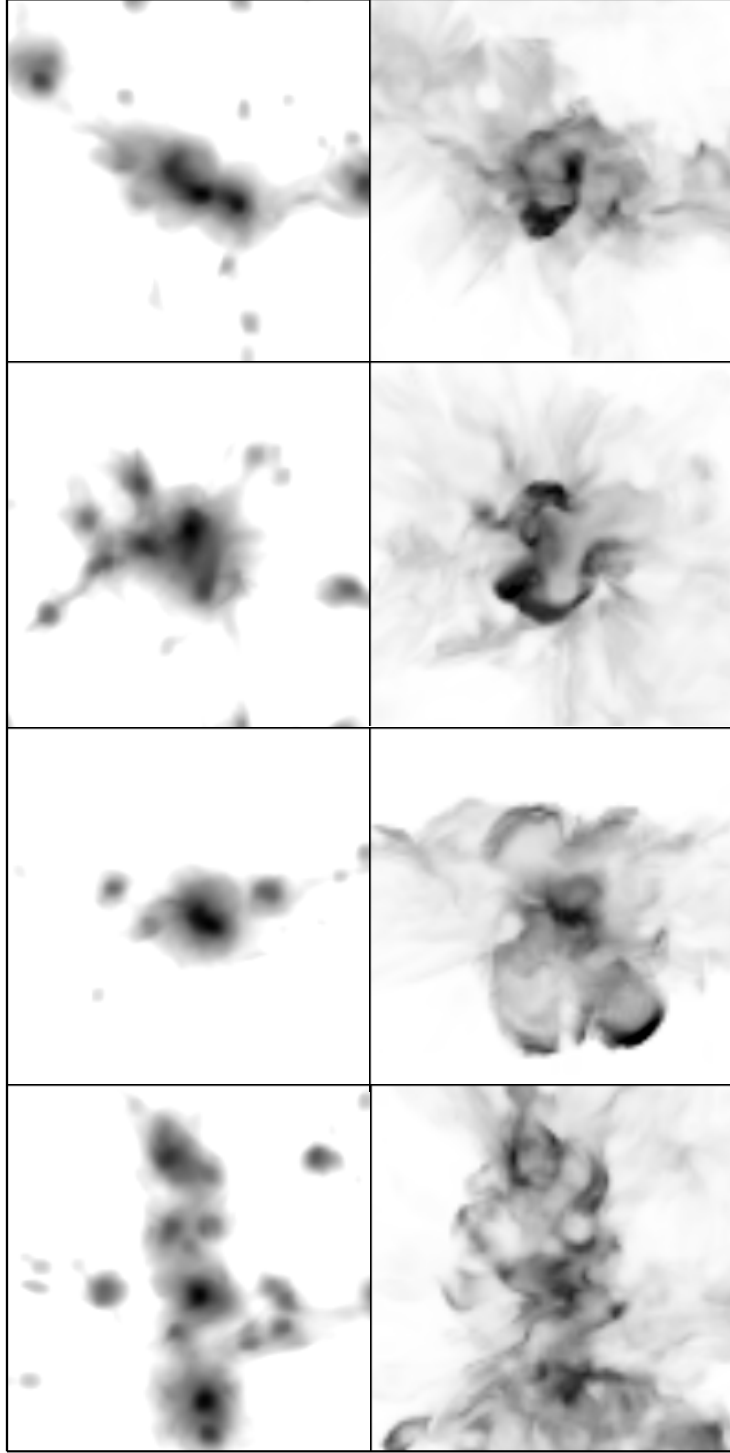


Figure 7.16. Bolometric surface brightness maps (left side) and luminosity-weighted temperature maps (right side) for clusters CDHM1-4; 16.2 Mpc on a side. The x-ray images show a logarithmic stretch of four decades while the temperature maps are linear and normalized to the virial temperature.

would they have the resolution to properly model the small, centrally located flows). In real clusters, the lack of a cooling flow is thought to be indicative of a recent merger, or some other major event, and so these clusters may have differences when compared to an unbiased sample, as in our simulated clusters. Also, the clusters presented here are, for the most part, smaller.

Nevertheless, they show a number of similar features. For example, most clusters shown here exhibit a decreasing temperature with radius (as was indicated by the radial profiles), which is also true of almost all of the clusters in the ASCA sample. The exception in our sample is cluster CDM1 which, as we have discussed, shows a very strong shock. Due its unusual degree of spherical symmetry, the shock shows up as a ring of enhanced temperature.

It is also useful to compare the fully resolved temperature maps with those presented in the observational format. For example, a few clusters (CDM3, CHDM3 and to a lesser extent, CDM2 and CHDM2) are undergoing, or are about to undergo, significant mergers. These show up as either separate emission peaks in the x-ray images or as elongations in the direction of the merger. Coupled with this is a tendency for the regions in the center and on an axis along the direction of the merger to be hotter than their surroundings. This is due to the pattern of shocks generated by the merger (which may not be head-on, producing a more complicated morphology than the planar, perpendicular shock a head-on collision generates). A similar morphology may be seen in some of the real clusters, for example A2319, A2256 and A754 (Markevitch 1996; Markevitch, Sarazin & Henriksen 1996).

Unfortunately, with the resolution afforded by these temperature maps (which is much better than previously available) it can still be difficult to easily explain the observed pattern of temperature variations. For example, cluster CDM2 has undergone a number of recent mergers, resulting in a complicated set of concentric shocks. However, in the binned temperature map (Figure 7.14), none of this is apparent due to the fact that a given region may overlap more than one coherent temperature structure.

Returning to the density maps for the CDM clusters (Figure 7.6–7.7) and the luminosity maps for the CHDM clusters (Figure 7.16), we see that, although the luminosity images are unrealistically deep, both models show a fair amount of substructure, as expected for $\Omega = 1$ cosmologies. The CHDM clusters in particular exhibit a great deal of structure within 5 Mpc of the cluster center, as might be predicted based on the more rapid increase of the non-linear mass in this model (see Chapter 6).

7.6 Conclusion

Based on these results, a coherent picture of the formation and structure of the hot gas halo of an X-ray cluster emerges. As in any hierarchical formation scenario, the cluster forms through a combination of mergers and continuous infall. Each large merger creates a quasi-spherical shock wave moving outward from the center. Its sphericity and strength are influenced by the environment the shock encounters. If the shock moves down a steep density incline into a low-density environment, it becomes hotter and moves more quickly. On the other hand, as a shock encounters a filament, it weakens, leaving the filament at a lower temperature than the rest of the intracluster material (although hotter than it was before). If the environment has a sufficiently high pressure, as in a subcluster, the shock may fail entirely, damping to a sound wave, and the material will be left on its original adiabat. As the subcluster continues to fall into the cluster, it encounters higher pressures which tend to compress and heat it. The dark matter velocity dispersion, on the other hand is not directly affected and appears to be largely unchanged until the subcluster approaches the cluster core more closely.

As a result of this infall, motions in the cluster gas are generated, creating a turbulent medium, despite the fact that the cluster is globally stable. The turbulence provides additional support against gravity, which causes the temperature to be lower than would otherwise be required (Figure 7.3). This provides an explanation for the observation made in chapter 6 that, while clusters follow the form of scaling laws derived from considerations of hydrostatic equilibrium, the temperatures are, on average, 30% lower than indicated

by such formulae. The magnitude of the turbulent motions are largest around the virial radius and decrease at smaller radii.

Within a cluster, we find that there is no significant correlation between the gas temperature and the dark matter velocity dispersion, probably due to the chaotic trajectories, but there is a correlation (albeit with some scatter) between the temperature and mean density within spheres of 300 and 600 kpc.

The simulations produce clusters which are in many ways similar to those observed. We compare directly with recent ASCA and ROSAT temperature maps of a few clusters and find that we can replicate a number of features of those images, such as the decrease in temperature with radius as well as the pattern of hotter than average regions during a merger.

Finally, we reiterate that these are adiabatic clusters and there are a number of physical processes that we have neglected. These include radiative cooling, which will tend to remove the densest clumps from the hot phase into small, cold, rotationally supported objects that may form stars. Another affect will be the formation of cooling flows in the central few hundred kpc of a cluster, greatly increasing the emissivity from this region. The stars in galaxies (or smaller objects) may generate winds which may heat the gas, increasing the entropy of the highest density regions. Magnetic fields may also influence the evolution of the cluster, most probably in its center.

Chapter 8

Adaptive Mesh Refinement Simulations of X-ray Clusters: Preliminary Results

8.1 Introduction

Due to their high luminosity and relative simplicity, the number density of X-ray clusters is one of our most precise measurements of the mass fluctuations in our universe. Combined with the observed anisotropy of the cosmic background radiation, it serves as a key constraint on cosmological models (Henry 1992; Eke, Cole & Frenk 1996). Unfortunately, there are still a number of unresolved difficulties in our understanding of clusters. These include the refusal of clusters to agree with some analytic scaling laws (Edge & Stewart 1991a), a result which adiabatic simulations seem unable to explain (Navarro, Frenk & White 1994 and previous chapters). Also, the decreased number of X-ray clusters at high redshift (Castander et al. 1993; Bower et al. 1994) is unexpected in the context of many popular models as well as being discrepant with optical observations of rich, distant clusters (Couchman 1991; Postman 1993). Having fixed the number density of clusters at $z = 0$, the rate of evolution is a strong indicator of cosmology, especially with regard to

the value of Ω , thus it is important to better understand the structure and formation of X-ray clusters.

While N-body studies provide much useful information (Cole & Lacey 1996), clusters are observationally identified either through their galaxies or by X-ray emission from a hot gas component. Since galaxies are very difficult to model correctly, and do not provide as straightforward a tracer of clusters as do X-ray observations, we turn to the baryonic gas. Most studies of individual X-ray clusters incorporating hydrodynamics have employed Lagrangian, particle-based methods (Evrard 1990; Katz & White 1993; Schindler & Müller 1993). Although these Smoothed Particle Hydrodynamics (SPH) methods provide excellent spatial resolution when combined with a suitable gravity solver, their shock-capturing capabilities are not as good as modern Eulerian methods. However, most cosmological Eulerian codes are hampered by a fixed grid and so provide good resolution in low-density regions, but poor resolution in high-density regions, such as the centers of X-ray clusters (Kang et al. 1994b).

There have been a number of attempts to overcome these problems, either by improving the shock-capturing capabilities of SPH, or adding adaptive resolution to grid methods. An example of the former is Shapiro et al. (1996), whose Adaptive SPH included both anisotropic smoothing interpolation and a more selective artificial viscosity algorithm. The latter approach is typified by Anninos & Norman (1994) who used a nested grid approach to improve the resolution in a single, pre-defined region. An alternative approach is to distort the grid in order to follow the collapsing regions (Pen 1995; Gnedin 1995).

In this chapter, we present a brief description of a new method which is designed to provide adaptive resolution combined with a modern, shock-capturing Eulerian hydrodynamics scheme. This Adaptive Mesh Refinement (AMR) method provided high resolution within small regions, the location of which are controlled automatically. After describing the numerical methodology in section 8.2, we present, in section 8.3, the results of a simulated xray-cluster in a volume $32 h^{-1}\text{Mpc}$ on a side, with cell sizes (in small regions) as small as $4 h^{-1}\text{kpc}$.

8.2 Methodology

The basic approach we take was first spelled out in the context of hydrodynamics by Berger & Colella (1989), which evolved from an earlier but similar scheme (Berger & Oliger 1984). In this section we will briefly describe the scheme, saving a full description for a future paper (Bryan & Norman 1996); a good general description of AMR is available in Neeman (1996).

8.2.1 The Grid Hierarchy

The grid hierarchy begins with the root grid which covers the entire domain of interest with a coarse, uniform, Cartesian grid. Then, as the solution evolves and interesting regions form, finer meshes are placed below these regions (we use the notation ‘below’ to refer to finer grids and ‘above’ for coarser grids). We restrict the ratio between cell sizes to be an integer, typically 2-4, and refer to a level as all the grids with the same cell size. In order to keep things as simple as possible, the edges of subgrids must coincide with the cell edge of its immediate parent (coarser) grid. Additionally, the hierarchy can be initialized with one or more static grids if a higher initial resolution is required (this feature will be used to simulated the X-ray cluster in section 8.3).

Given the hierarchy at some time t , we advance the solution in the manner of a W-cycle in a multigrid solver. First, we determine the maximum time step allowed for the coarsest grid based on a variety of accuracy and stability criteria and advance the grid by that time interval, Δt_0 . We then move down to the next level and advance all the grids on that level by a timestep Δt_1 ($\Delta t_1 \leq \Delta t_0$) which is the minimum of all the allowed timesteps for those grids. If there are more levels, we repeat this procedure until the bottom level of the hierarchy has been reached. Once there, we continue advancing the grids on the lowest level until they have ‘caught up’ to the next highest level above (i.e. $\sum \Delta t_l = \Delta t_{l-1}$). This procedure repeats itself until all grids have been advanced by a total time of Δt_0 .

Since interesting regions on the grid may move, the hierarchy must adapt itself. We do this whenever a level has caught up to the coarser level above it and consists of entirely rebuilding the grids on that level and below. This is done by applying the grid refinement criterion to the grids on that level, flagging zones which require extra grids. This criterion depends on the physical problem being simulated. We have implemented a number of options, including shock and steep gradient detectors, but in the problem described here, employ one based on the mass within a cell, imitating the Lagrangian nature of the SPH algorithm. Once a grid has a set of flagged cells, we run a machine-vision based algorithm (Berger & Rigoutsos 1991) to find edges and determine a good placement of subgrids. These subgrids must not overlap one another, must cover all flagged cells and their neighbouring cells, and be above a preset efficiency threshold, where the efficiency of a cell is defined as the ratio of flagged cells to total cells. Once these new subgrids have been identified, the solution from the next coarser grid is interpolated (see below) in order to initialize the values on the new grids. Finally, any overlap between these new subgrids and the old ones is identified and the solution within the regions of overlap is copied to the new subgrids. The entire procedure just outlined is then repeated on the new grids and in this way the entire hierarchy (from the original level examined and below) is rebuilt.

8.2.2 Hydrodynamics

To advance the gas state on any given grid by a timestep Δt , we use the higher-order accurate piecewise parabolic method (PPM) which requires cell-averaged quantities at time t and returns cell-averaged values at $t + \Delta t$. The algorithm used here is very similar to the one described in Chapter 3 but we employ the Direct Eulerian implementation (rather than Lagrange plus Remap) which has more straightforward flux information (Colella & Woodward 1984).

A grid has edges that require boundary information (three cells worth in each dimension for PPM). The root grid obtains this information in the usual fashion (periodically for most cosmological applications). Subgrids below the root grid must draw their bound-

aries from one of two sources. If available, the solution from any directly abutting grids on the same level is used; if not, the solution must be interpolated from the parent (coarser) grid above. We have experimented with a number of interpolation techniques, which must be fully three-dimensional (i.e. not split): the most successful has been a linear interpolator which is conservative — meaning that the sum of the conservative variables (e.g. mass, momentum) is constant over the coarse cell — and monotonic, which insures that no new extrema are introduced into the flow. These two characteristics are also very important in the basic PPM algorithm (Colella & Woodward 1984).

Once all the grids on a level have been advanced until they are synchronized with their parent grids, we must update the solution on the coarse grids that lie overtop the subgrids in order to ensure that all levels have the best solution available. This is done by summing the conserved quantities in the fine cells that correspond to a coarse cell and placing the result in the coarse cell ($q_{coarse} = \sum q_{fine}^i$). This accomplishes most of the update, however there is still a subtlety due to the difference between the fluxes around the boundary of each subgrids as computed by the grid, and by its subgrid. In order to correct for this difference, we modify all coarse cells that touch the edge of the subgrid but do not overlap, in order to reflect the more accurate fine grid fluxes.

8.2.3 Dark matter

The collisionless matter is modelled through particles. Since the particles follow the collapse of structure by definition, they are not adaptively refined. Nor are there duplicate sets of particles for each level; instead, each particle is associated with the most refined level available at its position in space and moved as the hierarchy is rebuilt. Thus, a particle has the same timestep and feels the same gravitational force as the grid at that level.

Although the particles are fixed in mass once initialized, we are free to create them with any set of masses and positions. For example, in the simulation described below, a static subgrid is included from the beginning in order to improve the initial baryonic mass resolution. On this subgrid, we also use smaller particles to improve the collisionless

mass resolution. One particle per initial grid point seems to provide approximately equal sampling between the dark matter and gas.

8.2.4 Gravity

As the hydrodynamical cell size is decreased, so must the gravitational softening length. This is accomplished through an adaptive particle-mesh technique, similar to the adaptive P³M scheme described by Couchman (1991). Beginning at the coarsest grid, all the particles (at this level and below) as well as the baryonic mass are deposited to a grid with a quadratic smoothing kernel (this is the Triangular Shaped Cloud, see Hockney & Eastwood 1980). The gravitational acceleration is then computed through the fast Fourier technique, allowing both open and periodic boundary conditions on the root grid (specifically, we use the S2 particle shape and the optimal Green’s function described in Hockney & Eastwood 1980). This is the acceleration which is then applied to the grid, resulting in a smoothed force which is interpolated back to the particles and cells with the same smoothing kernel as before. Since we use all the particles and the coarse grid contains all the baryonic mass, this is a complete force, due to all masses, differentiating it from the technique described in Villumsen 1989.

To compute a subgrid’s gravitational acceleration, we use the above procedure modified in three respects. First, only the particles on this grid and all grids directly below it are used (as well as the baryonic mass on the subgrid itself). Second, the Fourier method is modified to produce a force level which is smoothed at small radii, as before, but now also declines at large radii. This is done in order to match the force law computed on the next coarsest level, which leads to the third difference. In order to compute the total force on a particular particle or cell, we interpolate from not only the acceleration computed on this subgrid, but also from all coarser grids, adding each contribution. The result is a complete r^{-2} force law smoothed to the level of this grid with components from all higher levels.

8.2.5 Tests

We have performed a large number of tests, but will leave detailed descriptions for the method paper(s), simply listing some of them here. We have examined the behaviour of the hydrodynamics algorithm and interpolation functions when linear waves are passed into and out of a static refined region. The resulting wave reflection and transmission coefficients are less than 1% and greater than 99% for a wavelength of eight coarse cells, less than the attenuation which would have resulted simply due to numerical diffusion on the coarse mesh alone. This test was repeated with a Mach 2 shock wave which produced no anomalous features with amplitudes greater than 4-5%.

We have examined the algorithm's behaviour through a standard Sod shock tube test, correctly producing sharp shocks and contact discontinuities. The gravity module was tested by computing the acceleration due to analytic distributions. We have also performed a one-dimensional Zel'dovich pancake test (described in Chapter 3), successfully reproducing the accuracy of a 256 zone single grid result with an initial grid of 16 zones. One of the more demanding tests was to replicate (in three dimensions) the self-similar infall solution first fully described by Bertschinger (1985).

8.3 Results

We have simulated the formation of an adiabatic x-ray cluster in an $\Omega = 1$ universe. The initial spectrum of density fluctuations is CDM-like with a shape parameter of $\Gamma = 0.25$ (Efsthathiou et al. 1992b); the cluster itself is a constrained $3\text{-}\sigma$ fluctuation at the center (Hoffman & Ribak 1991), for a Gaussian filter of 10 Mpc. We use a Hubble constant of 50 km/s/Mpc and a baryon fraction of 10%. This cluster is the subject of a comparison project between twelve different simulation methods, the results of which will be presented in an upcoming paper (Frenk et al. 1996).

The simulation was initialized with two grids. The first is the root grid covering the entire 64 Mpc domain with 64^3 cells. The second grid is also 64^3 cells but is only 32 Mpc on a side and is centered on the cluster. Thus, over the region that forms the

cluster, we have an initial cell size of 500 kpc leading to an approximate mass resolution of $8.7 \times 10^8 M_\odot$ ($7.8 \times 10^9 M_\odot$) for the baryons (dark matter). We adopt a refinement mass for the baryons of $4M_{\text{initial}} \approx 3.5 \times 10^9 M_\odot$ (i.e. if the mass in any cell exceeds this value a finer mesh is created), but only allow refined grids within a box 25.6 Mpc on a side, centered on the cluster center since we are uninterested in objects outside this volume. Some objects will collapse outside this region and then move inside; these halos will not be properly modelled as high resolution is required throughout an object's evolution (Anninos & Norman 1996). We will focus mostly on the properties of the central cluster, which collapsed within the refined region. We have also run a set of AMR simulations for the same cluster with lower mass resolution and initial power in order to examine convergence.

The resulting cluster has a virial radius of 2.66 Mpc, defined as the radius within which the mean overdensity is 178 times the critical density. The resulting virial mass, temperature and one-dimensional velocity dispersion (for definitions, see Chapter 6) are $1.0 \times 10^{15} M_\odot$, 4.9 keV, 889 km/s.

In Figure 8.1, we show a typical example of the grid layout in this simulation. The top panel depicts the dark matter distribution in order to show the collapsed structure. A projection of the level hierarchy is shown below that with grids colour-coded by level. We do not show the full three-dimensional layout since, with about 400 grids, this would be too complicated to extract much useful information; however, the grid ‘shadows’ do demonstrate that the grid structure mirrors the mass morphology. The range of grid sizes and shapes is diverse, but most tend to be in the range of 10-60 zones per edge and somewhat rectangular. The images are 32 Mpc on a side; note the unrefined region around the boundary of the figure. An interesting side effect of the Lagrangian refinement criterion coupled with the varying cell size is that the root-mean-square fluctuations due to the shot noise from the finite number of particles is roughly constant (on a log basis).

The evolution of the projected baryon density and luminosity-weighted temperature fields are shown in Figures 8.2 and 8.3. These show that the collapse is highly filamentary and indeed, the resulting cluster dark matter distribution at $z = 0$ has a significant

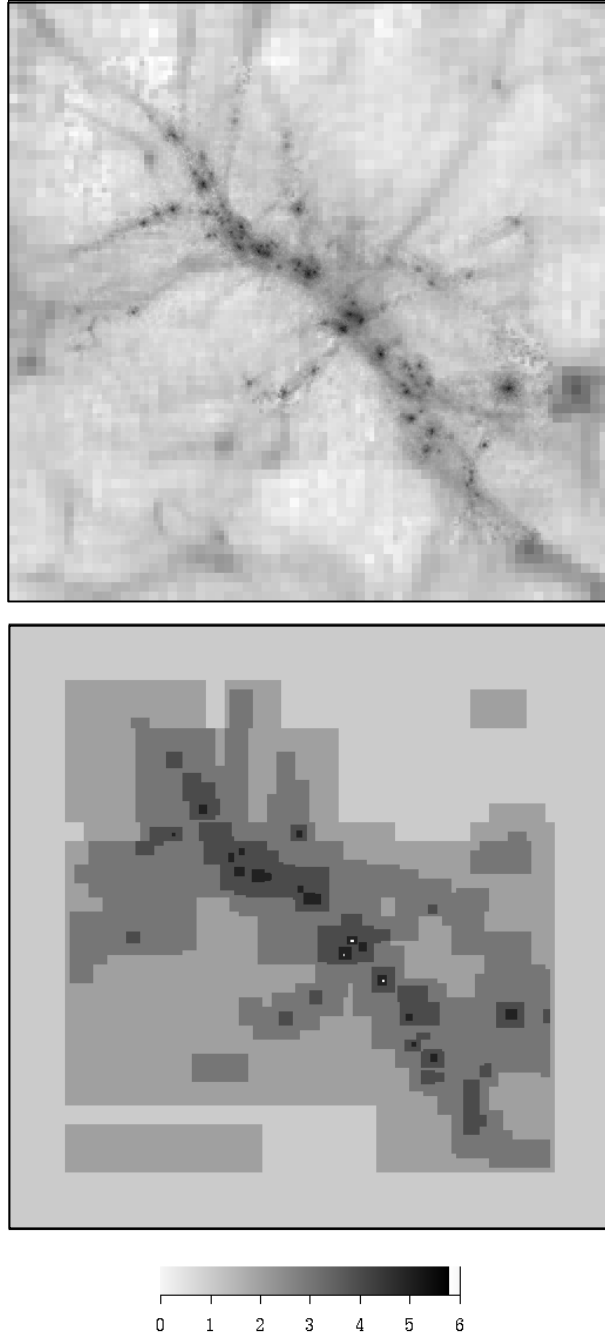


Figure 8.1. The logarithm of the dark matter surface density (top) and the projected grids (bottom), colour coded by level at $z = 2$. In order to increase the contrast of the three small level 6 grids, they have been coloured white. The figures are 32 Mpc on a side.

Table 8.1. Moments of Inertia

	x	y	z
Dark Matter			
x	0.832	0.166	0.000
y		0.763	0.093
z			0.484
Gas			
x	0.765	0.026	-0.020
y		0.787	0.037
z			0.652

asymmetry, as shown by the inertial moments ($I_{ij} = \sum m r_i r_j / \sum m$, computed within the virial radius) in Table 8.1. The gas is significantly more spherical, indicating that the pressure term is effective in quickly mixing orbits and the residual asphericity is most likely due solely to the gas response to the potential well of the dark matter.

The cluster formation process appears to be similar to that described in Chapter 7, although now we see a somewhat larger region (25.6 Mpc vs 12.8 Mpc). The initial objects that collapse are heavily biased to the area outlined by the main filament. The process of hierarchical merging then produces a series of shocks which spread into the outlying region surrounding the cluster. The last significant merger occurs at $z \sim 0.5$. The resulting distribution of density and temperature looks reminiscent of the halos studied previously.

The difference in terms of resolution becomes more apparent when we look at azimuthally-averaged radial profiles of the central cluster at $z = 0$. Figure 8.4 shows the baryonic and dark matter density profiles for this cluster. In order to gauge the convergence, results from three other AMR runs are also plotted. These runs had smaller initial grids (16^3 , 32^3 and 64^3) and therefore poorer mass resolution and less initial power. We also plot

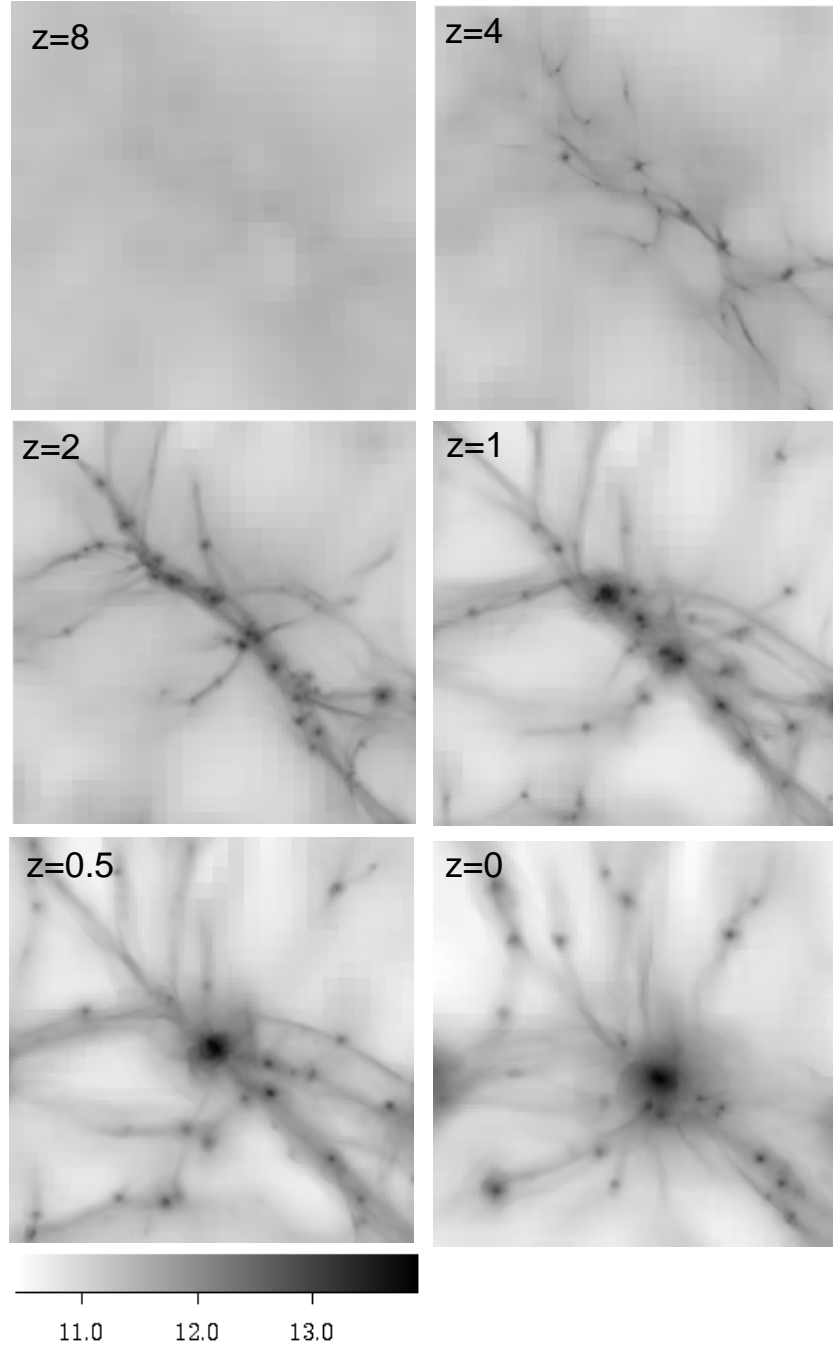


Figure 8.2. The evolution of the logarithm of the baryonic surface density field. The legend at the bottom left is in comoving M_{\odot}/Mpc^2 . Images are 25.6 Mpc on a side.

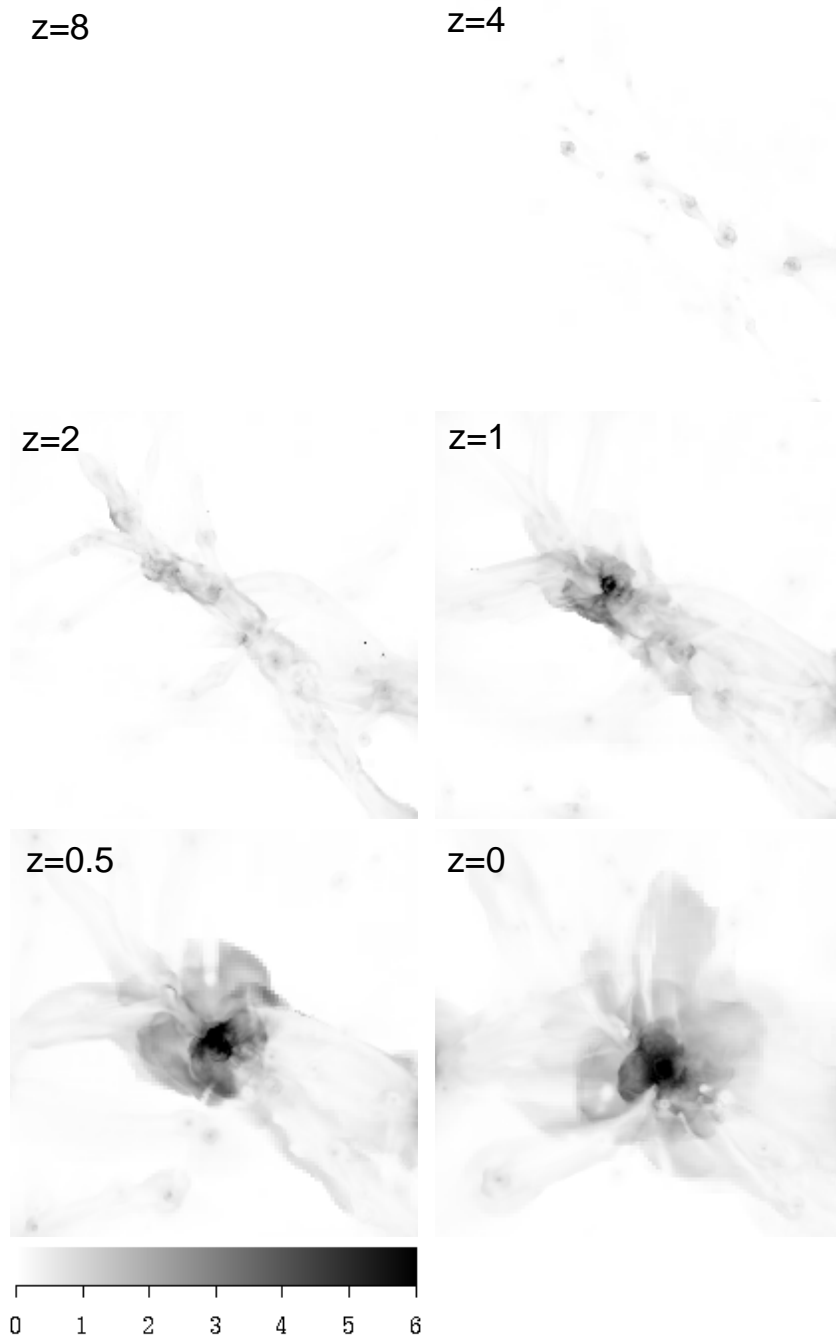


Figure 8.3. The evolution of the baryonic temperature field. The legend at the bottom left is in keV. Images are 25.6 Mpc on a side.

the profile from Navarro et al. (1996) for the dark matter,

$$\frac{\rho(r)}{\rho_{crit}} = \frac{\delta_0}{(r/r_s)(1 + r/r_s)^2}, \quad (8.1)$$

where $r_s = r_{vir}/c$ and δ_0 is set by the requirement that the mean density within the virial radius be 178 times the critical density. Setting the parameter $c = 8$ produces a remarkably good fit over three orders of magnitude. Lower resolution runs tend to fall off this curve on the low side. Lines above the curves indicate the changing slope with radius.

The gas density profile levels off at a few hundred kpc, around the knee in the dark matter profile. Lower resolution results exhibit systematically lower densities, and although we have not converged, the difference between the 64^3 initial grid and the higher-resolution run is slight. We remind the reader that this simulation does not include radiative cooling which would significantly affect the dynamics and structure of the inner few hundred kpc.

The turnover in density agrees with that seen in entropy, shown in Figure 8.5. There appears to be a cutoff in the entropy distribution, the cause of which is not currently understood. The temperature profile (same figure) is similar to some of those seen in the previous chapter, but rises to a larger value relative to the virial temperature than any of those clusters. For example, by $r/r_{vir} = 0.1$, $T/T_{vir} = 1.7$ (compare to Figure 3 of Chapter 7). Unfortunately, since we have only simulated a single cluster, we cannot be sure if this is a significant difference or simply a fluctuation.

The velocity-related profiles on the other hand, plotted in Figure 8.6, are in good agreement with the general trends of Chapter 7. The radial velocity shows infall around the virial radius and near zero net flow at smaller radii. The one-dimensional velocity dispersion of the dark matter (solid line in the bottom panel) rises from large radii to a peak slightly above σ_{vir} around $0.1r_{vir}$. However, now we can trace the dynamics much further, and see that it begins to fall again, dropping to $0.5\sigma_{vir}$ by $0.01r_{vir}$. The gas dispersion also mirrors those found earlier, but drops to a small constant value as $r \rightarrow 0$. This may be due to a bulk velocity of the central peak, since the velocity dispersion is

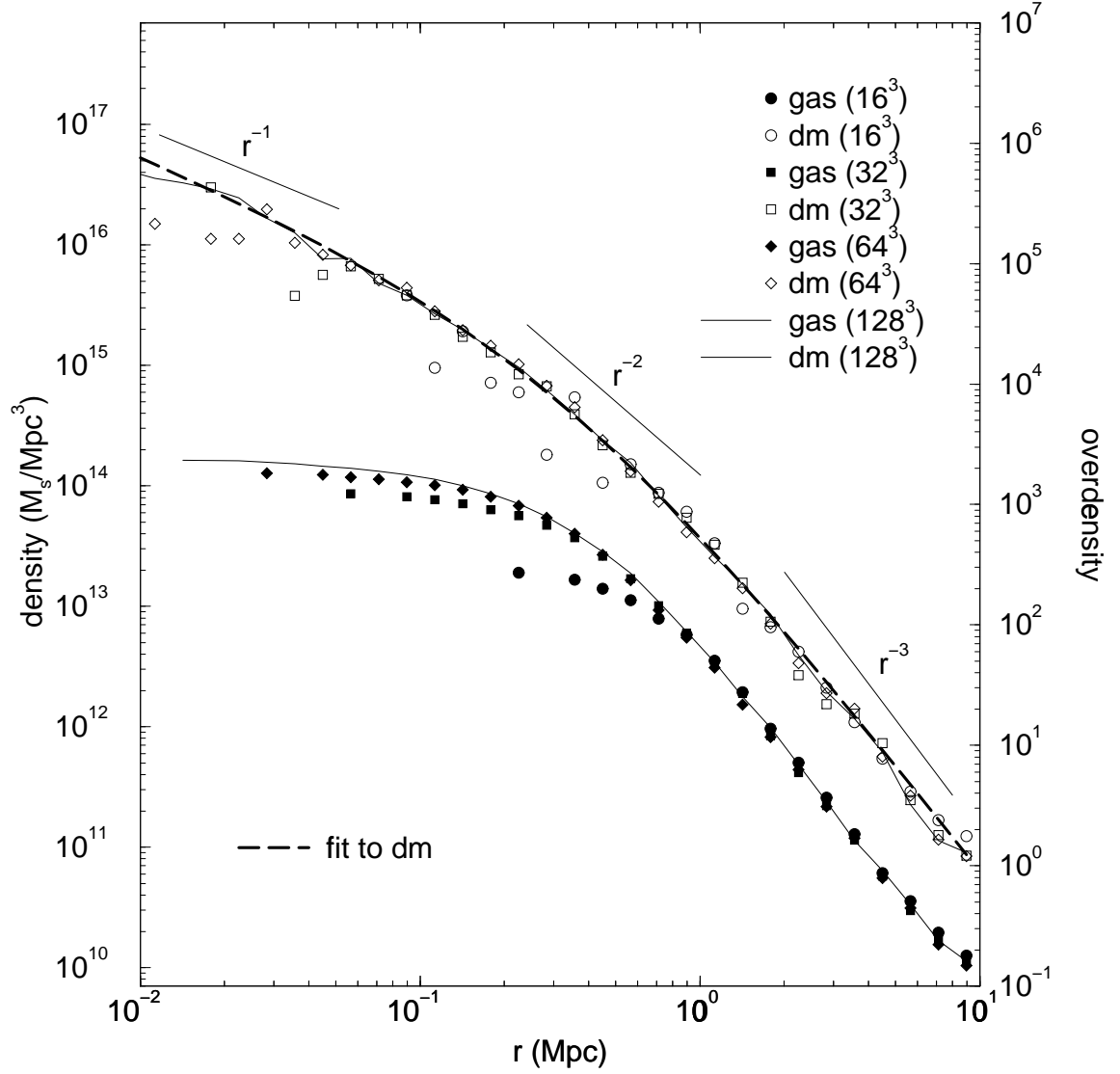


Figure 8.4. Dark matter and baryonic radial density profiles. Four different runs are shown with varying initial grids (16^3 , 32^3 , 64^3 and the effective 128^3 run). The solid dashed line is the fit from equation 8.1.

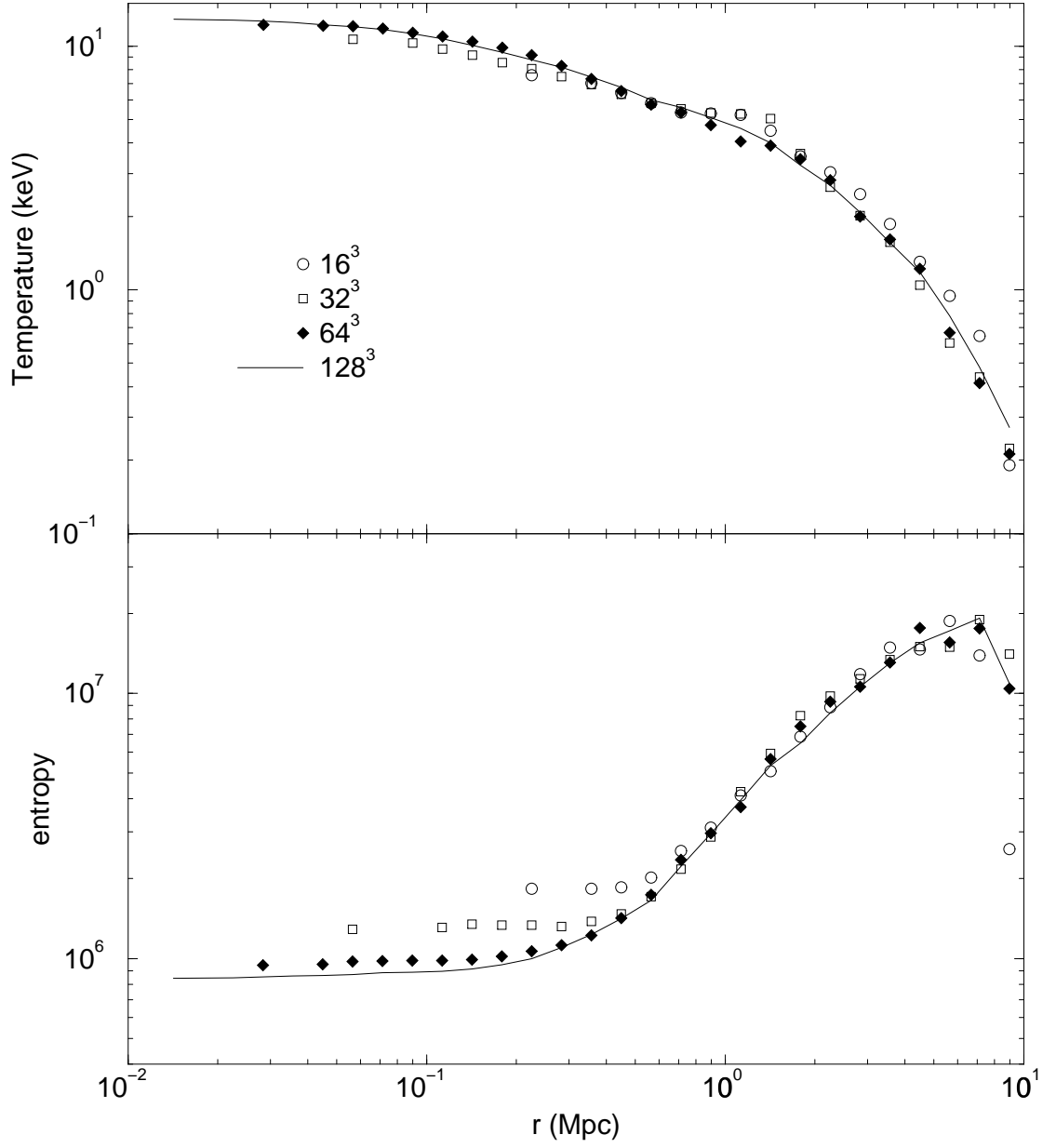


Figure 8.5. Temperature and entropy profiles. Four different runs are shown with varying initial grids (16^3 , 32^3 , 64^3 and the effective 128^3 run).

computed with respect to the center-of-mass velocity of the entire cluster (within the virial radius). The dark matter, but not the gas, shows a preference for radial orbits from $0.1r_{vir}$ – $1.0r_{vir}$. At lower radii, both are isotropic.

8.4 Conclusions

The AMR algorithm is complementary to other simulation techniques, such as SPH and Eulerian single grid method. The advantage of AMR is that it provides higher resolution than Eulerian methods and better shock capturing features than SPH codes. Further, it is more flexible than Lagrangian codes because we can control where the resolution is placed by changing the refinement criterion. Also, since each grid (more accurately, each level) advances with its own timestep the entire computation does not have to proceed at the speed of its slowest component. Another advantage over single grid methods is the smaller output size which allows more timesteps to be saved and analyzed. The primary disadvantage is that the scheme is quite complicated to code and modify; this implementation uses a combination of C++ to handle the dynamic grid hierarchy and FORTRAN 77 for computationally intensive tasks. Another drawback that will disappear with time is that the scheme is still quite young and hence, relatively untested.

Although the development and testing of the AMR algorithm is not fully complete, we demonstrate that it can model an X-ray cluster with many of the same characteristics of the single-grid code but with much higher resolution. The efficiency of the AMR method over a single grid for this simulation is quite high: a factor of 4000 in memory and 20 000 in CPU (conservatively), although, of course, the resulting solution is not as good in low density regions.



Figure 8.6. The radial velocity of the dark matter and gas (top panel), and the one-dimensional velocity dispersion, both total and radial (bottom panel).

Chapter 9

Conclusion

In the concluding chapter, we summarize the major results of the original work presented in Chapters 3-8 and then reflect on what this implies in terms of future work in this area.

9.1 Summary

A complete description of the numerical methodology used in the major portion of this thesis was presented in Chapter 3. We briefly described the hydrodynamics scheme chosen, the higher-order accurate piecewise parabolic method (PPM) and explain the changes required to make it work well in cosmological fluid flows. The collisionless matter which appears to gravitationally dominate clusters was modelled with particles while the gravitational force was calculated by solving Poisson's equation on a mesh. The second half of this chapter detailed a demanding series of tests that were aimed at gauging the scheme's performance when pushed to the limit of resolution.

In Chapter 4, we used the methods developed in the previous chapter to examine X-ray clusters in the once-popular Cold Dark Matter (CDM) model. By adopting a closed universe, a Hubble constant of 50 km/s/Mpc (which is well below most but not all recent determinations) and a baryon fraction of 6% of the critical density, the shape of the density fluctuations is fixed. The normalization of this spectrum is the remaining parameter and is set through the large-scale fluctuations of the cosmic background radiation

observed by the COBE experiment. We found that there are too many high-temperature and high-luminosity clusters as compared to observations. These results were compared to the identical model run with a different simulation code. Although the degree of numerical error is uncertain, the sign and magnitude of the expected discrepancy makes this model difficult to reconcile with observations.

Based on results like those just discussed, a number of alternative models have been proposed. In the fifth chapter, we investigated the Cold plus Hot Dark Matter (CHDM) model. The particular variant simulated involves a closed universe consisting of 30% neutrinos, 60% dark matter and 10% baryons with the same Hubble constant as before. The resulting cluster distribution matched observations reasonably well, both in terms of temperature and luminosity. A number of problems remain; the baryon fraction is below that indicated by cluster observations, but above the primordial nucleosynthesis result. Once again the numerical uncertainty was not well constrained.

This final difficulty provided the motivation for Chapter 6, which is the first detailed comparison between Eulerian hydrodynamical simulations and analytic theory. We began by carefully rederiving analytic predictions based on spherical symmetry, hydrostatic equilibrium and simplified structure assumptions. We then incorporated the expected effects of finite resolution on the cluster luminosity. Clusters were extracted from the simulation and compared to these scaling relations. The results showed excellent agreement with the predicted scaling behaviour for mass, temperature, dark matter velocity-dispersion and — once the finite resolution is factored in — total cluster luminosity. The normalization of the scaling laws however, did not, in some cases, agree perfectly with that derived. For example, the simulated temperatures were systematically lower, by a constant factor, than the values indicated by the scaling law. This result, which we believe to be robust, provides an improved normalization for the cluster mass-temperature relation. In the second section of this chapter, we combined these results with a simple prescription for predicting the number density of clusters with a given mass (the Press-Schechter relation) and compared the result to the simulations. The agreement was

reasonably good, which gives us increased confidence in both techniques. We ended the chapter by commenting on the implications for the CHDM model.

The work to this point dealt largely with bulk properties of clusters. In Chapter 7, we addressed the structure of X-ray halos through a simulation with considerably better resolution. Although we adopted a CDM model (with normalization compatible with cluster observations), the expectation is that general cluster properties will not be strongly dependent on this choice. First, we examined azimuthally averaged profiles and showed that the baryonic component is not completely thermalized, and is, in fact, partially supported by turbulent motions. This, we believe, causes a 25% reduction in the mean temperature, explaining a feature noted in the previous chapter. Then we discussed the temperature structure of clusters and showed that hierarchical formation results in a very large halo of hot gas which surrounds the cluster. This hot gas can affect smaller halos embedded within it, compressing and heating them. Also, large mergers create strong, quasi-spherical shocks that can result in the coherent outward motion of large parcels of gas. Finally, we computed observationally-motivated temperature maps and compared to recent ASCA measurements.

The final chapter presented some preliminary results from a new simulation technique, called Adaptive Mesh Refinement (AMR). We briefly outlined the algorithm and then presented some results from the simulation of an X-ray cluster. During this simulation, a nominal spatial resolution (in terms of box length to cell size) of 8192 was reached. Although incomplete, this work is important as AMR provides a number of advantages over other simulation techniques, combining high resolution with shock capturing Eulerian hydrodynamics.

9.2 Future Work

Although we have made much progress, much more remains to be done. Here we outline a few paths that we feel should be pursued in light of the results presented in this thesis. We believe we understand the bulk properties of adiabatic clusters in hierarchical structure

formation models, although higher resolution is essential for checking the conclusions and methodology described here. Also, many structural properties of adiabatic clusters are also clear. Here too we need higher resolution in order to probe the inner regions as well as a larger sample of simulated clusters. Nor have we addressed the statistics of cluster substructure, which may be a useful probe of Ω .

A shortcoming which is becoming more serious as the resolution increases and the uncertainty diminishes, is the absence of radiative cooling and stellar/galactic feedback. Although we have argued that the cooling time of the great clusters is longer than the Hubble time, it was much shorter at earlier epochs. The formation of stars and galaxies during this time may have an impact on the cluster structure due to the energy input of material from winds. While radiative cooling is easy to add (in fact, we have already done so), it will probably prove necessary to add some star formation in order to prevent overcooling. Unfortunately, the physics of star formation is extremely complicated even if we had adequate resolution; this forces us to use a parameterized approximation. Nevertheless, it is clear that such an approach is required. While difficult, adding more physics will have the additional benefit of improving our ability to compare simulations to observations, which is, after all, our ultimate aim.

List of References

Abell, G.O. 1958, ApJS3, 211

Abell, G.O. 1958, ARA&A3, 1

Abell, G.O., Corwin, H.G., Olowin, R.P. 1989, ApJS, 70, 1

Anninos, P., Norman, M.L., & Clarke, D.A. 1994, ApJ, 436, 11

Anninos, P. & Norman, M.L. 1996, ApJ, 459, 12

Bahcall, N.A. & Burgett, W. 1986, ApJ, 300, L35

Bahcall, N.A. 1988, ARA&A26, 631

Bahcall, N.A., & Cen, R.Y. 1992, ApJ, 398, L81

Bahcall, N.A., & Cen, R. 1993, ApJ, L49.

Bahcall, N.A., & Cen, R. 1994, ApJ, 426, 513

Bahcall, N.A., & Lubin, L.M. 1994, ApJ, 426, 513

Bardeen, J.M., Bond, J.R., Kaiser, M., & Szalay, A.S. 1986, ApJ, 304, 15

Bartlett, J.G, Silk, J. 1993, ApJ, 407, L45

Binney, J. & Tremain, S. 1987, Galactic Dynamics (Princeton: Princeton University Press), p. 228

Berger, M.J. & Olinger, J. 1984, J. Comp. Phys., 53, 484

- Berger, M.J. & Colella, P. 1989, *J. Comput. Phys.*, 82, 64
- Bertschinger, E. 1985, *ApJS*, 58, 39
- Berger, M. & Rigoutsos, I. 1991, *IEEE Transactions on Systems, Man, and Cybernetics*, 21, 1278
- Biviano, A., Girardi, M., Giuricin, G., Mardirossian, F., & Mezzetti, M. 1993, *ApJ*, 411, L13
- Bird, C.M. 1994, *AJ*, 107, 1637
- Blumenthal, G.R., Faber, S.M., Primack, J.R. & Rees, M.J. 1984, *Nature*, 311, 517
- Böhringer, H., Schwarz, R.A., Briel, U.G., Voges, W., Ebeling, H., Hartner, G., Crudace, R.G. 1992, in *Clusters and Superclusters of Galaxies* (Kluwer Publishers: Dordrecht), p. 71, ed. A.C. Fabian
- Bond, J.R. 1990, in *The Cosmic Microwave Background: 25 years later*, eds. N. Mandolesi and N. Vittorio (Dordrecht: Kluwer)
- Bond, J.R., & Myers, S.T. 1991a, in *Primordial Nucleosynthesis and Evolution of Early Universe Physics*, eds. K. Sato and J. Audouze (Kluwer, Dordrecht), p. 305
- Bond, J.R., & Myers, S.T. 1991b, in *Trends in Astroparticle Physics, Proceed. of the Nov. 1990 UCLA Conf.*, ed. D. Cline, (Singapore: World Scientific), p. 24
- Bond, J.R., Kaiser, N., Cole, S., Efstathiou, G. 1991, *ApJ*, 379, 440
- Bond, J.R. & Myers, S.T. 1996, *ApJS*, 103, 1
- Borgani, S., Plionis, M., Coles, P., Moscardini, L. 1994, *MNRAS*, submitted
- Bower, R.G., Böhringer, Brial, U.G., Ellis, R.S., Castander, F.J., & Couch, W.J. 1994, *MNRAS*, in press
- Branchini, E., Plionis, M., Sciamia, D.W. 1996, *ApJ*, 461, L17

- Briggs, F.H., Wolfe, A.M., Liszt, H.S., Davis, H.M., Turner, K.L. 1989, ApJ, 341, 650
- Bryan, G.L., Cen, R., Norman, M.L., Ostriker, J.P., Stone, J.M. 1994a, ApJ, 428, 405
- Bryan, G.L., Klypin, A., Loken, C., Norman, M.L., Burns, J.O. 1994b, ApJ, 437, L5
- Bryan, G.L., Norman, M.L., Stone, J.M., Cen, R., Ostriker, J.P. 1995, Comput. Phys. Comm., 89, 149
- Bryan, G.L., & Norman, M.L., 1996, in preparation
- Burns, J.O., Ledlow, M.J., Loken, C., Klypin, A., Voges, W., Bryan, G.L., Norman, M.L., White, R.A. 1996, ApJ, in press
- Bryan, G.L., & Norman M.L. 1996, in preparation
- Capri, A., Maurogordato, S. 1995, ApJ, 438, 507
- Castander, F.J., Ellis, R., S., Frenk, C.S., Dressler, A. & Gunn, J.E. 1994, ApJ424, L79
- Cavaliere, A. & Fusco-Femiano, R. 1976, *A&A*, 49, 137
- Cen, R. 1992, ApJS, 78, 341
- Cen, R. & Ostriker, J.P. 1992, ApJ, 399, L113
- Cen, R.Y., Gnedin, N.Y., Ostriker, J.P. 1993a, ApJ, 417, 387
- Cen, R. & Ostriker, J.P. 1993a, ApJ, 417, 387
- Cen, R. & Ostriker, J.P. 1993b, ApJ, 417, 415
- Cen, R., & Ostriker, J.P. 1994, ApJ, 431, 451
- Chiang, W.H., Ryu, D., and Vishniac, E.T. 1989, ApJ, 339, 603
- Cole, S. & Lacey, C. 1996, preprint (astro-ph/9510147)
- Colella, P. & Woodward, P.R. 1984, J. Comput. Phys., 54, 174

- Couch, W.J., Ellis, R.S., Malin, D.F., & MacLaren, I. 1991, MNRAS, 249, 606
- Couchman, H.M.P. 1991, ApJ, 368, 23
- Couchman, H.M.P., Thomas, P.A., Pearce, F.R. 1995, ApJ, 452, 797
- Cowie, L.L., Henriksen, M., & Mushotzky, R. 1987, ApJ, 317, 593
- Crone, M.M., Evrard, A.E., & Richstone, D.O. 1994, ApJ, 434, 404
- Crone, M.M., & Geller, M.J. 1995, ApJ, 110, 21
- Dalton, G.B., Efstathiou, G., Maddox, S.J., Sutherland, W.J. 1992, ApJ, 390, L1
- David, L.P., Slyz, A., Jones, C., Forman, W., & Vrtillek, S.D. 1993, ApJ, 412, 479
- Davis, M., Efstathiou, G., Frenk, C.S., & White, S.D.M. 1985, ApJ, 292, 371
- Davis, D.S., & Mushotzky, R.F. 1993, AJ, 105, 491
- Dekel, A., Blumenthal, G. Primack, J.R., & Oliver, S. 1989, ApJ, 338, L5
- Dekel, A. 1994, ARA&A, 32, 99
- Eastwood, J.W., & Brownrigg, D.R.K. 1979, J. Comput. Phys, 32, 24
- Ebeling, H., Allen, S.W., Crawford, C.S., Edge, A.C., Fabian, A.C., Böhringer, H., Voges, W., Huchra, J.P., to appear in Röntgenstrahlung from the Universe, Würzburg 1995.
- Ebeling, H., Voges, W., Böhringer, H., Edge, A.C., Huchra, J.P., Briel, U.G. 1996, MNRAS, submitted, astro-ph/9602080
- Edge, A. 1990, PhD Thesis, University of Leicester
- Edge, A.C., Stewart, G.C., Fabian, A.C., Arnaud, K.A. 1990, MNRAS, 245, 559
- Edge, A.C. & Stewart, G.C. 1991a, MNRAS, 252, 414

- Edge, A.C. & Stewart, G.C. 1991b, MNRAS, 252, 428
- Edge, A.C., Stewart, G.C., Fabian, A.C. 1992, MNRAS, 258, 177
- Efstathiou, G., Davis, M., Frenk, C.S., & White, S.D.M. 1985, ApJS, 57, 241
- Efstathiou, G., Davis, M., Frenk, C.S., White, S.D.M. 1985, ApJS, 57, 241
- Efstathiou, G., Bond, J.R., & White, S.D.M 1992, MNRAS, 258, 1p
- Efstathiou, G., Dalton, G.B., Sutherland, W.J., Maddox S.J. 1992, MNRAS, 257, 125
- Eke, V.R., Cole, S., & Frenk, C.S. 1996, MNRAS, submitted
- Evrard, A.E. 1988, MNRAS, 235, 911
- Evrard, A.E. 1990, ApJ, 363, 349
- Evrard, A.E., Summers, F., Davis, M., 1994, ApJ, 422, 11
- Evrard, A.E., Metzler, C.A. & Navarro, J.F. 1996, preprint astro-ph/9510058
- Fabian, A.C., Arnaud, K.A., Nulsen, P.E.J. 1984, MNRAS, 216, 923
- Fabian, A.C. 1994, ARA&A, 32, 277
- Fahlman, G., Kaiser, N., Squires, G., Woods, D. 1994, ApJ, 437, 56
- Forman, W., Bechtold, J., Blair, R., Giacconi, R., Van Speybroeck, L., & Jones, C. 1981, ApJ, 243, L133
- Frenk, C.S., White, S.D.M., Efstathiou, G., Davis, M. 1990, ApJ, 351, 10
- Frenk, C.S. et al. 1996, in preparation
- Gelb, J.M., & Bertschinger, E. 1994, ApJ, 436, 467
- Geller, M.J., & Beers, T.C. 1982, PASP, 94, 421

- Gioia, I.M., Henry, J.P., Maccacaro, T., Morris, S.L., Stocke, J.T., Wolter, A. 1990, *ApJ*, 356, L35
- Girardi, M., Fadda, D., Mardirossian, F., Mezzetti, M., Biviano, A. 1996, *ApJ*, 457, 61
- Gnedin, N.Y. 1995, *ApJS*, 97, 231
- Gorski, K.M., Hinshaw, G., Banday, A.J., Bennett, C.L., Wright, E.L., Kogut, A., Smoot, G.F., Lubin, P. 1994, *ApJ*, in press
- Grossman, S.A., & Narayan, R. 1988, *ApJ*, 324, L37
- Gursky, H., Kellogg, E., Murry, S., Leony, C., Tananbam, H., & Giacconi, R. 1971, *ApJ*, 167, L81
- Henriksen, M.J., & Markevitch, M.L. 1996, *ApJ*, 466, L79
- Henry, J.P., & Arnaud, K.A. 1991, *ApJ*, 372, 410
- Henry, J.P., Gioia, I.M., Maccacaro, T., Morris, S.L., Stocke, J.T., & Wolter, A. 1992, *ApJ*, 386, 408
- Henry, J.P. 1992, in *Clusters and Superclusters of Galaxies* (Kluwer Publishers: Dordrecht), ed. A.C. Fabian, p. 311
- Henry, J.P., Gioia, I.M., Huchra, J.P., Burg, R., Mclean, B., Böhringer, H., Bower, R.G., Briel, U.G., Voges, W., MacGillivray, H., Cruddace, R.G. 1995, *ApJ*, 449, 422
- Herbig, T., Lawrence, C.R., Readhead, A.C.S., & Gulkis, S. 1995, *ApJ*, 449, 5
- Hernquist, L. & Katz, N. 1989, *ApJS*, 70, 419
- Hockney, R.W., & Eastwood, J.W. 1980, *Computer Simulation Using Particles* (New York: McGraw-Hill)
- Hoffman, Y., & Ribak, E. 1991, *ApJ*, 380, 5

- Holtzman, J.A., Primack, J.R. 1993, ApJ, 405, 428
- Hunstead, R.W., Pettini, M., & Fletcher, A.B. 1990, ApJ, 356, 23
- Hunter, C. 1962, ApJ, 136, 594
- Irvine, W.M. 1965, Ann. Phys., 32, 322
- Jaffe, W. 1992, in Clusters and Superclusters of Galaxies (Kluwer Publishers: Dordrecht), p. 109, ed. A.C. Fabian
- Jain, B. & Berstchinger, E. 1994, ApJ, 431, 495
- Jing, Y.P., Mo, H.J., Borner, G., Fang, L.Z. 1993, ApJ, 411, 450
- Jing, Y.P. & Fang, L.Z. 1994, ApJ, 432, 438
- Jones, C. & Forman, W. 1984, ApJ, 276, 38
- Jones, C. & Forman, W. 1992, in Clusters and Superclusters of Galaxies (Kluwer Publishers: Dordrecht), p. 49, ed. A.C. Fabian
- Kaiser, N. 1986, MNRAS, 222, 323
- Kang, H., Cen, R.Y., Ostriker, J.P., & Ryu, D. 1994a, ApJ, 428, 1
- Kang, H., Ostriker, J.P., Cen, R., Ryu, D., Hernquist, L., Evrard, A.E., & Bryan, G.L. 1994b, ApJ, 430, 80
- Katz, N., Hernquist, L., Weinberg, D. 1992, ApJ, 399, L109
- Katz, N., & White, S.D.M. 1993, ApJ, 412, 455
- Katz, N., Weinberg, D., Hernquist, L. 1996, preprint, astro-ph/9509107
- Kauffmann, G. & Charlot, S. 1994, ApJ, 430, 97
- Kellogg, E., Baldwin, J.R., & Koch, D. 1975, ApJ, 199, 299

- Kitiyama, T. & Suto, Y. 1996, MNRAS, in press
- Klypin, A. & Kopylov, A. 1983, Sov. Astron. Lett., 9, 41
- Klypin, A., Holtzman, J., Primack, J.R., & Regöös, E. 1993, ApJ, 416, 1
- Klypin, A., & Rhee, G. 1994, ApJ, 428, 399
- Klypin, A., Borgani, S., Holtzman, J., Primack, J. 1994, ApJ, 444, 1
- Kofman, L., Klypin, A., Pogosyan, D., Henry, J.P. 1995, ApJ, submitted
- Kogut, A., Lineweaver, C., Smoot, G.F., Bennet, C.L., Banday, A., Bogges, N.W.,
Cheng, E.S., De Amici, G., Fixsen, D.J., Hinshaw, G., Jackson, P.D., Janssen,
H., Keegstra, P., Lowenstein, K., Lubin, P., Mather, J.C., Tenorio, L., Weiss, R.,
Wilkinson, D.T., Wright, E.L., 1993 ApJ, 419, 1
- Kowalski, M.P., Cruddace, R.G., Snyder, W.A., Fritz, G.G. 1993, ApJ, 412, 489
- Lacey, C. & Cole, S. 1993 MNRAS, 262, 627
- Lacey, C. & Cole, S. 1996, MNRAS, submitted
- Lanzetta, K.M. 1993, PASP, 105, 1063
- Lanzetta, K.M., Wolfe, A.M., Turnshek, D.A. 1995, ApJ, 440, 435
- Lahav, O., Edge, A.C., Fabian, A.C., Putnet, A. 1989, MNRAS, 238, 881
- Lauer, T.R., Postman, M. 1994, ApJ, 425, 418
- Layzer, D. 1964, ARA&A, 2, 341
- Lubin, L.M., Bahcall, N.A. 1993, ApJ, 415, L17
- Ma, C.-P. & Bertschinger, E. 1994, ApJL, 434, 5
- Ma, C.-P. 1996, preprint (astro-ph/9605198)

- Maddox, S.J., Sutherland, W.J., Efstathiou, G., Loveday, J. 1990, MNRAS, 242, 43P
- Markevitch, M., Yamashita, K., Furuzawa, A., Tawara, Y. 1994, ApJ, 436, L71
- Markevitch, N., Mushotzky, R., Inoue, H., Yamashita, K., Furuzawa, A., & Tawara, Y. 1996, ApJ, 456, 437
- Markevitch, M. 1996, ApJ, 465, L1
- Markevitch, M., & Vikhlinin, A. 1996, preprint, astro-ph/9605026
- Markevitch, M., 1996, preprint, astro-ph/9606113
- Markevitch, M.L., Sarazin, C.L., & Irwin, J.A. 1996, preprint, astro-ph/9606112
- Mellier, Y., Fort, B., & Kneib, J.P. 1993, ApJ, 407,33
- Merritt, D. 1987, ApJ, 313, 121
- Metzler, C. & Evrard, A. 1994, ApJ, 437, 564
- Miralda-Escudé, J. & Babul, A. 1994, ApJ, 449, 18
- Mo, H.J. & Miralda-Escudé, J. 1994, ApJ, 430, 25
- Mo, H.J., Jing, Y.P., White, S.D.M. 1996, MNRAS, submitted, astro-ph/9602052.
- Mohr, J.J., Evrard, A.E., Fabricant, D.G., & Geller, M.J. 1995, ApJ, 447, 8
- Mould, J., Huchra, J. P., Bresolin, F., Ferrarese, L., Ford, H. C., Freedman, W. L., Graham, J., Harding, P., Hill, R. Hoessel, J. G., Hughes, S. M., Illingworth, G. D., Kelson, D., Kennicutt, R. C., Jr., Madore, B. F., Phelps, R., Stetson, P. B., Turner, A. 1995, ApJ, 449, 413
- Mushotzky, R.F. 1984, PhyScr, T7, 157
- Mushotzky, R.F. 1992, in Clusters and Superclusters of Galaxies (Kluwer Publishers: Dordrecht), p. 91, ed. A.C. Fabian

- Myers, S.T., Baker, J.E., Readhead, A.C.S. 1993, preprint
- Navarro, J.F., & White, S.D.M. 1993, MNRAS, 265, 271
- Navarro, J.F., Frenk, C.S., White, S.D.M. 1994, preprint
- Navarro, J.F., Frenk, C.S., White, S.D.M. 1994, ApJ, 462, 563
- Neeman, H.J. 1996, PhD Thesis, University of Illinois
- Nichol, R.C., Ulmer, M.P., Kron R.G., Wirth, G.D., & Koo, D.C. 1994, ApJ, 267, 771
- Nolthenius, R., Klypin, A., Primack, J. 1994, ApJ, 422, L45
- Ostriker, J.P., 1993, ARA&A, 31, 689
- Peebles, P.J.E. 1980, The Large-Scale structure of the Universe (Princeton: Princeton University Press)
- Peebles, P.J.E. 1993, Principles of Physical Cosmology, p. 457
- Pen, U.-L. 1995, ApJS, 100
- Postman, M. 1993, in Observational Cosmology, ASP Conf. Ser. 51, edited by G. Chin-
carini, A. Iovino, T. Maccacaro, and D. Maccagne (ASP, San Francisco), p. 260
- Press, W.H., & Schechter, P., 1974, ApJ, 187, 425
- Raphaeli, Y., Ulmer, M., Gruber, D. 1994, ApJ, 429, 554
- Raymond, J.C. & Smith, B.W. 1977, ApJS, 35, 419
- Richstone, D., Loeb, A., & Turner, E.L. 1992, ApJ, 413, 492
- Richtmyer, R.D., & Morton, K.W. 1967, Difference Methods for Initial-Value Problems
(Interscience: New York), 2nd ed.
- Riess, A.G., Press, W.H., Kirshner, R.P. 1995, BAAS, 187, 17.12

- Romer, A.K., Collins, C.A., Böhringer, H., Ebeling, H., Voges, W., Cruddace, R.G., & MacGillivray, H.T. 1994, preprint
- Ruiz-Lapuente, P. 1996, *ApJ*, 465, 83L
- Ryu, D., Vishniac, E.T., Chiang, W.H. 1990, *ApJ*, 354, 389
- Ryu, D., Ostriker, J.P., Kang, H., & Cen, R. 1993, *ApJ*, 414, 1
- Sarazin, C.L. 1988, in *Cooling flows in clusters and galaxies* (Netherlands: Kluwer Academic Publishers), p. 1
- Sarazin, C.L. 1992, in *Clusters and Superclusters of Galaxies* (Kluwer Publishers: Dordrecht), ed. A.C. Fabian, p. 131
- Scaramella, R., Zamorani, G., Vettolani, G. 1991, *ApJ*, 376, L1
- Scaramella, R. 1992, *ApJ*, 390, L57
- Schechter, P. 1976, *ApJ*, 203, 297
- Schindler, S. & Müller, E. 1993, *A&A*, 272, 137
- Shapiro, P.R., Martel, H., Villumsen, J.V., Owen, J.M. 1996, *ApJS*, 103, 269
- Spitzer, L. Jr. 1978, *Physical Processes in the Interstellar Medium* (New York: Wiley)
- Squires, G., Kaiser, N., Babul, A., Fahlman, G., Woods, D., Neumann, D.M., Böhringer, H. 1996, *ApJ*, 461, 572
- Strang, G. 1968, *SIAM J. Num. Anal.*, 5, 506
- Stompor, R., Gorski, K.M., Banday, A.J. 1995, *MNRAS*, submitted
- Stone, J.M., & Norman, M.L. 1992, *ApJS*, 80, 753
- Sunyaev, R.A. & Zel'dovich, Ya.B. 1972, *Comm. Astrophys. Sp. Phys.*, 4, 173

- Sutherland, W.J. 1988, MNRAS, 234, 159
- The, L. & White, S. 1986, AJ, 92, 1248
- Thomas, P.A. & Couchman, H.M.P. 1992, MNRAS, 257, 11
- Trumper, J. 1990, Physikalische Blätter, 46, 137
- Tsai, J.C., Katz, N., Bertschinger, E. 1994, ApJ, 423, 553
- Villumsen, J.V. 1989, ApJS, 71, 407
- Walker, T.P., Steigman, G., Schramm, D.N., Olive, K.A., & Kang, H.S. 1990, ApJ, 376, 51
- Walter, C., & Klypin, A. 1996, ApJ, 462, 13
- Watkins, R., & Feldman, H. 1995, ApJ, 453, 73
- Waxman, E., & Miralda-Escudé, J. 1995, ApJ, 452, 1
- Weinberg, D.H., & Gunn, J.E. 1990, MNRAS, 247, 260
- White, D.A. & Fabian, A.C. 1995, MNRAS, 273, 72
- White, S.D.M. 1992 in Clusters and Superclusters of Galaxies (Kluwer Publishers: Dordrecht), ed. A.C. Fabian, p. 17
- White, S.D.M., Briel, U.G., & Henry, J.P. 1993, MNRAS, 261, L8
- White, S.D.M., Navarro, J.N., Evrard, A.E., & Frenk, C.S. 1993, Nature, 366, 429
- Woodward, P.R. & Colella, P. 1984, J. Comput. Phys., 54, 115
- Woodward, P.R. 1986 in Astrophysical Radiation Hydrodynamics (D. Reidel: Dordrecht), eds. K.-H. Winkler and M.L. Norman
- Wu, X.-P. 1994, ApJ, 435, 66

Yuan, W. 1991, Ph.D. Thesis, Drexel University

Zel'dovich, Ya.B. 1970, *Å*, 5, 84

Curriculum Vitae

Greg Bryan

Personal Information

Born: July 10, 1967 in Edmonton, Alberta, Canada
Citizenship: Canadian
Marital Status: Single

Education

Ph.D. (present program)	Astronomy, University of Illinois at Urbana-Champaign Urbana, Illinois, USA
B.Sc. (1989)	Physics, University of Calgary Calgary, Alberta, Canada

Awards

Astronomy Department Fellowship, University of Illinois, 1990
University of Calgary Scholarship, University of Calgary, 1985

Professional Associations

American Astronomical Society, junior member
Canadian Astronomical Society, student member

Refereed Publications

- “The X-ray Luminosity Function and Gas Mass Function for Poor + Rich Clusters of Galaxies”, Burns, J.O., Ledlow, M.J., Loken, C., Klypin, A., Voges, W., Bryan, G.L., Norman, M.L., & White, R.A., 1996, *Astrophysical Journal*, in press
- “A Piecewise Parabolic Method for Cosmological Hydrodynamics”, Bryan, G.L., Norman, M.L., Stone, J.M., Cen, R., Ostriker, J.P., 1995, *Computer Physics Communication* 89, 149.

- “A Parallel Self-consistent Field Code”, Hernquist, L., Sigurdsson, S., Bryan, G.L., 1995, *Astrophysical Journal*, 446, 717.
- “The Evolution of X-ray Clusters in a Cold Plus Hot Dark Matter Universe”, Bryan, G.L., Klypin, A., Loken, C., Norman, M.L., Burns, J.O., 1994, *Astrophysical Journal*, 437, L5.
- “A Comparison of Cosmological Hydrodynamic Codes”, Kang, H., Ostriker, J.P., Cen, R., Ryu, D., Hernquist, L., Evrard, A.E., Bryan, G.L., Norman, M.L., 1994, *Astrophysical Journal*, 430, 83.
- “X-ray Clusters from a High-Resolution Hydrodynamic PPM Simulation of the Cold Dark Matter Universe”, Bryan, G.L., Cen, R., Norman, M.L., Ostriker, J.P., Stone, J.M., 1994, *Astrophysical Journal*, 428, 405.
- “Energy Distributions of Symbiotic Novae”, Bryan, G.L., Kwok, S., 1991, *Astrophysical Journal*, 368, 252.
- “On the Formation of Carbon Stars,” Bryan, G.L., Volk, K., Kwok, S., 1991, *Astrophysical Journal*, 365, 301.

Non-Refereed Publications

- “High-Resolution 3D Simulations and Jet Turbulence”, Loken, C., Burns, K., Bryan, G., Norman, M. 1996, to appear in *Energy Transport in Radio Galaxies and Quasars*, ASP Conference Series, eds. P. Hardee, A. Bridle, and A. Zensus.
- “A Hydrodynamic Simulation of Cluster Formation”, Bryan, G.L., Norman, M.L., 1994, in *Numerical Simulations in Astrophysics*, eds. Franco, J., Lizano, S., Aguilar, L., Daltabuit, E. (Cambridge: Cambridge University Press), 73.
- “Adapting CMHOG to Cosmological Studies”, Bryan, G.L., 1992, NCSA Technical Report 004.